

Colloidal Electronics

by

(Albert) Tianxiang Liu

B.S. Chemical Engineering, California Institute of Technology, 2014

SUBMITTED TO THE DEPARTMENT OF CHEMICAL ENGINEERING IN PARTIAL
FULFILLMENT OF THE REQUIREMENTS FOR THE DEGREE OF

DOCTOR OF PHILOSOPHY IN CHEMICAL ENGINEERING

AT THE

MASSACHUSETTS INSTITUTE OF TECHNOLOGY

July 2020

© 2020 Massachusetts Institute of Technology. All rights reserved.

Signature of author.....
Department of Chemical Engineering
July 27, 2020

Certified by
Michael S. Strano
Carbon P. Dubbs Professor of Chemical Engineering
Thesis Supervisor

Accepted by
Patrick S. Doyle
Robert T. Haslam (1911) Professor of Chemical Engineering
Graduate Officer

Colloidal Electronics

by

(Albert) Tianxiang Liu

Submitted to the Department of Chemical Engineering
on July 27, 2020, in partial fulfillment of the requirements for the degree of
Doctor of Philosophy in Chemical Engineering

Abstract

Arming nano-electronics with mobility extends artificial systems into traditionally inaccessible environments. Carbon nanotubes (1D), graphene (2D) and other low-dimensional materials with well-defined lattice structures can be incorporated into polymer microparticles, granting them unique electronic functions. The resulting **colloidal electronic** ‘cells’, comprised of microscopic circuits connecting artificial ‘organelles’ (*e.g.*, generators, sensors, logic gates, *etc.*), combine the modularity of modern electronics with the characteristic mobility found in dispersive colloidal systems. Fundamental to **colloidal electronics** lie two challenges: **(1)** providing electrical energy to a microscopic system with limited footprint; and **(2)** developing energy efficient electronic devices and circuitries with low power consumption. In this context, my thesis introduces two concepts – *Autoperforation* and *Asymmetric Chemical Doping* – as means to fabricate and power electronic circuit elements on top of colloidal particles. These advances allow us to build the first **colloidal electronic** system that perform autonomous functions integrating energy harvesting, chemical detection and digital memory recording – all within a form-factor no larger than biological cells.

Thesis Supervisor: Michael S. Strano, Carbon P. Dubbs Professor of Chemical Engineering

Acknowledgements

I am forever grateful to have had Michael as my graduate advisor, who have continually fostered my scientific curiosity and encouraged my research independence. The extent to which his support has shaped my academic career cannot be overstated. Michael's positivity, creativity, and scientific leadership have played a critical role in my growth as a scientist.

I would like to thank Will Tisdale and Karthish Manthiram, for being a part of my Thesis Committee, for offering critical feedback at every step along the way, and for asking important questions to help me with my research and to steer me in the right direction. I would also like to thank Martin Bazant, Bill Deen, Jim Swan, Alan Hatton, and Klavs Jensen for their guidance and feedback on my thesis research.

During my time at MIT, I have had many memorable moments as a teacher. I am grateful for the support of Bill Deen and Martin Bazant during my time as a TA for 10.50, of Klavs Jensen and Michael during my time as a TA for 10.65, of Michael during my time as a project consultant for 10.26, and Benjamin Hansberry for the Teaching Development Fellow program.

I am extremely fortunate to have been surrounded by a group of talented colleagues within Michael's group. I am particularly thankful to the help of Yuichiro Kunai, Anton Cottrill, Sayalee Mahajan, Pingwei Liu, Jingfan Yang, Ge Zhang, and Allan Brooks. I would also like to thank the students whom I have had a good fortune to work with: Stephen Gibbs, Jamila Smith-Dell, Max Saccone, Linh Nguyen, Rafid Mollah, Yannick Eatmon, Paul Baynard, Ian Timothy, and Lexy LeMar.

My thesis work has also greatly benefitted from a number of collaborators: Marek Hampel and Tomás Palacios from MIT, Ana Pervan and Todd Murphey from Northwestern, Paul McEuen from Cornell, Josh Daymude Andrea Richa from Arizona State, Dan Goldman and Dana Randall from Georgia Tech.

I would also like to thank the following people who have helped me to navigate through career decisions: Michael, Karthish Manthiram, Connor Coley, Will Tisdale, Jim Swan, Bill Deen, Klavs Jensen, Kate Galloway, Ariel Furst, Crystal Chu, and Lennon Luo from MIT, Greg Fu, Mark Davis, John Seinfeld, Zhen-Gang Wang, and Max Saccone from Caltech, Ana Pervan and Todd Murphey from Northwestern, Josh Daymude from Arizona State, and Dana Randall from Georgia Tech.

The past six years would not have been possible without my former scientific advisors: Jack Roberts, Greg Fu, Mark Davis, Stacey Zones, Steve Sieck, Jim Lindberg, Andy Mobley, and Heriberto Hernandez-Soto. These mentors have been, are, and will always be a source of inspiration. I can only hope to provide my own students with a small fraction of what they have provided me.

I would not be where I am if it were not for my parents, Weimin Liu and Li Wang, and my partner, Stacey Fang. They have provided a tremendous amount of support in every way imaginable. For without their devotion, I would not have accomplished any of these, and without them, none of these accomplishments would have been meaningful.

Table of Contents

Abstract.....	3
Acknowledgements.....	4
Introduction to Colloidal Electronics.....	9
1.1 Colloidal State Machines: Autonomous Particles with On-Board Computation.....	14
1.1.1 What are Colloidal State Machines?.....	14
1.1.2 CSM Coagulation and Sedimentation.....	17
1.1.3 Materials-Enabled CSM Modules.....	18
1.1.4 CSM Systems Integration.....	27
1.1.5 Control and Robotics of Autonomous CSMs.....	33
1.1.6 Application of CSMs.....	37
1.1.7 Conclusions and Outlook.....	40
1.2 Direct Electricity Generation Mediated by Molecular Interactions with Low Dimensional Carbon Materials – A Mechanistic Perspective.....	42
1.2.1 Motivations for Solvent Mediated Energy Harvesting Methods.....	42
1.2.2 Mechanistic Overview.....	45
1.2.3 Perspectives, Application Space, and Energy Metrics.....	112
1.3 References.....	124
Sustainable Power Sources Based on High Efficiency Thermopower Wave Devices.....	144
2.1 Background on Thermopower Wave Technology.....	145
2.2 High Efficiency Thermopower Wave Devices.....	146
2.3 References.....	160
Electrical Energy Generation via Reversible Chemical Doping on Carbon Nanotube Fibers ...	163
3.1 Background on Excess Thermopower.....	164
3.2 From Thermopower Wave to Asymmetric Chemical Doping.....	166
3.3 Experimental Details.....	177
3.4 References.....	179
Observation of the Marcus Inverted Region of Electron Transfer from Asymmetric Chemical Doping of Pristine (<i>n, m</i>) Single-Walled Carbon Nanotubes.....	182
4.1 Background on Asymmetric Chemical Doping.....	183
4.2 Asymmetric Chemical Doping Mechanism – an Electron Transfer Theory.....	185

4.3	Experimental Details	203
4.4	References	204
Solvent-Induced Electrocatalysis at an Asymmetric Carbon Interface		207
5.1	Asymmetric Chemical Doping to Drive Electrochemical Transformations	208
5.2	References	227
Autoperforation of Two-Dimensional Materials as Method to Prepare Electronic Colloids		229
5.1	Autoperforation of Two-Dimensional Materials for Generating Two Terminal Memristive Janus Particles	230
5.2	Autoperforation of Two-Dimensional Materials to Generate Colloidal State Machines Capable of Locomotion.....	265
6.2.1	Patterned Pt Electrodeposition on Graphene Surfaces using Inkjet Printing.....	274
6.2.2	Pt-Coated Janus CSMs via Aligned Inkjet Printing and Autoperforation	280
6.2.3	Self-Driven Locomotion of Pt-Coated Janus Graphene-CSMs in H ₂ O ₂	281
6.2.3	Towards Navigation in a Complex Fluidic Network	283
6.2.4	Experimental Details.....	294
6.3	References	295
Collective Synchronization in Self-driven Chemo-mechanical Relaxation Oscillators		300
7.1	Background on Emergent Behavior and Relaxation Oscillators.....	300
7.2	The Physical Design that Results Synchronized Oscillation	302
7.3	An Analytical Model that Captures the Primary Mode of Oscillation.....	305
Outlook on Colloidal Electronics.....		310
8.1	Across the Solid-Liquid Interface: Energy Harvesting for Distributed Colloidal Electronic Systems.....	311
8.2	Self-powered Electrocatalysis as Means of Interparticle & Particle-to-Cell Communication.....	314
8.2.1	Field-assisted Electro-reduction of CO ₂ to C ₂₊ Products on Morphologically Controlled Metal Surfaces.....	315
8.2.2	MOF-Metal Hybrid Electrodes with Engineered Catalytic Pockets for Electro-Oxidative C-C Coupling.....	317
8.3	Low-power Nano-electronic Circuits and Their Incorporation into Microparticle Tracers to Enable Time-dependent Sensing and Continuous Information Recording	320
8.3.1	Fabrication of Vertically Aligned Memristor Arrays	320
8.3.2	Design and Optimization of a Local Timing Mechanism.....	322

8.3.3	Engineering Time-aware Colloidal Tracers for Time-dependent Continuous Information Recording	323
8.4	Putting It All Together – Static (Equilibrium) and Dynamic (Non-equilibrium) Assembly of Electronic Colloids into Integrated Electrical Networks	326
8.4.1	Top-down Integration of Colloidal Electronics into Functional Composites	326
8.4.2	Bottom-up Assembly of Colloidal Electronics into Artificial Efferent Neurons .	327
8.5	References	329

Chapter 1

Introduction to Colloidal Electronics

Articles that contribute to this chapter:

Liu, A. T.; Hempel, M.; Yang, J. F.; Pervan, A.; Koman, V. B.; Zhang, G.; Kozawa, D.; Murphey, T. D.; Palacios, T.; Strano, M. S. *submitted*

Liu, A. T.; Zhang, G.; Cottrill, A. L.; Kunai, Y.; Kaplan, A.; Liu, P.; Koman, V. B.; Strano, M. S. *Advanced Energy Materials* (2018), 8, 1802212

Liu, A. T.; Zhang, G.; Strano, M. S. *Robotic Systems and Autonomous Platforms* (2019), 389

Arming nano-electronics with mobility extends artificial systems into traditionally inaccessible environments. Carbon nanotubes (1D), graphene (2D) and other crystalline materials with well-defined lattice structures can be incorporated into polymer microparticles, granting them unique electronic functions.¹ The resulting **colloidal electronic** ‘cells’ (*ca.* 100 μm in diameter), comprised of microscopic circuits connecting artificial ‘organelles’ (*e.g.*, generators, sensors, logic gates, *etc.*), combine the modularity of modern electronics with the characteristic mobility found in dispersive colloidal systems. They perform autonomous functions integrating optical energy harvesting, chemical detection and digital memory recording – all within a form-factor no larger than biological cells.²

My thesis research seeks to advance device capabilities for individual **colloidal electronic** particles, and explore higher-order assemblies of these building-blocks into hierarchical **colloidal**

electronic matter (Figure 1-1). This research topic, positioned at the intersection between *materials design*, *chemical catalysis*, and *electronic device fabrication*, aims to address one central challenge: **Can we build materials the way nature builds us?** Biological scaffolds are constructed with long-range order that spans many orders of magnitude, affording control checkpoints not only at the molecular (*e.g.*, protein) level, but also on the micro- (*e.g.*, organelle) and meso- (*e.g.*, cellular) scales. The ability to create ‘tissue’-like colloidal electronic matter, consisting of heterogeneously integrated electronic ‘cells’, will enable access to complex functions observed previously only in biological systems (Figure 1-2).

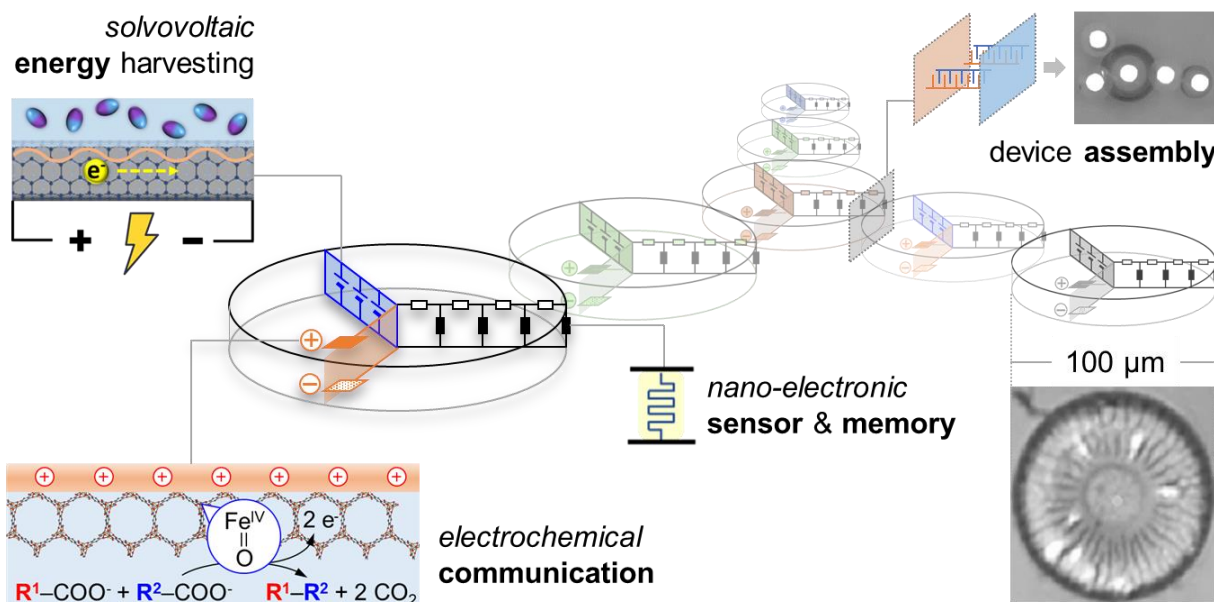


Figure 1-1. Colloidal electronic matter assembled using individual *electronic colloids*. In *colloidal electronics*, nano-electronic devices are integrated into a colloidal microparticle, conferring specific capabilities: *energy harvesting* (Chapter 2 – 4), *communication* (Chapter 5), *sensing and memory* (Chapter 6). The assembly of *colloidal electronic matter* is discussed in Chapter 7.

Specifically, my thesis builds toward a paradigm of rational design and synthesis of **colloidal electronics** by (1) developing *in situ* energy generation methods, (2) creating inter-particle communication techniques suitable for autonomous systems at the cellular scale, (3) designing energy efficient colloidal electronic devices and circuits that bring macroscopic functions to the microscale, and (4) establishing protocols to assemble hierarchical colloidal scaffolds with long-range spatial order via a combination of top-down (*e.g.*, 3D printing) and bottom-up (*e.g.*, guided self-assembly) approaches.

By laying the foundation towards this new class of materials, my studies generate new opportunities in environmental monitoring, biomedical sensing, distributed computing and human-machine interface. In the context of human health, several task-oriented applications enabled by the colloidal electronic technology can be pursued in the future (**Figure 2**). For example, one can develop **individual colloidal electronic devices** capable of (a) localized electrochemical communication with neurons, (b) time-dependent data acquisition that maps the spatial composition of mammalian gut microbiota, and **cooperative colloidal electronic systems** that can (c) be processed into smart textiles for advanced diagnostics, or (d) self-assemble into artificial neurons that reestablish synaptic connections to alleviate symptoms of spinal cord injury or neurodegenerative disorders. The future directions of **colloidal electronics** are expanded in further detail in the outlook sections of *Chapter 8*.

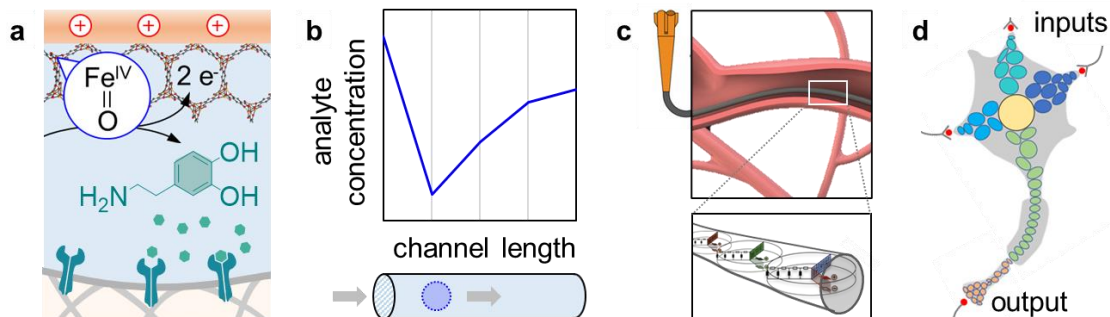


Figure 1-2. Task-oriented applications for individual (**a**, **b**) and ensemble (**c**, **d**) colloidal electronic matter. (**a**) *in situ* electro-chemical communication to cells; (**b**) Location-dependent data acquisition; (**c**) integrated smart textile; (**d**) self-assembled artificial neuron.

Minimizing the invasiveness of electronic devices, both in a *spatial* and a *temporal* sense, has motivated innovations such as *flexible* electronics^{3,4} that establish intimate tissue connections, and *transient* electronics⁵ that naturally decompose after their intended diagnostic window. **Colloidal electronics** – with microscopic sizes that allow them to be dispersed in, and travel with, the surrounding fluid to circulate and exit the body – represent the ultimate *flexible* and *transient* electronic system. The field of colloidal electronics aims to bring ubiquitous intelligence in the form of distributed systems. Fundamental to this new platform lie four challenges: **(1)** providing electrical energy to a microscopic system with limited footprint (*ca.* 1 picolitre or $10 \times 10 \times 10 \mu\text{m}^3$ in volume); **(2)** enabling inter-particle communication; **(3)** developing energy efficient devices and circuitries with low power requirements; and **(4)** forming a network of individual units that function in unison.

Electricity is the central energy currency in artificial programmable systems, akin to the role ATP plays in biological systems. The idea of creating a micrometer sized *autonomous* machine dates back to the 1950s,⁶ but was only (partially) realized over half a century later,² in part due to the

difficulties associated with active energy generation at the micrometer scale. Chemists and materials scientists have developed ‘*molecular machines*’ (ca. 1 nm) and ‘*active matter*’ (ca. 100 nm), which have been externally powered by either stochastic thermal interactions or global electromagnetic ‘tethers’, limiting the potential for these systems to achieve self-driven control. On the electronics side, the continuous shrinkage of semiconductor device footprint has given rise to ‘*micro-robots*’ (ca. 1 cm) and ‘*smart dusts*’ (ca. 1 mm). For characteristic device sizes (L) less than 100 μm , however, the mismatch between the amount of energy stored onboard ($\sim L^3$) and that required for basic device operations ($\sim L^2$) is prohibitive (**Figure 1-3**).⁷ Therefore, to provide colloidal electronics regular access to onboard electricity, an effective active energy harvesting method is essential.⁷

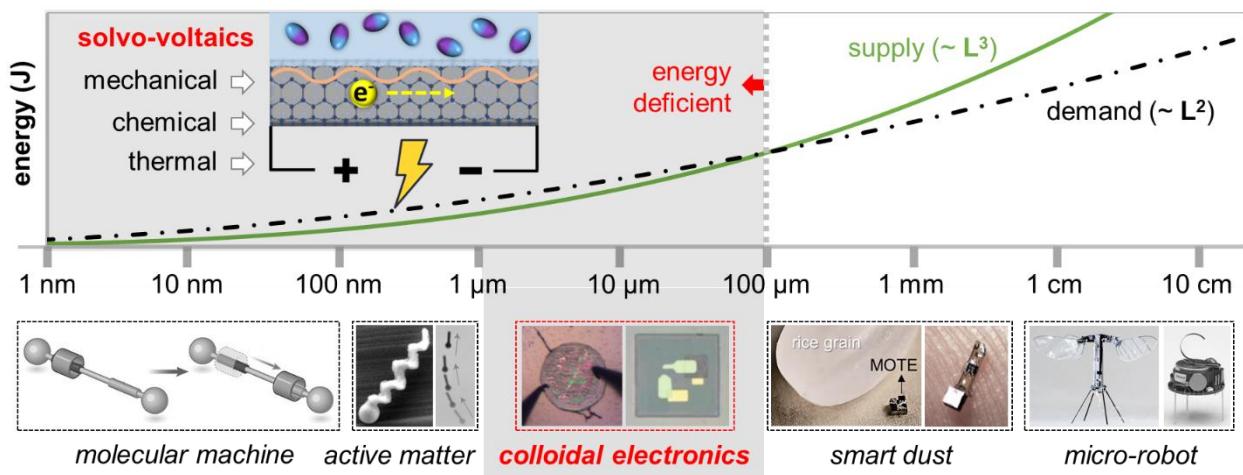


Figure 1-3. Energy *supply* and *demand* plotted for artificial autonomous systems at various scales. For devices with characteristic lengths under 100 μm , current energy storage and harvesting techniques are insufficient to power microsystems continuously.

To bridge this energy gap, the first part of my thesis explores different liquid-based energy harvesting methods more broadly known as the ‘*solvo-voltaic*’ effect,⁸ a phenomenon whereby

various local energy inputs are converted into electricity within a quantum-confined nanostructure (e.g., single-walled carbon nanotube, or SWCNT) by virtue of interactions with the surrounding solvent molecules. This technique stands out as a promising candidate to complement existing energy generation schemes like the photovoltaics, whose utility is diminished where visible light is not present. In the following two sections, I introduce one sub-type of **colloidal electronics** – Colloidal State Machines (CSMs), and present several ‘*solvo-voltaic*’ mechanisms in the literature by which electricity can be directly harvested from the ambient environment.

1.1 Colloidal State Machines: Autonomous Particles with On-Board Computation

A machine has components that work together to accomplish a task. Colloids are particles, usually less than 100 μm , that are small enough as to not settle out of solution. *Colloidal State Machines* (CSMs) are particles capable of functions such as *sensing*, *computation*, *communication*, *locomotion*, and *energy management* all controlled by the particle itself. Their design and synthesis is an emerging area of materials science research. Many CSM systems anticipate synthetic versions of biological cells in autonomy and may find ultimate utility in bringing these specialized functions to previously inaccessible locations. This perspective examines the emerging literature and highlights certain design principles and strategies towards the realization of CSMs. Potential applications to medicine; environmental monitoring; and geological, astrophysical and undersea exploration are highlighted.

1.1.1 What are Colloidal State Machines?

Colloidal State Machines (CSMs) are particle systems capable of *autonomous* functions, with examples only recently emerging from the electronics and robotics literature.² *Autonomy* in this setting is defined as the ability for machines to make decisions (or ‘compute’), without external

actuation and supervision. CSMs are distinct from ‘micro-robotic’ systems⁹, since the latter refer to mm to cm scale systems. They are also distinct from ‘nano-robotics’, and similarly ‘active matter’, since these terms most often describe a device controlled from a distance using magnetic fields or light, with an infrastructure off the entity itself. The concept of a *puppet* can be used to distinguish where computation and decision making are designed to occur, with CSMs designed for these tasks to be on the particle itself. Nature has evolved micron-sized entities capable of autonomy and computation. CSMs embody this new objective, harnessing emerging developments in nanofabrication, micro- and nano-electronics, materials science and autonomous control. The motivating vision is to extend nanoelectronics into traditionally inaccessible locations using colloidal microparticles.

CSMs follow a conceptual path from past efforts to miniaturize both electronics and robotics (**Figure 1-4**). Although remarkable progress has been made with silicon-based microsystems (sometimes referred to as ‘Smart Dust’)¹⁰ that integrate *sensing, computation, and communication*, these microsystems are static and have volumes typically larger than 1 mm³, which limit their potential application compared to CSMs. As a result, successful implementations of microscale electronic systems remain elusive in medicine except for environments where volume is less of a constraint, such as the mammalian digestive tract.¹¹ In contrast, CSMs are envisioned as autonomous, self-contained machines that allow modular, programmable functions, all embedded on substrates that enable mobility in surrounding media, with volumes *at least* 1000 times smaller than today’s silicon-based approaches.

Just like any biological cell, a CSM cannot function without a suite of well-coordinated ‘organelles’. We surveyed several early examples of CSMs in literature,^{1,2,12-15} and identified that they all possess the following five independently addressable modules (or a subset thereof): (1)

sensors for information input, (2) a central processing unit for logic computation and data storage, (3) communication channels (e.g., between neighboring devices for information transfer), (4) modes of actuation and locomotion, and (5) an on-board energy source (harvesting and/or storage) to power these circuit operations (**Figure 1-4**). In this perspective, we present the state-of-the-art in these five fundamental building blocks in the context of CSMs; an account of the progress that has been made; and a forward-looking vision towards building prototype electronic devices onto a colloidal particulate platform.

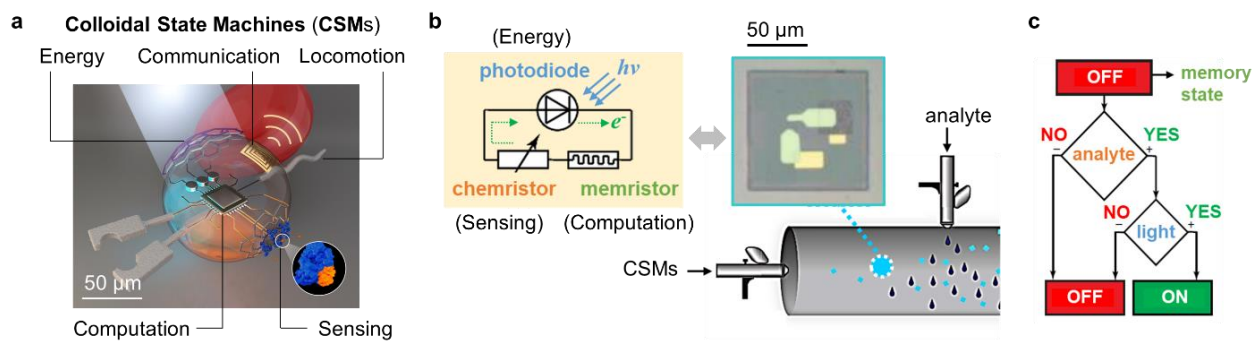


Figure 1-4. Colloidal State Machines (CSM) – concept and prototypes from the literature. **(a)** Schematic illustration of a CSM, prepared by Betsy Skrip. Scale bar, 50 μm. **(b)** Schematic illustration of an early CSM prototype being used for analyte and light detection inside a vapor chamber.² **Left:** Electrical circuit diagram of the CSM. The photodiode converts light into current, which turns on the memristor if and only if the chemiresistor detects a prescribed analyte. **Right:** Top view optical micrograph of the CSM used. Scale bar, 50 μm. Reproduced with permission.² Copyright 2018 Nature Publishing Group. **(c)** Block diagram for the CSM summarizing the combinational logic. The initial memory state OFF changes to ON only in the presence of both chemical and light signals. Reproduced with permission.² Copyright 2018 Nature Publishing Group.

1.1.2 CSM Coagulation and Sedimentation

1.1.2.1 CSM Coagulation – Colloidal Stability

An important factor for a colloidal system lies in its stability, which in general depends on particle charges and coating chemistry. Lyophilic colloids, which exhibit a high force of attraction between the particles and their embedded liquid, for instance, are known to result in very stable colloidal solutions (e.g., starch and proteins). These solvent-loving molecules, when adsorbed onto the surface of the particle, may provide steric or entropic stabilization.¹⁶ The concept of relative stability is important when it comes to CSM design, because as long as a CSM remains largely suspended throughout its duty cycle, one can treat this dispersion as ‘relatively stable’ – an acceptable condition for many applications. With proper selection of surface chemistry and dispersion solution, CSMs can be made stable in solution on the order of minutes to hours, long enough for most envisioned applications.

1.1.2.2 CSM Sedimentation – Particle Buoyancy

For CSM systems that do not coagulate, it is also important to consider whether each CSM particle can be individually suspended without settling out. The study of the translation of these nearly-neutrally-buoyant particles with size scales commensurate to that of the surrounding turbulence are often restricted to ideal spheres, despite the scarcity of regular shapes in such processes.

The full analytical equation of motion for spherical particles in an unsteady flow (i.e., the Maxey-Riley equation) has been derived in the Stokes regime.¹⁷ Despite its simplicity, this

model has been very effective in understanding CSM sedimentation behavior, not only in aqueous environments, but also in air. In the context of ‘aerosolizable electronics’, for example, the Maxey-Riley equation of motion has successfully modeled the transient behavior of CSM aerosol particles launched into the vapor phase using a nebulizer for environmental monitoring applications.² It predicts, for example, that CSMs below 100 μm in size can exhibit settling rates on the order of minutes or higher.

1.1.3 Materials-Enabled CSM Modules

Herein, we break down complex CSM operations into five fundamental modules (i.e., computation, sensing, communication, locomotion, and energy management) and analyze those enabling technologies that are promising for CSM applications.

1.1.3.1 Logic and Computing

Computation is at the core of most electronic systems. It processes input signals from sensors, stores relevant information, and generates output signals in response. Silicon-based electronics is the cheapest, most reliable, and smallest option to build integrated circuits. Due to continued transistor scaling, today transistors have nanometer-scale dimensions with densities of 23 transistors/ μm^2 while consuming about 1.5 pW/MHz each.¹⁸ Several microsystems approaching the size of a CSM have been demonstrated using silicon chips for computation (**Table 1-1**), which target biomedical applications,¹⁹ environmental sensing¹² and object verification²⁰ and range in power from 0.4 nW to 10 μW .

Low-dimensional materials like carbon nanotubes and 2D materials have been explored extensively in recent years given their favorable electrostatics and high carrier mobility.²¹ Transistors based on 2D materials and carbon nanotubes with promising device characteristics have been fabricated, enabling the development of more complex circuits.²² However, electronics based on these materials are still in their infancy and cannot compete with silicon in terms of cost, reliability, and system complexity at present. In the near future, silicon should be the primary choice to bring computing capabilities to CSMs.

Herein, we break down complex CSM operations into five fundamental modules (i.e., computation, sensing, communication, locomotion, and energy management) and analyze those enabling technologies that are promising for CSM applications.

Table 1-1. Example of microsystems that use silicon chips for computation.

Year	Microsystem Details			Computation			Communication		
	Application	Power	Size [μm]	Node	Complexity	Modality	Medium	Mode	Distance
1997	Sensor networks ²³	400 nW	~300x300x300	n/a	n/a	Light	Air	Passive	2 m
2004	RFID tags ²⁰	1.5 μW	400x400x60	180 nm	medium	RF	Air	Passive	1.2 mm
2013	Neural sensor ²⁴	10.5 μW	250x500x?	65 nm	medium	RF	Air	Passive	1 mm
2014	Pressure sensor ²⁵	5.3 nW	1200x825x?	180 nm	high	RF	Water+Air	Active	10 cm
2015	Neural sensor ^{26,27}	0.9 μW	800x800x800	n/a	n/a	US	Water	Passive	50 mm
2016	Chemical sensing ¹²	0.4 nW	200x100x10	180 nm	low	n/a	n/a	n/a	n/a
2017	Cell monitor ¹⁴	n/a	25x25x?	n/a	n/a	RF	Water	Passive	25 μm
2017	Glucose sensor ²⁸	63 nW	200x200x100	65 nm	medium	RF	Tissue	Passive	1.3 mm
2018	Neural stimulation ²⁹	27 μW	200x200x100	130 nm	medium	n/a	n/a	n/a	n/a
2018	Neural sensor ¹³	1 μW	57x250x330	180 nm	medium	Light	Tissue	Active	2.8 mm

2018	Temp. sensor ¹⁹	16 nW	360x400 x280	55 nm	high	Light	Air	Active	15.6 cm
------	----------------------------	-------	-----------------	----------	------	-------	-----	--------	---------

1.1.3.2 Sensing

Sensing plays a central role in most microsystems, allowing them to be aware of their location, environment, and neighbors, and subsequently triggering signaling and downstream responses. In the context of CSMs, a need for modular integration renders electric sensors the most relevant. While silicon-based sensors are the easiest to integrate with logic, silicon transistors are not ideal for many sensing applications. As a result, it is important to integrate new materials. However, there are many new materials and mechanisms that can be used to make microscale electrical sensors for CSM-type systems, resulting in a fairly broad field that has been subject to extensive analyses.³⁰

1.1.3.3 Communication

Communication between microsystems using electromagnetic, ultrasonic, optical and chemical means are summarized in **Figure 1-5**. Radio frequency (RF) communication is the standard choice for many technologies, yet antennas become increasingly inefficient when scaled down. Most reported RF systems at the sub-mm scale thus communicate data passively by backscattering the incoming signal, especially for medical applications.³¹ Similarly, the lowest power consumption in ultrasound (US) systems – best-suited for aqueous media such as water and biological tissues – is achieved when information is transmitted back passively. This approach has been used to build a neural recording device³² capable of transmitting data to a receiver 9 mm away. Light can also be used to communicate between CSMs, either by active light emission using light emitting diodes

(LED) or through indirect means such as modulating fluorescence or reflection of light.³³

In contrast to RF, optical systems scale well into the 1 to 100 μm range, although such communication is only feasible in transparent media such as water or air, and only locally.

A less conventional and little explored method of communication is through the emission and diffusion of molecules which serve as information carriers. Chemical communication is prevalent in nature, though it is slow and has a low bandwidth in contrast to the previously discussed modalities.³⁴ For applications with relaxed timing and sparse information content, however, this may be a viable option. One way to implement CSMs with chemical communication is to equip them with molecule reservoirs that only open when certain conditions are met.³⁵

There are several communication modalities available for CSMs under 100 μm , subject to environmental constraints. The decision on which technology should be implemented also depends on the communication mode, such as centralized base-to-unit communication or decentralized unit-to-unit communication. In general, the latter is more challenging due to limited on-board transmission power. However, in the context of CSMs, combining these two modes into what is known as ‘asymmetric communication’ presents further opportunities.

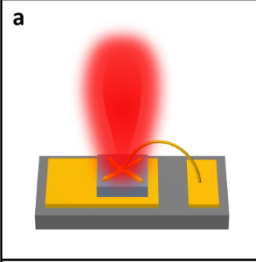
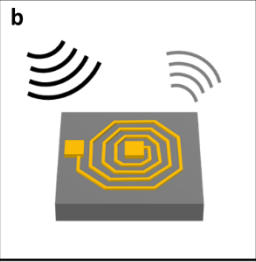

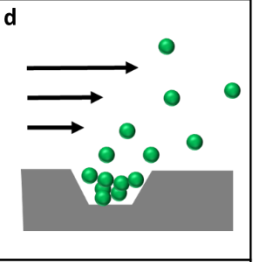
	a 	b 	c 	d 
	Light	EM Waves (RF)	Ultrasound	Diffusion
Distance scaling of transmitted power	r^{-2}	r^{-4} (<i>near-field</i>)	r^{-2}	r^{-3}
Suitable media	transparent: solid, liquid, gas	non-metallic: solid, liquid, gas	liquid	liquid, gas
Unsuitable media	opaque materials	metals	gas	solid

Figure 1-5. Overview of four communication modalities. **(a)** Light sources such as light emitting diodes can be used for optical communication. **(b)** Electromagnetic (EM) communication can be achieved by using small coils that either actively emit EM waves or backscatter the sender’s signal. The small footprint of the CSM typically prevents the integration of far field antennas, which will limit EM to the near-field. **(c)** Ultrasound can be employed for communication. The simplest way is to use piezo crystals that interact with the waves and are able to backscatter the signal from the sender selectively. **(d)** Molecular diffusion may be used to transmit information by controlling the amount and type of specific molecules.

1.1.3.3 Actuation and Locomotion

The ability to autonomously actuate differentiates CSMs from conventional SoCs. Scaling physical systems down to microscopic dimensions causes surface-born interactions, such as surface tension, drag, and adhesion, to dominate over volumetric bulk effects, such as mass and inertia.³⁶ One direct consequence is the optimal actuation strategies with which CSMs operate. In these length regimes, actuation mechanisms like chemical adhesion and surface forces become appealing choices, which scale more favorably than most

mechanical grippers.³⁶ In order to possess true *autonomy*, the operation of CSMs must be enabled by locally-stimulated actuators on board. Promising candidates include polymer- and gel-based actuators³⁷ and thin film bimorphs³⁸, the latter being especially preferable given their short response times.

Micro-swimmers generally fall into two categories: mechanical or chemical. The major challenge of microscale locomotion based on mechanical actuation arises from the *kinetic reversibility*: for tiny particles ($a \approx 10 \mu\text{m}$) swimming in water, Re is typically much less than 1. This dictates that any micro-swimmer actuating in a cyclical fashion will have no net motion in a Newtonian fluid,³⁹ a formidable hurdle to overcome for many mechanical micro-swimmers.

In contrast, a chemical micro-swimmer does not require moving parts to move through a medium.⁴⁰ One of the earliest examples of such autonomous motion was the Pt-Au bimetallic rod,⁴¹ from which various self-propulsion mechanisms have been explored. These include, but are not limited to: bubble propulsion,⁴² self-electrophoresis,⁴¹ self-diffusiophoresis,⁴³ self-thermophoresis,⁴⁴ and self-acoustophoresis⁴⁵. Even so, a generalizable design rule for guided locomotion to enable programmable CSM chemotaxis and phototaxis beyond proof-of-concept environments has yet to be discovered.

1.1.3.3 Energy Harvesting and Storage

Electric energy is critical to power functions like information processing, actuation, and communication. It is not surprising therefore that energy supply represents one of the greatest challenges for CSMs. **Figure 1-6e** plots the energy demand for a standard computation and the energy available as a function of device characteristic length a . A

picoliter ($1000 \mu\text{m}^3$) energy module comprised of the best commercial lithium-ion battery would only be able to power a 100 nW load for roughly 25 seconds ($2500 \text{ nW}\cdot\text{s}$). There is thus a clear energy gap to bridge, creating opportunities for advanced materials.

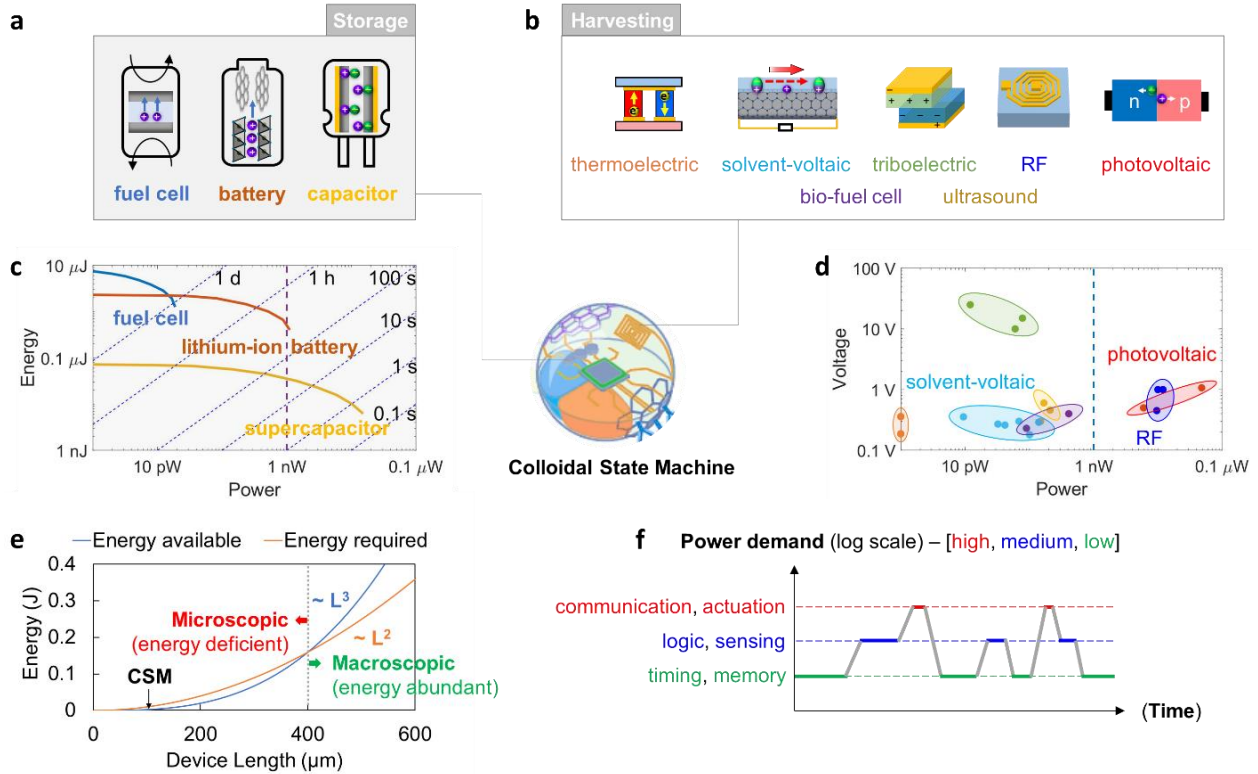


Figure 1-6. Energy harvesting and storage techniques relevant for Colloidal State Machines. **(a, b)** Potentially feasible electrical power sources on the scale of CSMs, categorized by mechanism, as storage **(a)** or harvesting **(b)** devices. **(c)** Ragone plot of energy storage devices at a limited volume of 1 pL. The parallel dashed lines represent the time of discharge. For example, if we discharge a Li-ion battery at 1 nW power, we follow the purple vertical line up and encounter the curve for battery between 1 h and 100 s, which means the battery will be fully discharged in several hundred seconds. The plot is based on a conservative estimation of the energy and power densities, with data from Pikul et. al.,⁴⁶ which also shows that with an optimized configuration and structure

of electrodes, the maximum accessible power density may be boosted by 10 times.⁴⁶ **(d)** Voltage-power characteristics of energy harvesting devices. The power output is estimated for a structure with $600 \mu\text{m}^2$ surface area, which is the maximum attainable for a $10 \times 10 \times 10 \mu\text{m}^3$ CSM. Solar cell is supposed to have 10% efficiency and put under 1 sun illumination (about 1 kW/m^2). **(e)** Estimated energy required for standard computation¹⁸ (20 transistors per μm^2 with each transistor consuming 5 nW at 3.4 GHz for computation time of 10 s) and electrochemically stored energy ($2.5 \text{ nJ}\cdot\mu\text{m}^3$) plotted as a function of device length. **(f)** Example duty cycle of a CSM, utilizing different energy sources at different power demands.

Some micro-batteries with interdigital electrodes and 3-D current collectors may possess power density 1 order of magnitude higher than the commercial lithium-ion batteries, with sacrificed energy density.⁴⁶ Nonetheless, with a system volume of 1 pL, batteries supply less than $0.1 \mu\text{W}$, which is sufficient for standby circuits but not enough for communication. Alternatively, supercapacitors can offer energy and power densities of up to $0.4 \text{ nJ}\cdot\mu\text{m}^{-3}$ and $10 \text{ pW}\cdot\mu\text{m}^{-3}$ respectively,⁴⁷ while regular dielectric capacitors offer much lower areal energy densities of $25\text{-}400 \text{ fJ}\cdot\mu\text{m}^{-2}$ but reach much higher power densities of up to $400 \text{ nW}\cdot\mu\text{m}^{-2}$ due to the quick discharge⁴⁸ – ideal for short bursts of communication or other brief, high power tasks (**Table 1-2**). The Ragone plot (**Figure 1-6c**) visualizes this trade-off between power and energy density.

Table 1-2. Energy storage technologies relevant in the context of CSM.

Technology	Energy Density	Power Density	V_{max}	Ref	Comments
Lithium-Ion Battery	$2.5 \text{ nJ}/\mu\text{m}^3$	$0.8 \text{ pW}/\mu\text{m}^3$	3-4 V	⁴⁹	<u>Assuming</u> full discharge in 1h
Thin-film Battery	$2\text{-}14 \text{ nJ}/\mu\text{m}^3$	$0.5\text{-}4 \text{ pW}/\mu\text{m}^3$	1-4 V	⁵⁰	<u>Assuming</u> full discharge in 1h
Super capacitor	$0.1\text{-}0.4 \text{ nJ}/\mu\text{m}^3$	$1\text{-}10 \text{ pW}/\mu\text{m}^3$	1-3 V	⁴⁷	
Dielectric capacitor	$25\text{-}400 \text{ fJ}/\mu\text{m}^2$	$25\text{-}400 \text{ nW}/\mu\text{m}^3$	2-5 V	⁵¹	Assuming $1\mu\text{s}$ discharge

To achieve partial or complete autonomy, prior CSM demonstrations have often relied on external energy harvesting. Chemical fuels have the highest energy density (e.g., $31.3 \text{ nJ}\cdot\mu\text{m}^{-3}$ in ethanol as opposed to $2.5 \text{ nJ}\cdot\mu\text{m}^{-3}$ in lithium ion batteries) and therefore represent a promising method to power micro-scale electronics. One example is thermopower waves.⁵² This technique requires no moving parts, and is capable of producing a pulse of high voltage ($> 5 \text{ V}$) and power ($0.11 \text{ nW } \mu\text{m}^{-3}$). Biotic and abiotic fuel cells have also been explored for direct conversion of chemical energy, providing a typical power density of $1 \text{ pW}\cdot\mu\text{m}^{-3}$ and a supply voltage of 0.5 V . RF energy harvesters can deliver a high-power density of $10\text{-}400 \text{ pW}\cdot\mu\text{m}^{-2}$ at a few millimeters distance and total transmit powers in the range of $50\text{-}2000 \text{ mW}$. However, these numbers are only rough guides since smaller coils ($< 100 \mu\text{m}$) typically operate in the near-field regime and down-scaling likely results in lower efficiencies (**Table 1-3**). The photovoltaic effect has been used extensively in autonomous microsystems for ambient and in-vivo applications.¹³ Given a pico-liter colloidal device, about 60 nW of power could be generated, assuming a 10% efficient solar cell and direct sun light ($\sim 1 \text{ nW}\cdot\mu\text{m}^{-2}$). For indoor applications, light sources are about 200 times less powerful⁵³ and would result in a usable power of 0.3 nW for the same device.

Table 1-3. Energy harvesting technologies relevant in the context of CSM.

Technology	Medium and Distance	Transmit Power	Receiving Power	Voltage	Footprint of coil/piezo/LED	Ref
RF coil	1.2 mm air	300 mW	$10 \text{ pW}/\mu\text{m}^2$	0.5 V	$400 \times 400 \mu\text{m}$	²⁰
RF coil	1 mm air	50 mW	$80 \text{ pW}/\mu\text{m}^2$	1.07 V	$250 \times 500 \mu\text{m}$	²⁴
RF coil	3 mm air + 4 mm muscle	2000 mW	$400 \text{ pW}/\mu\text{m}^2$	1.3 V	$200 \times 200 \mu\text{m}$	²⁹
Ultrasound	30 mm water	$720 \text{ mW}/\text{cm}^2$	$0.25 \text{ pW}/\mu\text{m}^3$	-	$127 \times 127 \times 127 \mu\text{m}$	²⁶

Ultrasound	50 mm water	7.2 mW/cm ²	0.35 pW/μm ³	0.46 V	800 x 800 x 800 um	27
Ultrasound	3 mm muscle	100 mW/cm ²	0.28 pW/μm ³	0.6-1.1 V	1 x 1 x 1.4 mm	54
Solar Cell	air	100 mW/cm ²	1.1 pW/μm ²	0.5 V	0.07 mm ²	25
Solar Cell	4.75 mm pig skin	325 mW/cm ²	160 pW/μm ²	0.45 V	2 x 2 mm	55
Solar Cell	1.3 mm pig skin	190 mW/cm ²	3.5 pW/μm ²	-0.3 V	135 x 135 um	28
Solar Cell	Air (microscope)	50 mW/cm ²	200 pW/μm ²	1.0 V	50 x 100 um	13
Solar Cell	15.6 cm air	4.5 mW/cm ²	0.4 pW/μm ²	0.65 V	180 x 230 um	19

Finally, there are emerging technologies that may be used to power colloidal systems in the future. A promising candidate is solvent interaction harvesting (or ‘solvovoltaics’⁸), which is particularly relevant to CSMs because it taps into their surrounding solvent environment. Alternatively, (mechanical) triboelectric generators could deliver power density in the range of 0.1 pW·μm⁻³ and high voltages on the order of 10 V.⁵⁶

As shown in **Figure 1-6c** and **d**, given the above strengths and weaknesses of each energy source, a CSM will likely integrate multiple energy storage and harvesting modules to accommodate different electric functions and situations. Assigning appropriate electricity generators to a specific purpose is the key to navigating the CSM across a potentially anisotropic energy landscape (**Figure 1-6f**).

1.1.4 CSM Systems Integration

The goal of CSM integration is to build complex, autonomous systems from individual building blocks, analogous to combining individual “organelles” (e.g., “nucleus” as CPUs, “mitochondria” as energy harvesters, “flagella” as actuators, etc.) into higher-order “cells”.

1.1.4.1 Top-down Technologies

Lithography is a staple technique for high-density monolithic circuits. It can pattern up to 300 mm wafers but requires flat substrates and a cleanroom environment. Optical

immersion lithography with self-aligned quadruple patterning achieves resolutions of 10 nm in industrial production.⁵⁷ Electron beam lithography, commonly used in academic settings, can even realize features down to 5 nm without the need for a photomask, however at lower throughput.⁵⁷ As a result, photo- and electron beam lithography will play an integral part in the fabrication of CSM building blocks, especially those requiring patterns on the nanometer scale at large scale. One recent example is Koman et. al's 2D material CSMs, which were mass fabricated using photolithography (**Figure 1-7b**).² Specifically, each individual machine, capable of combinational logic (**Figure 1-7c**), contains three 2D components: a MoS₂/WSe₂ photodiode as the power source, a MoS₂ chemiresistor as the switch, and a memristor memory (MoS₂ flakes between Au and Ag electrodes).

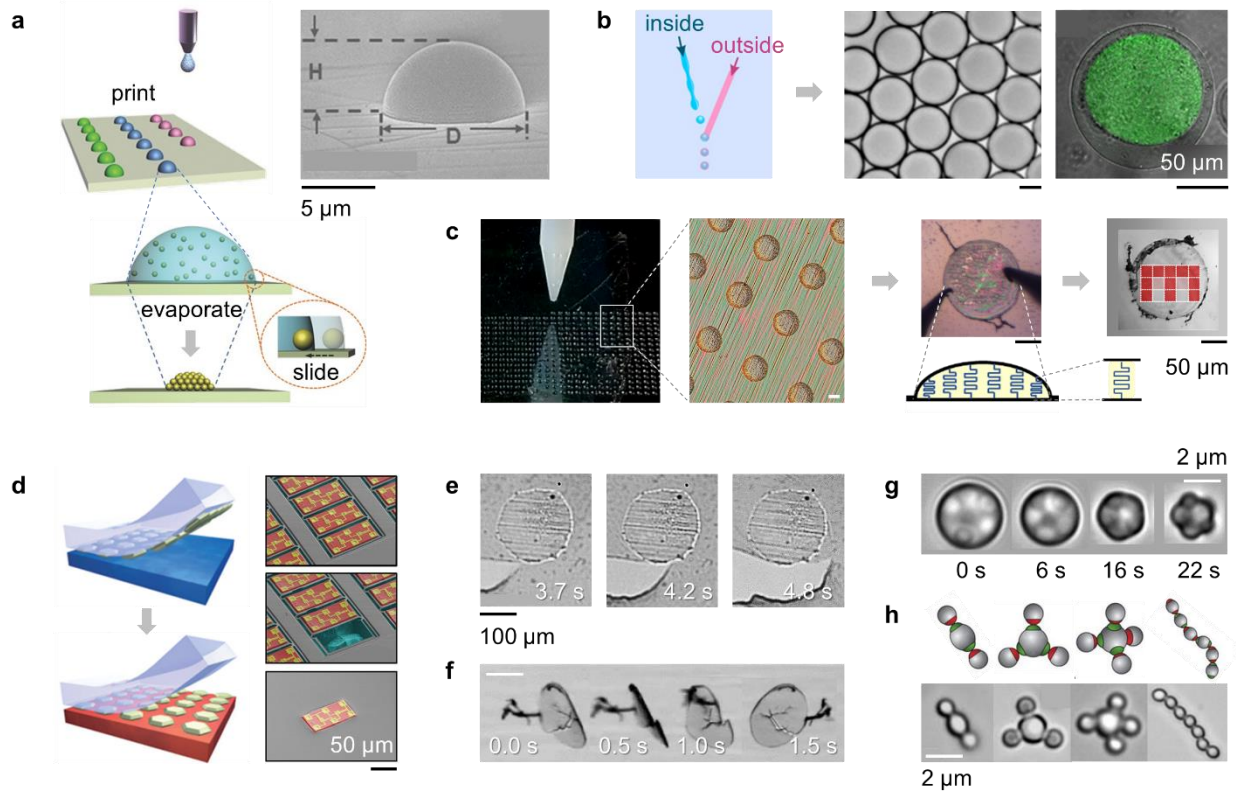


Figure 1-7. Selected examples for device integration relevant for colloidal electronic applications.

(a) Schematic illustration for the assembling process of ink-jet printed polystyrene beads into aggregated dome-shaped arrays. **Inset:** Scanning electron micrograph (SEM) of one such printed polystyrene micro-dome. Scalebar, 5 μm . Reproduced with permission.⁵⁸ Copyright 2014 Wiley VCH. **(b)** High throughput in-air microfluidic ink-jet printing of micro-suspensions of multiple compositions. **Left:** Schematic illustration of the technique that generates core-shell structures with inner (blue) and outer (red) layers. **Middle:** Spherical particle suspensions viewed via optical microscopy. **Right:** Multi-material (alginate-dextran-tyramine in H_2O) core-shell particles. All scalebars, 50 μm . Reproduced with permission.⁵⁹ Copyright 2018 American Association for the Advancement of Science. **(c)** Ink-jet printing of CSM particles consist of graphene encapsulated memristor arrays. **Left:** Optical image (**inset:** micrograph) of the printed microparticles. **Middle:** Top view of electrical testing a single graphene-encapsulated phosphorene-polystyrene composite microparticle (after solution lift-off and recapture) in a probe station. **Bottom-right inset:** schematic illustration of the cross-sectional view of the micro-particle – phosphorene nanoflakes (blue) inside a polystyrene matrix (yellow) forms arrays of memristor elements between the two encapsulating layers of graphene (black). **Top-right:** A 15-bit microparticle memristor array written via electronic probes. Vertical conductivity map (red – ON, clear – OFF) with the shape “M” overlaid on top of the microparticle tested. All scale bars, 50 μm . Reproduced with permission.¹ Copyright 2018 Nature Publishing Group. **(d)** **Left:** Schematic illustration of transfer printing. **Top-left:** Laminating a stamp against a donor substrate (blue) and then quickly peeling it away, pulling the microstructures from the donor substrate onto the stamp. **Bottom-left:** Contacting the stamp to the receiving substrate (red) and then slowly peeling it away transfers the microstructures from the stamp to the receiver (red). Reproduced with permission.⁶⁰ Copyright

2006 Nature Publishing Group. **Right:** False-colored SEM images of an array of devices, shown in sequence, after undercut etching (**top-right**), after removal of a single device from the donor wafer (**middle-right**), and after transfer printing of this device onto a receiving substrate (**bottom-right**). Scalebar, 50 μm . Reproduced with permission.⁶¹ Copyright 2017 National Academy of Sciences. **(e)** Optical micrographs showing fracture and crack propagation of the graphene layers around a single polymer disk. Scalebar, 100 μm . Reproduced with permission.¹ Copyright 2018 Nature Publishing Group. **(f)** Time-elapsd optical micrographs of an autoperforated graphene-encapsulated polymer disk rotating and translating in solution in a laminar flow field. Scalebar, 100 μm . Reproduced with permission.¹ Copyright 2018 Nature Publishing Group. **(g)** Time-elapsd optical micrographs during evaporation of the toluene, showing the emulsion encapsulation process. Particles freely diffuse about the surface of the droplet until, as more toluene evaporates, they touch one another, forming a spherical packing. Deformation of the interface then leads to a rapid rearrangement to a cluster. Scalebar, 2 μm . Reproduced with permission.⁶² Copyright 2003 American Association for the Advancement of Science. **(h)** Bright-field (**bottom** panels) and schematic images (**top** panels) showing colloidal “molecules” self-assembled from “patchy” particles pre-programed with complementary green and red DNA patches. Supra-colloidal “molecules” AB2, AB3 and AB4 are formed by mixing red monovalent with green divalent, trivalent and tetravalent particles. If complementary divalent particles are mixed, linear alternating “polymer” chains spontaneously assemble. Scalebar, 2 μm . Reproduced with permission.⁶³ Copyright 2012 Nature Publishing Group.

With recent advances in precision printing, additive manufacturing rises as a viable and relatively inexpensive alternative to traditional manufacturing methods. Unlike lithography, additive printing builds complex scaffolds through deposition, layer upon

layer. State-of-the-art printing processes achieve a minimum feature size of about 1 μm with alignment accuracies of several micrometers and printing speeds of about 1 m/s (**Figure 1-7a, b**).⁶⁴ For features that do not require nanometer precision, printing is inexpensive and compatible with a large variety of materials (e.g., nano- and microparticles of various shapes, thermoplastics, ceramics, polymer composites, low-dimensional materials, etc.). In practice, various ‘inks’ have been used to establish active or passive circuit elements, such as transistors, capacitors, resistors, memristors, etc. (**Figure 1-7c**),¹ suggesting printing as a complementary tool for CSM fabrication.⁵⁹

Another approach for top-down device assembly involves the combination of separate as-made modules, broadly categorized here as heterogeneous integration. This encompasses a wide spectrum of techniques, all the way from traditional integrated circuit methods like wire bonding, flip chip reflow soldering, through-chip via, and wafer bonding to recent materials transfer innovations such as fluidic self-assembly,⁶⁵ dry transfer printing (**Figure 1-7d**),⁶⁰ and wafer-scale layer-by-layer assembly.⁶⁶ Specifically, the combination of dry-transfer printing and device fabrication on sacrificial layers such as silicon on insulator may prove indispensable to CSMs. On one hand, it allows picking the best material for each building block, e.g., silicon for computation, III-V semiconductors for LEDs. On the other hand, this approach decouples fabrication constraints such as high temperature processing or chemical compatibility of each building block (**Figure 1-7d**).

1.1.4.2 Bottom-up Technologies

It is well-understood that material fracture can be controlled using a prescribed strain field, and the governing Griffith criterion has been demonstrated to operate down to the

nanometer limit within 2D lattices such as graphene.⁶⁷ Recently, Liu *et al.* successfully implemented the strategy of strain induced guided “automatic perforation” (or “autoperforation”) on 2D material sheets (monolayer graphene, MoS₂ and hBN), demonstrating the feasibility of using controlled defect self-assembly as a reliable and scalable nanofabrication method applicable to the production of electronic colloids.¹ This “autoperforation” strategy forms the basis for various types of autonomous micro-electronic devices capable of analyte detection and memory storage (**Figure 1-7c**).¹

Given that most of our current electronic material systems and fabrication methods are optimized for circuits in 2D, self-folding strategies, such as the ones inspired from origami and kirigami, have opened the door to creating complex 3D structures using planar fabrication techniques.³⁸ Recent work has demonstrated successful folding of polymers,⁶⁸ shape-memory alloys,⁶⁹ and 2D materials³⁸ at various length scales. Origami robots capable of autonomous actuation,³⁸ supervised locomotion⁷⁰ and reprogrammable self-assembly⁷¹ have also been fabricated *en masse*. With its inherent scale-free character, origami as a framework for metamaterial design has found utility across many geometric scales (mm, μm, nm).

Self-assembly is a process in which a system of pre-existing components spontaneously organizes into an ordered structure through no external supervision. Well-defined structures can be synthesized via processes such as emulsion encapsulation (**Figure 1-7g**)⁶² and DNA hybridization (**Figure 1-7h**).⁶³ Alternatively, colloids can be precisely organized and linked by a “lock and key” mechanism,⁷² patchy surface hydrophobicity,⁷³ or wetting forces (“colloidal fusion”).⁷⁴ On the other hand, dynamic, or out-of-equilibrium, assembly has also been examined extensively.⁷⁵ Although the literature in the self-assembly of

colloids is constantly growing, programmed-clustering of individual parts into CSMs with full electronic autonomy is still at its naissance.

1.1.5 Control and Robotics of Autonomous CSMs

1.1.5.1 Control of CSMs

Control is traditionally implemented through reconfigurable computing to calculate optimal or near-optimal decisions based on an objective.⁷⁶ However, as a system shrinks, reconfigurable computing takes a greater percentage of physical volume and energy budget, eventually becoming impractical. As a result, control of CSMs will be constrained to use limited computational resources, relying on the material properties of CSMs to implicitly perform operations normally reserved for computing.

Consequently, the control authority of CSMs (in the form of simple circuits,² logical operators, and individual elements of nonvolatile memory¹), will be internally represented in terms of discrete states – despite CSMs operating in and interacting with continuous environments. Systems with a combination of continuous and discrete components are *hybrid systems*.⁷⁷ **Figure 1-8a** shows a control architecture – a result of a hybrid, optimization-based approach⁷⁸ – capable of moving a CSM to a specified location. The CSM autonomously achieves its goal in continuous space, using only discrete actuation, discrete sensing, and a few logical operators.⁷⁸

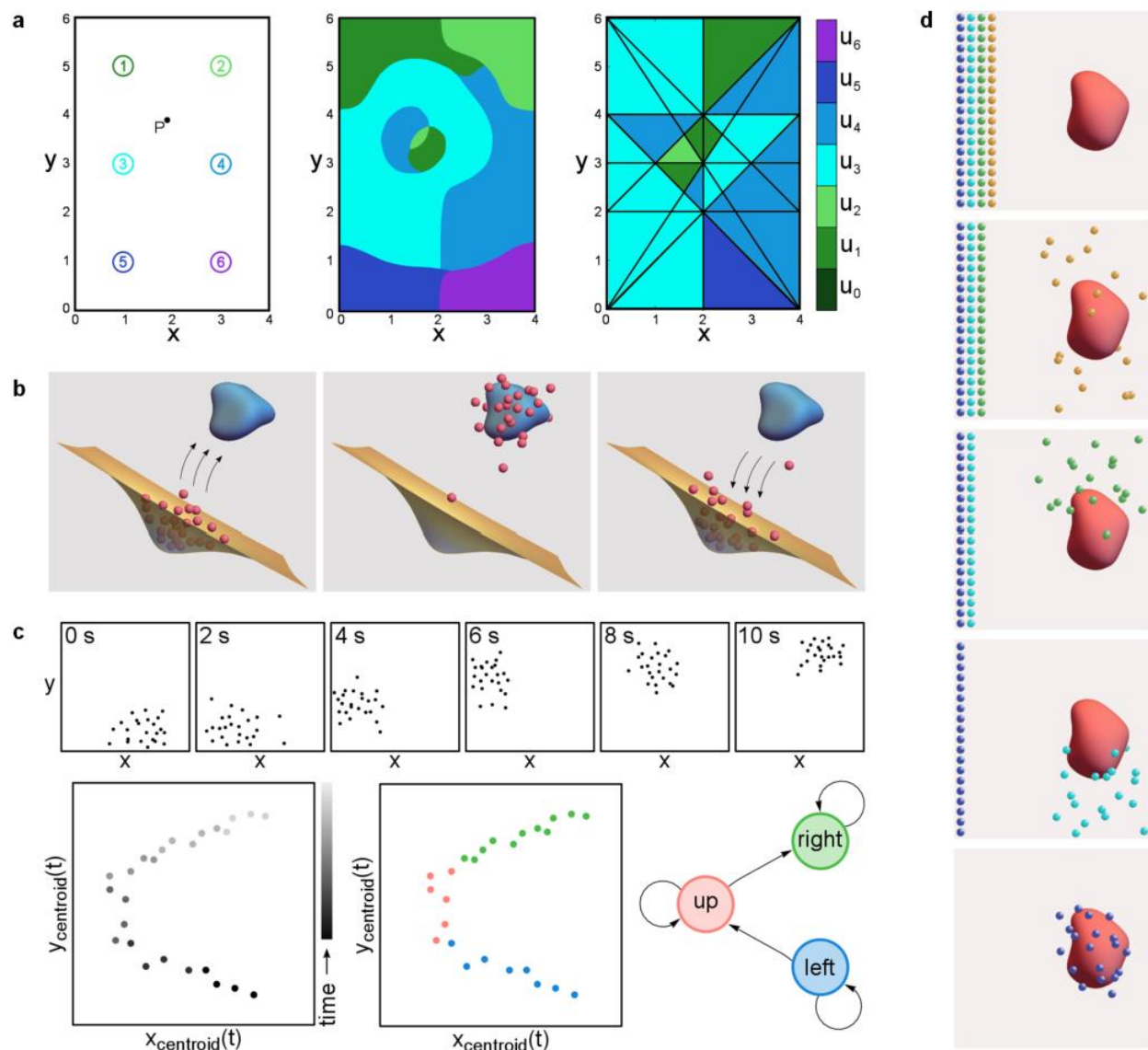


Figure 1-8. (a) Model-based control. **Left.** A planar environment with six different chemical sources. A CSM is able to locomote by choosing one of seven different control modes: being attracted toward a chemical potential at one of the six different sources ($u_1, u_2, u_3, u_4, u_5, u_6$), or staying still (u_0). The goal of the device is to go toward point P. **Middle.** A continuous control policy that indicates which control mode (shown with different colors) to use at each location in the 2D environment. The *discrete* control output is a function of *continuous* input variables $u(x,y)$. **Right.** A discretized control policy, where the environment is divided into regions that are able to

be differentiated using chemical comparators. The *discrete* control output is a function of *discrete* input regions $u(r)$. Reproduced with permission.⁷⁸ **(b)** The ensemble of CSMs (shown in pink) needs to find an energy source (the blue object), but in doing so diffuses. As a consequence, the CSMs need to then exploit environmental characteristics (the yellow pocket in the environment) to reassemble themselves into a non-diffuse ensemble. **(c)** Simulated data of individual particles (top) can be simplified to the ensemble's motion (left) which gets abstracted as three modes of transport (middle) that can then be encoded in a finite state machine (right) on board each CSM. The small number of behaviors that describe the complex dynamics lead to minimal computation elements the CSMs will need to employ to execute control. **(d)** An illustration of a sequence of rollouts that could enable CSMs to learn in a massively parallel fashion. Starting from an initial set of randomized rollouts, through intercell communication the policy can be updated, eventually leading to a policy that successfully encapsulates a mass.

If individual CSMs can be controlled, *ensembles* of CSMs should be able to achieve greater objectives. The control of systems of simple agents has been explored in many areas, such as “shortcut bridging” in army ants, where a stochastic, distributed algorithm enabled particles to self-assemble into bridges optimized for length and cost.⁷⁹ Similar global behaviors have been demonstrated in algorithms for compression or expansion, and separation or integration of heterogeneous agents.⁸⁰ Nevertheless, there are fundamental limitations on what a group of autonomous, memoryless mobile robots can achieve.^{81,82}

1.1.5.2 Emergent Behavior and Learning in CSMs

To make control decisions, a CSM directly modeling physical states is impractical. Instead, we assume the model is an *emergent* phenomenon, implying that an

ensemble of CSMs must detect, and exploit, emergent behavior to accomplish its goals. In **Figure 1-8b**, CSMs search for a blue object but diffuse as they do so. They must detect and exploit the yellow energy potential to avoid dispersion.

To discover emergence, the ensemble might assume a very limited model, which involves only a small number of unknown behaviors. In **Figure 1-8c**, a simulated ensemble of individually stochastic CSMs *on average* move in only a few ways. There are three distinct dynamic behaviors (translating left, up, and right) that the ensemble can choose based on sensory inputs. Once these emergent behaviors are identified,⁸³ they can be used in different combinations to execute tasks.

Despite computational limitations of individual CSMs, an ensemble is highly parallelizable – many individuals can be used in parallel *reinforcement learning*.⁸⁴ This enables the ensemble to update policies over multiple attempts, in response to varying task success. As illustrated in **Figure 1-8d**, devices of different colors (representing distinct rollouts) attempt to encapsulate an object. Later rollouts of CSMs update their policies in response to rewards reaped by earlier attempts, enabling ensembles to learn.

Even with limited computation, the examples above illustrate how CSMs can exhibit emergent intelligence. As a result, rather than autonomy being a consequence of exquisite sensing, actuation, and computation, autonomy will be the result of flexible interactions between the colloidal particle and its environment.

1.1.6 Application of CSMs

Autonomous Colloidal State Machines collect, manipulate, store, and exchange information without external supervision.^{2,85} When the highly-dispersed nature inherent to a colloidal system interfaces with the autonomy and programmability that stem from electronics, new capabilities emerge. We broadly classify these applications in three functional areas.

On the one hand CSMs can be used for signal processing and transduction from enclosed spaces – like the mammalian vasculature, microfluidic channels, and chemical/biosynthetic reactors² – as well as recording from remote locations like oil and gas conduits, rock crevices, waterbodies,¹ soil matrix,¹ or the atmosphere. Operating at cellular dimensions^{13,19} enables a different paradigm of human-matter interaction, allowing people to intimately interact with microscopic systems like never before (**Figure 1-9e**).

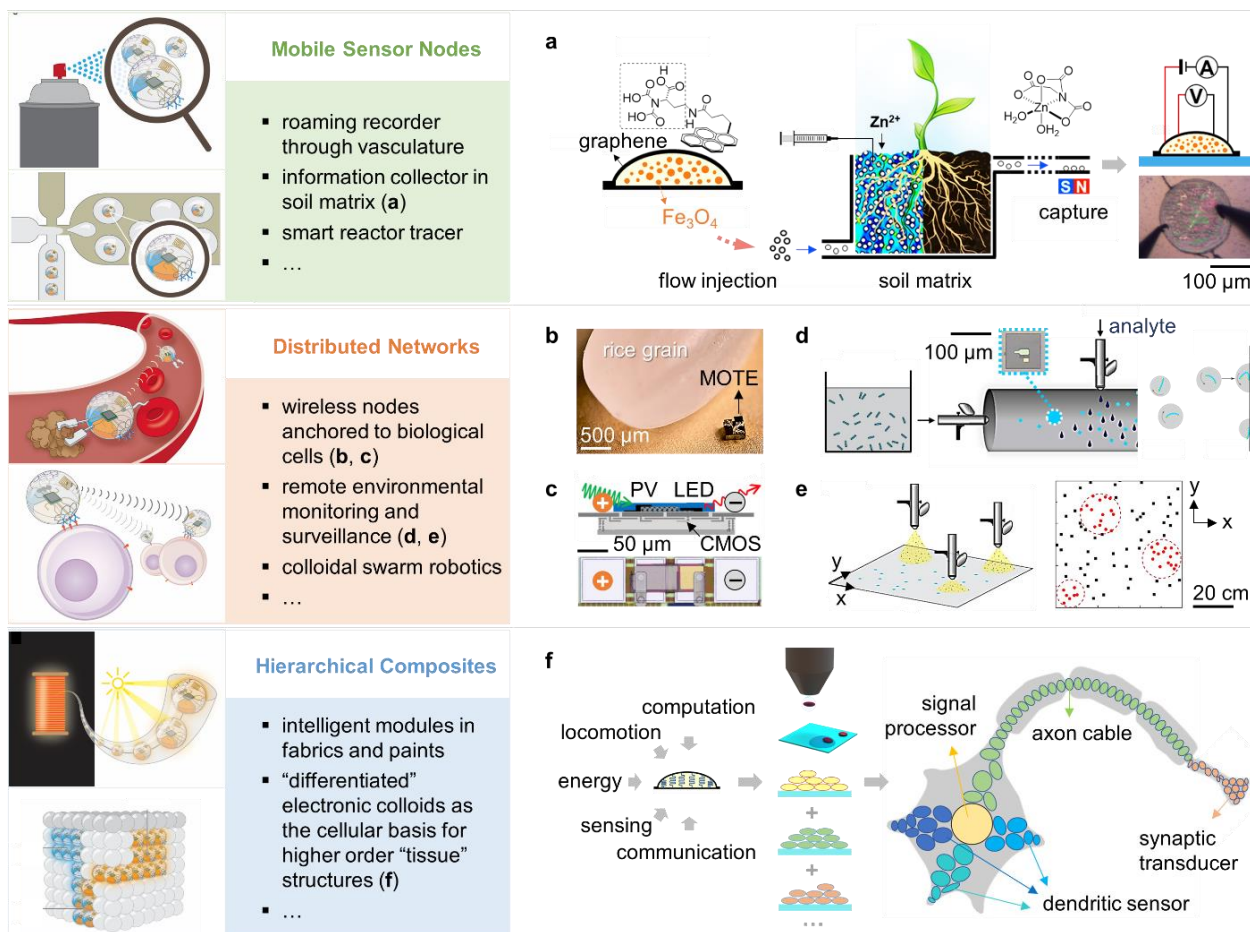


Figure 1-9. Demonstrated and potential applications for Colloidal State Machines. **(a)** Schematic illustration of the deployment of surface-functionalized colloidal electronic microparticles as chemical probes to detect and record the presence of various species, such as Zn^{2+} ions in the soil matrix. These colloidal devices can be retrieved via magnetic capture for electrical and optical readout. **Inset:** Optical micrograph of the colloidal electronic particle during the electrical readout. Scale bar, 100 μm . Reproduced with permission.¹ Copyright 2018 Nature Publishing Group. **(b)** A laser-powered 0.04 mm³ 16 nW wireless sensor MOTE with integrated central processing and optical communication units placed by a grain of rice. This system is capable of accurate cellular temperature measurement in vitro. Scale bar, 500 μm . Reproduced with permission.¹⁹ Copyright 2018 IEEE. **(c)** A 250 $\mu m \times 57 \mu m$ 1 μW MOTE capable of capturing and encoding

neural signals before transmitting the encoded signals. This system is powered by and communicates through an optical interface. Scale bar, 50 μm . Reproduced with permission.¹³ Copyright 2018 IEEE. **(d)** Experimental schematic showing remote detection and memory storage using CSMs aerosolized from their original colloidal suspension. The left nebulizer injects CSMs (teal squares) across the enclosed tube injected with an analyte (dark blue droplets) using the top nebulizer. CSMs are collected on the collector on the right, exposed to light, and their memory states are queried afterwards. Scale bar, 100 μm . Reproduced with permission.² Copyright 2018 Nature Publishing Group. **(e) Left:** Schematic illustration of large area sensing using CSMs. Analytes (yellow) are sprayed at three locations over an area with previously dispersed CSMs (teal squares). **Right:** Digitized positions of distributed CSMs. Dashed circles are eye guides, highlighting three areas exposed to the analyte. Turn ON responses (red) can be seen for those CSMs exposed to the analyte, as oppose to those that have not (OFF state, black). Scale bar, 20 cm. Reproduced with permission.² Copyright 2018 Nature Publishing Group. **(f)** Schematics illustrating the concept of assembling various derivatives of CSMs, each specializing in a different function, into higher-order tissue-like structures. The five basic modules (“organelles”) – logic and computation, communication, sensing, actuation and locomotion, energy harvesting and storage – are integrated into individual CSMs (“cell”). These individuals, by virtue of design, can be derived into a panel of synthetic variants, each fabricated at scale, and further assembled into secondary structures (yellow, blue, green, orange, etc.). Tertiary structures can be formed from ensembles of differentiated CSMs in order to accomplish more complex tasks at a larger scale, for instance, a synthetic neural signal transduction system. Illustrations prepared by B. Skrip.

Comprised of individual building blocks acting as independently controllable electronic devices, CSMs also transform the way we think about functional materials. Its particulate form-factor

allows it to be integrated into coatings, fibers and many other traditional material architectures. Its size allows it to achieve functional diversity by exploiting *system* diversity (i.e., a group of different discrete units) instead of packing more and more performance onto a single unit. In this way, the ensemble of CSMs becomes the system (**Figure 1-9a-d**).

Lastly, manufacturing electronic colloids at scale further promises hierarchical structures out of individual particles – analogous to the way biology builds *tissues* out of individual *cells*, functional domains that consist of various combinations of *differentiated* CSMs could be established. Some examples could be networks of artificial neurons (i.e., amplified electrical signal transduction) or synthetic myocardium (i.e., with pulsatile mechanical actuation) (**Figure 1-9f**). Given these properties, CSMs are well-poised to solve longstanding problems in medicine, information, and other disciplines.

1.1.7 Conclusions and Outlook

The field of Colloidal State Machines (CSM) is still in its early stages. The idea of CSM builds upon the already existing concepts of systems-on-a-chip (SoC)¹⁰ and microrobots. However, SoCs are non-mobile microsystems in the cubic millimeter range, whereas microrobots are often ‘supervised agents’ that require external control. CSMs are the next logical step in this development and raise the bar in terms of specifications. At a nanoliter or less in size, they are at least 1000 times smaller than SoC or microrobots and are designed to not settle out in fluidic environments, enabling a variety of new applications.

The 1966 science fiction film *Fantastic Voyage* popularized a lasting image of a miniaturized submarine small enough to navigate deep inside the human vasculature. Five decades later, constructing colloid-sized micro-machines is no longer mere fantasy.^{1,2,12-15} This emerging field is

highly interdisciplinary and building CSMs cannot be trivially accomplished by simply ‘scaling down or up’ contemporary technologies designed for larger or smaller systems. There are length-scale specific physical phenomena that make this infeasible, and require rethinking fabrication approaches and operational designs. To do so, it helps to generalize the concept of CSM as a microsystem that combines a subset, if not all, of the following building blocks: (1) computation, (2) sensing, (3) communication, (4) locomotion/actuation, and (5) energy harvesting.

Integrating all of these functions in a nanoliter ($10^6 \mu\text{m}^3$) volume is a challenging task. While monolithic integration of all components is desirable, no single materials class will suffice to realize all functions. A hetero-system featuring a diverse set of materials that best fits each function is ultimately desirable for assembling autonomous CSMs. In this perspective, we highlighted a few pioneering efforts that have used CSMs as distributed information probes in several otherwise inaccessible locations. Many opportunities lie ahead for disruptive innovations in medical, environmental monitoring and surveillance, as well as other creative uses of such technologies.

1.2 Direct Electricity Generation Mediated by Molecular Interactions with Low Dimensional Carbon Materials – A Mechanistic Perspective

Next generation off-the-grid electronic systems call for alternative modes of energy harvesting. The past two decades has witnessed the evolution of a wide spectrum of low dimensional carbon materials with extraordinary physical and chemical properties, ideal for micro-scale electrical energy storage and generation. Tremendous progress has been made in harnessing the energy associated with the interactions between these nano-structured carbon substrates and the surrounding molecular phases, subsequently converting them into useful electricity. This review summarizes the important theoretical and experimental milestones the field has reached to date, and further classifies these energy harvesting processes based on underlying physics, into five mechanistically distinct classes – phonon coupling, Coulombic scattering, electrokinetic streaming, asymmetric doping, and capacitive discharging. With a special mechanistic focus, we hope to resolve the fundamental attributes shared by this diverse array of molecular scale energy harvesting schemes, offer perspectives on key challenges, and ultimately establish design principles that guide further device optimization.

1.2.1 Motivations for Solvent Mediated Energy Harvesting Methods

There is a pressing need for alternatives to conventional energy generation techniques, due to the upper bounds on generator sizes set by the device footprint of the next generation micro- and nano-electronic systems. Recent developments in micro-fabrication techniques⁸⁶⁻⁸⁹ and understandings about low dimensional materials⁹⁰⁻¹¹⁷ have culminated into some of the most exciting demonstrations of microscopic electronic platforms capable of advanced logic computations, while not being tethered to any substrates and external power supplies.^{2,118} These systems represent

a giant leap forward in combining state-of-the-art technologies in modern electrical engineering with our understandings in the chemical and biological sciences, by interfacing digital systems with traditionally prohibitive environments. With numerous engineering possibilities in areas like circulating medical diagnostic devices and remote sensors in previously inaccessible locations, the Achilles' heel for such an electronic system at an extremely small length-scale has by and large been the energy constraint. While there has been tremendous progress towards improving the energy and power densities for traditional energy storage devices such as micro-batteries¹¹⁹⁻¹²² and supercapacitors¹²³⁻¹²⁷, their disadvantageous volumetric scaling poses fundamental constraints on important energy metrics that limit the application space of these electricity-demanding on-board electronics.

It is for this reason that energy harvesting strategies tapping into the surrounding environments that embody and intimately interface with these microscopic platforms hold great promise for the next generation untethered micro-electronic devices. Indeed, a series of harvesting strategies, including photovoltaics,¹²⁸⁻¹⁴⁰ piezo-electrics,¹⁴¹⁻¹⁴⁵ tribo-electrics,¹⁴⁶⁻¹⁴⁹ thermo-electrics,¹⁵⁰⁻¹⁵⁴ electro-magnetic transducers,¹⁵⁵⁻¹⁵⁷ fluidic electric generators,¹⁵⁸⁻¹⁶⁷ as well as bio-fuel cells¹⁶⁸⁻¹⁷⁷ have been devised in the attempt to tackle this challenge. It is worth noting, that once plugged into the environment, the energy density of such microscopic systems would no longer be limited by the device volume, for the environment can generally be treated as an infinite reservoir. Nevertheless, all the above listed harvesting strategies require a specific type of energy input, such as light, heat, mechanical movements, electro-magnetic fluctuations, or energy stored in chemical bonds; and built-in along-side this specificity are challenges associated with the intermittency of available input sources, as well as the versatility of the technology for universal implementation in various, potentially dynamic environments. Therefore, it would be ideal to develop energy

conversion processes that directly take advantage of the interactions between the energy harvesting units and their surrounding molecular environments (e.g., vapor, liquid, solid), without deliberately invoking the presence of temperature variation, photo-excitation, or chemical transformations.

As such, in the past two decades, with the advance of nanotechnology, there has been an explosive surge in research efforts towards the direct generation of electricity from molecular interactions with various low dimensional materials, in particular, nano-structured carbon materials. This exponential increase in the number of investigations has been accompanied by concomitant growth in device energy metrics as well, reaching energy and power densities comparable to those of the more conventional energy harvesting schemes, allowing demonstrations of practical utility.^{52,178,179} Owing in part to the rapid expansion of this relatively young field, however, much of its development has been primarily phenomenological, without a consensus on the underlying physical mechanism that governs said electricity generation. In this review, we attempt to give a comprehensive summary of all relevant theoretical and experimental studies to date, on the general concept of producing electrical energy using the interactions between a mobile molecular phase and a substrate consisting of nano-structured carbon materials. We will place a particular emphasis on the various mechanisms proposed as to how these molecular interactions can be designed to drive the flow of electric carriers in an external circuit. We will conclude with a curated list of mechanistically distinct primary physical processes that we believe are involved in the overall electricity generation, as well as an outlook towards the future of these phenomena and how they might be integrated into contemporary technologies. It is our hope that this review will serve not only as an entry point, a mechanistic tutorial and a thorough literature resource for the readership interested in this vibrant field, but also to stimulate further discussions about the underlying

principles of these interesting electricity generation phenomena, which hopefully will guide further device optimizations, eventually resulting in large-scale practical applications in the near future.

1.2.2 Mechanistic Overview

After only a little over a dozen years since its conception, the field of harvesting electrical energy from various molecule-nanomaterial interactions already has a fascinating history. In 2001, Kral and Shapiro¹⁸⁰ famously proposed two possible mechanisms to induce electricity in metallic single-walled carbon nanotubes (SWNTs) using a flowing liquid. The first consisted of a momentum transfer from the traversing liquid molecules to the acoustic phonons of the carbon lattice, resulting in a drag force on the free carriers within the nanotube; and the second involved a more direct Coulombic coupling between the ionic or polar molecules in the mobile liquid with the delocalized carriers in the solid carbon phase. Two years later, the experimental work by Sood et. al.,¹⁸¹ based on the latter mechanism, validated the possibility to generate electrical currents using a SWNT film deposited between two electrodes immersed in flowing liquid molecules. It was not long after that similar effects were demonstrated for semiconducting SWNTs,¹⁸² multi-walled carbon nanotubes (MWCNTs),¹⁸³ graphene,¹⁸⁴ and many other carbon based nanostructured materials. The past two decades have witnessed many breakthroughs in molecular scale energy harvesting, and have generated several principal classes of mechanisms that lay the foundation for further experimental explorations and device optimizations. In this section, we will take a heuristic approach through pivotal moments in the field's early development, already punctuated by several key publications. We combed through much of the theoretical proposals in the literature, organized them based on physical principles, and distilled them into what we consider the five most fundamental strategies in the molecular energy harvesting space. These are, in no particular order, the phonon coupling mechanism, the Coulombic scattering mechanism, the

streaming potential mechanism, the asymmetric doping mechanism, and the capacitive discharging mechanism. We will explore these five approaches in considerable detail. As we shall see, the interplay between one or more of these mechanisms has allowed us to extract electricity from low-grade energy inputs in almost every conceivable dimension (e.g., thermal, mechanical, chemical, optical, etc.), spanning three phases (i.e., vapor, liquid, and solid) of molecular building-blocks (Figure 1-10).

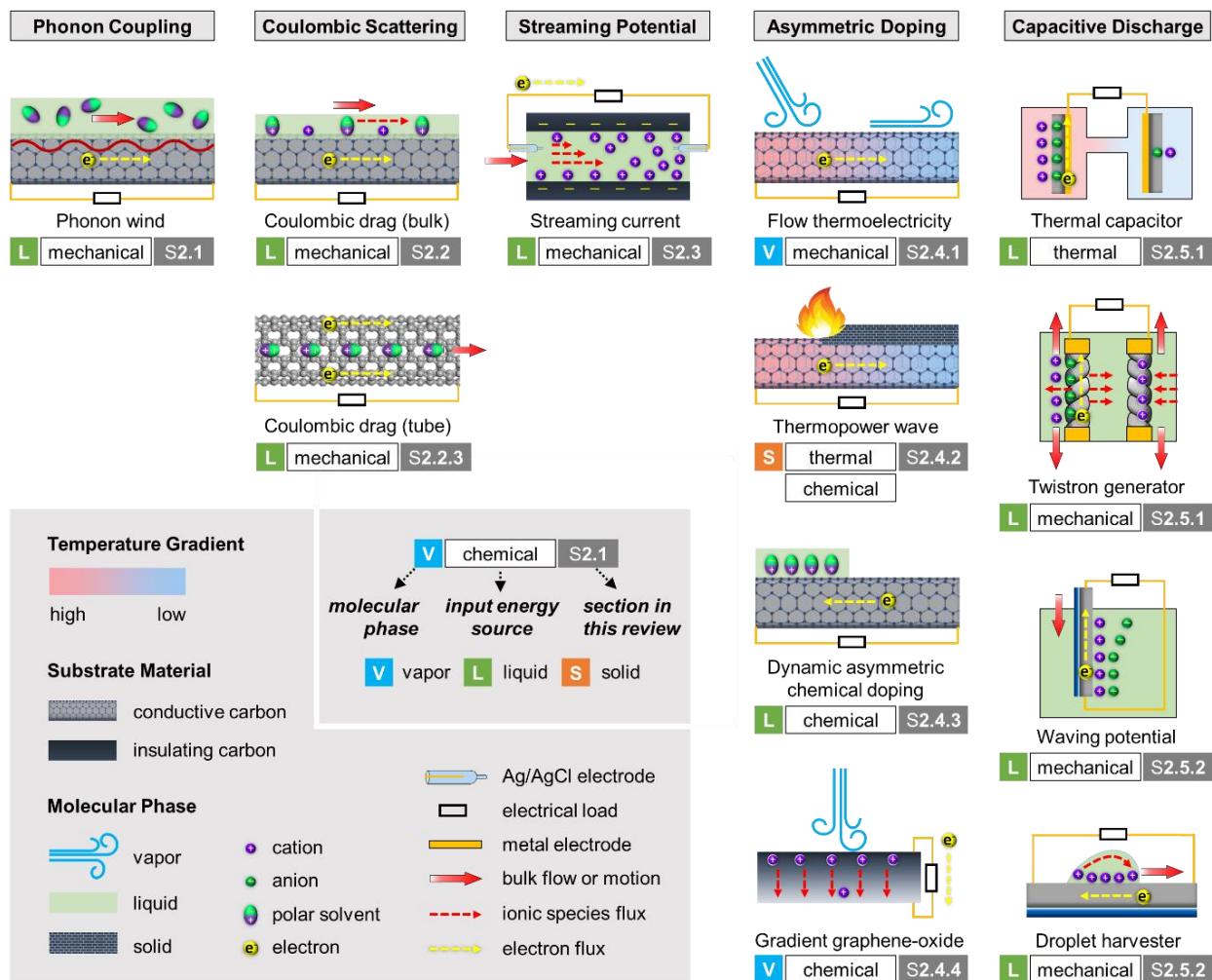


Figure 1-10. Schematic illustrations of typical mechanisms of harvesting energy from molecular interactions with nano-structured carbon materials.^{158-163,167} Each column summarizes the

approaches reported in the literature that fall under one of the five main mechanisms. Legends are listed at the bottom left corner.

1.2.2.1 The Phonon Coupling Mechanism

Whilst direct electric current induction within a single nanotube from interactions with nearby molecules awaits further exploration, examples associated with such a system have long been proposed and studied. The detailed mechanism of such an energy generation, however, is still under intense debate. One of the first investigations to propose the idea of driving an electric current via nanotube-liquid interactions was by Král and Shapiro,¹⁸⁰ where they outlined the theoretical foundations of pushing free electric carriers inside the tube by either a flow-excited lattice “phonon wind” or through localized Coulomb scattering in a “cog-wheel pumping” manner, both of which became prevalent models under much theoretical and experimental scrutiny (**Figure 1-11a**).

As a reverse process of a CNT electrochemical actuator,¹⁸⁵ where applied DC bias is shown to depolarize adsorbed ions on nanotube walls immersed in a NaCl solution, electric current in a layer of electron gas can, in principle, be induced by the exchange of momentum with another electron gas, moving in close vicinity.¹⁸⁰ This effect is analogous to, and motivated by, the coupled transport of carriers between 2D and 3D electron gas layers demonstrated in a AlGaAs/GaAs system.¹⁸⁶ This frictional drag observed between carriers in isolated double-quantum-well structures was first thought to occur through a Coulomb scattering process, free from a photon-assisted pathway,¹⁸⁷ before it was carefully reconsidered¹⁸⁸ and subsequently revised.¹⁸⁹ Indeed, it was shown that electrons in one layer can be driven by hot longitudinal acoustical phonons emitted by electrons running in the adjacent layer,¹⁸⁹

or, alternatively, pumped by surface acoustic waves across the material interface.¹⁹⁰ Likewise, in this liquid-driving mechanism for CNT ensembles by Král and Shapiro,¹⁸⁰ momentum transfer from the flowing liquid phase, both through phonon excitations, and directly from the fluctuating Coulombic fields, are considered:

$$J = J_{e-p} + J_{e-l} \approx 8ev_F\Delta n + 2ev_m n_{free} r_l \quad (1)$$

Here J , J_{e-p} , J_{e-l} represent the total induced electric current (J), the current driven by phonon wind (J_{e-p}), and the current driven by localized electric carriers through Coulombic interactions (J_{e-l}), respectively. These two contributions can be further broken down to the two subsequent terms on the right-hand side, with e denoting elemental charge; v_F and v_m denoting carrier intra-band velocity and liquid laminar flow velocity; Δn and n_{free} representing the difference of flow induced hot-phonon population and CNT free electric carrier density; and r_l being the fraction of these free carriers localized by the adsorbed molecular dipoles. It was further noted that the electric carriers driven by the associated “phonon wind” are close in nature to those in the thermoelectric phenomenon, with the knowledge that nanotubes immersed in liquids can be effectively doped by the fluctuating molecular dipoles,¹⁸⁵ translating the electrochemical coupling readily into CNT vibrational mode shifts.¹⁹¹ It was estimated that, for metallic tubes at least, free electrons are mostly driven by hot phonons around the tube walls, induced by the friction of the moving liquid, as opposed to the carrier localization brought about by Coulombic scattering.¹⁸⁰

1.2.2.2 The Coulombic Scattering Mechanism

1.2.2.2.1 Pulsating Asymmetric Ratchets

The first experimental demonstration of such a system was realized by Sood and co-workers,¹⁸¹ where they observed the flow of a liquid on SWNT bundles can induce a voltage in the direction of the flow. In this study, the authors placed SWNT bundles of 1 mm length (along the flow direction), 2 mm wide and 0.2 mm thick inside a laminar flow cell (**Figure 1-11b, inset**), and reported a logarithmic dependence of the voltage across the bundle as a function of the flow velocity (**Figure 1-11b**), with notable voltage saturation at flow velocities as low as $0.001 \text{ mm}\cdot\text{s}^{-1}$.¹⁸¹ They also found that, even when immersed in water at rest, a voltage on the order of 1 mV was developed across the bundle, which was treated as the electrochemical potential difference at the interface of the SWNT bundle with the metal electrodes, and subsequently subtracted out as an offset from the flow-induced voltage data. Furthermore, the authors pointed out that in the “phonon wind” mechanism that had predicted the generated electricity, the force exerted by the liquid on the surface of the nanotube is proportional to the shear viscosity (η) and the flow velocity (v_m). And this necessarily infers a positive linear dependence of the hot phonon-induced electric current (J_{e-p}) on both parameters, which disagrees with their observations of (i) a sublinear (logarithmic) voltage response to the flow velocity, (ii) the strong dependence of the generated voltage on liquid polarity, and (iii) the fact that viscosity acts to reduce the flow-induced voltage.¹⁸¹ These findings, as it turns out, favored a fluctuating Coulombic potential mechanism, which the authors formulated as “pulsating asymmetric ratchets”,¹⁸¹

involving the asymmetry provided by the velocity gradient at the liquid-SWNT interface.

The 1D confinement of the charge carriers in the nanotube, in particular, was identified to play an essential role to ensure an additive effect of these pulsating ratchets connected in series. A clear distinction was also drawn for the polarity of the induced electricity between the two competing mechanisms of phonon coupling and Coulombic scattering. In the viscous drag regime (*i.e.*, “phonon wind”), the carrier current follows the fluid flow, and hence the sign of the generated voltage is determined entirely by the identity of the major carriers within the CNTs (*i.e.*, electron or hole). Whereas for Coulombic scattering, irrespective of the substrate doping level, the dominant charge of the adsorbed species decides the direction of the voltage.¹⁸¹ Yet, for the traditional Coulombic coupling mechanism, the induced current J_{e-l} is predicted to increase linearly with the flow velocity. Hence, the physical picture of Coulombic drag was further generalized, using the fluctuation dissipation theorem, as space-time correlated Coulombic fluctuations that are inherent to the liquid electrolyte.¹⁹² The Langevin-equation based treatment of the nanotube charge carriers reveals the diminishing friction from these flow advected Coulombic fluctuations with increasing flow velocity, crucial to the justification of observed sublinear dependence of the charge drift velocity.¹⁹³ The divergence of Sood’s results from previous predictions, therefore, set the stage for a decade-long debate over the underlying physics, which has inspired remarkable technological advances using this phenomenon.

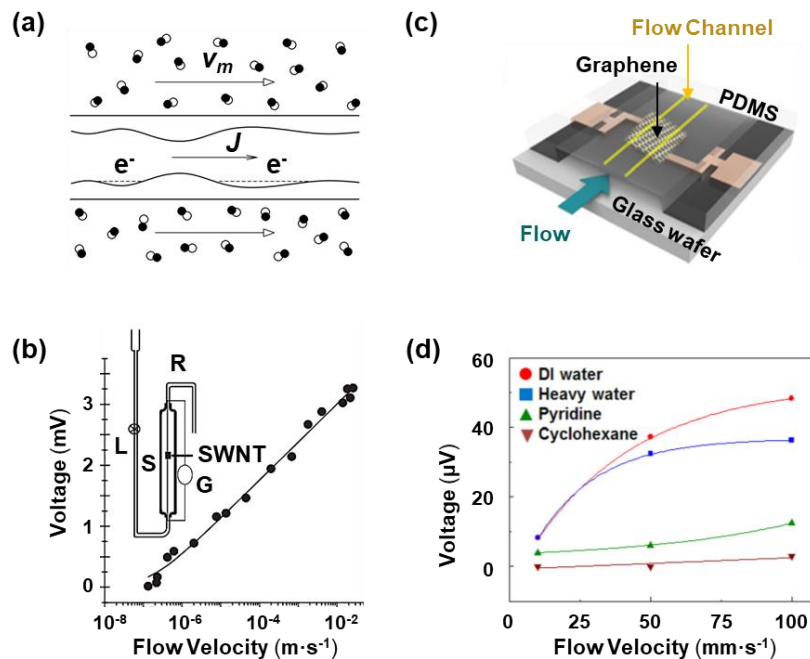


Figure 1-11. (a) Schematic illustration of a metallic nanotube immersed in a liquid, which flows along it with a bulk velocity v_m . Liquid molecules, denoted by pairs of circles, coat the annulus of the CNT in a form of slipping layers and generate a phonon wind in the CNT lattice.¹⁸⁰ (b) Variation of voltage developed as a function of water flow velocity. Solid line is a logarithmic fit. **Inset:** Experimental setup for the flow-induced voltage measurement, where R is the water reservoir, L is the flow controller, S is the cylindrical glass flow chamber, and G is the voltmeter.¹⁸¹ (c) Improved experimental setup for observing Coulombic drag on graphene. Note, the electrodes of the graphene sample (aligned parallel to flow) are not exposed to flow.¹⁹⁴ (d) Flow-induced open circuit voltage in several non-ionic liquids over monolayer graphene.¹⁹⁴

1.2.2.2.2 Stick-slip Thermal Activation

One of the criticisms for the “pulsating asymmetric ratchets” interpretation¹⁸¹ of the general Coulombic scattering mechanism, is that there appears to be no independent

physical evidence for such ratchet potentials.^{195,196} Instead, Persson et. al.¹⁹⁶ suggested a conceptually simpler, nonetheless effective, amendment for the original Coulombic-coupled carrier transport proposal.¹⁸⁰ Their approach takes inspiration from an electrokinetic model proposed by Helmholtz,¹⁹⁷ in which a streaming potential is induced by a liquid flowing past a solid substrate to equilibrate the imbalanced ions carried by fluid flow in the diffuse (Debye) layer at the interface.¹⁹⁵ Helmholtz's streaming potential, as will be expanded in the next section, is of course a distinct mechanism in and of itself, and shall not be confused with Persson's modification to the generic Coulombic scattering. Nevertheless, the electrokinetic model's insights within the Debye layer have proven to be instrumental to Persson's realization that this electronic double layer should be treated separately from the bulk. To account for the logarithmic growth of the voltage as a function of the flow velocity found in the Sood study,¹⁸¹ Persson et. al. envisioned a "stick-slip" mechanism to describe the motion of the ions adsorbed on the surface of the nanotube,¹⁹⁶ where the drifting of these otherwise surface-pinned ionic species are treated as thermally excited jumps over force-biased barriers, created by a monolayer of densely packed solvent molecules.^{198,199} Subsequent electric friction against the free carriers in the nanotube recovers the characteristic logarithmic voltage dependence on flow velocity.

To be more specific, the solvent molecules that had self-assembled into a 2D monolayer annular coating around the CNT would experience a pinning potential towards the nanotube surface,²⁰⁰ exerted by the adsorbed ionic species (*e.g.*, depicted here as cations, without loss of generality, **Figure 1-12a**).¹⁹⁶ These cations

are in turn dragged forward by the external fluid flow, sliding in a “stick-slip” fashion, with intervals of elastic deformation (loading phase) followed by rapid local yield events of the solvent molecules and the cations alike. During the loading phase the local stress within the solvent-cation block increases linearly with time, until reaching the critical stress σ_c , when the rapid rearrangement takes place and slides the block forward. Mathematically, the velocity v_a of the slipping cations (as well as other solvent molecules within the local 2D block) can be described as:¹⁹⁶

$$v_a = \frac{\mu E k_B T}{2\sigma_c L} \ln\left(\frac{v_0}{v_c}\right), \text{ where } v_c = \frac{\beta k_B T}{\alpha \sigma_c a L} \exp\left(-\frac{\sigma_c^2 L^2 a}{E k_B T}\right) \quad (2)$$

where a logarithmic dependence of the cation drifting velocity with respect to the average driving flow velocity v_0 naturally falls out. Here, μ is the ion drift mobility; L , a , and E measure the length, thickness, and elastic modulus of the stress block, respectively; α defines the slope of the linear velocity profile expected for a Newtonian fluid, in that $v = \alpha v_0$ (**Figure 1-12a**); and β represents the Arrhenius prefactor associated with the rate of thermally excited jumps over the adsorption pinning potential.

With the established ionic drift velocity, v_a , and a carrier density, n_e , in the CNT, the authors then derived both short circuit current and open circuit voltage as follows, based on a modified Drude model:¹⁹⁶

$$I_{SC} = \frac{\kappa}{1 + \kappa} 2\pi r n_e e v_a, \text{ where } \kappa = \frac{\eta \tau m_a n_a}{m_e n_e} \quad (3)$$

$$V_{OC} = \kappa R_0 2\pi r n_e v_a \quad (4)$$

where r measures the nanotube radius; η is the electronic friction coefficient; τ is the Drude relaxation time; n_a , m_a and m_e are the adsorbed ion concentration, mass, and electric carrier mass, respectively; and R_0 is the nanotube resistivity in the absence of any adsorbates. This marks one of the first models derived from first-principles, with quantifiable physical parameters, and it is one that makes falsifiable predictions. It also introduces streaming potential, albeit as a modified version, to explain the general phenomenon of flow-induced voltage. This molecular-level depiction by Persson et. al. ,¹⁹⁶ involving a layer of densely-packed molecules dragging the electronically-active adsorbed ionic species in response to the external flow field, represents an important theoretical milestone for understanding the electricity generation process.

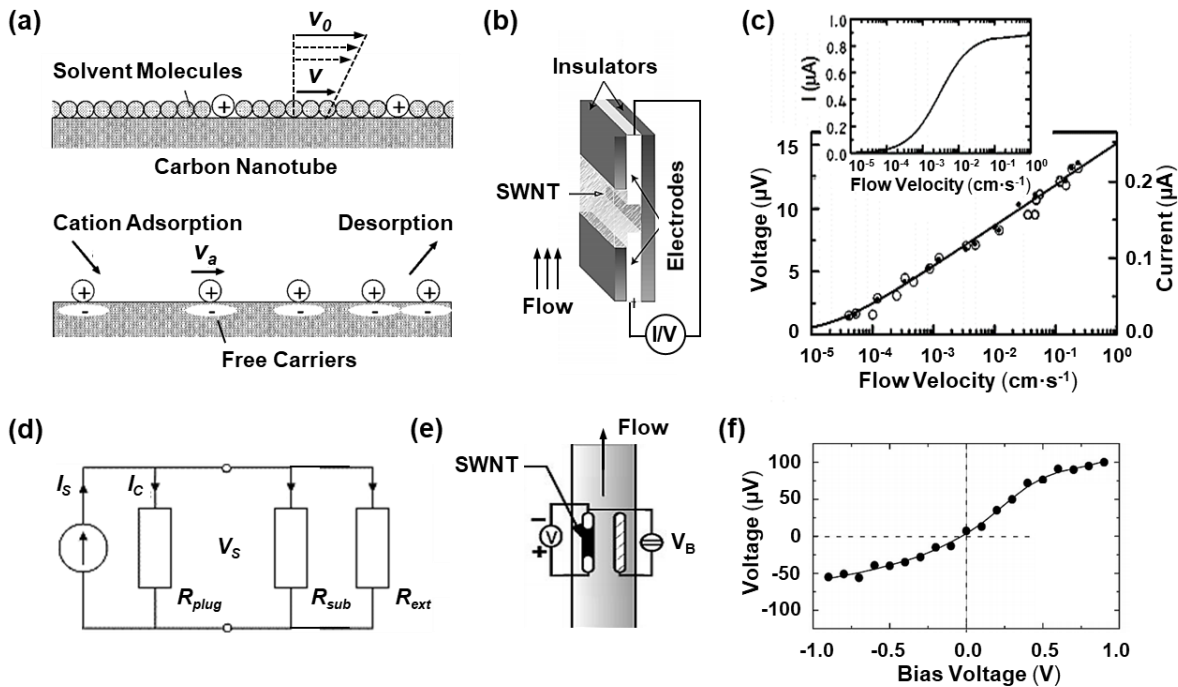


Figure 1-12. (a) Schematic illustration of the solid-liquid interface for carbon nanotubes immersed in fluid flow. Liquid molecules assemble into a 2D monolayer, which is pinned to the nanotube

surface by the adsorbed ions.¹⁹⁶ **(b)** Schematic illustration of the experimental set-up for measuring flow induced voltage across SWNT bundles. SWNTs are packed between two metal electrodes, with two insulating layers keeping the SWNTs in place.¹⁹² **(c)** Voltage (full circles) and current (open circles) measured as functions of the flow velocity. The solid line fits to a logarithmic function. **Inset:** a theoretical plot of the current versus flow velocity based on a generalized version of the pulsating asymmetric ratchets model.¹⁹² **(d)** An equivalent circuit model of the streaming current and potential, in the presence of a conductive solid substrate, when connected to an external load.²⁰¹ **(e)** Experimental set up to characterize the direction of the flow induced voltage as a function of the bias voltage, V_B , as measured with respect to the Au reference electrode immersed in the flow chamber.¹⁹² **(f)** Flow-induced voltage as a function of the bias voltage. The solid line serves as a guide to the eye.¹⁹²

1.2.2.2.3 Coulombic Scattering in 2D Materials

Sood et. al.'s pioneering results¹⁸¹ on the Coulombically-derived electricity using singled-walled carbon nanotube conduits, and the subsequent theoretical amendment set forth by Persson and co-workers,¹⁹⁶ have cemented Coulombic scattering as one of the fundamental mechanisms whereby electric carrier flow can be driven by a corresponding flow of an ionic liquid. Their explanation has captured the imaginations of many,^{145,182,183,202} including those in the 2-dimensional (2D) materials community. The 2D material graphene, hailed as a major scientific feat in modern condensed matter physics, possesses several outstanding electrical and mechanical properties, such as its extremely high electron mobility, tunable conductivity, and remarkable mechanical strength. Guided by the Coulombic scattering suite of mechanisms, voltage generation with a liquid phase flowing over

graphene has also been explored. A flow of acidic water (0.6 M HCl) over few-layer graphene film on Si/SiO₂ substrate, for example, reportedly generates *ca.* 30 mV, induced by the Coulombic coupling of the adsorbed Cl⁻ ions with the abundant free carriers in the graphene lattice.¹⁸⁴ The measured power density amazingly exceeds 100 W·m⁻², thanks to the excellent coupling between ions and free carriers.

This experimental work, however, was quickly challenged by a follow-up study arguing that flow-induced voltage should not be attributed to the coupling of charge carriers in graphene with the flowing ions in the solution phase, nor does it result from the drag force associated with the liquid-molecule-generated phonon wind.²⁰³ Rather, the graphene is said to mainly behave as a passive load connected between two electricity-generating electrodes. According to these authors, the electrode–solution interaction plays a central role in producing the observed voltage: as the sample is immersed in the acidified water, an electrochemical potential is introduced within the electrodes; the water flow changes the electrostatic potential, breaks the electrochemical balance, and introduces an observed voltage drop between the electrodes.

The conflicting evidence undermines the validity of applying the Coulombic scattering regime to graphene systems and was eventually resolved by an independent study from a different group.¹⁹⁴ To eliminate the possibility of the suspected electrode (Ti/Au) interaction with the solution, Lee et. al.¹⁹⁴ modified the original Dhiman¹⁸⁴ experimental set-up (**Figure 1-11c**) and showed that a voltage can indeed be generated using mono-layer graphene free from potential confounding electrode–solution interactions, reiterating the intrinsic energy

harvesting capability of these graphene surfaces under unidirectional liquid flow (**Figure 1-11d**).^{194,204} Note that in this set of experiments, Lee and colleagues used a series of polar non-ionic liquids (*e.g.*, de-ionized H₂O, D₂O, etc., **Figure 1-11d**),¹⁹⁴ as opposed to the previously explored acid and salt solutions,^{184,203} setting the field up for a more generalized understanding to the Coulombic drag approach.

In principle, the Coulombic coupling should also occur directly between dipoles of fluid molecules and free charge carriers. Even though the earlier stick-slip model explicitly invoked charged ionic species adsorbed onto the surface of nanotubes, this coupling effect should really be generalized to include dipole-to-carrier interaction as well. For non-ionic flow outside nanotubes, the CNT surface would prefer to interact with either the positive or the negative charge center of the fluid molecules, resulting in a layer of adsorbed polar solvents with dipoles aligned roughly perpendicular to the tube axis. The formation of this oriented solvent shell is similar to that of an electrical double layer in an ionic solution, and the electricity generation induced by its movement should also be described by the generalized Coulombic drag mechanism. Therefore, energy harvesting from polar, non-ionic fluid (*e.g.*, de-ionized water, EtOH, pyridine, etc.) flowing over graphene or SWNT should be possible, according to mechanisms such as the pulsating asymmetric ratchets or stick-slip thermal excitation.^{194,205-208} In fact, Sun and co-workers reported a voltage of 220 μV , which was generated by evaporation-driven flow of ethanol ($v \approx 6 \times 10^{-5} \text{ m}\cdot\text{s}^{-1}$) through SWNT ropes,²⁰⁷ showing good consistency with Sood et. al's data (150 μV for methanol at $v \approx 7 \times 10^{-5} \text{ m}\cdot\text{s}^{-1}$).¹⁸¹ In addition, they observed a saturating behavior of the generated current with respect to fluid

velocity and no dependence of electricity generation on the bias voltage (**Figure 1-11d**).^{205,206,208} The saturating behavior is consistent with the nearly logarithmic dependence observed by Sood et. al., and the lack of response to bias voltages can also be expected for non-ionic fluids.

1.2.2.2.4 Aligned Dipole-carrier Coupling Inside Carbon Nanotubes

On the other hand, what would happen for molecules travelling inside a carbon nanotube? Admittedly, flow inside nanotubes is expected to induce electric current in a slightly different manner, by virtue of the confined fluid structure. Water flow, for instance, exhibits unique behaviors in the interior of carbon nanotubes, as the water molecules form an intimate contact with the lumen of the SWNTs on the atomic level.²⁰⁹⁻²¹¹ The extremely confined space inside carbon nanotubes may break bulk water down into an unusual single-file configuration, which has been a fascinating area of theoretical and experimental research.²¹²⁻²¹⁸ As the diameter of SWNT decreases, the behavior of water deviates considerably from that of the bulk. Numerous simulations have predicted tube-like or chain-like arrangements of these water molecules, connected via hydrogen bonds, in SWNTs with medium (0.7 to 0.8 nm) to small (0.3 to 0.4 nm) diameters (**Figure 1-13a, b**).²¹⁹⁻²²¹ These structures may exhibit exotic thermodynamic properties, such as melting transitions above room temperature even at ambient pressure, an effect only recently verified on an experimental level.²²²⁻²²⁵ Most importantly, these structures share a common feature of molecular dipoles aligning parallel to the tube axis. This oriented chain of dipoles with alternating positive and negative charges, when moving, should

exert drag on free carries in a fashion distinct from the ordinary Coulombic drags more commonly associated with flow outside of the tube.

Experimentally, voltage generation induced by the flow of water inside a metallic SWNT was also reported, albeit using somewhat indirect measurements (**Figure 1-13c**).^{226,227} In this study by Sun and co-workers, individual SWNTs with an average diameter of 1.6 nm are “filled” with water vapor (**Figure 1-13c**). The inferred spontaneous “filling” of water stems from the fact that the SWNT channels possess a deep potential well in their interior, strong enough to break the hydrogen bonds of liquid water and pull single water molecules into the lumen of nanotube channels.^{222,228,229} A voltage difference of about 1 mV was observed across the SWNT when water was electrically driven to flow inside the tube. Flow induced electricity inside a single carbon nanotube, specifically, has since then become a hot area for many theoretical investigations. In particular, according to a molecular dynamics study, for a single-file water chain confined in (6,6) SWNTs, the electrostatic field of the water dipoles would polarize the nanotubes and induce a charge distribution on the nanotube surface, resulting a voltage difference of 17.2 mV between the two ends of the SWNT.²³⁰ Atomistic simulation of an energy harvesting process via the flow of a hydrochloric acid–water solution through a CNT has also been explored,²³¹ where the induced voltage along the axial direction is correlated with the corresponding ionic drift velocity. Nevertheless, experimental evidence for energy generation at this scale remains scarce and elusive.

On the flip side of a flow generator, there has been plenty of efforts on pumping water through carbon nanotubes using external electric fields.^{232,233} Early

theoretical works already showed that ionic movements inside a SWNT cause water to flow outside the tube due to a long-range Coulombic coupled process through the tube wall.^{234,235} Meanwhile, it has also been demonstrated that the coupling, despite being quite weak, between water dipoles and free charge carriers in the nanotube is mutual, i.e., a constant current can induce a directional water flow inside the nanotube, whereby the one-dimensional confinement of the nanotube channel ensures that the induced water flow is steady and concerted.^{226,232,233,236-240} In fact, in the study by Sun et.al mentioned earlier,²²⁶ the water is dragged by moving free charge carriers when an electric field is applied across one section of the SWNT (“motor” part in **Figure 1-13c**), and the generated voltage was measured on another section (“generator”, **Figure 1-13c**). There is a marked dependence of this water transport on the concentration of water vapor, exhibiting saturation kinetics at high concentrations, indicating maximal filling of the SWNT interior.²²⁶ It is also noted that semiconducting SWNTs perform worse as a water pump than the metallic ones, which is expected under the Coulombic scattering regime due to the reduced density of free charge carriers in s-SWNTs. This work has stimulated a plethora of ideas on active transport of molecules bearing a permanent dipole through nanometer sized channels, such as a nanometer water pump driven by the motion of nanoparticles across the membrane surface,²⁴¹ a current or oscillating charge driven water pump,²⁴²⁻²⁴⁴ a resonance-coupled mechanical wave driven water pump,²⁴⁵⁻²⁴⁸ a surface energy driven water pump,²⁴⁹ an ion coupled electric field driven water pump,²⁵⁰ a methane molecule driven water pump,²⁵¹ a rotating

magnetic-electric field driven water pump,²⁵² and of course, the more conventional nanoscale water pumps driven by a pressure gradient.²⁵³

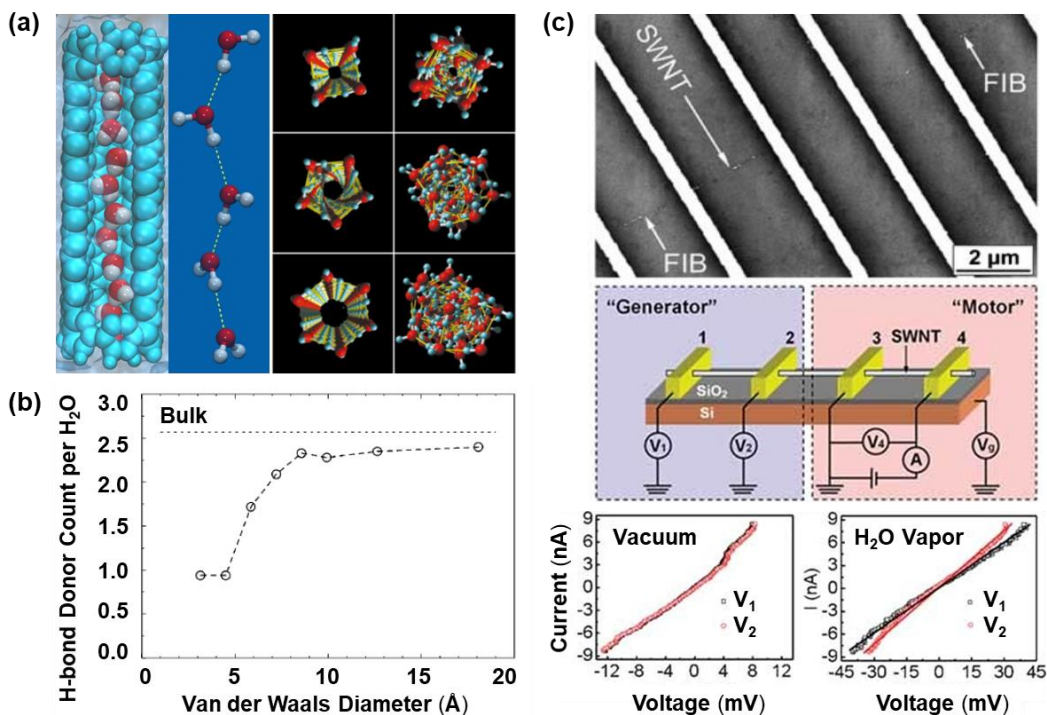


Figure 1-13. (a) Simulated structures of water molecules confined in carbon nanotubes: single-file arrangement of water molecules inside a single-walled (6,6) CNT and the corresponding hydrogen bond configuration (left two columns);²²⁴ square, pentagonal, and hexagonal ice nanotubes (and their corresponding liquid) formed in (14,14), (15,15) and (16,16) SWNTs (right two columns).²²² (b) Average number of hydrogen bond donors per water molecule inside carbon nanotubes of different diameters at 300 K.²²⁰ (c) **Top:** A typical scanning electron micrograph of an individual SWNT device prior to focused ion beam (FIB) cutting, with the SWNT sandwiched between the Ni/Au electrodes and the SiO₂/Si substrate. **Middle:** Schematic illustration of the SWNT device structure above. A suspended SWNT (in the presence of water vapor) is connected to four Ni/Au electrodes, where voltage is applied between electrodes 3 and 4 and the induced

voltage is measured between electrodes 1 and 2. **Bottom:** Measured potential of V_1 and V_2 as a function of current flowing through “Motor” part, showing zero voltage drop in vacuum (left) and non-zero voltage drop in water vapor (right).²²⁶

Finally, it is important to note the difference and relationship between Coulombic coupling and streaming potential. A Coulombic-coupled carrier drift model, at its heart, classifies this flow-induced electricity as a current generating phenomenon, in stark contrast to the classical electrokinetic picture of a streaming potential. First observed by Quincke^{254,255} in 1859 and quantitatively explained by Helmholtz¹⁹⁷ some twenty years later, the well-known streaming potential arises in many insulating porous materials in response to a liquid flow due to the counterion accumulation in a thin layer near the solid-liquid interface (*i.e.*, the Debye layer). In this purely ionic mechanism, the voltage appears as an electromotive force to counterbalance the charge build-up from the ionic current, while the mobile charge carriers (electrons and holes) in the solid play no role.¹⁹⁵ This would mean that if one characterizes the current-voltage relation in closed circuit, such as the one illustrated in **Figure 1-12b**, the pure electrokinetic mechanism would predict the ratio of the measured voltage over the current to be the internal resistance of the electrolyte (*c.a.*, 0.1 M Ω), as opposed to the electric resistance of the solid substrate (*c.a.*, 25 Ω), an effect confirmed by a follow-up study from Sood (**Figure 1-12c**).¹⁹² Moreover, an electrokinetic model would also forecast a linear dependence of the streaming potential, and the conduction current induced thereof, as a function of the flow velocity, which was once again demonstrated to be otherwise in Sood’s new experimental system (**Figure 1-12c**).¹⁹² However, as will be explained here

forth, these observations do not necessarily rule out a generalized streaming potential scheme, which decidedly is a voltage generating phenomenon and has a completely opposite prediction on the directionality of the output electricity. At the interface between an ionic liquid and a conducting solid, it is possible for these two phenomena (Coulombic drag and streaming potential) to co-exist, whereas one of them may be ruled out if either the liquid is non-ionic (i.e., streaming potential) or the solid is insulating (i.e., Coulombic drag).

1.2.2.3 The Streaming Potential Mechanism

As alluded to in previous sections, when a solution is pressed through a microscale or nanoscale porous plug, a streaming potential can be developed. The phenomenon is not restricted to carbon nanotubes, and was traditionally observed, in fact, almost exclusively in non-conductive substrates such as powdered glass and ivory chips.¹⁹⁵ This electrical response generally stems from the population imbalance of the mobile charges residing in the diffuse layer of the solution phase, due to a net ionic current (I_S , or streaming current) driven by the hydrodynamic flow Q , in response to a pressure drop ΔP over the porous plug. Subsequent charge polarization results in an electric field, E , inducing ionic motion in the opposite direction (I_C , or conduction current). At thermodynamic equilibrium (i.e., when $I_S + I_C = 0$), the induced electromotive force (V_S , or streaming potential) reaches its maximum, and the whole system can be conceptualized using the following equivalent circuit model (**Figure 1-12d**), in which the streaming current can be derived analytically:²⁰¹

$$I_S = \frac{A\varepsilon_0\varepsilon_r\Delta P\zeta}{\eta l} \quad (5)$$

where the l and A characterizes the pore length and cross-sectional area of the channel; the zeta potential, ζ , measures the electrical potential in the diffuse layer with respect to that of the bulk solution; ϵ_0 , ϵ_r , η define the vacuum permittivity, solution relative permittivity, and solution viscosity, respectively. In other words, the parameter grouping ($\epsilon_0 \epsilon_r$) represents the dielectric constant of the solution within the porous plug. The ionic conduction current can be formulated as:²⁰¹

$$I_C = \frac{A\sigma V_s}{l} \quad (6)$$

where σ measures the solution's ionic conductivity in the presence of an electric field. In the absence of an external load, for a non-conductive substrate, the maximum streaming potential across the plug, V_s^{max} , when steady state equilibrium conditions are met, is given by:²⁰¹

$$V_s^{max} = V_s \Big|_{I_s = -I_C} = \frac{\epsilon_0 \epsilon_r \Delta P \zeta}{\sigma \eta} \quad (7)$$

It should become clear at this point that this classical electrokinetic picture has not yet taken into account any contributions from the solid phase, other than it being electrically insulating, which is not the case in a highly conductive substrate, such as carbon nanotubes or graphene. In fact, the carbon nanotubes, by forming a percolating pathway between the two ends of the plug, act as a “shorting” load (R_{sub}) that drains the built-up streaming potential, generally not in a productive manner (**Figure 1-12d**). This, incidentally, also offers an alternative, streaming potential based, explanation to the earlier observed current-voltage relation affording an effective resistance much closer to that of the SWNT substrate

(**Figure 1-12c**),¹⁹² seen as the conductive substrate and the liquid phase forming two resistors in parallel (**Figure 1-12d**).

To be sure, the simplistic version of the streaming potential mechanism cannot account for the sub-linear voltage and current dependence on the flow velocity,¹⁹² and areas for improvement remain. It should be emphasized, however, these two mechanistically distinct approaches (*i.e.*, streaming potential and Coulombic scattering), while not mutually exclusive to one another, make very different predictions when it comes to the directionality of the generated electric field, as well as the closed-circuit current polarity. In the following experiment (**Figure 1-12e**),¹⁹² for instance, when the SWNT bundle is electrically biased with a positive voltage ($V_B > 0$, as referenced to an Au counter electrode in solution), an upward streaming current (parallel to liquid flow) of negatively charged ions in the diffuse layer is expected, resulting a positive flow-induced voltage with the depicted measurement setup (**Figure 1-12e**). This is due to the fact that, when the SWNT is positively doped (or p-doped), the reduced Fermi level of the nanotube would draw to its surface an electric double layer consisting of mostly negatively charged species.²⁵⁶ A Coulombic scattering mechanism, on the other hand, should predict an upward flux of positive carriers (holes, as major carriers under positive bias) within the nanotube, along with the upward hopping of the strongly adsorbed anions in the Stern layer (the ions closest to positively charged nanotube surface), in principle generating a negative voltage (**Figure 1-12e**). The result, as shown in **Figure 1-12f**,¹⁹² seemed to have favored the streaming potential proposal, from this perspective. Meanwhile, the sub-linear dependence of voltage on flow velocity might result from the offset of streaming potential by Coulombic drag.

Therefore, a comprehensive model including both streaming potential on conductive substrate and Coulombic drag might resolve the contradictions in the sections above.

In recent years, evaporation-driven water flow on functionalized nanostructured carbon materials has been explored for electricity generation. A typical device as shown in **Figure 1-14a** consists of a porous carbon black film with abundant functional groups (O–H, C–O, C=O, etc.) and two multiwalled carbon nanotube (MWCNT) electrodes patterned on a quartz substrate.²⁵⁷ With the lower half of the surface immersed, water will infiltrate the upper half via capillary force, and continuous flow is maintained by evaporation. A 4.5 cm long device is capable of generating a stable V_{oc} near 1 V, which can be turned off by sealing the water container (**Figure 1-14b**) or enhanced by flowing air (**Figure 1-14c**).¹⁷⁸ Aside from continuous flow driven by evaporation, directional infiltration of water droplets inside a porous carbon network has also been demonstrated as an energy source based on streaming potential (**Figure 1-14d**).²⁵⁸ The duration of electricity generation is shown to coincide with the time it takes for the droplet to dry (**Figure 1-14e, f**). While direct estimation and comparison of the magnitudes of voltage output amongst the three general mechanisms discussed thus far – phonon coupling (or momentum transfer), Coulombic scattering, and streaming potential – might be challenging, in part due to their heavy dependence on various unknown material parameters, one can apparently see from the reported experimental values to date that streaming potential tends to produce larger voltages, when compared with either momentum transfer or coulombic scattering. The elevated voltage output possibly stems from the higher resistivity of the substrates used for streaming potential measurements, making charge build-up easier. Nevertheless, this does not imply that streaming potential is always advantageous than the other two mechanisms.

A subtle point about measuring streaming current needs to be addressed here. Traditionally, non-polarizable electrodes (like Ag/AgCl) are used to form a closed circuit on insulating substrates^{201,259-262} because, in order for electricity to be generated and subsequently measured, electrodes must translate the ionic current into an electric one by allowing Faradic reactions to occur. However, CNT electrodes, which are almost ideally polarizable, were used in these recent studies to demonstrate energy harvesting via streaming potentials over nanostructured carbon black substrates (**Figure 1-14**).^{178,257,258} In the absence of any electrode reactions, a pure streaming potential phenomenon actually does not support continuous current generation in circuits consisting of both an ionic and electrically conductive medium (i.e., electrolyte and wire), simply because the built-up solution phase electric potential cannot be properly translated into the electric circuit. Hence, we speculate that, if the observed electricity is truly of electrokinetic origin, there might be some electrochemical reactions happening in these devices, oxidizing and reducing the porous carbon films near the positive and negative electrodes, respectively.

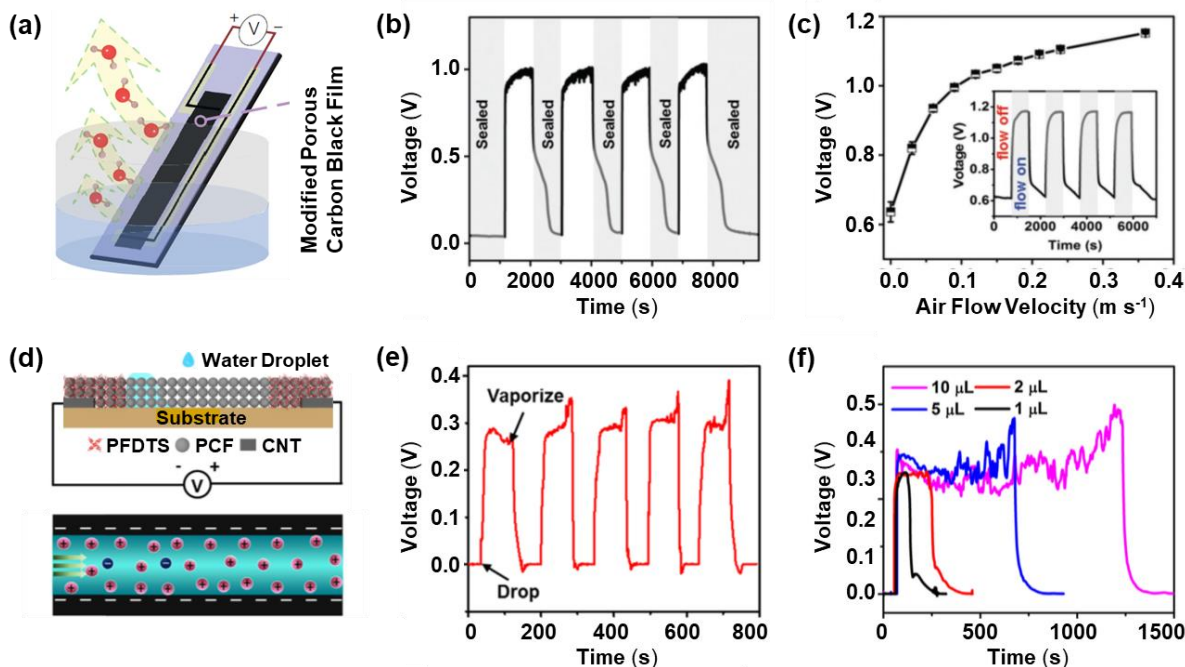


Figure 1-14. (a) Schematic of the device for measuring evaporation-induced streaming voltage. The device consists of a carbon black sheet and two MWCNT electrodes on a quartz substrate, which is inserted into DI water in a beaker.²⁵⁷ (b) Measured open circuit voltage (V_{oc}) of the device when the water beaker was periodically sealed and unsealed. (c) Enhancing open circuit voltage by increasing the velocity of air flow.¹⁷⁸ (d) **Top:** Schematic of a porous carbon film (PCF) device for water droplet infiltrating induced voltage. Selected regions of the device are modified with 1H,1H,2H,2H-perfluorodecyltriethoxysilane (PFDTs) to make it superhydrophobic.²⁵⁸ **Bottom:** Schematic showing the mechanism of streaming potential with negative charge on solid surface.²⁵⁸ (e) Open-circuit voltage obtained by repeatedly dropping 1 μL of water onto a porous carbon film. (f) Measured V_{oc} vs. time when water droplets with volumes of 1 μL , 2 μL , 5 μL and 10 μL were dropped onto the device.²⁵⁸

1.2.2.4 The Asymmetric Doping Mechanism

1.2.2.4.1 Gas Flow Induced Thermoelectricity

Shortly after the discovery of liquid flow induced electricity in SWNT bundles,¹⁸¹ Sood and co-workers reported that voltage can also be generated via gas flow (e.g., argon, nitrogen, oxygen) over SWNTs and various other semiconducting materials.²⁶³ However, the proposed mechanism featured an interplay of Bernoulli's principle and the Seebeck effect, which was fundamentally different from that in the liquid flow scenario. The initial observation of this effect involved placing a piece of semiconductor film at an angle α with respect to a gas inlet (**Figure 1-15a**). When the gas flow is turned on, Sood et. al. measured a voltage difference across the two ends of the film (**Figure 1-15b**).²⁶³ The magnitude and sign of the voltage depends on the properties of the solid. For argon at a flow velocity of 11 m/s, the voltage generated was $-16.4 \mu\text{V}$ for n-type Ge, whereas it was $5.9 \mu\text{V}$ for the sample of SWNT bundles.¹⁹² The authors rationalized that, as gas flow impinges onto the substrate, it decelerates/accelerates at the inlet/outlet end respectively, and the velocity variation will in turn create a pressure and therefore a temperature gradient along the film, as a consequence of energy conservation. It was subsequently determined that, this temperature drop, albeit small, is solely responsible for the observed voltage which is truly of thermoelectric origin. It is worth noting here that the general thermoelectric effect ultimately stems from a Fermi level gradient within the substrate materials in response to a temperature asymmetry, an effect reminiscent of a doping event.

The measured voltage shows a marked quadratic dependence on the Mach number (M) of the gas flow and is proportional to the Seebeck coefficient of the semiconductor. Approximating the process as adiabatic and the flowing gas as inviscid, as well as ideal, the following equations can be derived to explain the observed trend. Upon the application of the ideal gas law ($p \propto \rho T$), including the energy conservation relation ($u^2/2 + h = \text{const}$) and the sound velocity term ($c = \sqrt{\gamma p / \rho}$), one ends up with the expression in **Equation 8** for the pressure along a streamline:

$$\frac{p}{p_0} = \left(\frac{T}{T_0} \right)^{\frac{\gamma}{\gamma-1}} = \left[1 + \frac{1}{2}(\gamma-1)M^2 \right]^{-\frac{\gamma}{\gamma-1}} \approx 1 - \frac{1}{2}\gamma M^2 \quad (8)$$

In the equation and relations above, u represents the gas velocity far from the angle; $M = u/c$ denotes the Mach number; $\gamma = c_p/c_v$ is the adiabatic index (ratio of constant pressure heat capacity c_p to constant volume heat capacity c_v); $h = c_p T = \frac{\gamma}{\gamma-1} \frac{p}{\rho}$ is the specific enthalpy of the gas; p , ρ , and T correspond to the pressure, density, and temperature of the gas, which are also functions of position; p_0 and T_0 stand for its pressure and temperature at zero velocity. It should be noted that **Equation 8** is only valid when $M^2 \ll 1$, under which condition the density variation of the gas may also be ignored. As a result, we end up with the relationship below:

$$\frac{\Delta T}{T_0} = \frac{\Delta p}{p_0} = \frac{\gamma}{2} \Delta(M^2) \quad (9)$$

With the axial velocity being a function of the distance from the stagnation point (the inlet end): $u(x) \propto ux^{\alpha/(\pi-\alpha)}$, the final expression for the gas flow induced thermoelectric voltage can be written as:²⁶³

$$V = kS\Delta T \propto \frac{kT_0}{2} \gamma \cdot \Gamma_S M^2 \quad (10)$$

Here, k serves as a correction factor to account for the temperature difference between solid and gas. The theory above successfully captures the voltage's quadratic dependence on M (proportional to flow velocity) and linear dependence on Γ_S (Seebeck coefficient), both of which have been verified experimentally (**Figure 1-15c**).²⁶³ At larger Mach numbers, the expression in **Equation 10** needs to be further modified in light of the variations in gas density. The dependence of V on M and Γ_S remains the same, but the slope appears much smaller.²⁶³

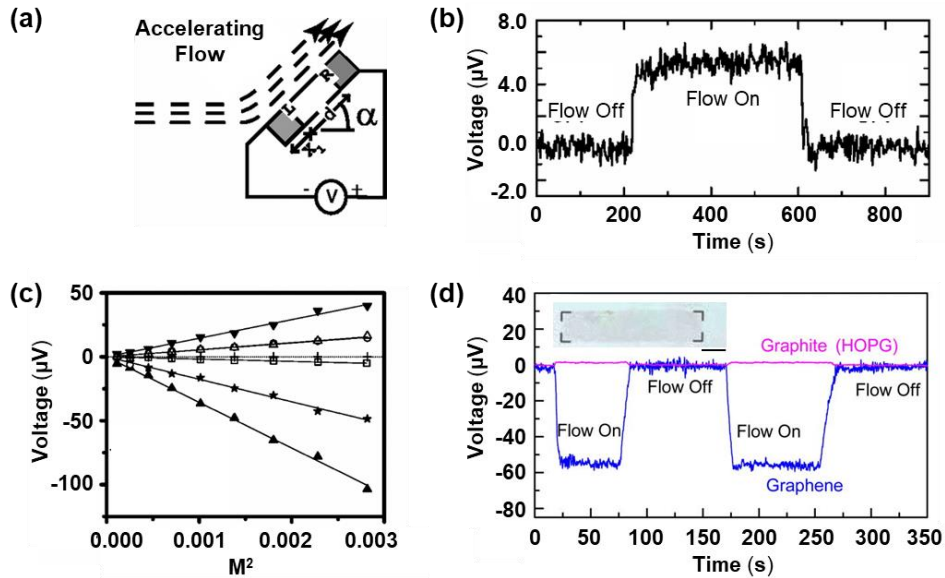


Figure 1-15. (a) Schematic of Sood et. al.'s sample set up for the gas flow induced electricity measurement. Shaded portions mark the electrodes. The positive terminal of the voltmeter is connected to the right (R) of the sample of active length d that is kept at an angle $\alpha = \pi/4$ with respect to the horizontal axis.¹⁹² (b) Typical response of n-doped Ge for a flow of argon gas at $7 \text{ m}\cdot\text{s}^{-1}$.¹⁹² (c) Dependence of the voltage magnitude on the flow velocity (represented as square of the Mach number, M^2) of nitrogen for (bottom to top) n -Si (filled triangles), n -Ge (stars), graphite (open squares), Pt metal (plus), SWNT (open circles), MWNT (open up triangles), and p -Si (filled down triangles). Solid lines are a fit to $V = AM^2$, where A represents a fitting parameter given in **Equation 10** as a grouping of several variables.¹⁹² (d) Typical voltage signal response of graphene and graphite for switching on/off the argon gas flow at $68 \text{ m}\cdot\text{s}^{-1}$. **Inset:** an optical image of the typical graphene sample used in the study, scale bar = 5 mm.²⁶⁴

This phenomenon has since been studied in a wide variety of semiconducting materials including Bi_2Te_3 ²⁶⁵ and doped Si and Ge.²⁶³ It was further discovered that surface functionalization of doped silicon wafers can increase the Seebeck coefficient, and hence improve the output voltage by more than an order of magnitude.²⁶⁶ More recent studies by Guo and colleagues shifted the focus to graphene substrates, where similar voltage responses have been recorded (**Figure 1-15d**).²⁶⁴ Further investigations of this effect on single and few-layer graphene show deviations from **Equation 10**: despite the monotonic increase of the Seebeck coefficient with layer number, the measured thermoelectric voltage is much higher in 2, 4, 5, 6, 7 layered samples than in 1, 3, 8 layered ones.^{264,267} The origin of this complex behavior may be due to the differences in stacking patterns, and has yet to be fully explained.

1.2.2.4.2 Thermopower Waves, Reaction-wave-triggered Doping Asymmetry

Another more exotic area to exploit molecular interactions with carbon nanostructures as a means for electricity generation is thermopower waves (TPWs). This approach involves coupling the exothermic nature of a chemical reaction with the advantageous electrical and thermal properties of a quantum-confined low-dimensional conduit, on which the reaction is carried out. It is a novel strategy to obtain electrical output using a thermal gradient, beyond what is possible via the conventional thermoelectric effect.

The Seebeck effect, or thermoelectric effect, describes the phenomenon of an equilibrium electric potential generated by a temperature difference across the ends of a thermoelectric material. The output thermoelectric voltage, ΔV_{TE} , as a function of the temperature gradient is given by the relation

$$\Delta V_{TE} = \int_{T_L}^{T_R} \Gamma_S \nabla T dx \quad (11)$$

where x is the spatial dimension for temperature variation; Γ_S is the Seebeck coefficient (or thermopower); T is the temperature state function, and T_L and T_R are the temperature at the left and right ends of the thermal conduit, respectively. Exploiting the traditional Seebeck effect requires thermoelectric materials to have high electrical conductivity that can enhance electron transport, but low thermal conductivity to maintain the temperature difference across the two ends of the device.

The thermopower wave phenomenon, on the other hand, capitalizes on the propagation of an exothermic chemical reaction on a conduit with both excellent electrical and thermal conductivities (**Figure 1-16a**). The first experimental demonstration of such thermopower waves utilizes vertically aligned carbon nanotubes (CNTs) as the conduit material (**Figure 1-16b**, panel **i** and **ii**).²⁶⁸ With a thermal conductivity on the order of $3000 \text{ W m}^{-1}\cdot\text{K}^{-1}$ and an electrical conductivity of around $10^6 \text{ S}\cdot\text{m}^{-1}$, CNT enjoys the rank as one of the best electrical and heat conductors to date.²⁶⁹ The high thermal conductivity renders CNTs less effective for traditional Seebeck applications. However, the phenomenon of thermopower waves takes full advantage of this property to drive the heat from the exothermic chemical reaction along the length of the nanotubes, accelerating the charge carriers entrained behind the accelerating reaction wave front and thereby producing high power electricity.

A typical thermopower wave (TPW) device consists of a uniform coating of molecules with high reaction enthalpies (*e.g.*, cyclotrimethylene-trinitramine) onto a quantum-confined substrate (*e.g.*, vertically aligned CNT array) using a technique called wet impregnation (**Figure 1-16b**).²⁶⁸ The TPW is then initiated with an external ignition source (*e.g.*, joule heater or laser), helping the high energy reactants to overcome the activation barrier. Exothermic reaction of the molecules releases heat, which is then accelerated forward, owing to the CNT's high thermal conductivity (**Figure 1-16c**). Subsequent heat transport ignites the fuel that lies in its path, thereby sustaining a self-propagating unidirectional soliton wave (*i.e.*, TPW, **Figure 1-16d**). Such TPW devices have been shown to exhibit high power

density comparable to that of Li-ion batteries ($80,000 \mu\text{W}\cdot\text{mm}^{-3}$ versus *c.a.* $10,000 \mu\text{W}\cdot\text{mm}^{-3}$ demonstrated for Li micro-batteries).²⁶⁹ The high power density of such devices provide attractive scaling for micro-electro-mechanical systems (MEMS)²⁷⁰ and smart dust applications.¹¹⁸ Over the half a decade since the discovery of TPWs, the field has made tremendous progress, pushing the boundary of accessible output voltages from tens of millivolts to 8.0 volts,²⁷¹ as well as an increase in energy efficiency by a factor of 10^6 (**Figure 1-16e**).⁵² Systematic efforts in optimizing reactant compositions²⁷²⁻²⁷⁷ and nano-structured conduit types^{271,278-289} have proven to be indispensable in TPW output enhancements (**Figure 1-16e**). Factors such as wave front velocity^{290,291} and molecular dopant electron affinity^{292,293} have been identified to play pivotal roles in the electricity generation process. Concomitant theoretical exercises have further elucidated the physical origin of this high-density electric power,²⁹⁴ including important milestones like the theory of excess thermopower,²⁹⁵ which ultimately culminated into the experimental realization of what is now known as asymmetric chemical doping (ACD).²⁹²

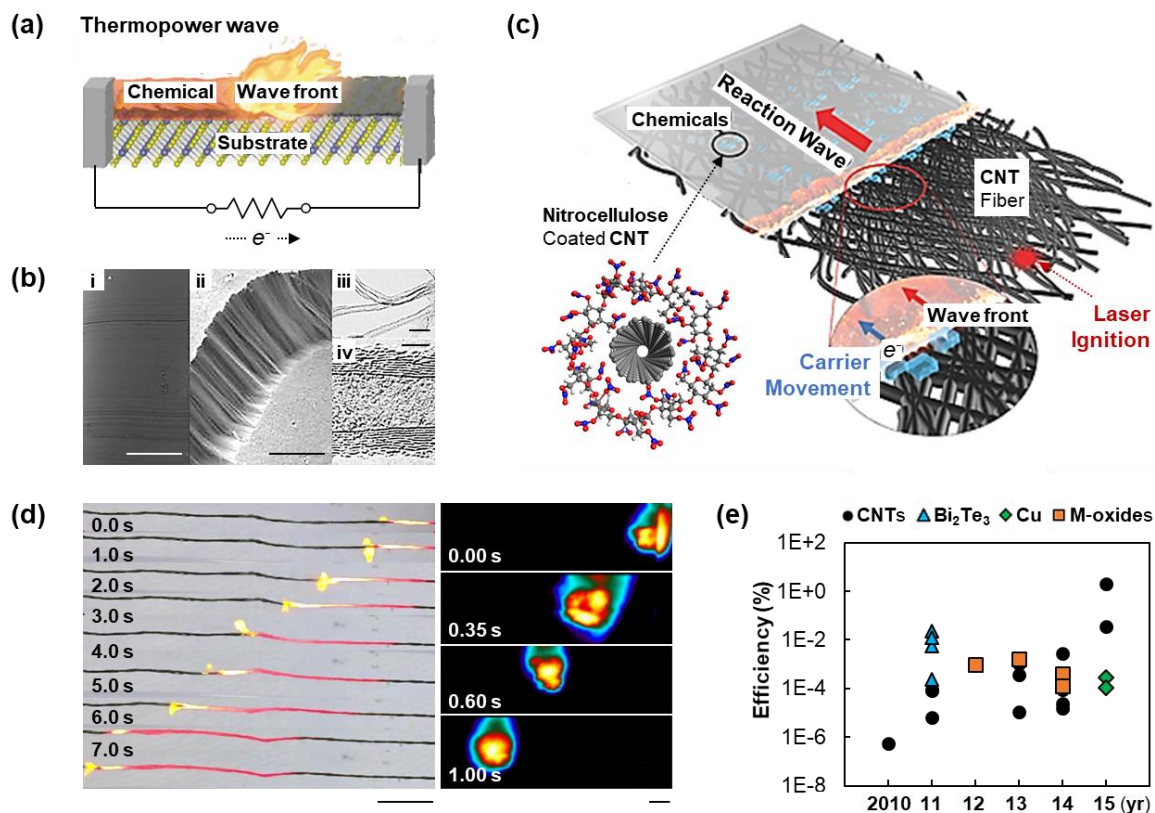


Figure 1-16. (a) Schematic illustration of a typical thermopower wave (TPW) device.²⁷¹ (b) Scanning electron micrographs (i, scale bar, 500 μm , and ii, scale bar, 10 μm) and transmission electron micrographs (iii, scale bar, 30 nm, and iv, scale bar, 5 nm) of the vertically aligned multi-walled carbon nanotubes used for the first reported thermopower wave electrical generator.²⁶⁸ (c) Detailed schematic illustration of a multi-walled carbon nanotube TPW generator, with nitrocellulose as the primary impregnated chemical reactant. **Inset:** a carbon nanotube surrounded by nitrocellulose molecules.²⁷⁶ Annular coatings of solid crystals between 6 and 9 nm in thickness wrapping a multiwalled carbon nanotube of *c.a.* 22 nm in diameter. (d) **Left:** time elapsed photographs of the traveling thermopower wave on a carbon nanotube yarn, using nitrocellulose as the primary reactant.⁵² **Right:** Time elapsed infra-red images of the propagation of a reaction wave on a graphene nano-pellets doped (5% by weight) nitrocellulose film (500 μm thick).²⁷⁵ (e)

Master plot for chemical to electrical conversion efficiencies of all thermopower wave device setups published to date, organized in terms of the substrate conduits used.⁵²

1.2.2.4.3 Excess Thermopower and the Asymmetric Chemical Doping

The theory of excess thermopower stems from an empirical observation that using carbon nanotube fibers as the thermal conduit, the thermopower wave generator devices produce power as much as 120% in excess of the predictions of the Seebeck effect.²⁹⁵ In fact, the magnitude of the voltage peak greatly exceeds the predictions of conventional thermopower in many cases. Using cyclotrimethylene trinitramine on aligned multi-walled carbon nanotube conduits (**Figure 1-16b**), for example, generates up to 220 mV pulses,²⁶⁸ with an average Seebeck coefficient (I_S) of only $-10 \mu\text{V/K}$,²⁹⁶ predicting a peak voltage of only 11 mV. Even more conventional thermoelectric materials, such as a thin-film Bi_2Te_3 ($I_S \approx 300 \mu\text{V/K}$), generates 150 mV at *c.a.* 600 K in a TPW measurement, with nitrocellulose as the reactant, compared to the Seebeck prediction of 90 mV.²⁷⁹ Likewise, TPWs from reacting nitrocellulose on ZnO substrates produce up to 500 mV, with Seebeck calculations accounting for only a fraction of the output (*c.a.*, 155 mV).²⁹⁷ The discrepancies between theory and experiment motivated the formulation of a new perspective towards the non-equilibrium TPW electricity generation process.

A continuum description of the thermoelectric effect within the relaxation time approximation begins with the drift-diffusion equation as the solution to the Boltzmann transport formalism describing carrier motion:²⁹⁵

$$J = -\sigma_h \left(E + \frac{\nabla\mu}{e} \right) - L_{12} \nabla T \quad (12)$$

where J represents current density, σ_h is the hole electrical conductivity, E is electric field, μ is chemical potential, e defines the elementary charge, L_{12} is an Onsager coupling coefficient, and T is the temperature. Here, the tensor form is neglected due to the high aspect ratio (>10) of typical TPW systems. In the limit of zero current, one can solve for E and integrate between the two ends of the TPW device from x_R to x_L to obtain the open circuit electric potential (V_{OC}):²⁹⁵

$$V_{OC} = -\int_{x_R}^{x_L} \left(\frac{\nabla\mu}{e} - \frac{L_{12}}{\sigma_h} \nabla T \right) dx = \frac{1}{e} (\mu_R - \mu_L) + \int_{T_R}^{T_L} \Gamma_S dT \quad (13)$$

Here, it has been noted that most thermoelectricity measurements (*e.g.*, for CNTs) do not include an explicit chemical or doping gradient, and hence the Seebeck coefficient Γ_S here is defined as $\Gamma_S \equiv L_{12}/\sigma_h = (E + \nabla\mu/e)/\nabla T$, specifically for the reference $\nabla\mu = 0$ case.²⁹⁵ This mathematical treatment formally separates the contribution of an explicit chemical potential gradient (first term on the right, **Equation 13**), that can arise from pure chemical doping, from that of a classic Seebeck effect (second term on the right, **Equation 13**), opening up a new design space for TPW output optimization, namely through intentional chemical doping.⁵²

Fundamentally, since chemical potential differences also drive carrier motion, differential doping between the reacted (hot, non-doped) and unreacted (cool, doped) ends of the CNTs can explain the excess voltage observed in TPW measurements. The theory of excess thermopower attributes the induced voltage as

the sum of two distinct sources, namely thermoelectricity and the voltage resulted by the non-equilibrium Fermi energy drop. The former is driven by the temperature difference existing across the thermal conduit, while the latter arises because of the carrier chemical potential difference existing across the same conduit established during the reaction wave propagation. Many attempts seeking the deconvolution of the $(\Delta\mu/e)$ contribution from the overall voltage output to support this theoretical framework have been made. And by carefully titrating the Fermi energies of a CNT fiber, using various ratios of known p- and n-dopants (*i.e.*, nitrocellulose and sodium azide, NaN_3), one could resolve the open circuit potential derived from the chemical potential term, decoupled from that of thermoelectricity (**Figure 1-17a**).²⁹² The observed linearity between the isolated $(\Delta\mu/e)$ voltage potential and the initial Fermi energy of the CNT electric carriers constitutes the first quantitative experimental evidence of the Excess Thermopower theory.

This synergistic effect between the NaN_3 -CNT coupling and thermoelectricity originates from the Fermi energy difference between the pristine, non-doped CNT and the NaN_3 -doped portion across the TPW wave front. It is further reasoned that there is no inherent theoretical basis for these two sources that drive carrier motion to be entangled with one another. Knowing that the combustion-aided, rapid de-doping process, resulting from the propagation of a reaction wave, is key to the $(\Delta\mu/e)$ voltage, one can then mimic this transient doping/de-doping process, and develop a strategy that completely isolates this chemical potential gradient from thermoelectricity (**Figure 1-17b**). Experimentally, this was first realized by selectively applying a liquid dopant (*e.g.*, p-doping acetonitrile, CH_3CN) toward

one end of the SWNT fiber at room temperature.²⁹² The technique is named asymmetric chemical doping (ACD), owing to a spatial asymmetry in the exposure of an otherwise symmetric CNT fiber to the CH₃CN liquid (**Figure 1-17c**). This, in turn, represents a unique SWNT-based voltage generation process led entirely by chemical doping, free from combustion and the parasitic heat loss thereof (**Figure 1-17d**). The reversible ACD electric output (with specific power as large as 26.7 mW·mg⁻¹) stems from a well-understood electron transfer process between the SWNT donors and the p-doping CH₃CN acceptor (**Figure 1-17e**), and it can be generalized into a larger family of small molecule organic solvents (**Figure 1-17f**).^{292,293} In particular, the SWNT-to-acceptor electron transfer (ET) rate constants that drive the ACD V_{OC} can be modeled with high fidelity using a chirality-associated Marcus theory (**Figure 1-17g, h**),²⁹³ suggesting that the energy gaps between SWNT and the lowest unoccupied molecular orbital (LUMO) of acceptor molecules dictate the ET process. This Marcus theory inspired description of the SWNT-to-acceptor ET rate can be expressed as²⁹³

$$k_{ET} = \sum_{(n,m)} P^{(n,m)} k_{ET}^{(n,m)} = \sum_{(n,m)} P^{(n,m)} \gamma_n \pi d^{(n,m)} \exp \left[-\frac{(\lambda^{(n,m)} - \Delta G^{(n,m)})^2}{4\lambda^{(n,m)} k_B T} \right] \quad (14)$$

where $d^{(n,m)}$, $\lambda^{(n,m)}$, and $\Delta G^{(n,m)}$ represent the nanotube diameter, ET reorganization energy between a SWNT/acceptor pair, and thermodynamic driving force, for chiral specific (n, m) -SWNTs, with $\pi d^{(n,m)}$ accounting for the surface area differences between different nanotubes. The parameter γ_n is referred to as the collision pre-factor, and k_B is the Boltzmann constant. To further link these parameters to measurable physical quantities, one can further expand $\Delta G^{(n,m)}$, the

thermodynamic driving force of the overall ET process for any chiral specific (n , m)-SWNT, as²⁹³

$$\Delta G^{(n,m)} = \left(E_F^{SWNT} - \frac{E_g^{(n,m)}}{2} \right) - E_F^A \quad (15)$$

where E_F^{SWNT} is the SWNT Fermi level, $E_g^{(n,m)}$ is the (n , m)-SWNT band gap, and E_F^A is the LUMO level of the acceptor molecule (**Figure 1-17c, e**); and the more esoteric reorganization energy $\lambda^{(n,m)}$ term (formally defined as the energy of a state where the polarization would correspond to the transfer of a unit amount of charge, but the real charge distribution is that before the transfer) as²⁹³

$$\lambda^{(n,m)} \approx (\Delta e)^2 \left[\frac{R_{12}^2}{2a_1^3} + \frac{1}{2a_2} - \frac{R_{12}^2}{a_1(R_{12}^2 - a_1^2)} \right] \left(\frac{1}{\epsilon_{op}} - \frac{1}{\epsilon_s} \right) \quad (16)$$

where, a_1 , a_2 , R_{12} , ϵ_{op} and ϵ_s indicate radii of SWNT, radii of acceptor, center-to-center separation distance, optical and static dielectric constant, respectively.

Despite the slightly more involved arithmetic, this expression of the doping electron transfer kinetics (k_{ET}), central to the asymmetric chemical doping mechanism, involves minimal fitting parameters and can be derived directly from first principle. Not only does the theory describe the experimental values of ET rates with high fidelity (**Figure 1-17g**), the measurements themselves also constitute the very first observations of a Marcus inverted region between ground state SWNT/acceptor pairs.²⁹³ To be clear, the “inverted region” is characterized by the volcano-shaped rate dependence on the driving forces of the ET, which, in this case, are defined by

the acceptor LUMO levels (**Figure 1-17g**). This means that there exists an optimal thermodynamic driving force for effective ET, and a further increase in the driving force actually reduces the ET rate.^{298,299} This is the hallmark of the original Marcus ET theory, which was reported for the first time some 60 years after its initial prediction in a non-photo-excited ground state SWNT/acceptor system.²⁹³ These efforts also establish the theoretical framework and a reliable procedure to predictively enhance the V_{OC} magnitude through the ACD phenomenon. In one set of experiments, the authors demonstrate this ability by amplifying the 80 mV CH_3CN doping voltage to 290 mV through injection of chloroacetonitrile ($\text{Cl-CH}_2\text{CN}$) on chirality enriched (8,4)-SWNTs.²⁹³ Several other types of SWNTs with varying chirality distributions have subsequently been tested, offering up to 500% (440 mV) V_{OC} enhancement in the absence of surface modifications.²⁹³ The remarkable agreement between experimental data and the theory paved the way towards a general approach to evaluate SWNT/acceptor ET rates. With an excellent control over the V_{OC} output, a broad array of compatible solvents, as well as the advantageous inverse length-scaling of the maximum power (**Figure 1-17f**), ACD rises to be a promising candidate for microscale energy generation.

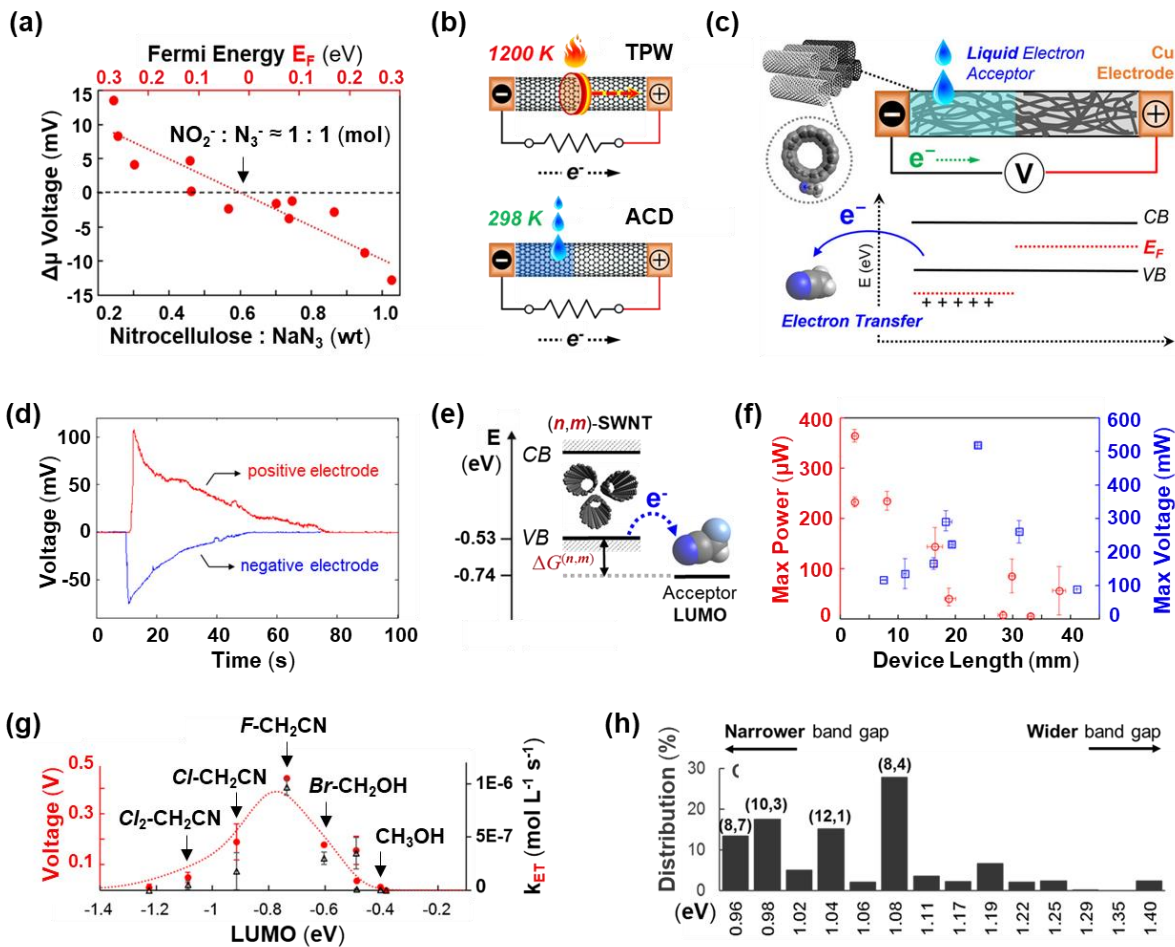


Figure 1-17. (a) Isolated chemical potential gradient ($\Delta\mu$) contribution to the overall output voltage as a function of the mass ratio of nitrocellulose (p-dopant) and sodium azide (NaN_3 , n-dopant) impregnated into the CNT network. Fermi energy (E_F) of the CNT carriers is measured separately using Raman spectroscopy. Linear fit suggests zero $\Delta\mu$ contribution to the overall voltage as the p- and n-dopant molar ratio is at unity.²⁹² (b) Contrasting two voltage generation techniques: thermopower wave (TPW, top) and the asymmetric chemical doping (ADC, bottom).²⁹² (c) Schematic illustration for the generation of an open-circuit voltage through asymmetric acetonitrile (*i.e.*, CH_3CN) doping of a SWNT network and its effect on its Fermi level (E_F), conduction band (CB), and valence band (VB).²⁹³ (d) Typical open-circuit voltage profiles

of CH₃CN (20 μL) injected onto a CNT fiber (0.2 mg, 3 mm × 15 mm × 0.1 mm). When CH₃CN is injected onto the CNT connected to the positive electrode, a negative open-circuit voltage is observed, and vice versa. **(e)** Schematic band diagram of (n,m)-SWNTs and an acceptor molecule. $\Delta G^{(n,m)}$ is driving force for electron transfer from the (n,m)-SWNTs to the acceptor. **(f)** Closed circuit maximum power (red) and open-circuit voltage (blue) generated using oxidized CNT fibers plotted against CNT fiber length. All samples prepared are standardized to 3 mm of width. The error bars represent standard deviation of measurements across different devices ($n = 3$). **(g)** Maximum open-circuit voltages obtained versus LUMO levels of various small molecule acceptors using CG200 SWNTs. Black triangles represent the rate constant of electron transfer. The error bars represent 95% confidence intervals ($n = 5$). Dashed lines indicate fitting lines for maximum voltage by Marcus theory.²⁹³ **(h)** Chirality distributions for the CG 200 SWNT sample obtained from a deconvolution of the UV-vis spectra.²⁹³

1.2.2.4.4 Asymmetric Functional Group Concentration

Asymmetric chemical doping benefits from a concentration gradient of electrons (or holes), which is created by the spatial asymmetry of doping level inside semiconductor materials. The ever growing research objectives and ever advancing boundaries of possibility over the past decade have seeded the recent development of a related, but mechanistically distinct strategy, which takes advantage of a preformed asymmetric functional group gradient built-in the material architecture to achieve the asymmetric doping effect upon uniform dopant exposure.

As a specific example, graphene oxide films (GOF) with a preformed oxygen-containing group gradient (gradient GOF, or g-GOF) can be constructed to harvest

electrical energy directly from moisture, the vapor form of liquid water, generating voltages up to 34 mV and conversion efficiency up to 62%.³⁰⁰ Further optimizations have resulted in a three-dimensional assembly of g-GOF, also known as g-3D-GO, with substantially enhanced single device voltage output (up to 260 mV), surpassing the performance of many predecessors.³⁰¹ Using a technique called moisture-electric annealing,³⁰⁰ the as-prepared g-GOF or g-3D-GO exhibit an intrinsic oxygen content gradient gradually increasing from the top to the bottom (**Figure 1-18a**), confirmed simultaneously by X-ray diffraction (XRD) patterns, X-ray photoelectron spectroscopy (XPS) measurements, cross-section scanning electron microscopic (SEM) image and the corresponding oxygen elemental mapping from X-ray energy dispersive spectroscopy (**Figure 1-18b-d**).

The proposed mechanism of electricity generation process can be summarized as follows (**Figure 1-18e**):³⁰⁰ (i) the g-3D-GO adsorbs water molecules upon exposure to moisture; (ii) the accumulation of water molecules weakens the $O^{\delta-}-H^{\delta+}$ bond within the oxygen-containing moieties in GO, releasing free H^+ ,^{126,302} (iii) the inherent gradient distribution of oxygen-containing groups accordingly leads to the concentration gradient of H^+ ; (iv) the induced potential and free electron movement of external circuit are thereupon generated once the H^+ diffusion occurs due to the drive of concentration gradient. Quantitatively, as the absorbed water fills g-3D-GO, the bound $H^{\delta+}$, dissociates from its charge neutral position, and the subsequent gradient distribution enables an ionic diffusion process that can be described as³⁰⁰

$$J_{diff} = -qD \frac{dC}{dx} \quad (17)$$

where J_{diff} , q , D , C and x represent diffusion current density, electric quantity of elementary charge, diffusion coefficient, concentration of $H^{\delta+}$ along the x-axis perpendicular to the two surfaces of g-3D-GO, and the distance in between, respectively. The drift induced electric field (E_i) between two sides of g-3D-GO arises once the $H^{\delta+}$ reaches the oxygen-poor region, defined by the relation $J_{drift} = \sigma E_i$, where J_{drift} and σ are the drift current density and electrical conductivity. Thermodynamic equilibrium is satisfied when $J_{diff} + J_{drift} = 0$, yielding an expression for the induced potential (V_i)

$$V_i = \int E_i dx = \frac{qD}{\sigma} \int \nabla C dx \quad (18)$$

This suggests that the magnitude of induced voltage is defined by the $H^{\delta+}$ gradient present in the “diffusion layer,” which is ultimately established through the O-gradient within g-3D-GO. As such, V_i appears to be proportional to ΔC , *i.e.* the difference of concentration between the electrodes.³⁰¹

This mechanism is similar to asymmetric chemical doping (ACD) in that: it also involves a spatial asymmetry in the concentration of charge carriers, whose diffusion builds up an electric field and generates energy. Nevertheless, the two mechanisms utilize different charge carriers and distinct strategies to create the spatial asymmetry. It is worth mentioning that GO may act as a permselective membrane to induce a Donnan potential, because of the negatively charged functional groups.³⁰³ The build-up of a Donnan potential, however, requires two reservoirs with different salt concentrations separated by the selective membrane, which is different from the mechanism we are looking at here.

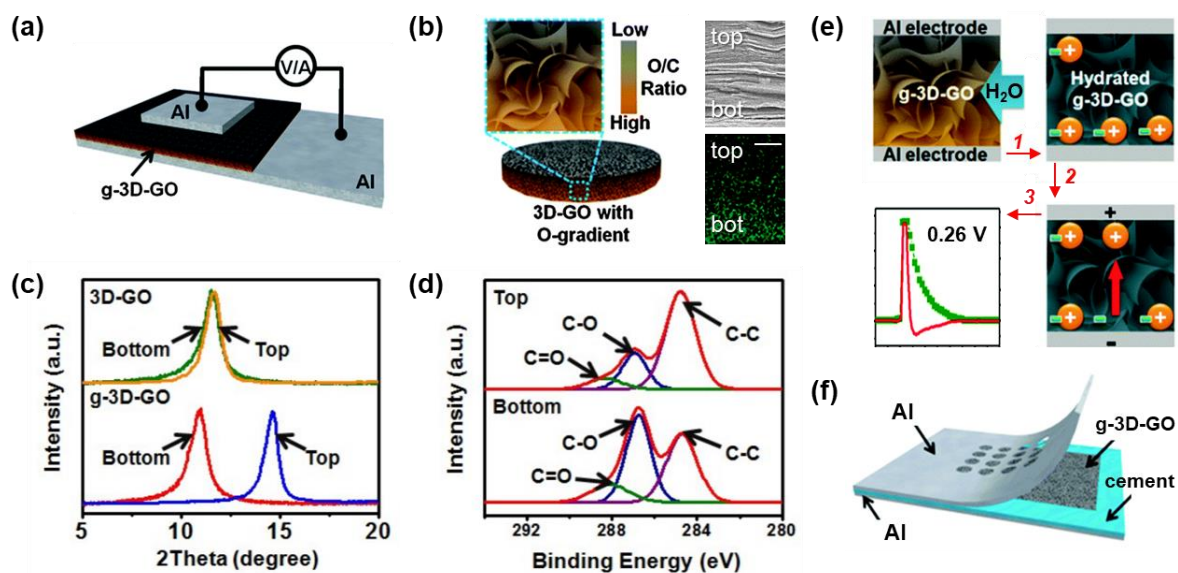


Figure 1-18. (a) Schematic illustration of a prototype chemical potential energy harvester based on g-3D-GO that is sandwiched between aluminum electrodes. (b) **Left:** Schematic g-3D-GO tablet prepared by polarization method, which induces a gradient of oxygen-containing groups in 3D-GO using moisture/electric field. **Right:** Cross-section SEM image and the corresponding oxygen mapping from X-ray energy dispersive spectroscopy of g-3D-GO (scale bar, 10 μm). (c) XRD patterns of the top and bottom sides of as-prepared g-3D-GO, respectively. This reveals that the top and the bottom sides have the distinct peak shift dissimilar to the initial 3D-GO, which suggests the structural polarization has indeed induced the change of interlayer structure. (d) XPS spectra of the top and bottom sides of as-prepared g-3D-GO, respectively. The O/C atomic ratio for the bottom side of g-3D-GO is *ca.* 0.56, slightly higher than that of GO starting material (*ca.* 0.44) but much higher than that of the top-surface (*ca.* 0.19) (e) Schematic illustration of the voltage generation mechanism: 1) the gradient distribution of oxygen-containing groups (*e.g.*, carboxyl and hydroxy) in g-3D-GO; 2) free hydrogen ions (H^+) ionization from oxygen-containing groups upon water absorption and the establishment of a density gradient of H^+ ; 3) free H^+ diffusion from high density side to low density side, inducing electrical potential, driving electrons

to move from the bottom electrode to the top electrode along an external circuit. **(f)** Optimized design of a chemical potential energy harvesting cell, where g-3D-GO is sandwiched between two pieces of aluminum foil and insulated by cement. An air hole array is preformed on the aluminum foil to guarantee an expedited transport of water molecules into the g-3D-GO layer.³⁰¹

This ACD related energy harvesting strategy based on an ionic gradient present in graphene oxide frameworks has led to a surge of interesting demonstrations.²²⁵ The aforementioned moisture-electric-annealing technique,³⁰¹ for example, has been used to great effect for the fabrication of a breath-powered write-once-read-many-times (WORM) memory device **(Figure 1-19a, b)**.³⁰⁴ As a ubiquitous digital memory technology found in compact discs (CDs) and digital video disks (DVDs), the WORM-type memory is secure for data storage, in which information cannot be modified once written. This 24-bit WORM-type memory device features a graphene oxide nanoribbon network membrane (GOR-NM) pressed onto an aluminum (Al) substrate with printed silver (Ag) electrode **(Figure 1-19c)**. The “writing” process relies on the “moisture-electric-annealing”, during which the applied electric field polarizes the vertical composition of the “pristine” GOR-NM, yielding a “written” gradient-GOR-NM (or g-GOR-NM) version, with more oxygen containing groups towards the top anode **(Figure 1-19d)** that are capable of moisture-assisted voltage generation. Upon subsequent hydration, which constitutes the “reading” process, the oxygen containing groups within the g-GOR-NM are ionized to produce free cations (H^+) and locally confined anions ($O^{\delta-}$, covalently bonded with GOR skeleton), drawing a counteracting voltage against the diffusive H^+ current **(Figure 1-19e)**. This unique moisture-triggered potential

is only present in “written” g-GOR-NM pixels, as opposed to the “pristine” ones (Figure 1-19e), affording an ON/OFF ratio above 10^6 and stable over 1000 cycles (Figure 1-19f).³⁰⁴

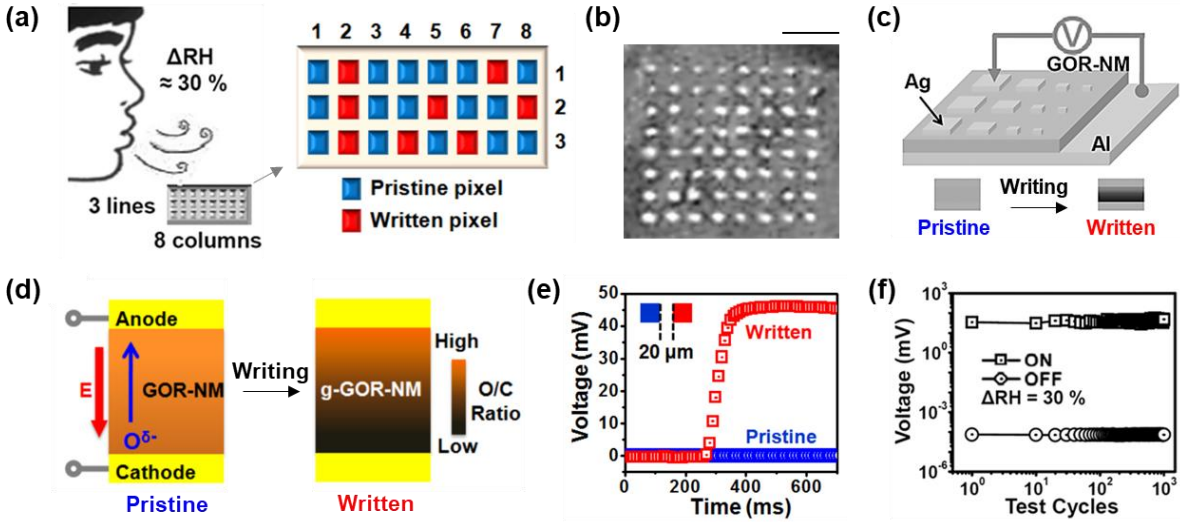


Figure 1-19. (a) Schematic illustration of a prototype WORM-chip with 24 pixels (three lines and eight columns), which can be read by human breathing. (b) Optical image of GOR-NM-based WORM-type memory cell array (scale bar, 1 mm). (c) Schematic illustration of the WORM-type memory fabricated by pressing a GOR-NM onto an Al substrate with printed Ag top electrode. (d) **Left:** structural polarization of GOR-NM, where E (with red arrow) and $O^{\delta-}$ represent the applied electric field and oxygen-containing ions (moving along the blue arrow), respectively. **Right:** gradient distribution of oxygen-containing groups in g-GOR-NM. (e) Voltage signals of adjacent ($20\ \mu\text{m}$ apart) written and pristine devices when subjected to 30% ΔRH , suggesting low risk of cross talk between adjacent cells. (f) Collected signals from moisture-powered reading process with 30% ΔRH for 1000 cycles.³⁰⁴

This concept has since then been scaled up and integrated into flexible textiles to realize an information storage mask activated by human breath (**Figure 1-20a**).³⁰⁵ The active component of this graphene oxide fiber generator consists of interdigitated reduced-graphene-oxide (RGO, as electrodes) and oxygen-gradient graphene oxide (g-GO), again prepared using the “moisture-electric-annealing” technique (**Figure 1-20b**). This single g-GO fiber with millimeter length and a diameter of 80 μm is reported to generate up to 355 mV and 1.06 $\text{mA}\cdot\text{cm}^{-2}$ at 35% relative humidity (ΔRH).³⁰⁵ It should be noted that the general voltage generation strategy based on ionic diffusion is not limited to graphene oxides. Other materials, such as graphene quantum dots (GQDs),³⁰⁶ asymmetrically functionalized porous carbon film (PCF, **Figure 1-20c**),³⁰⁷ and 3D polypyrrole (PPy) foam (**Figure 1-20d, inset**),³⁰⁸ have all been shown to effectively generate electricity through interaction with moisture, highlighting the importance of the preformed anionic gradient and the hydration-triggered cation transport. Similarly, carbon nanotube yarns with differences in their oxidation levels can also be used to generate electricity from quiescent water, even though the authors ascribed the phenomenon to some irreversible chemical reaction of CNT with water.³⁰⁹ In all of these material systems, the spatial symmetry is broken to establish the necessary anionic gradient. With the asymmetrically functionalized PCF, for example, a side-selective plasma treatment is essential for the formation of the oxide concentration heterogeneity (**Figure 1-20c, top**) and the subsequent voltage generation (**Figure 1-20c, bottom**).³⁰⁷ In the case of the gradient 3D polypyrrole framework (g-3D-PPy),³⁰⁸ interestingly, this electric generation behavior is able to be extended to other

organic and inorganic solvent vapors, where the authors observed reduced electrical output with decreased solvent polarity (**Figure 1-20d**). More recently, electricity generation is also realized by directional flow of moisture in pristine graphene oxide.^{310,311} While these findings certainly underscore the broad applicability of this energy harvesting process, the fact that electricity can be drawn even from polar *aprotic* solvents and without any embedded asymmetry potentially offers opportunities for subtle amendments to the proposed mechanism.

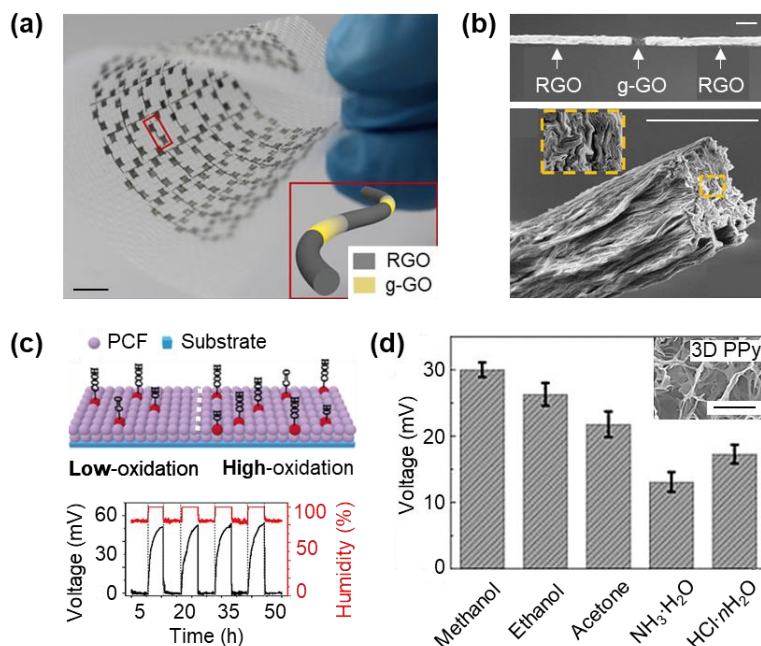


Figure 1-20. (a) Optical image of the integrated flexible textile of graphene oxide fiber generator (scale bar, 1 cm). **Inset:** schematic illustration of the interdigitated reduced-graphene-oxide (RGO) and oxygen-gradient graphene oxide (g-GO) fiber.³⁰⁵ (b) **Top:** Optical microscopy image of the graphene oxide fiber generator, showing interdigitated RGO and g-GO regions. **Bottom:** SEM images of the oxygen-gradient graphene oxide (g-GO) fiber, showing the well-ordered stacking of GO sheets. (scale bars, 100 μm).³⁰⁵ (c) **Top:** schematic illustration of a porous carbon film (PCF)

device for harvesting adsorption-induced potential. The right side is functionalized by plasma treatment, which has a higher content of oxygen-containing functional groups. **Bottom:** measured voltage across the PCF device with oscillating humidity conditions.³⁰⁷ **(d)** The voltage outputs of the vapor triggered voltage generator based on the gradient 3D polypyrrole framework (g-3D-PPy) under various solvent vapors (250 ppm). **Inset:** SEM image of the 3D PPy framework architecture (scale bar, 10 μm).³⁰⁸

1.2.2.5 The Capacitive Discharge Mechanism

1.2.2.5.1 Twist Generator and Thermally Chargeable Supercapacitor

An energy harvesting technique very much related to that of the asymmetric chemical doping can be characterized as capacitive discharging, in which the electrochemical double layer capacitance established across the CNT-solvent interface is exploited to convert mechanical (or thermal) energy into electricity.¹⁷⁹ Here, instead of biasing solvent access onto a single CNT fiber, asymmetry is created on a systemic level by separating the active nanotube material from the counter electrode all together (**Figure 1-21a**).¹⁷⁹ This design allowed Baughman and co-workers to place the entire CNT fiber in solution as the working electrode, which, when in electrochemical equilibrium with the surrounding fluid, functions as a surface-area-controlled charge capacitor, allowing electricity generation when stretched or twisted.^{179,312-314}

Because a chemical potential difference exists between the CNT working electrode and the surrounding electrolyte, immersing it into the electrolyte generates an equilibrium charge,¹⁷⁹ much like the equilibrium state proposed in the Coulombic

coupling mechanism for an ionic liquid (**Figure 1-12a**) or chemical doping in the case of a polar aprotic solvent (**Figure 1-17c, e**). In fact, the potential of zero charge (PZC), or sometimes called “formal potential”, which characterizes this equilibrium charge state of the nanotubes, can be experimentally determined and is shown to be consistent with predictions of the classic Nernst equation,³¹⁵ if one treats the solvent p- or n-doped nanotubes as oxidized or reduced populations, respectively. It follows then, when stretched (or equivalently, twisted), the decreased CNT fiber interfacial surface area reduces its double-layer capacitance (C), ejecting charge (Q), and thereby producing a voltage change according to $Q = CV$, which enables electrical energy conversion (**Figure 1-21a, inset**).^{179,313,314}

Having observed that twisting a non-coiled CNT yarn in solution can generate an electric current, Baughman and co-workers developed an elegant approach for mechanical energy harvesting by stretching a coiled yarn submerged in the electrolyte.³¹⁴ It is hypothesized that the radial compression (**Figure 1-21b**)³¹⁶ of the CNT coil reduces the inner surface area available for interaction with the ions, thus expelling the ionic species (positively or negatively charged, depending on the electrolyte). The eviction of the ions results in an inward electric current of the complementary charge out from the yarn, creating the induced potential.³¹⁴ Indeed, the authors found that, when a homochiral CNT yarn (with yarn twist and coiling in the same direction) is stretched, the coiling is partially converted to increased yarn twist, which increases yarn density, decreasing its capacitance, and hence elevates the voltage output (**Figure 1-21c**).¹⁷⁹ They also reported decreasing intrinsic bias voltage (at 0% strain) with increasing pH, which led to the conclusion

that a low-pH electrolyte is hole-injecting (p-doping), while a high-pH electrolyte is electron-injecting (n-doping).¹⁷⁹ The culmination of these detailed insights into the voltage generation mechanism allowed Baughman and co-workers to demonstrate a peak electrical power density exceeding 250 W per kilogram of yarn in the absence of an external bias (**Figure 1-21d**).¹⁷⁹ These CNT yarn based energy harvesters are used in the ocean to harvest wave oscillation (**Figure 1-21e**), integrated with thermally driven artificial muscles to convert temperature fluctuations to electricity, sewn into textiles for use as self-powered respiration sensors, and used to charge a storage capacitor (**Figure 1-21f**).¹⁷⁹

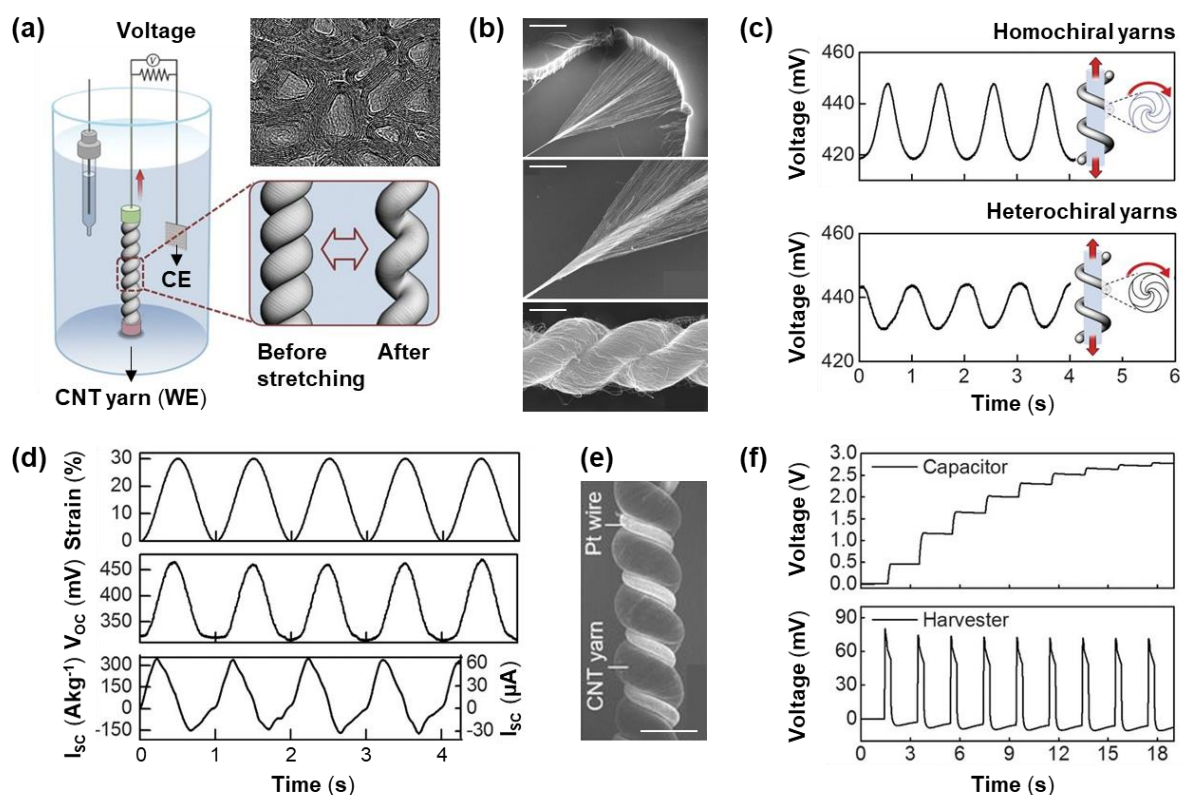


Figure 1-21. (a) Schematic illustration of a torsionally tethered coiled CNT working electrode (WE), reference electrode, and counter electrodes (CE) in an electrolyte, zooming in on the coiled

yarn before and after stretch. **Inset:** TEM image showing a multiwalled carbon nanotube collapse to increase inter-nanotube van der Waals energy in the bundle.¹⁷⁹ **(b) Top and Middle:** SEM images, at two different magnifications, of a carbon nanotube yarn in the process of being simultaneously drawn and twisted during spinning from a nanotube forest.³¹⁶ **Bottom:** SEM image of a two-ply CNT yarn.³¹⁶ Scale bars represent 200 μm , 50 μm , and 2 μm , respectively. **(c)** Open-circuit voltage versus time during 60% stretch in 0.1 M HCl for homochiral (**top**) and heterochiral (**bottom**) yarns produced by mandrel coiling on a 300%-elongated, 0.5-mm-diameter rubber core, showing opposite stretch-induced voltage. **Insets:** opposite changes in yarn twist during stretch of homochiral and heterochiral coils.¹⁷⁹ **(d)** Sinusoidally applied tensile strain and resulting change in open-circuit voltage (V_{OC}) and short-circuit current (I_{SC}) for a cone-spun coiled harvester.¹⁷⁹ **(e)** SEM image of the CNT harvester after incorporation of a Pt wire current collector for ocean-wave harvesting. Scale bar represents 100 μm .¹⁷⁹ **(f)** Charging a 5- μF capacitor to 2.8 V using a CNT yarn harvester (weighing 19.2 mg) and a boost converter circuit. The boost converter output was rectified through a Schottky diode before charging the capacitor.¹⁷⁹

An equivalent circuit model can be drawn to describe Baughman's twistrion generator (**Figure 1-22a**), which also captures the working principle of several other types of harvesters (**Figure 1-22b-d**).³¹⁷⁻³¹⁹ In the case of a twistrion generator, C_{WE} and C_{CE} represent the total capacitance of CNT yarn (working electrode) and counter electrode, respectively. R_{ext} and R_{ion} are the external load resistance and ionic resistance of the solution. As the CNT yarn is stretched or twisted, its effective surface area and capacitance will change accordingly, while C_{CE} always remains constant. Consequently, charges will be redistributed between two capacitors,

leading to a current flow through the load. Assuming that the surface area is a sinusoidal function of time:

$$C_{WE}(t) = C_0 A(t) = C_0 (A_0 + \Delta A \sin(\omega t)) \quad (19)$$

The voltage on the external resistance is related to the charge transferred from C_{WE} to C_{CE} ($q(t)$). The output voltage can be derived by solving the following differential equation numerically.

$$V = R_{ext} \frac{dq(t)}{dt} = \frac{R_{ext}}{R_{ext} + R_{ion}} \left(\frac{Q_{WE} - q(t)}{C_{WE}(t)} - \frac{Q_{CE} + q(t)}{C_{CE}} \right) \quad (20)$$

In the equation above, C_0 , which is the specific areal capacitance of CNT, is considered constant throughout the measurement. Changes in C_{WE} could normally be caused by the varying CNT surface areas exposed to the electrolyte, or, from device to device, could occur through variations in C_0 . The areal capacitance of the electrical double layer (C_0) may be approximated as two capacitors resulting from the Helmholtz layer (C_H) and the diffuse layer (C_D) connected in series.^{320,321}

$$\frac{1}{C_0} \approx \frac{1}{C_H} + \frac{1}{C_D} \approx \frac{1}{C_{dipole}} + \frac{1}{C_{IHP-OHP}} + \frac{1}{C_D} = \frac{d_{H_2O}}{\epsilon_0 \epsilon_{dipole}} + \frac{d_{ion}}{2\epsilon_0 \epsilon_{IHP-OHP}} + \frac{L_D}{\epsilon_0 \epsilon_r} \quad (21)$$

The first term comes from the highly oriented water dipoles in the Inner Helmholtz Plane (IHP), which is the closest layer to the electrode surface. The second term is the contribution of solvated ions at the Outer Helmholtz Plane (OHP). The dielectric constants of water inside OHP ($\epsilon_{IHP-OHP}$) and IHP (ϵ_{dipole}) are different from the bulk value (ϵ_r), due to the restricted motion of water molecules and the

strong electric field near surface.³²²⁻³²⁴ The thicknesses of the inner and outer Helmholtz layers are largely dictated by the size of water molecule (d_{H_2O}) and ions (d_{ion}). The last term, which is the capacitance of diffuse layer, is actually only important in dilute solutions. The thickness of diffuse layer is characterized by Debye length (L_D):

$$L_D = \sqrt{\frac{\epsilon_0 \epsilon_r k_B T}{e^2 \sum_i z_i^2 n_i^0}} \quad (22)$$

It is obvious that Debye length is dependent on temperature, which reduces C_D as temperature increases. Besides, as the dielectric constant of a liquid usually decreases with temperature, the other two terms in **Equation 21** also show implicit dependence on T .

This “thermal expansion” of the electrical double layer has been utilized to harvest thermal energy.³²⁵⁻³²⁷ The simplest version of this device is comprised of two identical porous carbon electrodes immersed in two beakers containing the same electrolyte (**Figure 1-22e**).³²⁸⁻³³¹ By altering the temperature of one container and maintaining the other at a fixed temperature, the system works analogously to the one depicted in **Figure 1-22a**, exhibiting a high thermoelectric factor (dV/dT) of up to 6 mV/K.^{332,333} Using essentially the same mechanism as the “twistron” generator, this constitutes a novel approach of harvesting energy from low grade heat (or waste heat), which appears to be more effective than conventional solid-state thermoelectric materials in certain scenarios. There exists many other strategies for thermal or chemical energy harvesting following the similar fluctuating double

layer capacitance mechanism, discussed in detail among several other review articles.³³⁴⁻³³⁶ A few examples include: constructing a thermal capacitive cycle as shown in **Figure 1-22f, g** (similar to a heat engine cycle),^{337,338} mixing two electrolytes with different salt concentrations (changing n_i^0 in **Equation 22**),^{335,336,339-342} and combining the ionic Seebeck effect (Soret effect) with the thermal charging of a supercapacitor.³⁴³⁻³⁴⁸ It should be clarified that a large portion of supercapacitors nowadays are pseudocapacitors, which store charges by fast and reversible surface redox reactions (faradic processes), while double layer capacitors are non-faradic in principle.^{127,349-353} These pseudocapacitors can also exhibit “thermal charging” behaviors during each thermal cycle, which, strictly speaking, embody a different phenomenon associated with the kinetics of surface reactions.³⁵⁴

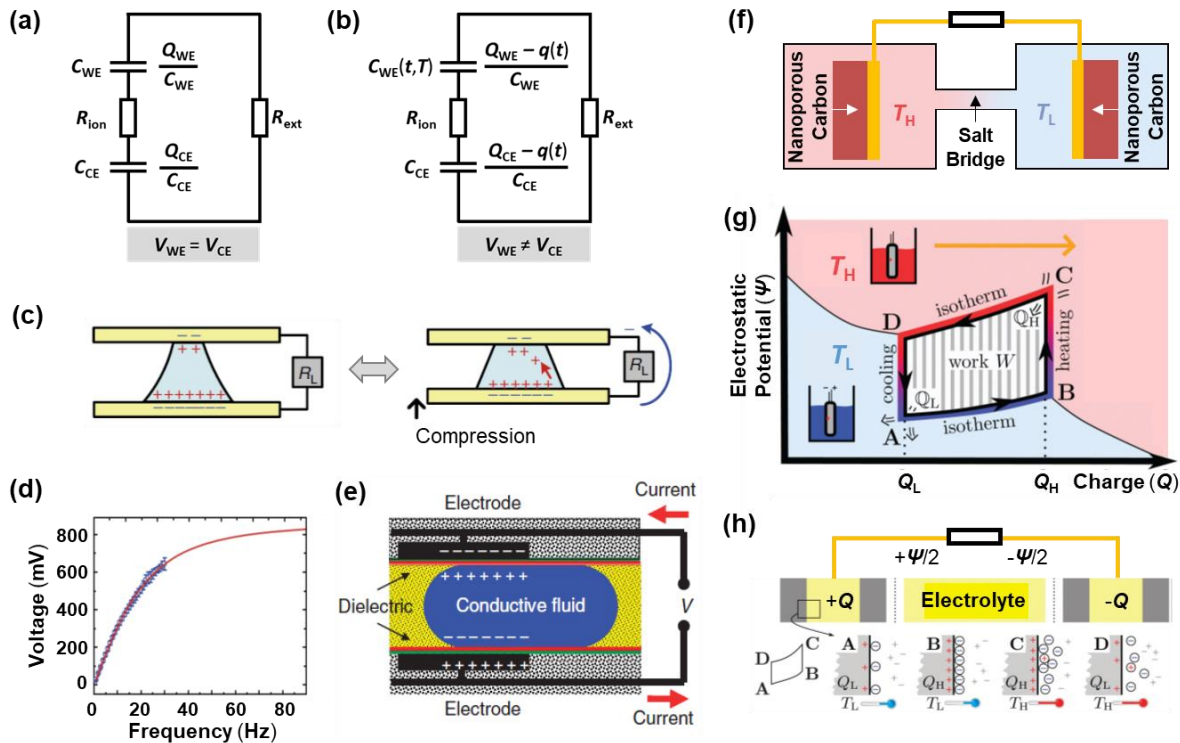


Figure 1-22. Equivalent circuit model for a twist generator at equilibrium **(a)** and after stretching **(b)**, which is also applicable to other generators employing a “varying capacitor area” type mechanism.³¹⁷⁻³¹⁹ **(c)** Schematic diagram of the working principle for a water bridge generator: during press-and-release, the contact area between water and hydrophobic top plate changes with time, while the area on the hydrophilic bottom plate remains unchanged, leading to current generation.³¹⁸ **(d)** Average voltage output of a water bridge generator as a function of vibrational motion frequency.³¹⁸ **(e)** Schematic illustration of charge distribution in the electrical double layer of a microchannel generator based on the so-called “reverse electro-wetting” mechanism.³¹⁷ The droplet and the electrode are connected to the external electrical circuit that provides a constant bias voltage between the droplet and the electrode. External mechanical actuation is used to move the droplet in such a way as to force a decrease of its overlap with the dielectric-film-coated electrode. This results in the decrease of the total charge that can be maintained at the droplet liquid–solid interface. The excessive electrical charge then flows back through the electrical circuit that connects the droplet and the electrode, generating electrical current that can be used to power the external load. In this scheme, as the droplet moves in and out of alignment with the electrified thin-film-dielectric-coated electrodes, the amount of the electrical charge at the electrodes changes causing electrical current to flow.³¹⁷ **(f)** Configuration of a thermally chargeable supercapacitor using nanoporous carbon.³²⁵ **(g)** Voltage—charge (Ψ — Q) diagram of a thermal capacitive cycle.³³⁷ The proposed cycle ABCDA is defined by the change of electrostatic potential (Ψ) between high (H) and low (L) for temperatures T and charges Q of the device. Capacitive thermal energy extraction is based on increased thermal motion and a related entropic change in the electric double layer. The supercapacitor is composed of an electrolyte reservoir and two porous electrodes, each

modeled as a parallel plate capacitor.³³⁷ **(h)** Schematic charge distribution on the surface of one electrode corresponding to the four states (ABCD) depicted in **(g)**.³³⁷

1.2.2.5.2 Droplet Motion Generator and Waving Potential

Aside from exploiting the capacitance of existing double layers, formation of a double layer on newly created solid-liquid interfaces may potentially convert mechanical energy to electricity as well. Guo and colleagues, for example, performed an elegant study probing a sub-mV voltage generated by moving a single droplet of ionic solution over a strip of monolayer graphene.³⁵⁵ Mechanistically, the authors reject the idea of using fluid flow to generate voltages across graphene through streaming potential, emphasizing that a potential cannot be induced by a flowing liquid without a pressure gradient; nor do they subscribe to a Coulomb drag scheme (a process whereby the repulsive interactions between electrons in spatially separated conductors enable a current flowing in one of the conductors to induce a voltage drop in the other),³⁵⁶⁻³⁵⁸ due to an apparent electrical double layer formed at the interface of ionic liquids and graphene that would screen the effect of the Coulomb interactions.³⁵⁹ Instead, they propose an electrokinetic model where an electrical double layer (EDL) is formed at the droplet/graphene interface, which is driven forward by the moving droplet, charging and discharging at the front and rear of the droplet.³⁵⁵ This gives rise to an electric potential proportional to the velocity and number of droplets. The potential is also found to be dependent on the concentration and ionic species of the droplet and decreases sharply with an increasing number of graphene layers.

In this physical picture, Na^+ ions spontaneously adsorb onto the monolayer graphene, assembling a layer of negative charges across the liquid-solid interface to form a double layer capacitor (**Figure 1-23a**). When the droplet moves along the graphene surface, Na^+ ions adsorb at the front end, advancing the double layer capacitor forward while drawing electrons from the graphene. The concurrent desorption at the rear end discharges the capacitor and releases the electrons into the graphene lattice (**Figure 1-23b**). This entire process gives rise to a decreased electron density ahead of the moving droplet as compared to the static state, resulting in an electrical potential pointing from the front to the rear. An equivalent circuit model is then created, with the dynamic front and rear boundaries of the droplet as capacitors C_F and C_R in charging and discharging modes (**Figure 1-23c**). Here, R_L , R_d and R_{r+c} represent the resistances across the liquid, the graphene under the droplet, and the graphene outside the droplet combined with the contact resistance, respectively. Taking the pseudocapacitance per unit area, C_0 , to be determined by the graphene–solution system, the changing rates of the pseudocapacitance at the front and rear can be calculated as $dC_F/dt = -dC_R/dt = C_0Wv$ for a droplet moving at velocity v from left to right, where W is the width of the graphene strip under the droplet. It follows that the equivalent current is then the rate of transferred electrons dq_e/dt

$$I = -\frac{dq_e}{dt} = \psi \frac{dC_F}{dt} = -\psi \frac{dC_R}{dt} = -\psi WC_0v \quad (23)$$

where ψ is defined as the equivalent surface potential of graphene relative to the adsorbed hydrated Na^+ layer. The induced open-circuit voltage is given by

$$V = R_d I = -L R_{sq} \psi C_0 v \quad (24)$$

where R_{sq} is the square resistance of the graphene and L is the length of the droplet. According to the proposed model, the multiplying of the induced voltage by an array of droplets can be considered as a series connection of multiple current sources with internal resistances (**Figure 1-23d**). As is expected from the electric double-layer theory, the induced electrical potential depends on the ionic species (**Figure 1-23e**), with NH_4^+ and Mg^{2+} drawing larger amounts of image electrons, and H_2O not effective at all. Interestingly, the authors saw reversed polarity of electricity generation from HCl solution, agreeing with the molecular picture of exceptionally strong adsorption of hydronium H_3O^+ ions onto the graphene lattice,²⁰³ rendering Cl^- ions as the dominant mobile species in double layer, drawing positive charges in the graphene as opposed to negative carriers in other cases.³⁵⁵ Interestingly, a recent molecular dynamics simulation study finds that, the voltage induced by moving a nanometer-sized imidazole ionic liquid droplet over graphene saturates with increased velocity of motion, an effect reminiscent to the behavior observed in Coulombic drag type of experiments (**Figure 1-11b, d, f** and **Figure 1-12c**).³⁶⁰ This result does not contradict with that of Guo and co-workers' (**Figure 1-23e**), seeing that Guo's velocity is two orders of magnitude lower than the predicted saturation velocity from the MD simulation (5 to 10 m/s), and therefore sits comfortably within the linear regime. Nevertheless, the parity between the velocity dependences of the generated voltages for two seemingly unrelated mechanisms does offer hope to potentially unify the underlying theories describing a droplet generator and Coulombic drag.

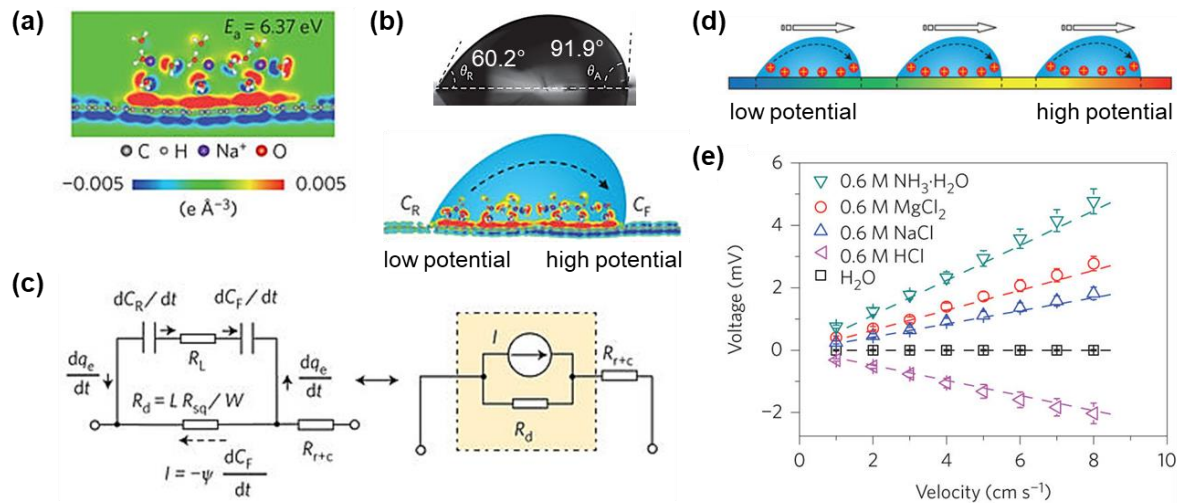


Figure 1-23. (a) DFT results for the distribution of differential charge near monolayer graphene caused by adsorbing one to three rows of hydrated sodium cations and the corresponding adsorption energy (E_a). (b) **Top:** a droplet of 0.6 M NaCl solution on a graphene surface with advancing and receding contact angles of *ca.* 91.9° and 60.2° , respectively. **Bottom:** schematic illustration of the potential difference induced by a moving droplet. (c) Equivalent circuit for (b). Solid arrows indicate the flow direction of electrons in graphene and Na^+ ions in the droplet. (d) Schematic illustration and equivalent circuit for three moving droplets on graphene. (e) Voltage induced by three droplets of different solutions.³⁵⁵

This seminal work has stimulated a series of subsequent reports within the capacitive discharging framework. While there have been evidences suggesting that a continuous flow of an ionic liquid along graphene may have limited potential for voltage induction,^{203,355,361} a network structure of graphene grids woven by crisscrossed graphene micron-ribbons can be designed specifically to capture the electrical energy imparted by the continuous ionic fluid, taking full advantage of lessons learned from droplet flow.^{362,363} Other creative applications such as an “all-

weather” photovoltaic have also been implemented, combining an electron-enriched graphene electrode with a dye-sensitized solar cell that generates electricity even at rainy days, enabled by the formation of the π -electro/cation electrical double-layer capacitors at the graphene/raindrop interface.³⁶⁴⁻³⁶⁷ It should also be noted that continuing efforts are being made to replace, and tune the concentration of, the active ionic species within the flowing liquid. Graphene oxide (GO) and hexagonal boron nitride (hBN), insulating 2D materials with band gaps of 3.6 and 5.2 eV, for example, have been exfoliated to make aqueous solutions that are capable of droplet-based voltage induction on graphene.³⁶⁸ Specifically, the carboxylic acid groups on the edges of the GO nanosheets are deprotonated to yield negatively charged moieties, leading to negatively charged aqueous suspensions. By moving a droplet of 2D GO nanosheets aqueous solution along graphene, an electric potential proportional to GO concentration, as well as the droplet velocity, can be generated within the graphene layer.³⁶⁸

The droplet generator concept has seeded the discovery of another closely related phenomenon called “waving potential”, which, as its name suggests, harvests energy from water waves. Electrical potentials of opposite polarities are produced in a monolayer graphene sheet inserted into or withdrawn from an ionic liquid-air boundary (**Figure 1-24a**).³⁶¹ Energy harvesting from simulated ocean waves is then realized based on this mechanism with many different materials, such as CNT fiber (**Figure 1-24d**), zinc oxide nano-films, and carbon black/polymer composite films.³⁶⁹⁻³⁷¹ The moving droplets approach and that of a waving generator bear copious similarities, evident in many aspects: the same linear dependence on

moving/inserting velocity (**Figure 1-24e** and **Figure 1-24b**); the same trend of molecular dependence of device performances (**Figure 1-23b** and **Figure 1-24c**), and the extremely close values of the generated voltages. Nevertheless, the mechanism for the waving potential has not been fully worked out, certainly not to the same degree as in the case of the droplet generators. Since the ionic adsorption and desorption events do not occur simultaneously, a continuous ionic current does not fall out naturally when the system is translated to an equivalent circuit, hence the picture shown in **Figure 1-24c** and the corresponding model (**Equation 24**) are not fully applicable in explaining waving potential. More interestingly, the magnitude of the waving potential increases with larger anion radius in a CNT fiber generator (**Figure 1-24e**), exactly opposite to the trend observed on graphene (**Figure 1-24b**). This discrepancy between these two systems may be a hint of distinct surface interactions on different materials and might offer opportunities to further probe the adsorption behavior and ionic motion at solid-electrolyte interfaces.

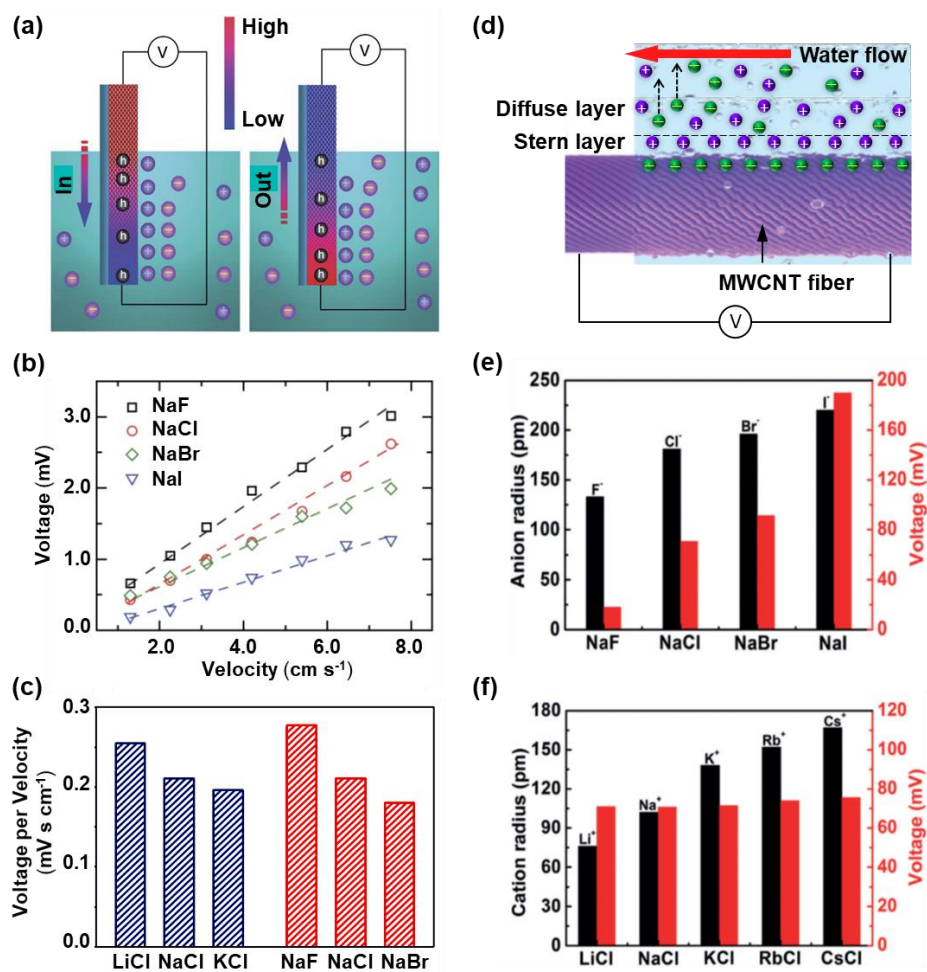


Figure 1-24. (a) Schematic illustration of formation/destruction of electrical double layer by ion adsorption/desorption on the surface of graphene during the insertion (left)/extraction (right) processes. Induced potential difference and hole concentration gradient in the graphene sheet are also illustrated.³⁶¹ (b) Peak voltages as functions of velocity of graphene insertion into a series of sodium halide solutions (waving generator).³⁶¹ (c) Fitted slope of voltage versus velocity for different alkali metal chloride and sodium halide solutions (droplet generator).³⁵⁵ (d) Schematic diagram of experimental setup and mechanism suggested for a CNT fiber based flow generator.³⁷⁰ (e) Open circuit voltage for a CNT fiber based flow generator in sodium halide solutions.³⁷⁰ (f) Open circuit voltage for a CNT fiber based flow generator in alkali metal chloride solutions.³⁷⁰

Guo's mechanistic insights³⁵⁵ have also been extended towards many other materials, including chemically doped graphene (such as n-doped graphene),³⁷² carbon nanotube,³⁷³ graphene-X composite materials (e.g., PEDOT or poly(3,4-ethylenedioxythiophene)³⁷⁴ and PANi or polyaniline³⁷⁵). In particular, the role of the underlying substrate (e.g., PTFE or polytetrafluoroethylene,³⁷⁶ Si/SiO₂,³⁶⁶ LiNO₃, PVDF, or polyvinylidene fluoride³⁷⁷) in the electricity generation process is carefully explored.^{366,376} Recently, by probing the behavior of interfacial water using sum-frequency vibrational spectroscopy (SFVS) (**Figure 1-25a**), Yang et.al. revealed the crucial rule of substrate polarity in the droplet generator.³⁷⁸ It is shown that graphene supported by low-polarity substrate like poly-methyl methacrylate (PMMA), will not adsorb any ions in water, and therefore does not generate voltage as the droplet moves on it (**Figure 1-25b**). On the other hand, the generated voltage is much larger on substrates with higher polarity, reaching 100 mV on polyethylene terephthalate (PET) and 500 mV on strongly polarized ferroelectric PVDF (**Figure 1-25c, d**). In another example, by introducing a triboelectric effect between graphene and the polytetrafluoroethylene (PTFE) template underneath, effectively suppressing the charge screening caused by the anions in the diffuse layer of the EDL, an increased power output of *ca.* 1.9 μ W is demonstrated.³⁷⁶ Reliable droplet-induced electricity generation with non-ionic DI water is also achieved using a graphene-PVDF heterostructure (**Figure 1-26a**),³⁷⁷ in which the authors observe a characteristic linear dependence of voltage on device internal resistance (**Figure 1-26b**), as expected from **Equation 24**. Similarly, the authors propose an equivalent circuit model to explain this continuous charge-discharge

phenomenon, with the distinction of using a piezoelectronic-induced charge imbalance, as opposed to the Na^+ doping which is only present in ionized water (**Figure 1-26c, d**).³⁷⁷ Also worth noting is the recent development of a graphene-Si Schottky diode based a 2D hybrid nanogenerator, with concurrent energy harvesting from sunlight and water flow (**Figure 1-26e**).³⁶⁶ In this work, two different metal electrodes are adopted to build an asymmetric internal potential profile in the graphene channel, allowing for energy generation (25.6 mV) from sunlight in the 2D graphene plane (**Figure 1-26f**). Augmented by the capacitive discharge effect, when water flows over the graphene surface under illumination, an additional voltage (2.54 mV) can be generated at the same time (**Figure 1-26g**). This flow-induced voltage arises from an additional charge transfer in the graphene channel induced by a continuous doping and undoping of the graphene by water, a *p*-dopant, owing to a reversible wetting and unwetting effect of water during the water flowing process (**Figure 1-26h**).

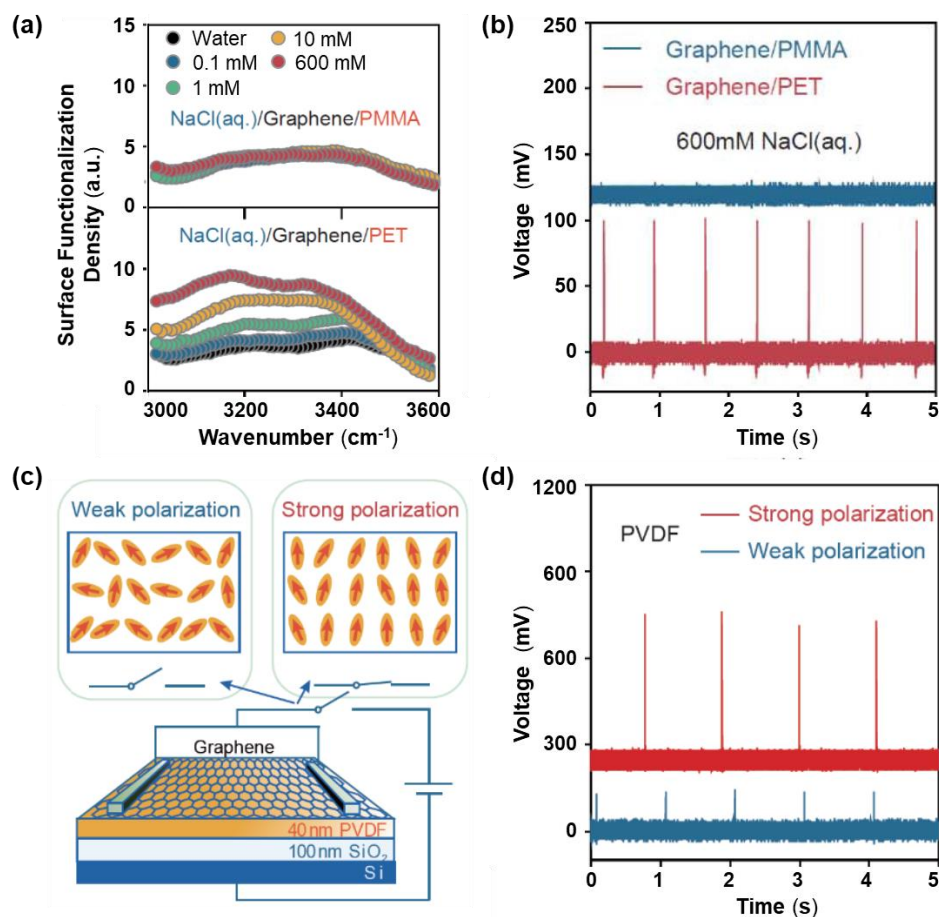


Figure 1-25. (a) Sum-frequency intensity spectra from the interfaces of NaCl(aq.)/graphene/PMMA (top) and NaCl(aq.)/graphene/PET (bottom), respectively, for a set of different NaCl concentrations in the solution. The nearly identical spectra for all concentrations indicate that all interfaces are essentially neutral, with no ion adsorption for graphene on PET substrate. In contrast, the SF intensity spectra from the interfaces of NaCl(aq.)/graphene/PET increase with NaCl concentration, indicating an increasing density of ions at the interfaces. (b) Voltage-time traces for droplet generator on graphene supported by PMMA and PET, respectively. (c) Sketch of a device made of a graphene/PVDF/SiO₂/Si structure that can be gated across the layers by a bias voltage. The domain alignment of PVDF film along the surface normal can be controlled by the bias. (d) Measured voltage spikes from the device showing that they are weak

when PVDF is in the weakly polarized state and strongly enhanced when PVDF is in the stronger polarized state.³⁷⁸

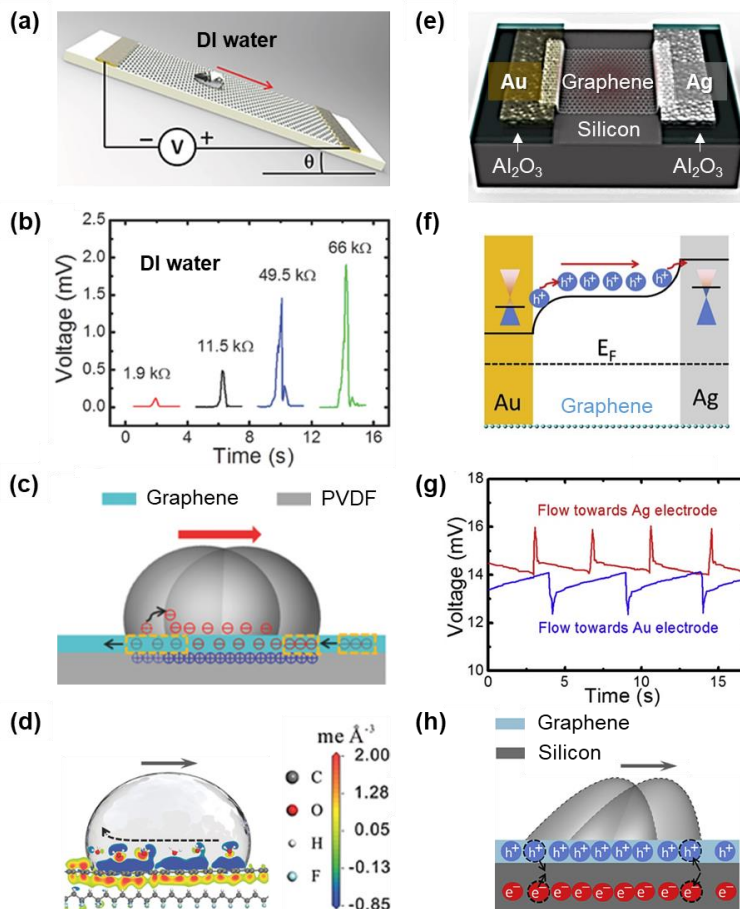


Figure 1-26. (a) Schematic diagram of the experimental setup for measuring the electrical response to the flow of a certain volume of water over a graphene-PVDF heterostructure, which is fixed on a slope; the positive end of the multimeter is connected to the flowing direction of the water.³⁷⁷ (b) Typical generated voltage responses to the flow of DI water over several nanogenerators with different resistances of the graphene between the two electrodes, where lower resistance corresponds to lower voltage output.³⁷⁷ (c) Dynamic charging–discharging process when the water is flowing over the graphene surface; more carriers are being attracted to the front side whereas the excessive carriers at the rear side are being repelled.³⁷⁷ (d) DFT results for the

distribution of the electron density difference near monolayer graphene with PVDF piezoelectric substrate, illustrating the potential difference induced by a moving pure water droplet.³⁷⁷ **(e)** Schematic structure of the graphene-Si 2D hybrid nanogenerator.³⁶⁶ **(f)** The asymmetric potential profile in the lateral direction of this nanogenerator, which leads to a directional move of the photo-generated holes in the 2D graphene plane, allowing energy harvesting from sunlight.³⁶⁶ **(g)** Voltage responses to the flow of DI water over graphene-Si Schottky diode under room light illumination.³⁶⁶ **(h)** Dynamic charge transfer process in the graphene/Si Schottky diode when the water droplet is flowing along the graphene surface. More photogenerated carriers will be separated at the front side of the droplet, whereas the excessive photo-generated carriers will flow back to the depletion region in Si substrate at the rear side of the droplet. As a result, the excess holes in graphene can be driven to move from the rear side to the front side of the droplet.³⁶⁶

In principle, droplet motion generators and waving potential generators are both enabled by the specific adsorption and subsequent desorption of ions on solid surfaces, and they should not be restricted to the interfaces between graphene and aqueous solutions.³⁷⁹ In fact, it has been demonstrated that the ion adsorption process is dictated largely by the substrate underneath the graphene, except in the case of H_3O^+ .^{355,378} Graphene, then, solely serves as a conductive channel, and can be replaced by other conductors or semiconductors, such as Au, Indium Tin Oxide (ITO), or doped silicon.³⁸⁰⁻³⁸² Furthermore, the conductive channel can be coated with some hydrophobic and dielectric materials and need not be in contact with the droplet.³⁸³⁻³⁸⁶ Since the generated voltage is determined by the adsorbed ion species, rational design of coating layers may enable specific detection of certain charged molecules in the solution. As a prototype, Kim and colleagues

demonstrated a pH sensor by incorporating amino groups into their hydrophobic coating layer.³⁸⁷ Nonetheless, even the characterization of the electrical double layer itself is very hard, let alone its formation and interaction with solid.³⁸⁸⁻³⁹⁶ As a result, fundamental details about the dynamics of ion adsorption, double layer formation and carrier motion remain largely unexplored and require continued research effort.

1.2.3 Perspectives, Application Space, and Energy Metrics

To put everything in perspective, these five major classes of molecular energy harvesting mechanisms (phonon coupling, Coulombic scattering, streaming potential, asymmetric doping, and capacitive discharging), collectively have become sort of an atomic scale blueprint that helps guide researchers to navigate through these intricate molecule-substrate interactions (**Figure 1-10**). It should come across as somewhat surprising, therefore, that this review constitutes the very first time, for these mechanisms to be presented together, compared side by side, as parallel contributing factors to a set of deceptively simple electricity induction processes (**Figure 1-10**). Granted, the types of electricity generating phenomena we have touched upon throughout this article span a large family of participating molecules (including vapors, solids, aqueous ionic liquids, and polar organics), as well as a broad scope of input energy sources (e.g., thermal, mechanical, chemical, optical, etc.), let alone the myriad of nanostructured carbon materials that are at our disposal (e.g., carbon nanotubes, graphene, graphene oxides, graphene nanoribbons, fullerenes, and amorphous carbon of various kinds), but it is important for us to realize, and call upon, a more unified theory that can thread these seemingly disconnected dots together and paint a complete molecular picture that adequately describes the electronic responses of any solid-electrolyte interfaces. As was alluded to in earlier sections, while each one of these mechanisms

bears substantial individual merit, perhaps rightfully so considering the amount of successes they have enjoyed modeling experimental data, there have been gathering evidences of intra-mechanistic synergies that invite future studies to consider these approaches as cooperative units, rather than competitive theories. Sood's early mechanistic work on ionic flow over carbon nanotubes (**Figure 1-12f**),¹⁹² for instance, revealed a possible co-existence of Coulombically dragged electrons and the streaming potential; and more recently, Guo's graphene droplet studies³⁶⁰ suggested a unified explanation connecting the originally proposed capacitive discharge mechanism with Coulombic scattering, just to name a few. After all, the series of molecular events (e.g., diffusion, adsorption, electronic interactions, etc.) that are required to drive bulk electron movements come with great complexity, and likely demand a consolidated effort for an accurate mechanistic interpretation. In other words, it is almost certain that for realistic systems, all of these five fundamental processes take place simultaneously. The real challenge, then, should be assigning proper weights to the convoluted mechanisms based on physical insights and determining the rate-limiting step for design and engineering purposes. We might even liken the process of discovering and formulating various electricity generating mechanisms to that of solving individual pieces of a bigger puzzle. It is only after we have deciphered each individual component and their relative connectivity, that we can start to piece together the larger physical picture and shed light on the hidden truth.

It is also possible for us now to consider, in higher-level terms, what the design criteria for existing and future novel physical processes to harvest electricity via these molecule-substrate interactions are. Based on what we have learned from these five mechanisms, the three pillars of a successful current induction strategy seem to be: (i) the existence of a broken symmetry parallel to the direction of the desired electron flow, be it a transient spatially asymmetric dopant access^{292,293} or

a pre-established functional group concentration gradient^{300,301} in the asymmetric chemical doping suite of mechanisms, or the opposite coiling direction for the working and counter electrode in the case of a “twistron” generator;¹⁷⁹ (ii) an advantageous coupling between a physical entity to electrical carriers within the solid substrate, such as the interaction between adsorbed sodium cations and free electrons in the graphene lattice in the cases of a droplet generator³⁵⁵ and waving potential,³⁶¹ or the mechanically excited vibrational mode driven carrier motion seen in the phonon coupling mechanism;¹⁸⁰ (iii) an external stimulus that perturbs the systemic thermodynamic equilibria, thereby injecting energy into the leading physical entity identified in (ii), like mechanically triggered flow in Coulombic scattering,¹⁸¹ evaporation (thermal) induced streaming potential,²⁵⁷ or exothermic water adsorption facilitated moisture driven electron flow.³⁰⁰ Despite their perceived simplicity, these three criteria really are fundamental to any energy harvesting schemes, and it would benefit future studies in this space to carefully consider what these three pillars correspond to within their particular mechanisms before proceeding to further detailed analyses.

Another important question to consider is potential application spaces. What can these new types of energy harvesting devices be ultimately used for? In the previous section, we have covered, under each specific mechanistic class, several clever utility demonstrations in specific scenarios. Looking ahead, one might browse through the following list of general directions for inspiration.

- (i) Going large. Scaling up nanoscale or microscale generators either in dimension or in quantity can be enormously beneficial. There are many such examples in nature, like the scaling-up of actin-myosin filament pairs leading to skeletal muscle contraction, or the number scaling of algae or micro planktons that influence atmospheric compositions on a global scale. These molecular scale energy harvesting techniques

could in principle be implemented at a scale comparable to that of photo-voltaics for solar energy harvesting. As a matter of fact, both the “twistron”¹⁷⁹ and the waving potential generators³⁶¹ have been tested for large scale tidal wave energy harvesting, and the graphene droplet generators have been grafted on top of a solar cell for augmented solar energy harvesting during rainy days.^{364,367}

- (ii) Going small. As motivated from the very beginning, scaling down is perhaps the singularly most unique advantage for these molecular energy harvesting techniques, one that cannot be replaced by any conventional approaches. Extending nanoelectronics into traditionally inaccessible locations using devices with form factors of a colloidal microparticle represents an emerging field at the intersection of materials science and semiconductor physics.³⁰ The idea to interface electronic platforms with the environment is a powerful one, not only one that addresses several key challenges that we face today (such as remote autonomous sensing³⁹⁷ and integration of local objects into a global digital network, aka, the internet of things), but also one that opens up possibilities for the next generation of smart micro-biomedical devices in the near future.³⁹⁸ The miniaturization of robotic and electronic systems is currently an accelerating research trend, motivating the exploration of the limits of the trade-off between size and function. This constant battle has by and large been a result of the device energy constraint. The concept of cubic millimeter-size devices, also known as “smart dust”, was not designed for fluid dispersion given the target size, but nevertheless, constitutes early attempts towards miniaturized autonomous electronics.^{32,399} It is clear that power density limits further downwards scaling. Lithium microbatteries typically have $0.1 \text{ nW}\cdot\mu\text{m}^{-3}$ with energy capacities of $1 \text{ nJ}\cdot\mu\text{m}^{-3}$,⁴⁰⁰ while

basic electronic devices, like quartz oscillators and radio frequency identification (RFID) tags, consume approximately 100 nW and 10 μ W, respectively.⁴⁰⁰ To ensure longer operational times, prior demonstrations of autonomous microsystems often rely on external energy harvesting. In particular, some versions of smart dust harvested energy from wireless electromagnetic radiation, limiting the device operation to a distance of just a few meters.³² Unfortunately, this approach appears to do even worse with respect to downward scaling, due primarily to receiver size limitations,²⁶ a well-known fact in the classic antenna theory.⁴⁰¹ Alternative energy harvesting techniques, such as chemical power harvesting,⁴⁰² bacteria-derived power,⁴⁰³ acoustic (ultrasound) wave harvesting,³² magnetic field harvesting,⁴⁰⁴ and light harvesting,⁴⁰⁵ are continuously being developed. They typically deliver between 0.1 and 10 nW (per $100\times 100\ \mu\text{m}^2$) of power, which to date is not enough for conventional electronic needs. Therefore, for micro-scale energy harvesting techniques, generation persistency and power density represent the two greatest unmet challenges, both of which molecular scale energy harvesting should eventually rise up to tackle.

- (iii) Going persistent. Device persistency could be interpreted in many ways. Since most of the molecular energy harvesting concepts operate at benign ambient conditions and are inherently reversible processes,^{179,257,292,361} they are naturally good candidates for persistent energy harvesting for sensor node type devices at remote, previous inaccessible locations. This also opens up avenues for “power on demand” types of operations where traditional grid-scale energy generations and power supplies are infeasible.^{406,407} One could even take energy persistency to the next level, making them into rare event power sources, in which a rare event occurs at some unknown time

distant into the future and requires a sudden burst of power for signal transduction. Some of the energy generation concepts we touched upon use chemical energy as their input source, which degrades very slowly and typically possesses a long shelf-life. Thermopower wave devices,^{52,268} for example, fit this profile and should be able to address the need of a singular high-power electrical burst for some future rare event deep into the time horizon.

- (iv) Going flexible. The accumulating interest in wearable technologies has paved the way for molecular energy harvesting to enter our daily lives. With much of the research focuses attracted to developing flexible electronic circuits and transistor units,⁴⁰⁸ flexible power sources have received relatively less attention. Of course, these flexible circuits need to be powered by something, preferably something established like a lithium ion battery, sitting well inside the zone of engineering comfort. The problem is, and may remain to be, that existing battery materials are not that flexible, and rightfully so because lithium intercalation, for example, is a delicate process and is generally considered hard to control even in a rigid framework.⁴⁰⁹ One natural solution is to dice up the rigid lithium cell into smaller pieces onto a flexible substrate to achieve at least partial flexibility.⁴¹⁰ Another popular approach has been revamping energy generation technologies all together in a wearable setting, and this is where a lot of the molecular energy harvesting strategies using nanostructured materials could shine. Almost all of the carbon substrates we have covered in this review are, first and foremost, mechanically flexible. Not surprisingly, some studies have already incorporated their molecular energy harvesting devices into a flexible fabric for powering personal electronic devices.^{179,309} Before the dust settles on a universally acknowledged front-

runner in flexible energy generation or storage, this should remain a fruitful application space for many years to come.

This, of course, brings us to the long-awaited subject of energy metrics and device performances. At this point, one should not have to belabor the argument that for self-contained electrical storage and generation devices, such as supercapacitors and fuel cells, it is always important to simultaneously consider two parallel optimizations – one for energy density and the other for power density. Power issues aside, the energy optimization still presents an engineering nightmare because “energy capacity” is a parameter fundamentally linked to the “amount” of energy carrying units, and therefore must decrease as a consequence of device volume down scaling. Electrical power, on the other hand, is associated with how “fast” energy carriers can be produced, transmitted or consumed. Even though in most devices the power density still limited by corresponding electrode area, pushing electric carriers through a unit area of electrode does not have a flux “cap”, like the one in energy storage, which sets fundamental bound how much energy carrying “units” one can pack within a given volume. After all, frictions can almost always be reduced, but compressing something beyond its closely packed limit, feels like a challenge tough to beat.

In this regard, a molecular scale energy harvesting technique typically gets a free energy pass, since it normally is plugged into an “infinite energy reservoir”, and has, therefore, only the power density is-sue to deal with. To this end, we constructed in **Figure 1-27**, a master plot of representative molecular energy harvesting strategies discussed in this review, as a function of (in some cases estimated) power densities. We also included in **Table 1-4** additional detailed information on the state of the art, notably on device types, energy sources, participating molecules, and so forth. The reason we have chosen to also highlight the maximum output voltages is that,

for practical purposes, a device's threshold voltage often limits the kind of electronic circuits it can power, either to charge an ultra-low powered step-up converter (c.a. 50 mV), to light up an LED (c.a. 1.5 V), or to directly be integrated onto a commercial circuit board (c.a. 5 V). With these two metrics in mind, this master plot hopefully can deliver a global view on the relative strengths and weaknesses for each of these five classes of mechanisms discovered so far, as well as for the energy technologies they have inspired. For instance, streaming potential driven harvesting techniques (**Figure 1-27**, orange) have generated some of the highest reported voltages to date but lack the corresponding current driving capabilities, resulting in relatively modest power densities. Thermopower wave devices, while enjoying relatively high ranks within the metrics we have chosen (**Figure 1-27**, purple), actually draw its electricity from a combustion reaction (**Figure 1-10**) and is a lot less reversible than some of the other techniques. Overall, tremendous amount of progress has been made, particularly over the past few years, in the space of molecular interaction enabled electrical energy generation; however, challenges remain in areas like mechanistic elucidation, power density optimization, and device integration into the practical electronic networks for grid-scale energy operations.

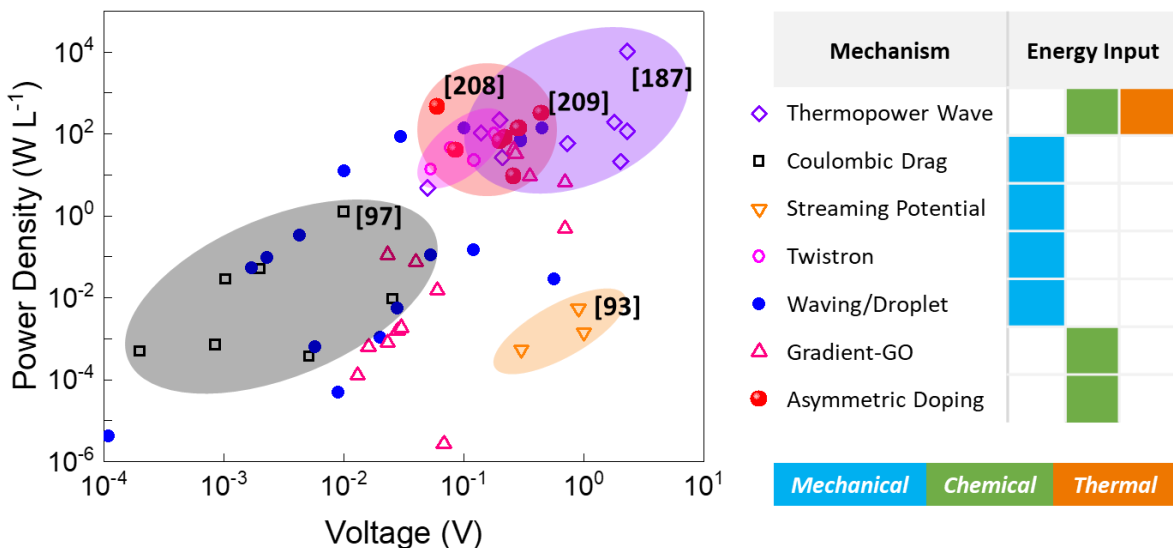


Figure 1-27. Master plot showing the volumetric power density versus open circuit voltage of energy harvesting devices based on molecular interaction with nanostructured carbon materials, categorized according to their mechanism. The range of performance is indicated by the color-corresponding transparent ellipse for several typical mechanisms.

Table 1-4. Summary of the energy sources, molecular phases (orange: vapor; purple: ionic aqueous; blue: non-ionic aqueous; green: polar organic; gray: solid), device sizes, constitutional materials, and performance of energy harvesters based on molecular interaction.

Ref.	Mechanism	Energy source	Molecular phase	Device Size	V_{oc} (V)	Power density ($W \cdot L^{-3}$)	Material
226		Mechanical	Water vapor		0.005		Single CNT
			HCl solution		0.01	1.25	
181		Mechanical	Water	$2 \times 1 \times 0.2 \text{ mm}^3$	0.002	0.05	SWNT bundles
			Methanol		0.0002	0.0005	
207		Thermal & Surface	Ethanol	$\pi \times 0.3^2 \times 25 \text{ mm}^3$	0.00022	4.756×10^{-5}	SWNT rope
206	Coulombic Drag	Mechanical	Water	$\pi \times 7.5^2 \times 50 \text{ mm}^3$	0.02555	0.00924	Graphene 3D foam
205		Mechanical	Ethanol	$\pi \times 7.5^2 \times 50 \text{ mm}^3$	0.00511	0.00037	Graphene 3D foam
208		Thermal & Surface	Ethanol	$20 \times 2 \text{ mm}^2 \times 1 \text{ }\mu\text{m}$	0.00103	0.02810	SWNT film
194		Mechanical	Water Pyridine	$5 \times 5 \text{ mm}^2 \times 1 \text{ nm}$	4.82×10^{-5} 1.24×10^{-5}	0.02323 0.00154	Monolayer Graphene
184		Mechanical	HCl solution	$30 \times 16 \text{ }\mu\text{m}^2 \times 5 \text{ nm}$	0.03	1.875×10^7	Few-layer Graphene
204		Mechanical	Water		0.00049		Monolayer Graphene
178	Streaming Potential	Thermal & Surface	Water	$3.5 \times 4.5 \text{ cm}^2 \times 16 \text{ }\mu\text{m}$	0.9	0.00549	Porous carbon film
257			Water	$1 \times 2.5 \text{ cm}^2 \times 70 \text{ }\mu\text{m}$	1	0.00143	Carbon black
258			Water	$5 \times 0.7 \text{ cm}^2 \times 5 \text{ }\mu\text{m}$	0.3	0.00055	Porous carbon film
263	Gas Flow Thermoelectric	Mechanical	Ar		1.2×10^{-4}		n-Si
			Ar		2×10^{-5}		SWNT or MWNT
264			Ar	$25 \times 5 \text{ mm}^2 \times 1 \text{ nm}$	5.8×10^{-5}	8.4×10^{-4}	Monolayer Graphene

267			Ar	15×8 mm ² ×2 nm	2.5×10 ⁻⁴	0.0465	Bilayer Graphene		
268	Thermopower Wave	Chemical Reaction	TNA/NaN ₃	3×0.5×0.5 mm ³	0.21	26.667	MWCNT		
279			NC/NaN ₃	14×5×0.35 mm ³	0.14	105.21	Bi ₂ Te ₃		
278			NC/NaN ₃	14×5×0.35 mm ³	0.2	71.362	Sb ₂ Te ₃		
277			Picramide/NaN ₃		0.04		DNP-SWNT		
297			NC/NaN ₃		0.5		ZnO		
295			Picramide/NaN ₃	10×1×0.5 mm ³	0.05	4.8077	SWNT		
280			TNA/NaN ₃	5×1.5×0.2 mm ³	0.2	222.22	Sb ₂ Te ₃ Coated MWCNT		
281			NC/NaN ₃	14×5×0.25 mm ³	1.8	195.92	MnO ₂		
282			Collodion/NaN ₃	5.5×13.5×0.1 mm ³	2.3	116.06	ZnO		
283			Picric acid/NaN ₃		0.175		VA-MWCNT		
272			Picric acid/NaN ₃		0.1567		VA-MWCNT		
273			Collodion/NaN ₃	6.5×13.5×0.11 mm ³	2.02	21.137	CuO–Cu ₂ O–Cu		
285			Collodion/NaN ₃	6.5×13.5×0.11 mm ³	0.61		Co _x O _y –ZnO		
274			Collodion/NaN ₃		1.45		MWCNT–Mg–MgO		
52			Thermopower Wave	Chemical Reaction	Sucrose-KNO ₃ /NaN ₃	100×3×0.1 mm ³	0.02	0.07092	SWNT
271					NC/NaN ₃	10×1×0.1 mm ³	2.3	10332	Single crystal Bi ₂ Te ₃
276	NC-NaNO ₃ /NaN ₃	18.7×10.6×0.5 mm ³			0.732	58.008	MWCNT		
287	Picric acid/NaN ₃				0.403		CNT–PZT		
292	Asymmetric Chemical Doping	Chemical Adsorption	MeCN	15×3×0.1 mm ³	0.085	40.139	SWNT		
			MeCN	2.6×3×0.1 mm ³	0.06	467.69	O-SWNT		
			MeCN	16.5×3×0.1 mm ³	0.17	28.736	O-SWNT		
			MeCN	38×3×0.1 mm ³	0.09	4.8448	O-SWNT		
			Cl-MeCN		0.29	140.17	SWNT (HiPCo)		
			F-MeCN		0.22	80.667	SWNT (HiPCo)		
			F-acetone	5×3×0.1 mm ³	0.285	135.375	SWNT (HiPCo)		
			F-MeCN		0.44	322.67	SWNT (CG200)		
293			Cl-MeCN		0.2	66.667	SWNT (CG200)		
307		Chemical Adsorption	Water vapor	5×1 cm ² ×20 μm	0.068	2.739×10 ⁻⁶	Porous carbon film		

309	Asymmetric Chemical Composition	Chemical Reaction	Water	$4 \times 10 \text{ mm}^2 \times 50 \mu\text{m}$	0.45	140.625	Oxidized CNT fiber
300			Water vapor	$5 \times 5 \text{ mm}^2 \times 2.8 \mu\text{m}$	0.023	0.11295	gradient GO film
301			Water vapor	$1 \times 1 \text{ cm}^2 \times 50 \mu\text{m}$	0.26	41.6	gradient GO film
304			Water vapor	$5 \times 5 \text{ mm}^2 \times 400 \mu\text{m}$	0.04	0.075	gradient GO film
305			Water vapor	$80 \times 80 \times 100 \mu\text{m}^3$	0.355	9.4075	GO fiber
306			Gradient Graphene Oxide	Chemical Adsorption	Water vapor	$1.5 \times 0.5 \text{ mm}^2 \times 0.5 \mu\text{m}$	0.27
	Water vapor				0.06	0.015	
	Ethanol vapor				0.028	0.00161	
308	Methanol vapor	$2 \times 2 \text{ mm}^2 \times 100 \mu\text{m}$			0.03	0.001875	polypyrrole
	Acetone vapor				0.023	0.000805	
	$\text{NH}_3 \cdot \text{H}_2\text{O}$ vapor				0.013	0.00013	
	$\text{HCl} \cdot n\text{H}_2\text{O}$ vapor				0.016	0.00064	
310	Asymmetric Moisturizing	Chemical Adsorption			Water vapor	$5 \times 5 \text{ mm}^2 \times 90 \mu\text{m}$	0.7
311			Water vapor	$\pi \times 0.5^2 \text{ mm}^2 \times 10 \mu\text{m}$	0.7	6.6845	GO film
179	Twist Generator	Mechanical	0.1 M HCl solution		0.18	100.69	MWNT yarn
			1 M NaCl solution	$\pi \times 35^2 \mu\text{m}^2 \times 2 \text{ cm}$	0.05326	13.891	
			1 M HCl solution		0.121576	22.680	
344	Thermally Chargeable Supercapacitor	Thermal	2 M EMIM TFSI in MeCN	$\pi \times 3^2 \times 0.4 \text{ mm}^3$	0.045	0.11937	Nanoporous Carbon
361	Waving Potential	Mechanical	0.6 M NaCl	$2 \times 10 \text{ cm}^2 \times 1 \text{ nm}$	0.1	138.89	Monolayer graphene/PET Au
			0.6 M NaCl	$2 \times 5 \text{ cm}^2 \times 50 \text{ nm}$	6×10^{-5}	5.7×10^{-4}	
369			0.6 M NaCl	$8 \times 4 \text{ cm}^2 \times 50 \text{ nm}$	0.053	0.10973	ZnO/PET
370			4 M NaCl	$100 \times 2.5 \text{ mm}^2 \times 260 \text{ nm}$	0.3	68.865	MWCNT-OMC fiber
371			0.6 M NaCl	$3 \times 5 \text{ cm}^2 \times 70 \mu\text{m}$	0.0201	0.00108	Graphene-CB-PU
355	Droplet Generator	Mechanical	0.6 M NaCl	$11 \times 0.5 \text{ cm}^2 \times 1 \text{ nm}$	0.0017	0.05254	Monolayer graphene/PET
			0.6 M MgCl_2	$11 \times 0.5 \text{ cm}^2 \times 1 \text{ nm}$	0.0023	0.09618	
			0.6 M $\text{NH}_3 \cdot \text{H}_2\text{O}$	$11 \times 0.5 \text{ cm}^2 \times 1 \text{ nm}$	0.0043	0.33618	
			0.6 M CuCl_2	$4.8 \times 0.5 \text{ cm}^2 \times 1 \text{ nm}$	0.03	85.227	
362		Mechanical	0.6 M CuCl_2	$7 \times 0.5 \text{ cm}^2 \times 1 \mu\text{m}$	0.12	0.14694	Graphene grid/PDMS

368	Mechanical	0.6 M NaCl	2×0.5 cm ² ×1 μm	1.09×10 ⁻⁴	4.16×10 ⁻⁶	Graphene grid/PDMS
373	Mechanical	0.5 mg/mL GO	1×1 cm ² ×1 nm	0.01	12.5	Monolayer graphene/SiO ₂ /Si
373	Mechanical	0.9 M NaCl	1×1 cm ² ×50 μm	0.0058	0.00062	SWCNT/glass
367	Solar & Mechanical	0.6 M NaCl	5×5 cm ² ×1 nm	6.2×10 ⁻⁵	0.01922	Monolayer graphene/ITO
366	Solar & Mechanical	Water	6×2 cm ² ×10 μm	0.02814	0.00550	Monolayer graphene/n-Si diode
376	Mechanical	0.6 M NaCl	7×3.5 cm ² ×10 μm	0.57	0.02792	Monolayer graphene/PTFE
364	Solar & Mechanical	0.6 M NaCl	2×5 cm ² ×10 μm	2.51×10 ⁻⁵	3.424×10 ⁻⁷	rGO-DSSC/PET
374	Mechanical	0.6 M HCl		3.79×10 ⁻⁴		PEDOT-graphene-PtCo/FTO
377	Mechanical	0.01 M NaCl	6×2 cm ² ×30 μm	0.009	4.8913×10 ⁻⁵	Graphene/PVDF
375	Mechanical	0.6 M NaCl		8.5×10 ⁻⁵		PANI-graphene/FTO

NC: Nitro-cellulose; TNA: cyclotrimethylene trinitramine; MeCN: Acetonitrile; EMIM TFSI: 1-Ethyl-3-methylimidazolium bis(trifluoromethylsulfonyl)imide; PET: poly-ethylene terephthalate; CB: carbon black; PU: polyurethane; OMC: ordered mesoporous carbon; PDMS: polydimethylsiloxane; PTFE: polytetrafluoroethylene; DSSC: dye-sensitized solar cell; PEDOT: poly(3,4-ethylenedioxythiophene); ITO: indium tin oxide; FTO: fluorine-doped tin oxide

1.2.4 Conclusions and Outlook

Energy harvesting from molecular interactions between the environment and the interfacing nano-structured materials has attracted growing scientific attention over the past two decades (**Figure 1-10**). The surge in the amount of efforts have boosted the power densities of such devices by orders of magnitude, even beyond conventional energy harvesting schemes (**Figure 1-27**). The diversity of energy sources and various types of molecular interactions are especially intriguing, as these energy harvesting strategies are considered prime candidates to power next-generation colloidal nano-electronic systems, which need to draw energy from all kinds of environments. Of course, the already impressive list of demonstrated methodologies (**Figure 1-10**) represents only the tip of the iceberg that is the library of versatile energy technologies driven by the interactions between carbon nanostructures and the surrounding molecular environments. Tremendous work is

necessary to deepen our knowledge about the power generation process, which will in turn help guide device performance optimizations and broaden their application spaces. In that regard, successful integration of molecular-interaction based power sources into dispersed nano-electronic systems, such as colloidal state-machines, would be highly desired. Endless possibilities await, for those with a creative mindset to unlock the enormous power lying beneath these tiny, nanoscale molecular interactions.

1.3 References

- (1) Liu, P.; Liu, A. T.; Kozawa, D.; Dong, J.; Yang, J. F.; Koman, V. B.; Saccone, M.; Wang, S.; Son, Y.; Wong, M. H.; Strano, M. S. *Nature Materials* **2018**, *17*, 1005.
- (2) Koman, V. B.; Liu, P.; Kozawa, D.; Liu, A. T.; Cottrill, A. L.; Son, Y.; Lebron, J. A.; Strano, M. S. *Nature Nanotechnology* **2018**, *13*, 819.
- (3) Hong, G.; Fu, T.-M.; Qiao, M.; Viveros, R. D.; Yang, X.; Zhou, T.; Lee, J. M.; Park, H.-G.; Sanes, J. R.; Lieber, C. M. *Science* **2018**, *360*, 1447.
- (4) Kim, Y.; Chortos, A.; Xu, W.; Liu, Y.; Oh, J. Y.; Son, D.; Kang, J.; Foudeh, A. M.; Zhu, C.; Lee, Y.; Niu, S.; Liu, J.; Pfattner, R.; Bao, Z.; Lee, T.-W. *Science* **2018**, *360*, 998.
- (5) Kang, S.-K.; Murphy, R. K. J.; Hwang, S.-W.; Lee, S. M.; Harburg, D. V.; Krueger, N. A.; Shin, J.; Gamble, P.; Cheng, H.; Yu, S.; Liu, Z.; McCall, J. G.; Stephen, M.; Ying, H.; Kim, J.; Park, G.; Webb, R. C.; Lee, C. H.; Chung, S.; Wie, D. S.; Gujar, A. D.; Vemulapalli, B.; Kim, A. H.; Lee, K.-M.; Cheng, J.; Huang, Y.; Lee, S. H.; Braun, P. V.; Ray, W. Z.; Rogers, J. A. *Nature* **2016**, *530*, 71.
- (6) Feynman, R. P. *California Institute of Technology, Engineering and Science magazine* **1960**.
- (7) Liu, A. T.; Strano, M. S. *Nature Reviews Materials* **2019**.
- (8) Liu, A. T.; Zhang, G.; Cottrill, A. L.; Kunai, Y.; Kaplan, A.; Liu, P.; Koman, V. B.; Strano, M. S. *Adv Energy Mater* **2018**, *8*, 1802212.
- (9) Jafferis, N. T.; Helbling, E. F.; Karpelson, M.; Wood, R. J. *Nature* **2019**, *570*, 491.
- (10) Warneke, B.; Last, M.; Liebowitz, B.; Pister, K. S. J. *Computer* **2001**, *34*, 44.
- (11) Kalantar-Zadeh, K.; Berean, K. J.; Ha, N.; Chrimes, A. F.; Xu, K.; Grando, D.; Ou, J. Z.; Pillai, N.; Campbell, J. L.; Brkljača, R.; Taylor, K. M.; Burgell, R. E.; Yao, C. K.; Ward, S. A.; McSweeney, C. S.; Muir, J. G.; Gibson, P. R. *Nature Electronics* **2018**, *1*, 79.
- (12) Funke, D. A.; Mayr, P.; Straczek, L.; McCaskill, J. S.; Oehm, J.; Pohl, N. In *2016 IEEE International Conference on Electronics, Circuits and Systems (ICECS)* 2016, p 512.

- (13) Lee, S.; Cortese, A.; Gandhi, A.; Agger, E.; McEuen, P. L.; Molnar, A. C. *IEEE Transactions on Biomedical Circuits and Systems* **2018**, 1.
- (14) Hu, X.; Aggarwal, K.; Yang, M. X.; Parizi, K. B.; Xu, X.; Akin, D.; Poon, A. S. Y.; Wong, H. S. P. *Physical Review Applied* **2017**, 8, 014031.
- (15) Gómez-Martínez, R.; Hernández-Pinto, A. M.; Duch, M.; Vázquez, P.; Zinoviev, K.; de la Rosa, E. J.; Esteve, J.; Suárez, T.; Plaza, J. A. *Nature Nanotechnology* **2013**, 8, 517.
- (16) Fan, F.; Stebe, K. J. *Langmuir* **2005**, 21, 1149.
- (17) Maxey, M. R.; Riley, J. J. *The Physics of Fluids* **1983**, 26, 883.
- (18) AMD 2018.
- (19) Wu, X.; Lee, I.; Dong, Q.; Yang, K.; Kim, D.; Wang, J.; Peng, Y.; Zhang, Y.; Saliganc, M.; Yasuda, M. In *2018 IEEE Symposium on VLSI Circuits*; IEEE: 2018, p 191.
- (20) Usami, M. In *Proceedings of 2004 IEEE Asia-Pacific Conference on Advanced System Integrated Circuits* 2004, p 2.
- (21) Fiori, G.; Bonaccorso, F.; Iannaccone, G.; Palacios, T.; Neumaier, D.; Seabaugh, A.; Banerjee, S. K.; Colombo, L. *Nature Nanotechnology* **2014**, 9, 768.
- (22) Shulaker, M. M.; Hills, G.; Park, R. S.; Howe, R. T.; Saraswat, K.; Wong, H. S. P.; Mitra, S. *Nature* **2017**, 547, 74.
- (23) Chu, P. B.; Lo, N. R.; Berg, E. C.; Pister, K. S. J. In *Proceedings IEEE The Tenth Annual International Workshop on Micro Electro Mechanical Systems. An Investigation of Micro Structures, Sensors, Actuators, Machines and Robots* 1997, p 350.
- (24) Biederman, W.; Yeager, D. J.; Narevsky, N.; Koralek, A. C.; Carmena, J. M.; Alon, E.; Rabaey, J. M. *IEEE Journal of Solid-State Circuits* **2013**, 48, 960.
- (25) Ghaed, M. H.; Chen, G.; Haque, R.; Wieckowski, M.; Kim, Y.; Kim, G.; Lee, Y.; Lee, I.; Fick, D.; Kim, D.; Seok, M.; Wise, K. D.; Blaauw, D.; Sylvester, D. *IEEE Transactions on Circuits and Systems I: Regular Papers* **2013**, 60, 3152.
- (26) Seo, D.; Carmena, J. M.; Rabaey, J. M.; Maharbiz, M. M.; Alon, E. *Journal of Neuroscience Methods* **2015**, 244, 114.
- (27) Seo, D.; Tang, H.; Carmena, J. M.; Rabaey, J. M.; Alon, E.; Boser, B. E.; Maharbiz, M. M. In *2015 37th Annual International Conference of the IEEE Engineering in Medicine and Biology Society (EMBC)* 2015, p 2673.
- (28) Driscoll, S. O.; Korhummel, S.; Cong, P.; Zou, Y.; Sankaragomathi, K.; Zhu, J.; Deyle, T.; Dastgheib, A.; Lu, B.; Tierney, M.; Shao, J.; Gutierrez, C.; Jones, S.; Yao, H. In *2017 IEEE Radio Frequency Integrated Circuits Symposium (RFIC)* 2017, p 256.
- (29) Khalifa, A.; Karimi, Y.; Wang, Q.; Garikapati, S.; Montlouis, W.; Stanačević, M.; Thakor, N.; Etienne-Cummings, R. *IEEE Transactions on Biomedical Circuits and Systems* **2018**, 12, 521.

- (30) Kwak, S.-Y.; Wong, M. H.; Lew, T. T. S.; Bisker, G.; Lee, M. A.; Kaplan, A.; Dong, J.; Liu, A. T.; Koman, V. B.; Sinclair, R.; Hamann, C.; Strano, M. S. *Annual Review of Analytical Chemistry* **2017**, *10*, 113.
- (31) Weinstein, R. *IT Professional* **2005**, *7*, 27.
- (32) Seo, D.; Neely, R. M.; Shen, K.; Singhal, U.; Alon, E.; Rabaey, J. M.; Carmena, J. M.; Maharbiz, M. M. *Neuron* **2016**, *91*, 529.
- (33) Withey, P. A.; Vemuru, V. S. M.; Bachilo, S. M.; Nagarajaiah, S.; Weisman, R. B. *Nano Letters* **2012**, *12*, 3497.
- (34) Park, J.; Oh, S.; Kim, Y.; Park, K.; Cho, S. In *2015 International Conference on Information and Communication Technology Convergence (ICTC) 2015*, p 1362.
- (35) Farra, R.; Sheppard, N. F.; McCabe, L.; Neer, R. M.; Anderson, J. M.; Santini, J. T.; Cima, M. J.; Langer, R. *Science Translational Medicine* **2012**, *4*, 122ra21.
- (36) Ceylan, H.; Giltinan, J.; Kozielski, K.; Sitti, M. *Lab on a Chip* **2017**, *17*, 1705.
- (37) Palagi, S.; Mark, A. G.; Reigh, S. Y.; Melde, K.; Qiu, T.; Zeng, H.; Parmeggiani, C.; Martella, D.; Sanchez-Castillo, A.; Kapernaum, N.; Giesselmann, F.; Wiersma, D. S.; Lauga, E.; Fischer, P. *Nature Materials* **2016**, *15*, 647.
- (38) Miskin, M. Z.; Dorsey, K. J.; Bircan, B.; Han, Y.; Muller, D. A.; McEuen, P. L.; Cohen, I. *Proceedings of the National Academy of Sciences* **2018**, *115*, 466.
- (39) Purcell, E. M. *American journal of physics* **1977**, *45*, 3.
- (40) Moran, J. L.; Posner, J. D. *Annual Review of Fluid Mechanics* **2017**, *49*, 511.
- (41) Paxton, W. F.; Baker, P. T.; Kline, T. R.; Wang, Y.; Mallouk, T. E.; Sen, A. *Journal of the American Chemical Society* **2006**, *128*, 14881.
- (42) Li, J.; Rozen, I.; Wang, J. *ACS Nano* **2016**, *10*, 5619.
- (43) Howse, J. R.; Jones, R. A. L.; Ryan, A. J.; Gough, T.; Vafabakhsh, R.; Golestanian, R. *Physical Review Letters* **2007**, *99*, 048102.
- (44) Jiang, H.-R.; Yoshinaga, N.; Sano, M. *Physical Review Letters* **2010**, *105*, 268302.
- (45) Wang, W.; Castro, L. A.; Hoyos, M.; Mallouk, T. E. *ACS Nano* **2012**, *6*, 6122.
- (46) Pikul, J. H.; Gang Zhang, H.; Cho, J.; Braun, P. V.; King, W. P. *Nat Commun* **2013**, *4*, 1732.
- (47) Choi, J.-H.; Lee, C.; Cho, S.; Moon, G. D.; kim, B.-s.; Chang, H.; Jang, H. D. *Carbon* **2018**, *132*, 16.
- (48) González, A.; Goikolea, E.; Barrena, J. A.; Mysyk, R. *Renewable and Sustainable Energy Reviews* **2016**, *58*, 1189.
- (49) Manthiram, A. *ACS Central Science* **2017**, *3*, 1063.
- (50) Matsuda, Y.; Kuwata, N.; Kawamura, J. *Solid State Ionics* **2018**, *320*, 38.
- (51) Chiu, P.-Y.; Ker, M.-D. *Microelectronics Reliability* **2014**, *54*, 64.

- (52) Mahajan, S. G.; Liu, A. T.; Cottrill, A. L.; Kunai, Y.; Bender, D.; Castillo, J.; Gibbs, S. L.; Strano, M. S. *Energy & Environmental Science* **2016**, *9*, 1290.
- (53) Jean, J.; Brown, P. R.; Jaffe, R. L.; Buonassisi, T.; Bulović, V. *Energy & Environmental Science* **2015**, *8*, 1200.
- (54) Charthad, J.; Weber, M. J.; Chang, T. C.; Arbabian, A. *IEEE Journal of Solid-State Circuits* **2015**, *50*, 1741.
- (55) Sankaragomathi, K.; Perez, L.; Mirjalili, R.; Parviz, B.; Otis, B. In *Proceedings of the IEEE 2014 Custom Integrated Circuits Conference* 2014, p 1.
- (56) Cao, X.; Jie, Y.; Wang, N.; Wang, Z. L. *Adv Energy Mater* **2016**, *6*, 1600665.
- (57) Hasan, R. M. M.; Luo, X. *Nanomanufacturing and Metrology* **2018**, *1*, 67.
- (58) Kuang, M.; Wang, J.; Bao, B.; Li, F.; Wang, L.; Jiang, L.; Song, Y. *Advanced Optical Materials* **2014**, *2*, 34.
- (59) Visser, C. W.; Kamperman, T.; Karbaat, L. P.; Lohse, D.; Karperien, M. *Science Advances* **2018**, *4*, eaao1175.
- (60) Meitl, M. A.; Zhu, Z.-T.; Kumar, V.; Lee, K. J.; Feng, X.; Huang, Y. Y.; Adesida, I.; Nuzzo, R. G.; Rogers, J. A. *Nature Materials* **2005**, *5*, 33.
- (61) Chang, J.-K.; Fang, H.; Bower, C. A.; Song, E.; Yu, X.; Rogers, J. A. *Proceedings of the National Academy of Sciences* **2017**, *114*, E5522.
- (62) Manoharan, V. N.; Elsesser, M. T.; Pine, D. J. *Science* **2003**, *301*, 483.
- (63) Wang, Y.; Wang, Y.; Breed, D. R.; Manoharan, V. N.; Feng, L.; Hollingsworth, A. D.; Weck, M.; Pine, D. J. *Nature* **2012**, *491*, 51.
- (64) Gao, M.; Li, L.; Song, Y. *Journal of Materials Chemistry C* **2017**, *5*, 2971.
- (65) Chung, S. E.; Park, W.; Shin, S.; Lee, S. A.; Kwon, S. *Nature Materials* **2008**, *7*, 581.
- (66) Kang, K.; Lee, K.-H.; Han, Y.; Gao, H.; Xie, S.; Muller, D. A.; Park, J. *Nature* **2017**, *550*, 229.
- (67) Zhang, P.; Ma, L.; Fan, F.; Zeng, Z.; Peng, C.; Loya, P. E.; Liu, Z.; Gong, Y.; Zhang, J.; Zhang, X. *Nat Commun* **2014**, *5*, 3782.
- (68) Na, J. H.; Evans, A. A.; Bae, J.; Chiappelli, M. C.; Santangelo, C. D.; Lang, R. J.; Hull, T. C.; Hayward, R. C. *Advanced Materials* **2015**, *27*, 79.
- (69) Rogers, J.; Huang, Y.; Schmidt, O. G.; Gracias, D. H. *Mrs Bulletin* **2016**, *41*, 123.
- (70) Felton, S.; Tolley, M.; Demaine, E.; Rus, D.; Wood, R. *Science* **2014**, *345*, 644.
- (71) Hawkes, E.; An, B.; Benbernou, N. M.; Tanaka, H.; Kim, S.; Demaine, E.; Rus, D.; Wood, R. J. *Proceedings of the National Academy of Sciences* **2010**, *107*, 12441.
- (72) Sacanna, S.; Irvine, W. T. M.; Chaikin, P. M.; Pine, D. J. *Nature* **2010**, *464*, 575.
- (73) Lee, H.-Y.; Shin, S. H. R.; Drews, A. M.; Chirsan, A. M.; Lewis, S. A.; Bishop, K. J. M. *ACS Nano* **2014**, *8*, 9979.

- (74) Gong, Z.; Hueckel, T.; Yi, G.-R.; Sacanna, S. *Nature* **2017**, *550*, 234.
- (75) Grzybowski, B. A.; Fitzner, K.; Paczesny, J.; Granick, S. *Chemical Society Reviews* **2017**, *46*, 5647.
- (76) Rao, S. S. *Engineering optimization: theory and practice*; John Wiley & Sons, 2009.
- (77) Axelsson, H.; Wardi, Y.; Egerstedt, M.; Verriest, E. *Journal of Optimization Theory and Applications* **2008**, *136*, 167.
- (78) Pervan, A.; Murphey, T. D.
- (79) Andrés Arroyo, M.; Cannon, S.; Daymude, J. J.; Randall, D.; Richa, A. W. *Natural Computing* **2018**, *17*, 723.
- (80) Cannon, S.; Daymude, J.; Gokmen, C.; Randall, D.; Richa, A. *A Local Stochastic Algorithm for Separation in Heterogeneous Self-Organizing Particle Systems*, 2018.
- (81) Ando, H.; Oasa, Y.; Suzuki, I.; Yamashita, M. *IEEE Transactions on Robotics and Automation* **1999**, *15*, 818.
- (82) Flocchini, P.; Prencipe, G.; Santoro, N.; Widmayer, P. *Theoretical Computer Science* **2008**, *407*, 412.
- (83) Savoie, W.; Berrueta, T. A.; Jackson, Z.; Pervan, A.; Warkentin, R.; Li, S.; Murphey, T. D.; Wiesenfeld, K.; Goldman, D. I. *Science Robotics* **2019**, *4*, eaax4316.
- (84) Sutton, R. S.; Barto, A. G. *Introduction to Reinforcement Learning*; MIT Press, 1998.
- (85) Yang, J. F.; Liu, P.; Koman, V. B.; Liu, A. T.; Strano, M. S. In *Robotic Systems and Autonomous Platforms*; Walsh, S. M., Strano, M. S., Eds.; Woodhead Publishing: 2019, p 361.
- (86) Franssila, S. *Introduction to Microfabrication*; 2 ed.; Wiley & Sons, 2010.
- (87) Hu, C. C. *Modern Semiconductor Devices for Integrated Circuits*; Pearson, 2010.
- (88) Luttge, R. *Microfabrication for Industrial Applications*; Elsevier, 2011.
- (89) McDonald, J. C.; Duffy, D. C.; Anderson, J. R.; Chiu, D. T.; Wu, H. K.; Schueller, O. J. A.; Whitesides, G. M. *Electrophoresis* **2000**, *21*, 27.
- (90) Iijima, S.; Ichihashi, T. *Nature* **1993**, *363*, 603.
- (91) Jiao, L. Y.; Zhang, L.; Wang, X. R.; Diankov, G.; Dai, H. J. *Nature* **2009**, *458*, 877.
- (92) Kawata, S.; Sun, H. B.; Tanaka, T.; Takada, K. *Nature* **2001**, *412*, 697.
- (93) Kosynkin, D. V.; Higginbotham, A. L.; Sinitiskii, A.; Lomeda, J. R.; Dimiev, A.; Price, B. K.; Tour, J. M. *Nature* **2009**, *458*, 872.
- (94) Novoselov, K. S.; Fal'ko, V. I.; Colombo, L.; Gellert, P. R.; Schwab, M. G.; Kim, K. *Nature* **2012**, *490*, 192.
- (95) Novoselov, K. S.; Geim, A. K.; Morozov, S. V.; Jiang, D.; Katsnelson, M. I.; Grigorieva, I. V.; Dubonos, S. V.; Firsov, A. A. *Nature* **2005**, *438*, 197.

- (96) Stankovich, S.; Dikin, D. A.; Dommett, G. H. B.; Kohlhaas, K. M.; Zimney, E. J.; Stach, E. A.; Piner, R. D.; Nguyen, S. T.; Ruoff, R. S. *Nature* **2006**, *442*, 282.
- (97) Tans, S. J.; Verschueren, A. R. M.; Dekker, C. *Nature* **1998**, *393*, 49.
- (98) Treacy, M. M. J.; Ebbesen, T. W.; Gibson, J. M. *Nature* **1996**, *381*, 678.
- (99) Wildoer, J. W. G.; Venema, L. C.; Rinzler, A. G.; Smalley, R. E.; Dekker, C. *Nature* **1998**, *391*, 59.
- (100) Zhang, Y. B.; Tan, Y. W.; Stormer, H. L.; Kim, P. *Nature* **2005**, *438*, 201.
- (101) Geim, A. K.; Novoselov, K. S. *Nat. Mater.* **2007**, *6*, 183.
- (102) Radisavljevic, B.; Radenovic, A.; Brivio, J.; Giacometti, V.; Kis, A. *Nat. Nanotechnol.* **2011**, *6*, 147.
- (103) Gattass, R. R.; Mazur, E. *Nat. Photonics* **2008**, *2*, 219.
- (104) Mak, K. F.; Lee, C.; Hone, J.; Shan, J.; Heinz, T. F. *Phys. Rev. Lett.* **2010**, *105*.
- (105) Novoselov, K. S.; Jiang, D.; Schedin, F.; Booth, T. J.; Khotkevich, V. V.; Morozov, S. V.; Geim, A. K. *Proc. Natl. Acad. Sci. U.S.A.* **2005**, *102*, 10451.
- (106) Baughman, R. H.; Zakhidov, A. A.; de Heer, W. A. *Science* **2002**, *297*, 787.
- (107) Berger, C.; Song, Z. M.; Li, X. B.; Wu, X. S.; Brown, N.; Naud, C.; Mayou, D.; Li, T. B.; Hass, J.; Marchenkov, A. N.; Conrad, E. H.; First, P. N.; de Heer, W. A. *Science* **2006**, *312*, 1191.
- (108) Bonaccorso, F.; Colombo, L.; Yu, G. H.; Stoller, M.; Tozzini, V.; Ferrari, A. C.; Ruoff, R. S.; Pellegrini, V. *Science* **2015**, *347*, 1246501.
- (109) Coleman, J. N.; Lotya, M.; O'Neill, A.; Bergin, S. D.; King, P. J.; Khan, U.; Young, K.; Gaucher, A.; De, S.; Smith, R. J.; Shvets, I. V.; Arora, S. K.; Stanton, G.; Kim, H. Y.; Lee, K.; Kim, G. T.; Duesberg, G. S.; Hallam, T.; Boland, J. J.; Wang, J. J.; Donegan, J. F.; Grunlan, J. C.; Moriarty, G.; Shmeliov, A.; Nicholls, R. J.; Perkins, J. M.; Grievson, E. M.; Theuwissen, K.; McComb, D. W.; Nellist, P. D.; Nicolosi, V. *Science* **2011**, *331*, 568.
- (110) Geim, A. K. *Science* **2009**, *324*, 1530.
- (111) Lee, C.; Wei, X. D.; Kysar, J. W.; Hone, J. *Science* **2008**, *321*, 385.
- (112) Li, X. S.; Cai, W. W.; An, J. H.; Kim, S.; Nah, J.; Yang, D. X.; Piner, R.; Velamakanni, A.; Jung, I.; Tutuc, E.; Banerjee, S. K.; Colombo, L.; Ruoff, R. S. *Science* **2009**, *324*, 1312.
- (113) Novoselov, K. S.; Geim, A. K.; Morozov, S. V.; Jiang, D.; Zhang, Y.; Dubonos, S. V.; Grigorieva, I. V.; Firsov, A. A. *Science* **2004**, *306*, 666.
- (114) Thess, A.; Lee, R.; Nikolaev, P.; Dai, H. J.; Petit, P.; Robert, J.; Xu, C. H.; Lee, Y. H.; Kim, S. G.; Rinzler, A. G.; Colbert, D. T.; Scuseria, G. E.; Tomanek, D.; Fischer, J. E.; Smalley, R. E. *Science* **1996**, *273*, 483.
- (115) Xu, M. S.; Liang, T.; Shi, M. M.; Chen, H. Z. *Chem. Rev.* **2013**, *113*, 3766.

- (116) Liu, P.; Cottrill, A. L.; Kozawa, D.; Koman, V. B.; Parviz, D.; Liu, A. T.; Yang, J.; Tran, T. Q.; Wong, M. H.; Wang, S.; Strano, M. S. *Nano Today* **2018**.
- (117) Youngwoo, S.; Daichi, K.; Albert Tianxiang, L.; Volodymyr, B. K.; Qing Hua, W.; Michael, S. S. *2D Materials* **2017**, *4*, 025091.
- (118) Sailor, M. J.; Link, J. R. *ChemComm* **2005**, *0*, 1375.
- (119) Pikul, J. H.; Zhang, H. G.; Cho, J.; Braun, P. V.; King, W. P. *Nat Commun* **2013**, *4*, 1732.
- (120) Ren, J.; Li, L.; Chen, C.; Chen, X.; Cai, Z.; Qiu, L.; Wang, Y.; Zhu, X.; Peng, H. *Adv. Mater.* **2013**, *25*, 1155.
- (121) Oudenhoven, J. F.; Baggetto, L.; Notten, P. H. *Adv. Energy Mater.* **2011**, *1*, 10.
- (122) Sun, K.; Wei, T. S.; Ahn, B. Y.; Seo, J. Y.; Dillon, S. J.; Lewis, J. A. *Adv. Mater.* **2013**, *25*, 4539.
- (123) El-Kady, M. F.; Kaner, R. B. *Nat. Commun.* **2013**, *4*, 1475.
- (124) Wang, K.; Zou, W. J.; Quan, B. G.; Yu, A. F.; Wu, H. P.; Jiang, P.; Wei, Z. X. *Adv. Energy Mater.* **2011**, *1*, 1068.
- (125) Wu, Z. S.; Feng, X. L.; Cheng, H. M. *Natl. Sci. Rev.* **2014**, *1*, 277.
- (126) Gao, W.; Singh, N.; Song, L.; Liu, Z.; Reddy, A. L. M.; Ci, L.; Vajtai, R.; Zhang, Q.; Wei, B.; Ajayan, P. M. *Nat. Nanotechnol.* **2011**, *6*, 496.
- (127) Zhang, L. L.; Zhao, X. *Chem. Soc. Rev.* **2009**, *38*, 2520.
- (128) Gunes, S.; Neugebauer, H.; Sariciftci, N. S. *Chem. Rev.* **2007**, *107*, 1324.
- (129) Kojima, A.; Teshima, K.; Shirai, Y.; Miyasaka, T. *J. Am. Chem. Soc.* **2009**, *131*, 6050.
- (130) Burschka, J.; Pellet, N.; Moon, S. J.; Humphry-Baker, R.; Gao, P.; Nazeeruddin, M. K.; Gratzel, M. *Nature* **2013**, *499*, 316.
- (131) Liu, M. Z.; Johnston, M. B.; Snaith, H. J. *Nature* **2013**, *501*, 395.
- (132) Oregan, B.; Gratzel, M. *Nature* **1991**, *353*, 737.
- (133) Tian, B. Z.; Zheng, X. L.; Kempa, T. J.; Fang, Y.; Yu, N. F.; Yu, G. H.; Huang, J. L.; Lieber, C. M. *Nature* **2007**, *449*, 885.
- (134) Atwater, H. A.; Polman, A. *Nat. Mater.* **2010**, *9*, 865.
- (135) Atwater, H. A.; Polman, A. *Nat. Mater.* **2010**, *9*, 205.
- (136) Li, G.; Shrotriya, V.; Huang, J. S.; Yao, Y.; Moriarty, T.; Emery, K.; Yang, Y. *Nat. Mater.* **2005**, *4*, 864.
- (137) Huynh, W. U.; Dittmer, J. J.; Alivisatos, A. P. *Science* **2002**, *295*, 2425.
- (138) Khaselev, O.; Turner, J. A. *Science* **1998**, *280*, 425.
- (139) Kim, J. Y.; Lee, K.; Coates, N. E.; Moses, D.; Nguyen, T. Q.; Dante, M.; Heeger, A. J. *Science* **2007**, *317*, 222.

- (140) Lee, M. M.; Teuscher, J.; Miyasaka, T.; Murakami, T. N.; Snaith, H. J. *Science* **2012**, 338, 643.
- (141) Ozgur, U.; Alivov, Y. I.; Liu, C.; Teke, A.; Reshchikov, M. A.; Dogan, S.; Avrutin, V.; Cho, S. J.; Morkoc, H. *J. Appl. Phys.* **2005**, 98.
- (142) Wang, Z. L.; Song, J. H. *Science* **2006**, 312, 242.
- (143) Bernardini, F.; Fiorentini, V.; Vanderbilt, D. *Phys. Rev. B* **1997**, 56, 10024.
- (144) Park, S. E.; Shrouf, T. R. *J. Appl. Phys.* **1997**, 82, 1804.
- (145) Wang, X. D.; Song, J. H.; Liu, J.; Wang, Z. L. *Science* **2007**, 316, 102.
- (146) Fan, F. R.; Tian, Z. Q.; Wang, Z. L. *Nano Energy* **2012**, 1, 328.
- (147) Fan, F. R.; Lin, L.; Zhu, G.; Wu, W. Z.; Zhang, R.; Wang, Z. L. *Nano Lett.* **2012**, 12, 3109.
- (148) Wang, Z. L. *ACS Nano* **2013**, 7, 9533.
- (149) Wang, Z. L.; Chen, J.; Lin, L. *Energy Environ. Sci.* **2015**, 8, 2250.
- (150) Snyder, G. J.; Toberer, E. S. *Nat. Mater.* **2008**, 7, 105.
- (151) Venkatasubramanian, R.; Siivola, E.; Colpitts, T.; O'Quinn, B. *Nature* **2001**, 413, 597.
- (152) Hochbaum, A. I.; Chen, R. K.; Delgado, R. D.; Liang, W. J.; Garnett, E. C.; Najarian, M.; Majumdar, A.; Yang, P. D. *Nature* **2008**, 451, 163.
- (153) Hsu, K. F.; Loo, S.; Guo, F.; Chen, W.; Dyck, J. S.; Uher, C.; Hogan, T.; Polychroniadis, E. K.; Kanatzidis, M. G. *Science* **2004**, 303, 818.
- (154) Poudel, B.; Hao, Q.; Ma, Y.; Lan, Y. C.; Minnich, A.; Yu, B.; Yan, X. A.; Wang, D. Z.; Muto, A.; Vashaee, D.; Chen, X. Y.; Liu, J. M.; Dresselhaus, M. S.; Chen, G.; Ren, Z. F. *Science* **2008**, 320, 634.
- (155) Lu, X.; Wang, P.; Niyato, D.; Kim, D. I.; Han, Z. *IEEE Commun. Surv. Tut.* **2015**, 17, 757.
- (156) Le, T.; Mayaram, K.; Fiez, T. *IEEE J. Solid-St. Circ.* **2008**, 43, 1287.
- (157) Nasir, A. A.; Zhou, X. Y.; Durrani, S.; Kennedy, R. A. *IEEE Trans. Wireless Commun.* **2013**, 12, 3622.
- (158) Fan, F. R.; Tang, W.; Wang, Z. L. *Adv. Mater.* **2016**, 28, 4283.
- (159) Chen, J.; Yang, J.; Li, Z. L.; Fan, X.; Zi, Y. L.; Jing, Q. S.; Guo, H. Y.; Wen, Z.; Pradel, K. C.; Niu, S. M.; Wang, Z. L. *ACS Nano* **2015**, 9, 3324.
- (160) Zhu, G.; Su, Y. J.; Bai, P.; Chen, J.; Jing, Q. S.; Yang, W. Q.; Wang, Z. L. *ACS Nano* **2014**, 8, 6031.
- (161) Su, Y. J.; Wen, X. N.; Zhu, G.; Yang, J.; Chen, J.; Bai, P.; Wu, Z. M.; Jiang, Y. D.; Wang, Z. L. *Nano Energy* **2014**, 9, 186.
- (162) Lin, Z. H.; Cheng, G.; Lin, L.; Lee, S.; Wang, Z. L. *Angew. Chem. Int. Ed.* **2013**, 52, 12545.

- (163) Lin, Z. H.; Cheng, G.; Wu, W. Z.; Pradel, K. C.; Wang, Z. L. *ACS Nano* **2014**, *8*, 6440.
- (164) Siria, A.; Poncharal, P.; Bianco, A. L.; Fulcrand, R.; Blase, X.; Purcell, S. T.; Bocquet, L. *Nature* **2013**, *494*, 455.
- (165) Feng, J.; Graf, M.; Liu, K.; Ovchinnikov, D.; Dumcenco, D.; Heiranian, M.; Nandigana, V.; Aluru, N. R.; Kis, A.; Radenovic, A. *Nature* **2016**, *536*, 197.
- (166) Jiaqing, X.; Meng-Fang, L.; Jiangxin, W.; Long, G. S.; Kaushik, P.; See, L. P. *Adv. Energy Mater.* **2017**, *7*, 1701243.
- (167) Zong-Hong, L.; Gang, C.; Sangmin, L.; C., P. K.; Lin, W. Z. *Adv. Mater.* **2014**, *26*, 4690.
- (168) Osman, M. H.; Shah, A. A.; Walsh, F. C. *Biosens. Bioelectron.* **2010**, *26*, 953.
- (169) Osman, M. H.; Shah, A. A.; Walsh, F. C. *Biosens. Bioelectron.* **2011**, *26*, 3087.
- (170) Williams, C. B.; Yates, R. B. *Sens. Actuators A Phys.* **1996**, *52*, 8.
- (171) Chaudhuri, S. K.; Lovley, D. R. *Nat. Biotechnol.* **2003**, *21*, 1229.
- (172) Logan, B. E. *Nat. Rev. Microbiol.* **2009**, *7*, 375.
- (173) Logan, B. E.; Hamelers, B.; Rozendal, R. A.; Schrorder, U.; Keller, J.; Freguia, S.; Aelterman, P.; Verstraete, W.; Rabaey, K. *Environ. Sci. Technol.* **2006**, *40*, 5181.
- (174) Lewis, N. S.; Nocera, D. G. *Proc. Natl. Acad. Sci. U.S.A.* **2007**, *104*, 20142.
- (175) Nocera, D. G. *Acc. Chem. Res.* **2012**, *45*, 767.
- (176) Reece, S. Y.; Hamel, J. A.; Sung, K.; Jarvi, T. D.; Esswein, A. J.; Pijpers, J. J. H.; Nocera, D. G. *Science* **2011**, *334*, 645.
- (177) Leech, D.; Kavanagh, P.; Schuhmann, W. *Electrochimica Acta* **2012**, *84*, 223.
- (178) Ding, T.; Liu, K.; Li, J.; Xue, G.; Chen, Q.; Huang, L.; Hu, B.; Zhou, J. *Adv. Funct. Mater.* **2017**, *27*.
- (179) Kim, S. H.; Haines, C. S.; Li, N.; Kim, K. J.; Mun, T. J.; Choi, C.; Di, J.; Oh, Y. J.; Oviedo, J. P.; Bykova, J.; Fang, S.; Jiang, N.; Liu, Z.; Wang, R.; Kumar, P.; Qiao, R.; Priya, S.; Cho, K.; Kim, M.; Lucas, M. S.; Drummy, L. F.; Maruyama, B.; Lee, D. Y.; Lepró, X.; Gao, E.; Albarq, D.; Ovalle-Robles, R.; Kim, S. J.; Baughman, R. H. *Science* **2017**, *357*, 773.
- (180) Král, P.; Shapiro, M. *Phys. Rev. Lett.* **2001**, *86*, 131.
- (181) Ghosh, S.; Sood, A. K.; Kumar, N. *Science* **2003**, *299*, 1042.
- (182) Lee, S. H.; Kim, D.; Kim, S.; Han, C.-S. *Appl. Phys. Lett.* **2011**, *99*, 104103.
- (183) Liu, J. W.; Dai, L. M.; Baur, J. W. *J. Appl. Phys.* **2007**, *101*, 064312.
- (184) Dhiman, P.; Yavari, F.; Mi, X.; Gullapalli, H.; Shi, Y.; Ajayan, P. M.; Koratkar, N. *Nano Lett.* **2011**, *11*, 3123.

- (185) Baughman, R. H.; Cui, C.; Zakhidov, A. A.; Iqbal, Z.; Barisci, J. N.; Spinks, G. M.; Wallace, G. G.; Mazzoldi, A.; De Rossi, D.; Rinzler, A. G.; Jaschinski, O.; Roth, S.; Kertesz, M. *Science* **1999**, *284*, 1340.
- (186) Solomon, P. M.; Price, P. J.; Frank, D. J.; La Tulipe, D. C. *Phys. Rev. Lett.* **1989**, *63*, 2508.
- (187) Gramila, T. J.; Eisenstein, J. P.; MacDonald, A. H.; Pfeiffer, L. N.; West, K. W. *Phys. Rev. Lett.* **1991**, *66*, 1216.
- (188) Jauho, A.-P.; Smith, H. *Phys. Rev. B* **1993**, *47*, 4420.
- (189) Bønsager, M. C.; Flensberg, K.; Yu-Kuang Hu, B.; MacDonald, A. H. *Phys. Rev. B* **1998**, *57*, 7085.
- (190) Talyanskii, V. I.; Shilton, J. M.; Pepper, M.; Smith, C. G.; Ford, C. J. B.; Linfield, E. H.; Ritchie, D. A.; Jones, G. A. C. *Phys. Rev. B* **1997**, *56*, 15180.
- (191) Rao, A. M.; Eklund, P. C.; Bandow, S.; Thess, A.; Smalley, R. E. *Nature* **1997**, *388*, 257.
- (192) Ghosh, S.; Sood, A. K.; Ramaswamy, S.; Kumar, N. *Phys. Rev. B* **2004**, *70*, 205423.
- (193) Sood, A. K.; Ghosh, S.; Das, A. *Pramana* **2005**, *65*, 571.
- (194) Lee, S. H.; Jung, Y.; Kim, S.; Han, C.-S. *Appl. Phys. Lett.* **2013**, *102*, 063116.
- (195) Cohen, A. E. *Science* **2003**, *300*, 1235.
- (196) Persson, B. N. J.; Tartaglino, U.; Tosatti, E.; Ueba, H. *Phys. Rev. B* **2004**, *69*, 235410.
- (197) Helmholtz, H. *Ann. Phys. (Berl.)* **1879**, *243*, 337.
- (198) Odelius, M.; Bernasconi, M.; Parrinello, M. *Phys. Rev. Lett.* **1997**, *78*, 2855.
- (199) Zangi, R.; Mark, A. E. *Phys. Rev. Lett.* **2003**, *91*, 025502.
- (200) Ghosh, S.; Gadagkar, V.; Sood, A. K. *Chem. Phys. Lett.* **2005**, *406*, 10.
- (201) Olthuis, W.; Schippers, B.; Eijkel, J.; van den Berg, A. *Sens. Actuators B Chem.* **2005**, *111-112*, 385.
- (202) Tan, Z. Q.; Yamamoto, K.; Qiu, N.; Hashishin, T.; Ohara, S. *Appl. Phys. Lett.* **2014**, *105*, 033906.
- (203) Yin, J.; Zhang, Z.; Li, X.; Zhou, J.; Guo, W. *Nano Lett.* **2012**, *12*, 1736.
- (204) Lee, S. H.; Kang, Y. B.; Jung, W.; Jung, Y.; Kim, S.; Noh, H. *Nanoscale Res. Lett.* **2013**, *8*, 487.
- (205) Huang, W.; Wang, G.; Gao, F.; Qiao, Z.; Wang, G.; Chen, M.; Deng, Y.; Tao, L.; Zhao, Y.; Fan, X.; Sun, L. *J. Phys. Chem. C* **2014**, *118*, 8783.
- (206) Huang, W.; Wang, G.; Gao, F.; Qiao, Z.; Wang, G.; Tao, L.; Chen, M.; Yu, F.; Yang, H.; Sun, L. *Nanoscale* **2014**, *6*, 3921.
- (207) Liu, Z.; Zheng, K. H.; Hu, L. J.; Liu, J.; Qiu, C. Y.; Zhou, H. Q.; Huang, H. B.; Yang, H. F.; Li, M.; Gu, C. Z.; Xie, S. S.; Qiao, L. J.; Sun, L. F. *Adv. Mater.* **2010**, *22*, 999.

- (208) Liu, Z.; Hu, L. J.; Liu, J.; Qiu, C. Y.; Zhou, H. Q.; Hashim, D. P.; Shi, G.; Peng, C.; Najmaei, S.; Sun, L. F.; Lou, J.; Ajayan, P. M. *Nano Lett.* **2011**, *11*, 5117.
- (209) Yang, X.; Feng, M.; Chen, Y.; Lu, H.; Zhou, X. *Theoretical and Applied Mechanics Letters* **2013**, *3*, 032008.
- (210) Park, H. G.; Jung, Y. *Chem. Soc. Rev.* **2014**, *43*, 565.
- (211) Král, P.; Wang, B. *Chem. Rev.* **2013**, *113*, 3372.
- (212) Chan, Y.; Hill, J. M. *J. Membr. Sci.* **2011**, *372*, 57.
- (213) Kyakuno, H.; Matsuda, K.; Yahiro, H.; Inami, Y.; Fukuoka, T.; Miyata, Y.; Yanagi, K.; Maniwa, Y.; Kataura, H.; Saito, T.; Yumura, M.; Iijima, S. *J. Chem. Phys.* **2011**, *134*, 244501.
- (214) Su, J.; Guo, H. *J. Chem. Phys.* **2011**, *134*, 244513.
- (215) Cambré, S.; Schoeters, B.; Luyckx, S.; Goovaerts, E.; Wenseleers, W. *Phys. Rev. Lett.* **2010**, *104*, 207401.
- (216) Wu, K.; Zhou, B.; Xiu, P.; Qi, W.; Wan, R.; Fang, H. *J. Chem. Phys.* **2010**, *133*, 204702.
- (217) Dzubiella, J.; Hansen, J.-P. *J. Chem. Phys.* **2005**, *122*, 234706.
- (218) Waghe, A.; Rasaiah, J. C.; Hummer, G. *J. Chem. Phys.* **2002**, *117*, 10789.
- (219) Noon, W. H.; Ausman, K. D.; Smalley, R. E.; Ma, J. *Chem. Phys. Lett.* **2002**, *355*, 445.
- (220) Mashl, R. J.; Joseph, S.; Aluru, N. R.; Jakobsson, E. *Nano Lett.* **2003**, *3*, 589.
- (221) Vaitheeswaran, S.; Rasaiah, J. C.; Hummer, G. *J. Chem. Phys.* **2004**, *121*, 7955.
- (222) Koga, K.; Gao, G. T.; Tanaka, H.; Zeng, X. C. *Nature* **2001**, *412*, 802.
- (223) Agrawal, K. V.; Shimizu, S.; Drahushuk, L. W.; Kilcoyne, D.; Strano, M. S. *Nat. Nanotechnol.* **2017**, *12*, 267.
- (224) Chakraborty, S.; Kumar, H.; Dasgupta, C.; Maiti, P. K. *Acc. Chem. Res.* **2017**, *50*, 2139.
- (225) Cheng, H. H.; Huang, Y. X.; Shi, G. Q.; Jiang, L.; Qu, L. T. *Acc. Chem. Res.* **2017**, *50*, 1663.
- (226) Zhao, Y.; Song, L.; Deng, K.; Liu, Z.; Zhang, Z.; Yang, Y.; Wang, C.; Yang, H.; Jin, A.; Luo, Q.; Gu, C.; Xie, S.; Sun, L. *Adv. Mater.* **2008**, *20*, 1772.
- (227) Chen, M.; Yu, F.; Hu, L.; Sun, L. *Sci. Bull.* **2012**, *57*, 181.
- (228) Hummer, G.; Rasaiah, J. C.; Noworyta, J. P. *Nature* **2001**, *414*, 188.
- (229) Berezhkovskii, A.; Hummer, G. *Phys. Rev. Lett.* **2002**, *89*, 064503.
- (230) Yuan, Q.; Zhao, Y.-P. *J. Am. Chem. Soc.* **2009**, *131*, 6374.
- (231) Xu, B.; Chen, X. *Phys. Chem. Chem. Phys.* **2013**, *15*, 1164.

- (232) Li, J.; Gong, X.; Lu, H.; Li, D.; Fang, H.; Zhou, R. *Proc. Natl. Acad. Sci. U.S.A.* **2007**, *104*, 3687.
- (233) Gong, X.; Li, J.; Lu, H.; Wan, R.; Li, J.; Hu, J.; Fang, H. *Nat. Nanotechnol.* **2007**, *2*, 709.
- (234) Wang, B. Y.; Kral, P. *J. Am. Chem. Soc.* **2006**, *128*, 15984.
- (235) Wang, B. Y.; Kral, P. *Phys. Rev. Lett.* **2008**, *101*.
- (236) Choi, W.; Lee, C. Y.; Ham, M. H.; Shimizu, S.; Strano, M. S. *J. Am. Chem. Soc.* **2011**, *133*, 203.
- (237) Choi, W.; Ulissi, Z. W.; Shimizu, S. F. E.; Bellisario, D. O.; Ellison, M. D.; Strano, M. S. *Nat. Commun.* **2013**, *4*, 2397.
- (238) Lee, C. Y.; Choi, W.; Han, J. H.; Strano, M. S. *Science* **2010**, *329*, 1320.
- (239) Lu, D.; Li, Y.; Rotkin, S. V.; Ravaioli, U.; Schulten, K. *Nano Lett.* **2004**, *4*, 2383.
- (240) Maiti, A.; Andzelm, J.; Tanpipat, N.; von Allmen, P. *Phys. Rev. Lett.* **2001**, *87*, 155502.
- (241) Su, J.; Zhao, Y.; Fang, C.; Bilal Ahmed, S.; Shi, Y. *Phys. Chem. Chem. Phys.* **2017**, *19*, 22406.
- (242) Jiaye, S.; Keda, Y. *Nanotechnology* **2016**, *27*, 095701.
- (243) Lu, H.; Nie, X.; Wu, F.; Zhou, X.; Kou, J.; Xu, Y.; Liu, Y. *J. Chem. Phys.* **2012**, *136*, 174511.
- (244) Xiu, P.; Zhou, B.; Qi, W.; Lu, H.; Tu, Y.; Fang, H. *J. Am. Chem. Soc.* **2009**, *131*, 2840.
- (245) Zhou, X.; Wu, F.; Liu, Y.; Kou, J.; Lu, H.; Lu, H. *Phys. Rev. E* **2015**, *92*, 053017.
- (246) Zhou, X.; Wu, F.; Kou, J.; Nie, X.; Liu, Y.; Lu, H. *J. Phys. Chem. B* **2013**, *117*, 11681.
- (247) Kou, J.; Zhou, X.; Lu, H.; Xu, Y.; Wu, F.; Fan, J. *Soft Matter* **2012**, *8*, 12111.
- (248) Qiu, H.; Shen, R.; Guo, W. *Nano Research* **2011**, *4*, 284.
- (249) Kou, J.; Mei, M.; Lu, H.; Wu, F.; Fan, J. *Phys. Rev. E* **2012**, *85*, 056301.
- (250) Dzubiella, J.; Allen, R. J.; Hansen, J.-P. *J. Chem. Phys.* **2004**, *120*, 5001.
- (251) Yu, H. Q.; Li, H.; Zhang, J. X.; Liu, X. F.; Liew, K. M. *Carbon* **2010**, *48*, 417.
- (252) Li, X.-P.; Kong, G.-P.; Zhang, X.; He, G.-W. *Appl. Phys. Lett.* **2013**, *103*, 143117.
- (253) Su, J.; Guo, H. *J. Phys. Chem. B* **2012**, *116*, 5925.
- (254) Quincke, G. *Ann. Phys. (Berl.)* **1859**, *183*, 1.
- (255) Quincke, G. *Ann. Phys. (Berl.)* **1860**, *186*, 38.
- (256) Kazaoui, S.; Minami, N.; Matsuda, N.; Kataura, H.; Achiba, Y. *Appl. Phys. Lett.* **2001**, *78*, 3433.

- (257) Xue, G. B.; Xu, Y.; Ding, T. P.; Li, J.; Yin, J.; Fei, W. W.; Cao, Y. Z.; Yu, J.; Yuan, L. Y.; Gong, L.; Chen, J.; Deng, S. Z.; Zhou, J.; Guo, W. L. *Nat. Nanotechnol.* **2017**, *12*, 317.
- (258) Li, J.; Liu, K.; Xue, G.; Ding, T.; Yang, P.; Chen, Q.; Shen, Y.; Li, S.; Feng, G.; Shen, A. *Nano Energy* **2018**, *48*, 211.
- (259) Delgado, A. V.; Gonzalez-Caballero, F.; Hunter, R. J.; Koopal, L. K.; Lyklema, J. *J. Colloid Interface Sci.* **2007**, *309*, 194.
- (260) van der Heyden, F. H. J.; Bonthuis, D. J.; Stein, D.; Meyer, C.; Dekker, C. *Nano Lett.* **2007**, *7*, 1022.
- (261) Guo, W.; Cheng, C.; Wu, Y. Z.; Jiang, Y. A.; Gao, J.; Li, D.; Jiang, L. *Adv. Mater.* **2013**, *25*, 6064.
- (262) Hon, K. C.; Zhao, C. L.; Yang, C.; Low, S. C. *Appl. Phys. Lett.* **2012**, *101*.
- (263) Sood, A. K.; Ghosh, S. *Phys. Rev. Lett.* **2004**, *93*, 086601
- (264) Yin, J.; Zhou, J. X.; Li, X. M.; Chen, Y. Q.; Tai, G. A.; Guo, W. L. *Appl. Phys. Lett.* **2011**, *99*, 073103.
- (265) Sarkar, S. S.; Ghosh, S.; Sood, A. K. *Sens. Actuators A Phys.* **2007**, *137*, 209.
- (266) Satheesh, U.; Prakash, P.; Devaprakasam, D. *J. Appl. Phys.* **2017**, *121*, 025501.
- (267) Li, X. M.; Yin, J.; Zhou, J. X.; Wang, Q.; Guo, W. L. *Appl. Phys. Lett.* **2012**, *100*, 183108.
- (268) Choi, W.; Hong, S.; Abrahamson, J. T.; Han, J.-H.; Song, C.; Nair, N.; Baik, S.; Strano, M. S. *Nature Materials* **2010**, *9*, 423.
- (269) Choi, W.; Abrahamson, J. T.; Strano, J. M.; Strano, M. S. *Materials Today* **2010**, *13*, 22.
- (270) Walther, D. C.; Ahn, J. *Progress in Energy and Combustion Science* **2011**, *37*, 583.
- (271) Singh, S.; Mun, H.; Lee, S.; Kim, S. W.; Baik, S. *Advanced Materials* **2017**, *29*, 1701988.
- (272) Taehan, Y.; Hayoung, H.; Dong-Cheol, J.; Kang Yeol, L.; Jongsup, H.; Changsik, S.; Wonjoon, C. *Nanotechnology* **2014**, *25*, 445403.
- (273) Lee, K. Y.; Hwang, H.; Shin, D.; Choi, W. *J. Mater. Chem. A* **2015**, *3*, 5457.
- (274) Lee, K. Y.; Hwang, H.; Shin, D.; Choi, W. *Nanoscale* **2015**, *7*, 17071.
- (275) Jain, S.; Park, W.; Chen, Y. P.; Qiao, L. *J. Appl. Phys.* **2016**, *120*, 174902.
- (276) Hwang, H.; Shin, D.; Yeo, T.; Choi, W. *Adv. Mater. Interf.* **2017**, *4*, 1600908.
- (277) Abrahamson, J. T.; Song, C.; Hu, J. H.; Forman, J. M.; Mahajan, S. G.; Nair, N.; Choi, W.; Lee, E.-J.; Strano, M. S. *Chemistry of Materials* **2011**, *23*, 4557.
- (278) Walia, S.; Weber, R.; Sriram, S.; Bhaskaran, M.; Latham, K.; Zhuiykov, S.; Kalantar-zadeh, K. *Energy & Environmental Science* **2011**, *4*, 3558.

- (279) Walia, S.; Weber, R.; Latham, K.; Petersen, P.; Abrahamson, J. T.; Strano, M. S.; Kalantar-zadeh, K. *Advanced Functional Materials* **2011**, *21*, 2072.
- (280) Hong, S.; Kim, W.; Jeon, S.-J.; Lim, S. C.; Lee, H.-J.; Hyun, S.; Lee, Y. H.; Baik, S. *The Journal of Physical Chemistry C* **2013**, *117*, 913.
- (281) Walia, S.; Balendhran, S.; Yi, P.; Yao, D.; Zhuiykov, S.; Pannirselvam, M.; Weber, R.; Strano, M. S.; Bhaskaran, M.; Sriram, S.; Kalantar-zadeh, K. *The Journal of Physical Chemistry C* **2013**, *117*, 9137.
- (282) Lee, K. Y.; Hwang, H.; Choi, W. *ACS Applied Materials & Interfaces* **2014**, *6*, 15575.
- (283) Hwang, H.; Yeo, T.; Um, J.-E.; Lee, K. Y.; Kim, H.-S.; Han, J.-H.; Kim, W.-J.; Choi, W. *Nanoscale Res Lett* **2014**, *9*, 536.
- (284) Taehan, Y.; Hayoung, H.; Yonghwan, C.; Dongjoon, S.; Wonjoon, C. *Nanotechnology* **2015**, *26*, 305402.
- (285) Lee, K. Y.; Hwang, H.; Choi, W. *Small* **2015**, *11*, 4762.
- (286) Shin, D.; Hwang, H.; Yeo, T.; Seo, B.; Choi, W. *ACS Appl. Mater. Interfaces* **2016**, *8*, 31042.
- (287) Taehan, Y.; Hayoung, H.; Dongjoon, S.; Byungseok, S.; Wonjoon, C. *Nanotechnology* **2017**, *28*, 065403.
- (288) Hong, S.; Hong, S.; Lee, T.-R.; Kim, Y.-J.; Ryu, C.; Baik, S. *Energy & Environmental Science* **2011**, *4*, 2045.
- (289) Yang, G.; Wu, Z.; Wang, W.; Zhang, Z.; Hu, Z. *Nano Energy* **2017**, *42*, 195.
- (290) Abrahamson, J. T.; Choi, W.; Schonenbach, N. S.; Park, J.; Han, J.-H.; Walsh, M. P.; Kalantar-zadeh, K.; Strano, M. S. *ACS Nano* **2011**, *5*, 367.
- (291) Abrahamson, J. T.; Strano, M. S. *The Journal of Physical Chemistry Letters* **2010**, *1*, 3514.
- (292) Liu, A. T.; Kunai, Y.; Liu, P.; Kaplan, A.; Cottrill, A. L.; Smith-Dell, J. S.; Strano, M. S. *Advanced Materials* **2016**, *28*, 9752.
- (293) Kunai, Y.; Liu, A. T.; Cottrill, A. L.; Koman, V. B.; Liu, P.; Kozawa, D.; Gong, X.; Strano, M. S. *J. Am. Chem. Soc.* **2017**, *139*, 15328.
- (294) Jain, S.; Mo, G.; Qiao, L. *J. Appl. Phys.* **2017**, *121*, 054902.
- (295) Abrahamson, J. T.; Sempere, B.; Walsh, M. P.; Forman, J. M.; Şen, F.; Şen, S.; Mahajan, S. G.; Paulus, G. L. C.; Wang, Q. H.; Choi, W.; Strano, M. S. *ACS Nano* **2013**, *7*, 6533.
- (296) Baxendale, M.; Lim, K. G.; Amaratunga, G. A. J. *Phys. Rev. B* **2000**, *61*, 12705.
- (297) Walia, S.; Weber, R.; Balendhran, S.; Yao, D.; Abrahamson, J. T.; Zhuiykov, S.; Bhaskaran, M.; Sriram, S.; Strano, M. S.; Kalantar-zadeh, K. *Chem Commun* **2012**, *48*, 7462.
- (298) Marcus, R. A. *J. Chem. Phys.* **1956**, *24*, 966.

- (299) Marcus, R. A. *Reviews of Modern Physics* **1993**, *65*, 599.
- (300) Zhao, F.; Cheng, H.; Zhang, Z.; Jiang, L.; Qu, L. *Adv. Mater.* **2015**, *27*, 4351.
- (301) Zhao, F.; Liang, Y.; Cheng, H.; Jiang, L.; Qu, L. *Energy Environ. Sci.* **2016**, *9*, 912.
- (302) Kim, S.; Zhou, S.; Hu, Y.; Acik, M.; Chabal, Y. J.; Berger, C.; de Heer, W.; Bongiorno, A.; Riedo, E. *Nat. Mater.* **2012**, *11*, 544.
- (303) Huang, L.; Pei, J.; Jiang, H.; Li, C.; Hu, X. *Mater. Res. Bull.* **2018**, *97*, 96.
- (304) Zhao, F.; Wang, L.; Zhao, Y.; Qu, L.; Dai, L. *Adv. Mater.* **2017**, *29*, 1604972.
- (305) Liang, Y.; Zhao, F.; Cheng, Z.; Zhou, Q.; Shao, H.; Jiang, L.; Qu, L. *Nano Energy* **2017**, *32*, 329.
- (306) Huang, Y.; Cheng, H.; Shi, G.; Qu, L. *ACS Appl. Mater. Interfaces* **2017**, *9*, 38170.
- (307) Liu, K.; Yang, P.; Li, S.; Li, J.; Ding, T.; Xue, G.; Chen, Q.; Feng, G.; Zhou, J. *Angew. Chem. Int. Ed.* **2016**, *55*, 8003.
- (308) Xue, J.; Zhao, F.; Hu, C.; Zhao, Y.; Luo, H.; Dai, L.; Qu, L. *Adv. Funct. Mater.* **2016**, *26*, 8784.
- (309) He, S.; Zhang, Y.; Qiu, L.; Zhang, L.; Xie, Y.; Pan, J.; Chen, P.; Wang, B.; Xu, X.; Hu, Y. *Adv. Mater.* **2018**, *30*, 1707635.
- (310) Xu, T.; Ding, X.; Shao, C.; Song, L.; Lin, T.; Gao, X.; Xue, J.; Zhang, Z.; Qu, L. *Small* **2018**, *14*, 1704473.
- (311) Liang, Y.; Zhao, F.; Cheng, Z.; Deng, Y.; Xiao, Y.; Cheng, H.; Zhang, P.; Huang, Y.; Shao, H. B.; Qu, L. *Energy Environ. Sci.* **2018**.
- (312) Tissaphern, M.; Jiyong, O.; Mikhail, K.; Eddie Chi Wah, F.; Mei, Z.; Shaoli, F.; Ray, H. B.; John, D. W. M. *Smart Mater. Struct.* **2007**, *16*, S243.
- (313) Mirfakhrai, T.; Oh, J.; Kozlov, M.; Fang, S.; Zhang, M.; Baughman, R. H.; Madden, J. D. In *Artificial Muscle Actuators Using Electroactive Polymers*; Vincenzini, P., BarCohen, Y., Carpi, F., Eds.; Trans Tech Publications Ltd: Durnten-Zurich, 2009; Vol. 61, p 65.
- (314) Mirfakhrai, T.; Oh, J. Y.; Kozlov, M.; Fang, S. L.; Zhang, M.; Baughman, R. H.; Madden, J. D. In *Advances in Science and Technology*; Trans Tech Publ: 2008; Vol. 61, p 65.
- (315) Tanaka, Y.; Hirana, Y.; Niidome, Y.; Kato, K.; Saito, S.; Nakashima, N. *Angew. Chem. Int. Ed.* **2009**, *48*, 7655.
- (316) Zhang, M.; Atkinson, K. R.; Baughman, R. H. *Science* **2004**, *306*, 1358.
- (317) Krupenkin, T.; Taylor, J. A. *Nat. Commun.* **2011**, *2*, 448.
- (318) Moon, J. K.; Jeong, J.; Lee, D.; Pak, H. K. *Nat. Commun.* **2013**, *4*, 1487.
- (319) Liu, K.; Zhou, Y.; Yuan, F.; Mo, X.; Yang, P.; Chen, Q.; Li, J.; Ding, T.; Zhou, J. *Angew. Chem. Int. Ed.* **2016**, *128*, 16096.

- (320) Allen J. Bard, L. R. F. *Electrochemical Methods: Fundamentals and Applications*; 2 ed.; Wiley, 2000.
- (321) Carl H. Hamann, A. H., Wolf Vielstich *Electrochemistry (2nd Edition)*; Wiley-VCH, 2007.
- (322) Booth, F. *J. Chem. Phys.* **1951**, *19*, 391.
- (323) Booth, F. *J. Chem. Phys.* **1955**, *23*, 453.
- (324) Wang, H. N.; Pilon, L. *J Phys Chem C* **2011**, *115*, 16711.
- (325) Xu, B. X.; Liu, L.; Lim, H.; Qiao, Y.; Chen, X. *Nano Energy* **2012**, *1*, 805.
- (326) Qiao, Y.; Punyamurtual, V. K.; Han, A.; Lim, H. *J. Power Sources* **2008**, *183*, 403.
- (327) Lim, H.; Lu, W. Y.; Qiao, Y. *Appl. Phys. Lett.* **2012**, *101*, 063902.
- (328) Lim, H.; Zhao, C.; Qiao, Y. *Phys. Chem. Chem. Phys.* **2014**, *16*, 12728.
- (329) Lim, H.; Lu, W. Y.; Chen, X.; Qiao, Y. *Nanotechnology* **2013**, *24*.
- (330) Lim, H.; Shi, Y.; Wang, M.; Qiao, Y. *Appl. Phys. Lett.* **2015**, *106*, 223901.
- (331) Lim, H.; Lu, W. Y.; Chen, X.; Qiao, Y. *Int. J. Electrochem. Sci.* **2012**, *7*, 2577.
- (332) Lim, H.; Shi, Y.; Qiao, Y. *Int. J. Green Energy* **2018**, *15*, 53.
- (333) Lim, H.; Shi, Y.; Qiao, Y. *Appl. Phys. A* **2016**, *122*.
- (334) Al-zubaidi, A.; Ji, X. X.; Yu, J. *Sustain. Energ. Fuels* **2017**, *1*, 1457.
- (335) Rica, R. A.; Ziano, R.; Salerno, D.; Mantegazza, F.; van Roij, R.; Brogioli, D. *Entropy* **2013**, *15*, 1388.
- (336) Jia, Z. J.; Wang, B. G.; Song, S. Q.; Fan, Y. S. *Renew. Sust. Energ. Rev.* **2014**, *31*, 91.
- (337) Hartel, A.; Janssen, M.; Weingarh, D.; Presser, V.; van Roij, R. *Energy Environ. Sci.* **2015**, *8*, 2396.
- (338) Wang, X.; Feng, S.-P. *Frontiers in Mechanical Engineering* **2017**, *3*, 20.
- (339) Boon, N.; van Roij, R. *Mol. Phys.* **2011**, *109*, 1229.
- (340) Rica, R. A.; Ziano, R.; Salerno, D.; Mantegazza, F.; Bazant, M. Z.; Brogioli, D. *Electrochim. Acta* **2013**, *92*, 304.
- (341) Lian, C.; Kong, X.; Liu, H. L.; Wu, J. Z. *J. Phys. Condens. Matter* **2016**, *28*.
- (342) Janssen, M.; Hartel, A.; van Roij, R. *Phys. Rev. Lett.* **2014**, *113*.
- (343) Stout, R. F.; Khair, A. S. *Phys. Rev. E* **2017**, *96*.
- (344) Bonetti, M.; Nakamae, S.; Huang, B. T.; Salez, T. J.; Wiertel-Gasquet, C.; Roger, M. *J. Chem. Phys.* **2015**, *142*.
- (345) Jiao, F.; Naderi, A.; Zhao, D.; Schlueter, J.; Shahi, M.; Sundstrom, J.; Granberg, H.; Edberg, J.; Ail, U.; Brill, J.; Lindstrom, T.; Berggren, M.; Crispin, X. *J. Mater. Chem. A* **2017**, *5*, 16883.

- (346) Zhao, D.; Wang, H.; Khan, Z. U.; Chen, J. C.; Gabrielsson, R.; Jonsson, M. P.; Berggren, M.; Crispin, X. *Energy Environ. Sci.* **2016**, *9*, 1450.
- (347) Wang, H.; Zhao, D.; Khan, Z. U.; Puzinas, S.; Jonsson, M. P.; Berggren, M.; Crispin, X. *Adv. Electron. Mater.* **2017**, *3*, 1700013.
- (348) Wang, H.; Ail, U.; Gabrielsson, R.; Berggren, M.; Crispin, X. *Adv. Energy Mater.* **2015**, *5*.
- (349) Arico, A. S.; Bruce, P.; Scrosati, B.; Tarascon, J.-M.; Van Schalkwijk, W. *Nat. Mater.* **2005**, *4*, 366.
- (350) Simon, P.; Gogotsi, Y. *Nat. Mater.* **2008**, *7*, 845.
- (351) Wang, H. L.; Casalongue, H. S.; Liang, Y. Y.; Dai, H. J. *J. Am. Chem. Soc.* **2010**, *132*, 7472.
- (352) Raccichini, R.; Varzi, A.; Passerini, S.; Scrosati, B. *Nat. Mater.* **2015**, *14*, 271.
- (353) Kaempgen, M.; Chan, C. K.; Ma, J.; Cui, Y.; Gruner, G. *Nano Lett.* **2009**, *9*, 1872.
- (354) Wang, J. J.; Feng, S. P.; Yang, Y.; Hau, N. Y.; Munro, M.; Ferreira-Yang, E.; Chen, G. *Nano Lett.* **2015**, *15*, 5784.
- (355) Yin, J.; Li, X.; Yu, J.; Zhang, Z.; Zhou, J.; Guo, W. *Nat. Nanotechnol.* **2014**, *9*, 378.
- (356) Gorbachev, R. V.; Geim, A. K.; Katsnelson, M. I.; Novoselov, K. S.; Tudorovskiy, T.; Grigorieva, I. V.; MacDonald, A. H.; Morozov, S. V.; Watanabe, K.; Taniguchi, T.; Ponomarenko, L. A. *Nat. Phys.* **2012**, *8*, 896.
- (357) Weber, C. P.; Gedik, N.; Moore, J. E.; Orenstein, J.; Stephens, J.; Awschalom, D. D. *Nature* **2005**, *437*, 1330.
- (358) Price, A. S.; Savchenko, A. K.; Narozhny, B. N.; Allison, G.; Ritchie, D. A. *Science* **2007**, *316*, 99.
- (359) Nandi, D.; Finck, A. D. K.; Eisenstein, J. P.; Pfeiffer, L. N.; West, K. W. *Nature* **2012**, *488*, 481.
- (360) Shao, Q. F.; Jia, J. J.; Guan, Y. J.; He, X. D.; Zhang, X. P. *J. Chem. Phys.* **2016**, *144*, 124703.
- (361) Yin, J.; Zhang, Z.; Li, X.; Yu, J.; Zhou, J.; Chen, Y.; Guo, W. *Nat. Commun.* **2014**, *5*, 3582.
- (362) Lao, J.; He, Y.; Li, X.; Wu, F.; Yang, T.; Zhu, M.; Zhang, Y.; Sun, P.; Zhen, Z.; Cheng, B.; Zhu, H. *Nano Research* **2015**, *8*, 2467.
- (363) He, Y.; Lao, J.; Yang, T.; Li, X.; Zang, X.; Li, X.; Zhu, M.; Chen, Q.; Zhong, M.; Zhu, H. *Appl. Phys. Lett.* **2015**, *107*, 081605.
- (364) Tang, Q.; Wang, X.; Yang, P.; He, B. *Angew. Chem. Int. Ed.* **2016**, *55*, 5243.
- (365) Tang, Q.; Yang, P. *J. Mater. Chem. A* **2016**, *4*, 9730.
- (366) Zhong, H.; Wu, Z.; Li, X.; Xu, W.; Xu, S.; Zhang, S.; Xu, Z.; Chen, H.; Lin, S. *Carbon* **2016**, *105*, 199.

- (367) Zhang, Y.; Tang, Q.; He, B.; Yang, P. *J. Mater. Chem. A* **2016**, *4*, 13235.
- (368) Zhong, H.; Li, X.; Wu, Z.; Zhang, S.; Xu, Z.; Chen, H.; Lin, S. *Appl. Phys. Lett.* **2015**, *106*, 243903.
- (369) Li, X. M.; Shen, C.; Wang, Q.; Luk, C. M.; Li, B. W.; Yin, J.; Lau, S. P.; Guo, W. L. *Nano Energy* **2017**, *32*, 125.
- (370) Xu, Y. F.; Chen, P. N.; Zhang, J.; Xie, S. L.; Wan, F.; Deng, J.; Cheng, X. L.; Hu, Y. J.; Liao, M.; Wang, B. J.; Sun, X. M.; Peng, H. S. *Angew. Chem. Int. Ed.* **2017**, *56*, 12940.
- (371) Tan, J.; Duan, J.; Zhao, Y.; He, B.; Tang, Q. *Nano Energy* **2018**.
- (372) Okada, T.; Kalita, G.; Tanemura, M.; Yamashita, I.; Meyyappan, M.; Samukawa, S. *Appl. Phys. Lett.* **2018**, *112*, 023902.
- (373) Kim, J.; Lee, J.; Kim, S.; Jung, W. *ACS Appl. Mater. Interfaces* **2016**, *8*, 29877.
- (374) Wang, Y. L.; Duan, J. L.; Zhao, Y. Y.; Duan, Y. Y.; Tang, Q. W. *Nano Energy* **2017**, *41*, 293.
- (375) Wang, Y.; Duan, J.; Zhao, Y.; He, B.; Tang, Q. *Renew. Energy* **2018**, *125*, 995.
- (376) Kwak, S. S.; Lin, S.; Lee, J. H.; Ryu, H.; Kim, T. Y.; Zhong, H.; Chen, H.; Kim, S.-W. *ACS Nano* **2016**, *10*, 7297.
- (377) Zhong, H.; Xia, J.; Wang, F.; Chen, H.; Wu, H.; Lin, S. *Adv. Funct. Mater.* **2017**, *27*, 1604226.
- (378) Yang, S.; Su, Y.; Xu, Y.; Wu, Q.; Zhang, Y.; Raschke, M. B.; Ren, M.; Chen, Y.; Wang, J.; Guo, W. *arXiv preprints* **2018**, 1801.07878.
- (379) Yang, Z. C.; Halvorsen, E.; Dong, T. *Appl. Phys. Lett.* **2012**, *100*, 213905.
- (380) Kwon, S. H.; Park, J.; Kim, W. K.; Yang, Y.; Lee, E.; Han, C. J.; Park, S. Y.; Lee, J.; Kim, Y. S. *Energy Environ. Sci.* **2014**, *7*, 3279.
- (381) Park, J.; Song, S.; Shin, C.; Yang, Y.; Weber, S. A. L.; Sim, E.; Kim, Y. S. *Angew. Chem. Int. Ed.* **2018**, *57*, 2091.
- (382) Yang, D.; Mosadegh, B.; Ainla, A.; Lee, B.; Khashai, F.; Suo, Z.; Bertoldi, K.; Whitesides, G. M. *Advanced Materials* **2015**, *27*, 6323.
- (383) Tang, Q.; Duan, Y.; He, B.; Chen, H. *Angew. Chem. Int. Ed.* **2016**, *55*, 14412.
- (384) Park, J.; Yang, Y.; Kwon, S. H.; Kim, Y. S. *J. Phys. Chem. Lett.* **2015**, *6*, 745.
- (385) Park, J.; Song, S.; Yang, Y.; Kwon, S. H.; Sim, E.; Kim, Y. S. *J. Am. Chem. Soc.* **2017**, *139*, 10968.
- (386) Kwon, S. H.; Kim, W. K.; Park, J.; Yang, Y.; Yoo, B.; Han, C. J.; Kim, Y. S. *ACS Appl. Mater. Interfaces* **2016**, *8*, 24579.
- (387) Yang, Y.; Park, J.; Yoon, S. G.; Kim, Y. S. *Nano Energy* **2017**, *40*, 447.
- (388) Siretanu, I.; Ebeling, D.; Andersson, M. P.; Stipp, S. L. S.; Philipse, A.; Stuart, M. C.; van den Ende, D.; Mugele, F. *Sci. Rep.* **2014**, *4*.

- (389) Lis, D.; Backus, E. H. G.; Hunger, J.; Parekh, S. H.; Bonn, M. *Science* **2014**, *344*, 1138.
- (390) Horinek, D.; Netz, R. R. *Phys. Rev. Lett.* **2007**, *99*.
- (391) Ricci, M.; Spijker, P.; Voitchovsky, K. *Nat. Commun.* **2014**, *5*, 4400.
- (392) Kudin, K. N.; Car, R. *J. Am. Chem. Soc.* **2008**, *130*, 3915.
- (393) Collins, L.; Jesse, S.; Kilpatrick, J. I.; Tselev, A.; Varenky, O.; Okatan, M. B.; Weber, S. A. L.; Kumar, A.; Balke, N.; Kalinin, S. V.; Rodriguez, B. J. *Nat. Commun.* **2014**, *5*, 3871.
- (394) Roger, K.; Cabane, B. *Angew. Chem. Int. Ed.* **2012**, *51*, 5625.
- (395) McCarty, L. S.; Whitesides, G. M. *Angew. Chem. Int. Ed.* **2008**, *47*, 2188.
- (396) Abel, B. *Annu. Rev. Phys. Chem.* **2013**, *64*, 533.
- (397) Salem, D. P.; Gong, X.; Liu, A. T.; Koman, V. B.; Dong, J.; Strano, M. S. *J. Am. Chem. Soc.* **2017**, *139*, 16791.
- (398) Bellisario, D. O.; Liu, A. T.; Kozawa, D.; Han, R.; Harris, J. K.; Zabala, R. B.; Wang, Q. H.; Agrawal, K. V.; Son, Y.; Strano, M. S. *J. Phys. Chem. C* **2017**, *121*, 22550.
- (399) Alivisatos, A. P.; Chun, M.; Church, G. M.; Deisseroth, K.; Donoghue, J. P.; Greenspan, R. J.; McEuen, P. L.; Roukes, M. L.; Sejnowski, T. J.; Weiss, P. S.; Yuste, R. *Science* **2013**, *339*, 1284.
- (400) Ferrari, S.; Loveridge, M.; Beattie, S. D.; Jahn, M.; Dashwood, R. J.; Bhagat, R. J. *Power Sources* **2015**, *286*, 25.
- (401) Balanis, C. A. *Proceedings of the IEEE* **1992**, *80*, 7.
- (402) Zebda, A.; Cosnier, S.; Alcaraz, J. P.; Holzinger, M.; Le Goff, A.; Gondran, C.; Boucher, F.; Giroud, F.; Gorgy, K.; Lamraoui, H.; Cinquin, P. *Scientific Reports* **2013**, *3*, 1516.
- (403) Kim, H.; Kim, M. J. *Electric Field Control of Bacteria-Powered Microrobots (BPMs) Using a Static Obstacle Avoidance Algorithm*, 2015; Vol. 32.
- (404) Servant, A.; Qiu, F.; Mazza, M.; Kostarelos, K.; Nelson, B. J. *Advanced Materials* **2015**, *27*, 2981.
- (405) Chang, S. T.; Paunov, V. N.; Petsev, D. N.; Velev, O. D. *Nature Materials* **2007**, *6*, 235.
- (406) Cottrill, A. L.; Liu, A. T.; Kunai, Y.; Koman, V. B.; Kaplan, A.; Mahajan, S. G.; Liu, P.; Toland, A. R.; Strano, M. S. *Nat Commun* **2018**, *9*, 664.
- (407) L., C. A.; Song, W.; Tianxiang, L. A.; Wen-Jun, W.; S., S. M. *Adv. Energy Mater.* **2018**, *8*, 1702692.
- (408) Alex, C.; I., K. G.; Raphael, P.; Desheng, K.; Pei, L.; Roda, N.; Ting, L.; Huiliang, W.; Nan, L.; Ying-Chih, L.; Myung-Gil, K.; Won, C. J.; Sangyoon, L.; Zhenan, B. *Adv. Mater.* **2016**, *28*, 4441.
- (409) Bai, P.; Li, J.; Brushett, F. R.; Bazant, M. Z. *Energy Environ. Sci.* **2016**, *9*, 3221.

(410) Guoyu, Q.; Bin, Z.; Xiangbiao, L.; Haowei, Z.; Arvind, S.; Joseph, F. N.; Qian, C.; Mingqiang, N.; Boyu, Q.; Yi, L.; Songliu, Y.; Jia, Z.; Xi, C.; Yuan, Y. *Adv. Mater.* **2018**, *30*, 1704947.

Chapter 2

Sustainable Power Sources Based on High Efficiency Thermopower Wave Devices

Article that contributes to this chapter:

Mahajan, S. G.*; Liu, A. T.*; Cottrill, A. L.; Kunai, Y.; Bender, D.; Castillo, J.; Gibbs, S. L.; Strano, M. S. *Energy & Environmental Science* (2016), 9, 1290

There is a pressing need to find alternatives to portable power sources such as Li-ion batteries, which contain toxic metals, present recycling difficulties due to harmful inorganic components, and rely on elements in finite global supply. Thermopower wave (TPW) devices, which convert chemical to electrical energy by means of self-propagating reaction waves guided along nanostructured thermal conduits, have the potential to address this demand. Herein, we demonstrate orders of magnitude higher chemical-to-electrical conversion efficiency of thermopower wave devices, in excess of 1%, with sustainable fuels such as sucrose and NaN_3 for the first time, that produce energy densities on par with Li-ion batteries operating at 80% efficiency (0.2 MJ/L versus 0.8 MJ/L). We show that efficiency can be increased significantly by selecting fuels such as sodium azide or sucrose with potassium nitrate to offset the inherent penalty in chemical potential imposed by strongly p-doping fuels, a validation of the predictions of Excess Thermopower theory. Such TPW devices can be scaled to lengths greater than 10 cm and durations longer than 10s, an over 5-fold improvement over the highest reported values, and they are capable of powering a commercial LED device. Lastly, a mathematical model of wave propagation, coupling thermal and electron transport with energy losses, is presented to describe

the dynamics of power generation, explaining why both unipolar and bipolar waveforms can be observed. These results represent a significant advancement toward realizing TPW devices as new portable, high power density energy sources that are metal-free.

2.1 Background on Thermopower Wave Technology

Current battery technology is typically comprised of toxic metals, presenting problems for recycle, and environmental exposure.¹ There is a pressing need for portable power sources that are sustainable, preferably using materials that are not in finite supply or mined from the earth, such as lithium.² Over the past decade, researchers have explored many potential alternatives, namely secondary batteries made with other metals,²⁻⁵ pure organic materials,⁶ graphitic carbon nitride,⁷ and even exotic bio-organic materials like DNA for energy conversion and storage.⁸ Numerous reports have given high merits for nanotechnologies (i.e. functionalized graphene⁹ and strongly coupled inorganic-nano-carbon hybrid materials¹⁰) in this field. Such approaches benefit from their use of metal free, organic materials, but have not yet demonstrated power or energy densities commensurate with power sources such as the Li-ion battery, at any size or time scale. The scaling with electrode area fundamentally limits specific power and energy output. Thermopower waves are a potential solution because the approach uses a self-propagating reaction wave to control the duration of energy release, accessing high power densities from simple, chemical fuels. First reported in 2010, thermopower waves convert chemical energy in the form of an adsorbed fuel directly to electrical current by means of self-propagating reaction waves guided along nanostructured thermal conduits. Such TPW devices have been shown to exhibit high power density comparable to that of Li-ion batteries ($80,000 \mu\text{W}/\text{mm}^3$ versus about $10,000 \mu\text{W}/\text{mm}^3$ demonstrated for Li microbattery).¹¹ The high power and

energy densities of such devices provide attractive scaling for Micro-Electro-Mechanical Systems (MEMS),¹² smart dust applications,¹³ or wireless sensor network nodes.¹⁴ Conduit types have included multi-walled carbon nanotubes (MWNTs);¹¹ single-walled carbon nanotubes (SWNT);¹⁵ SWNT yarns; ZnO;^{16,17} Bi₂Te₃ coated on alumina and terracotta;^{18,19} Sb₂Te₃ coated on alumina, terracotta and MWNTs;^{18,20} and MnO₂ coated alumina.²¹ Fuels employed for TPW studies, on the other hand, have included 2, 4, 6-Trinitroaniline (TNA), picramide and nitrocellulose (with sodium azide),^{15,22} and nanothermites consisting of aluminum (Al) iron oxide (γ -Fe₂O₃).²³ However, the efficiency of energy conversion is an issue that has not been significantly addressed to date, and reported data have ranged from 10⁻⁶ to 10⁻³ %. In this work, we show that such efficiency limitations have been dominated by radiative losses, convective losses and fuel selections that necessarily set up a partially-cancelling thermopower wave, limiting power generation. Improved design and fuel complexation gives rise to devices that exceed efficiencies of 1 % for the first time, commensurate with experimental power source technologies.²⁴ These results are inspired by a mathematical wave model that allows one to describe the transient voltage profile of the traveling thermal wave, capturing many important aspects of the wave dynamics. In many ways, this conceptual advance allows us to push the boundaries of the future portable power sources comprised of carbon nanomaterials, which challenges the current state of the art from both an energy and a sustainability point of view.

2.2 High Efficiency Thermopower Wave Devices

Electrical power generation with the propagation of the concomitant reaction wave is described by the theory of excess thermopower, which describes the induced voltage as the sum of two distinct sources, namely thermoelectricity and the transient chemical potential

gradient. The former is driven by the temperature difference existing across the thermal conduit, while the latter arises because of the chemical potential difference existing across the conduit.²⁵

$$\Delta V_{TPW} = S(T_{back} - T_{front}) - \frac{1}{e}(\mu_{back} - \mu_{front}) \quad (25)$$

Here, S is the Seebeck coefficient of the device; T is the temperature; μ is the chemical potential of the dominant charge carriers in the system, holes or electrons, and the subscript *front* and *back* denotes the spatial frontend and backend of the SWNT conduit, respectively. One can then define a chemical-to-electrical conversion efficiency (η) as the ratio of the output electrical energy to the input chemical energy into the system:

$$\eta = \frac{\int_{t_{start}}^{t_{end}} \frac{\Delta V_{out}^2}{R_{ext}} dt}{m_{fuel} (-\Delta H_{rxn})} \quad (26)$$

Here, t is the time coordinate, with the subscript indicating the start and end of the experiment; m_{fuel} is the mass of the chemical fuel used and ΔH_{rxn} represents its specific heat of reaction. The value of η does not include the initiation energy as it is generally orders of magnitude smaller than the denominator. Historically η has not exceeded approximately 10⁻³% in the literature, primarily due to limitations in fuel coupling²⁵ (as shown below), radiative and convective losses. **Figure 2-1a** shows a circuit diagram of a TPW device as a source producing an open circuit voltage ΔV_{OC} with an internal resistance R_{int} which produces an output voltage ΔV_{out} over an external resistance R_{ext} .²⁶ **Figure 2-1b** shows a typical (bipolar) voltage output obtained from a nitrocellulose-SWNT yarn TPW device. One consequence of the excess thermopower theory is that the additive chemical potential

contribution, which is a fuel property, resulting significant variance in the $\Delta\mu$ contribution. Different fuels also change the adiabatic reaction temperature, affecting temperature driven voltage output as well.²⁷ A screening of potential fuels produced two of notable interest, namely sodium azide (NaN_3) and a carbohydrate fuel in the form of sucrose with a premixed oxidizer, potassium nitrate (KNO_3). We observed that these fuels led to a substantially improved efficiency as compared to a standard nitrocellulose fuel (**Figure 2-1c**). Up to 100 times improvement was observed for NaN_3 despite the fact that at 320 J gm^{-1} it has a heat of combustion $1/10^{\text{th}}$ of nitrocellulose (4200 J gm^{-1}).²⁸ Sucrose with KNO_3 dissolved in water at 35:65 ratio also consistently demonstrated more than a factor of 10 higher efficiency, despite having a similar heat of combustion to nitrocellulose.

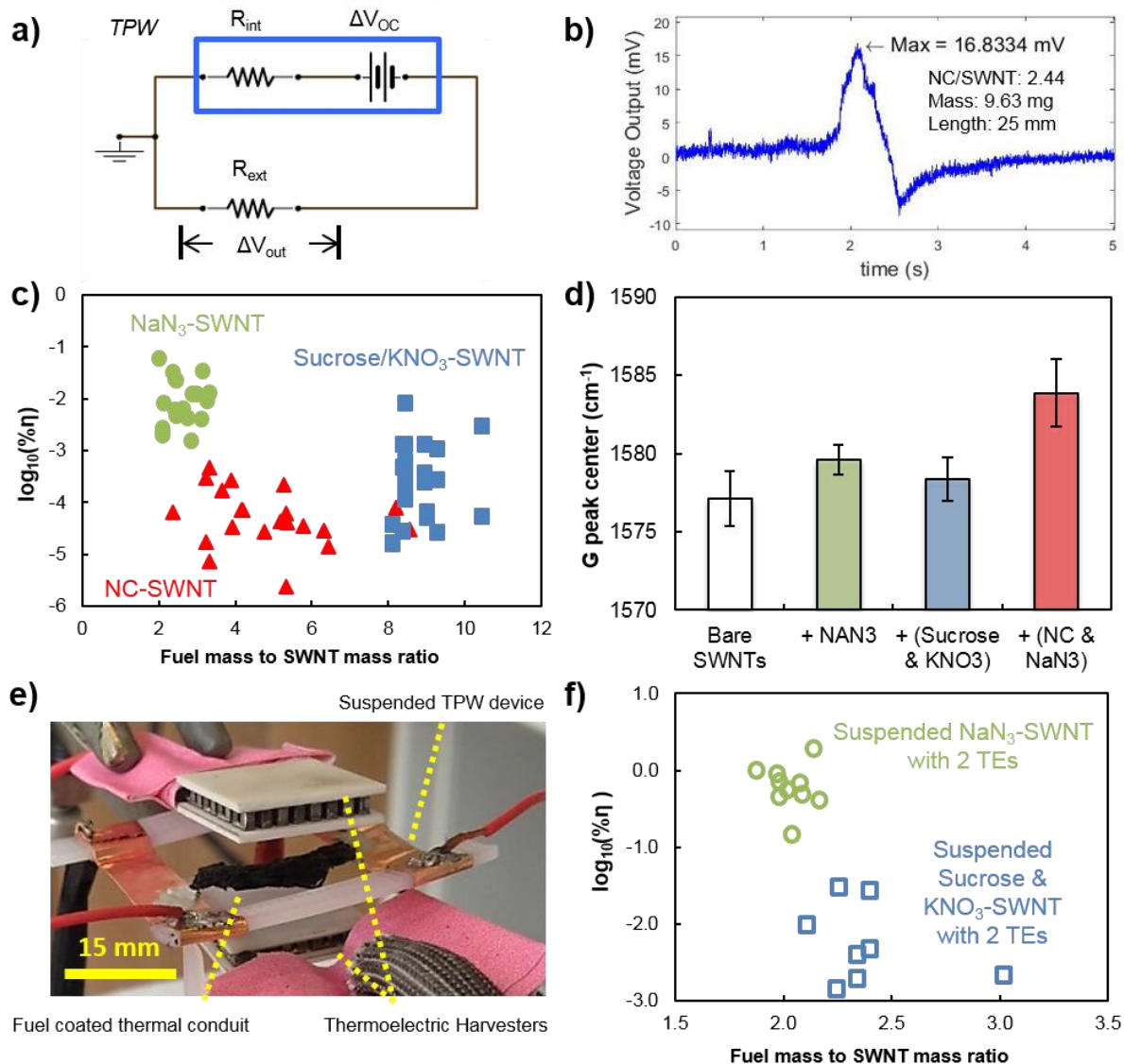


Figure 2-1. (a) Circuit diagram for the electrical analysis of thermopower wave (TPW) devices where we connect an external load R_{ext} to measure the voltage drop ΔV_{out} across it. (b) Sample of an actual thermopower wave voltage output. The voltage output for this 25 mm long reaction wave lasts for about 1.2 s. (c) Chemical to electrical conversion efficiency of TPW devices using different fuels: Nitrocellulose (NC), Sodium azide and Sucrose with KNO_3 . (d) Doping analysis using Raman spectroscopy for different fueled and unfueled SWNT samples. The error bars represent 95% confidence intervals. (e) A picture of an experimental setup involving TE harvesters

(seen as white squares) suspended above and below a TPW device. **(f)** Chemical to electrical conversion efficiencies of the updated TPW wave setups (i.e., including the electrical output from the reaction wave as well the TE harvesters).

With a decreased heat of combustion (therefore a reduced contribution from the thermoelectric effect), the amplified output electrical energy is accounted for by the enhanced excess thermopower ($\Delta\mu$ contribution) led by the favorable chemical doping.²⁷ To further investigate the effect of doping on the SWNT by the different chemical fuels tested, Raman spectroscopy analyses were performed (**Figure 2-1d**) where the G peak Raman shifts were converted to Fermi energies using the data reported by Farhat *et al.* and a method outlined in Abrahamson *et al.* (modified below).^{27,29,30} With the presence of nitro groups, the electron withdrawing nitrocellulose is known to p-dope graphene and SWNT.²⁷ With this insight, we calculate a Fermi energy of -0.21 eV for the bare SWNT (1577 cm^{-1}) (known to be p-doped by O_2), and -0.28 eV for the nitrocellulose/ NaN_3 doped SWNT (1584 cm^{-1}). As was found from model regression of experimental data (below). This p-doping by chemical fuel actually generates an opposing electronic wave, reducing efficiency. It is noteworthy that with a Raman shift around 1579 cm^{-1} , NaN_3 and sucrose/ KNO_3 either lower the p-doping losses (-0.23eV) or supportively n-dope (+0.40 eV) the SWNT as compared with nitrocellulose/ NaN_3 . In either case, the Fermi level difference (and hence the chemical potential gradient) of at least 0.05 eV between the doped states of SWNT justifies the higher electrical energy output observed for using solely NaN_3 or sucrose/ KNO_3 as chemical fuels. This link between fuel properties and efficiency, supported by the excess thermopower theory, promises further improvements in fuel design for TPW devices.

It is also noted that the temperatures of propagating TPW wavefronts can approach the adiabatic limit (2427 K for nitrocellulose) leading to substantial heat losses from the device. We find that suspending TPW devices within an airgap flanked by two parallel Bi_2Te_3 thermoelectric (TE) harvesters is effective for capture of radiative and convective energy losses (**Figure 2-1e**). Combined with fuels such as sucrose- KNO_3 and NaN_3 , efficiencies in excess of 1 % can be achieved in this configuration (**Figure 2-1f**). This scheme necessarily generates more electrical energy than conventional thermophotovoltaic or combustion schemes by adding the high power density TPW.^{31,32} There does not appear to be a correlation between adiabatic reaction temperature (760 K for NaN_3 and 1043K for sucrose/ KNO_3) and efficiency, an indication that TPW devices are generally not limited by the conventional thermoelectric term, and operate distinctly from thermophotovoltaics.²⁴

Reaction waves such as TPWs are theoretically solitons with highly nonlinear properties arising from the exponential thermal source term associated with reaction. This exponential term partially cancels any dissipation that would be observed from thermal diffusion, predicting infinite propagation along an infinite conduit. To test this empirically, we generated TPW devices of increasing length. Sample voltage outputs from NaN_3 -based and sucrose/ KNO_3 -based TPW devices are shown in **Figure 2-2a**, displaying opposite polarity voltage pulses from opposing propagation directions, as expected. As seen from **Figure 2-2b**, the duration of energy generation scales linearly with length, and its wave propagation is captured in **Figure 2-2c**, with notable cooling behind the advancing wavefront. The discovery of the linear scaling of voltage duration versus device length suggests a potential route to the scaling-up of TPW devices. Indeed, with this knowledge in hand, we demonstrate the longest SWNT-based TPW device reported to date, both in terms of length

(over 10 cm) and duration of energy generation (7 s). The wave propagation of said device is presented in **Figure 2-2c**, and this linear scaling of voltage duration to device length clearly goes beyond the limited length window investigated in the past (**Figure 2-2d**).

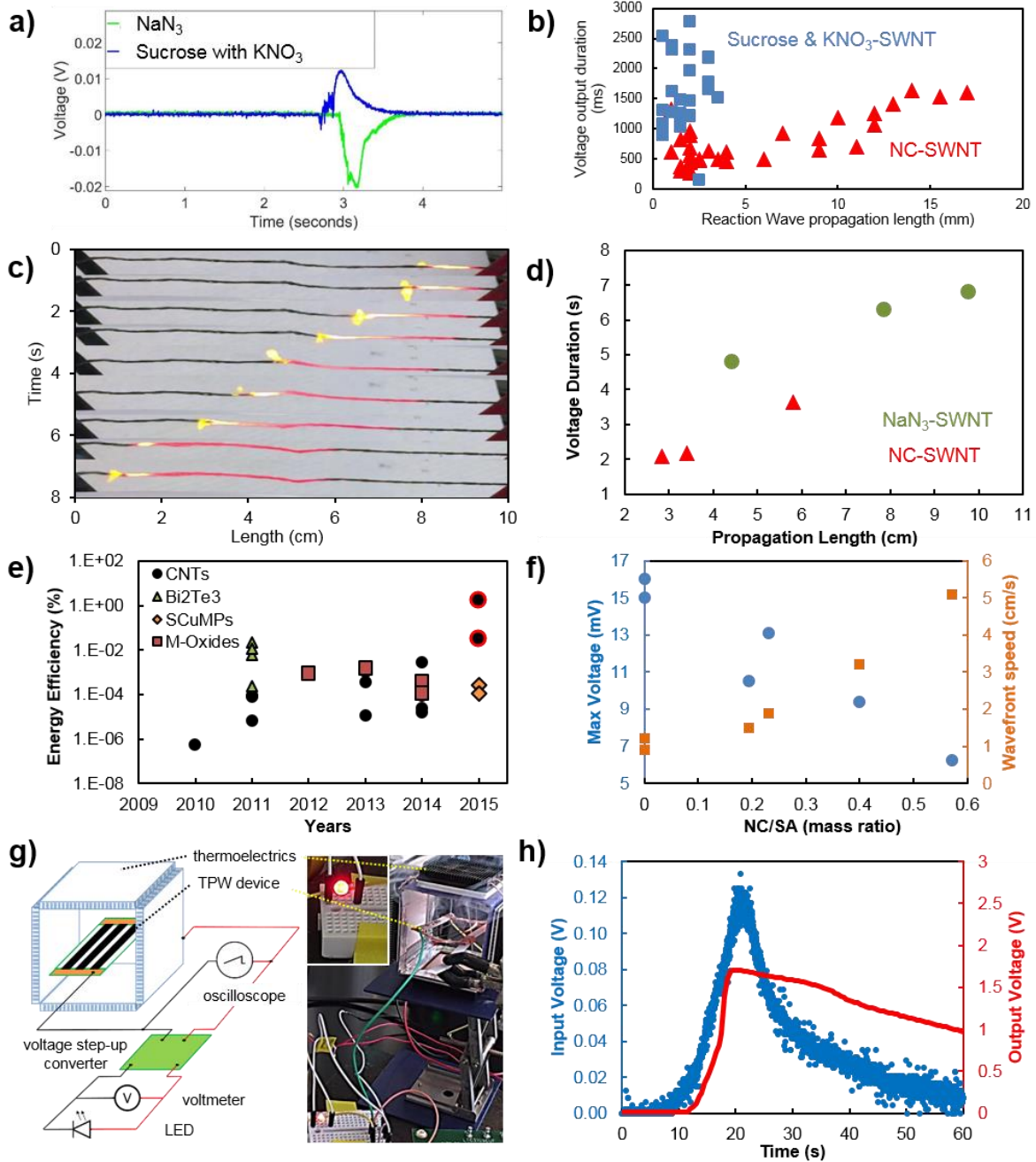


Figure 2-2. (a) Sample voltage output from SWNT thermopower reaction waves launched using sodium azide and sucrose/KNO₃. (b) Voltage output duration plotted against device length for

nitrocellulose (NC) coated SWNTs and sucrose/ KNO_3 coated SWNTs in the sub-centimeter regime. **(c)** Time elapsed pictures displaying the reaction wave propagation on a 10 cm long NaN_3 -SWNT TPW device. **(d)** Decimeter-scale NaN_3 and nitrocellulose (NC) coated SWNTs showing linear scaling between voltage durations and wave propagation length. **(e)** Master plot for chemical to electrical conversion efficiencies of all thermopower wave device setups published so far. The highest efficiency highlighted points in 2015 correspond to this work. **(f)** Maximum voltage and speed of the reaction wavefront plotted against increasing nitrocellulose (NC) to sodium azide (SA) ratio. **(g)** Schematic of the TPW-thermoelectric harvester setup coupled with a voltage step-up converter that illuminated a red LED (shown on the right) for 20 s. **(h)** The input and output voltage measured across the step-up converter (a DC-to-DC power converter with an output voltage greater than its input voltage) plotted as a function of time. The LED stays on while the output voltage is above 1.5 V.

The results demonstrated in this work are a clear advance over the state of the art, and systems examined in the literature that have focused on conduit type. **Figure 2-2e** charts the increase in efficiency from approximately 10^{-6} % for SWNT-based devices in 2010 and subsequent increase as conventional TE materials were examined in the years following by other researchers.^{15-23,33-35} While higher Seebeck coefficient conduit types do maximize the conventional thermoelectric output,¹⁹ this current work highlights the importance of the excess thermopower through constructive chemical doping toward increasing efficiency. Initially discovered by us, the use of nitrocellulose as a solid state fuel due to its high combustion enthalpy has been adopted by many researchers.^{17-19,21,33} This work further reveals a criteria for selecting better performing fuels for TPW propagation, namely NaN_3 and sucrose/ KNO_3 , by taking advantage of their favorable

electronic interactions with SWNTs. The observed increase in energy output by reducing the nitrocellulose level (as indicated by the decreased nitrocellulose/ NaN_3 ratio in **Figure 2-2f**) can be attributed to both the enhanced maximum peak voltage, as well as the prolonged energy output duration. To clarify, our current work (**Figure 2-2e**, red) demonstrates the highest TPW device efficiencies to date with or without the use of external energy harvesting. These advances pave the way for future chemical fuel optimization through rational design for SWNT-based TPW or even broader applications. As a demonstration of a practical use of the current high efficiency device, we use three NaN_3 -fueled SWNTs connected in series with thermoelectric residual heat harvesters to charge a voltage step-up converter (**Figure 2-2g**). For the first time, we are able to reach 1.5 V, power and sustain a commercial light-emitting diode (LED) for over 20 s (**Figure 2-2h**), a practical milestone that promises additional gains in energy and power density.

Lastly, these observations are coupled to a detailed mechanistic model to provide insights on how conduit type, fuel and thermal losses contribute to energy and power density, as well as efficiency. Using the excess thermopower concept as a starting point, this model is capable of describing the transient voltage output of TPW by simultaneously solving the heat and mass transport equations that govern the TPW propagation along the SWNT fiber. The transient temperature and mass profiles are then used to predict ΔV_{TPW} , including the time-dependent variation of doping levels as fuel reacts along the wavefront.²⁵ As shown previously, a 1D self-propagating TPW can be analyzed by studying the corresponding heat and mass transfer for a one-dimensional reaction system of continuous fuel layers.³⁶

The system is initially at ambient temperature T_{amb} . The heat of reaction ($-\Delta H$) is assumed to be temperature invariant, with the reaction modeled as first order with an Arrhenius

activation energy E_a and attempt frequency prefactor k_0 . This formulation assumes a fast thermal equilibrium between the thermal conduit and the fuel layer.³⁶ The non-dimensional forms of the heat and mass balance equations are as follows, which can be solved using method of lines, with the space domain discretized as shown in **Figure 2-3a**.

$$\frac{\partial u}{\partial \tau} = \frac{\partial^2 u}{\partial \xi^2} + y \exp\left(-\frac{1}{u}\right) - w_{rad} (u^4 - u_{amb}^4) - w_{conv} (u - u_{amb}) \quad (27)$$

$$\frac{\partial y}{\partial \tau} = \beta y \exp\left(-\frac{1}{u}\right) \quad (28)$$

where u and y represent the non-dimensional temperature and fuel concentration, both of which are a function of the dimensionless space (ξ) and time (τ); w_{rad} and w_{conv} correspond to the dimensionless net radiative and convective heat transfer coefficients, respectively. Non-dimensionalization of variables also gives rise to an important factor β , the inverse dimensionless adiabatic temperature rise:

$$\beta = \frac{C_{p,CNT} E_a}{(-\Delta H) R} \quad (29)$$

where $C_{p,CNT}$ is the heat capacity of the SWNT conduit and R is the gas constant.

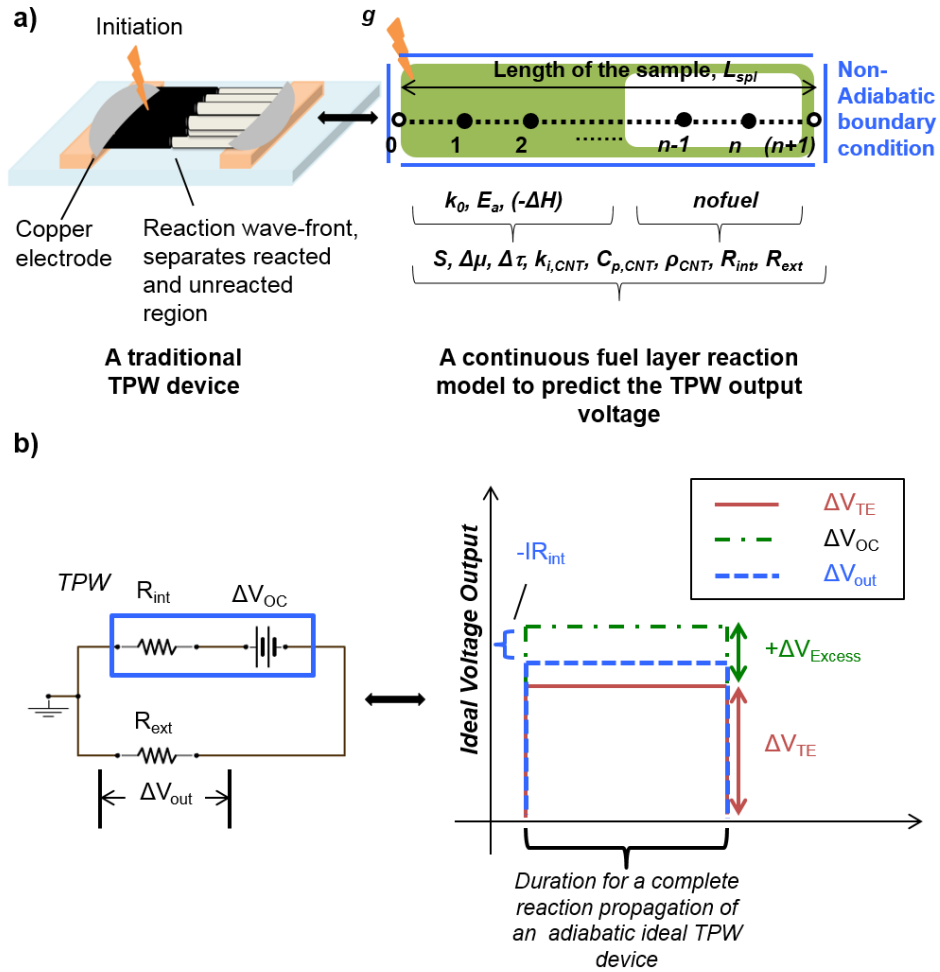


Figure 2-3. (a) The left shows a schematic of a traditional thermopower wave device with a reaction wave propagation along a fuel coated thermal conduit connected to copper tape electrodes and supported on a glass slide. The right is a visualization of a model of a continuous layer of a fuel undergoing reaction to predict or fit the voltage output from a thermopower wave device. All of the properties (except the device’s external heat loss properties) needed to completely define a thermopower wave device using such a scheme have been noted. (b) The left shows a schematic of the electrical circuit diagram for analyzing the output voltage ΔV_{out} across an external resistor R_{ext} powered by a thermopower wave device with internal resistance R_{int} . The right shows an ideal voltage output profile for an adiabatic thermopower wave device undergoing complete reaction

propagation. The open circuit voltage ΔV_{OC} from a thermopower wave device is contributed to by the temperature gradient and the chemical potential gradient.

TPW devices can be modeled as voltage sources giving rise to a transient open circuit voltage difference (ΔV_{TPW}) across its ends. When connected to an external electrical load or electrical resistance, we obtain useable output voltage (ΔV_{out}) and current flow through the load. If we can estimate the magnitude of the thermal gradient and the chemical potential gradient, for a system with a known Seebeck coefficient S , we can calculate the expected open circuit voltage (ΔV_{TPW}) for a given pair of fuel-thermal conduit TPW device. Using the values of the internal resistance of the TPW device (R_{int}) and the resistance of the load attached (R_{ext}), we can compute the expected output voltage (ΔV_{out}). In **Figure 2-3b**, we present a schematic of a circuit diagram for a TPW device with the expected voltage output.

$$\Delta V_{out} = \frac{S(T_{back} - T_{front}) - \frac{1}{e}(\mu_{back} - \mu_{front})}{1 + \frac{R_{int}}{R_{ext}}} \quad (30)$$

This model allows us to gain intuitive understandings about the different trends observed in voltage output profiles.³⁷ From selected sample fits (SWNTs fueled with nitrocellulose), shown in **Figure 2-4**, it is clear that this model predicts the experimental results with fairly high accuracy and consistency. When the reaction wave undergoes complete propagation, we expect a double polarity thermoelectric voltage output contribution, where the voltage output peak after complete wave propagation is smaller in magnitude, such as what is seen in **Figure 2-2b**. The effect of excess thermopower will either boost or oppose the first of

the double polarity peaks, depending on the sign of the Seebeck coefficient of the SWNT cluster and the type of doping induced by the fuel. When the thermoelectric and the excess thermopower voltage contributions oppose each other, the first peak which is ideally higher in magnitude (as compared to the reverse polarity second peak) is repressed, as shown in **Figure 2-4c**. In the case of partial propagation, we expect a single polarity thermoelectric voltage output (e.g. **Figure 2-4f**), since the reaction wave stops in the middle of the conduit and never reaches the other end to create the opposite temperature gradient. Again, depending on whether the effect of excess thermopower boosts or opposes the thermoelectric voltage output, one expects to see ‘kinks’ or multiple peaks in the single polarity peak voltage output. Examples of these situations can be found in **Figure 2-4a, b, d, and e**. The most interesting takeaway from these fits is that for the 20 nitrocellulose-SWNT TPW samples that were fitted, 17 samples show the effect of excess thermopower opposing the voltage output due to the thermoelectric effect. This finding agrees with the Raman results discussed earlier in **Figure 2-1d**, where we concluded that the p-doping nitrocellulose generates an excess thermopower voltage opposite to its thermoelectric counterpart, reducing the overall energy output of the nitrocellulose TPW devices. This qualitative agreement between our model and experimental Raman measurements strengthens our confidence in the current theoretical construct and its prospects in aiding further TPW device optimization.

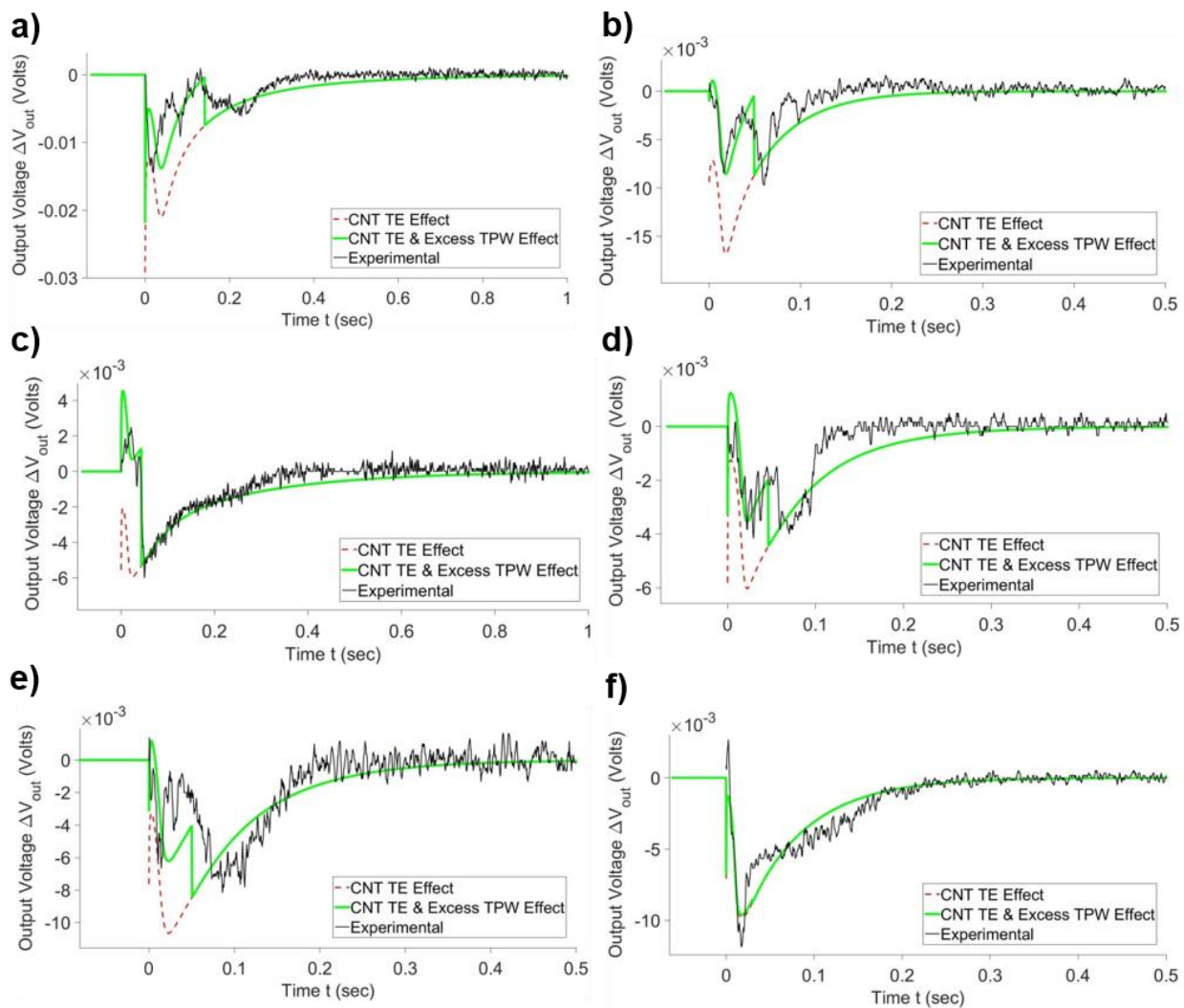


Figure 2-4. (a-f) Thermopower wave voltage output prediction for experimental samples. The experimental output is shown in black, the model-predicted thermoelectric output is shown in red dotted lines, and the final model-predicted output is shown in green.

In summary, on the basis of the theory of excess thermopower, the chemical to electrical conversion efficiency of thermopower wave devices was improved from $10^{-3} \%$ to $10^{-2} \%$ by using novel fuels such as NaN_3 and sucrose/ KNO_3 . Combining this improved performance of thermopower waves with external thermoelectric harvesting, we demonstrate a net energy conversion efficiency of up to 1 % and successfully illuminate

an LED for 20 s. We propose a detailed 1D heat and mass transfer model to be used in combination with the theory of excess thermopower to explain the experimental voltage outputs from thermopower wave devices. The theoretical analyses for the voltage outputs from nitrocellulose-SWNTs, in combination with Raman spectroscopy and a variety of controlled experiments, suggest that choosing n-doping fuels might further boost the efficiency of these SWNT fiber-based thermopower wave devices.

2.3 References

- (1) Melot, B. C.; Tarascon, J. M. *Accounts of Chemical Research* 2013, 46, 1226.
- (2) Orikasa, Y.; Masese, T.; Koyama, Y.; Mori, T.; Hattori, M.; Yamamoto, K.; Okado, T.; Huang, Z.-D.; Minato, T.; Tassel, C.; Kim, J.; Kobayashi, Y.; Abe, T.; Kageyama, H.; Uchimoto, Y. *Scientific Reports* 2014, 4, 5622.
- (3) Kim, H.; Jeong, G.; Kim, Y.-U.; Kim, J.-H.; Park, C.-M.; Sohn, H.-J. *Chemical Society Reviews* 2013, 42, 9011.
- (4) Zhao, X.; Ma, L. *International Journal of Hydrogen Energy* 2009, 34, 4788.
- (5) McKerracher, R. D.; Ponce de Leon, C.; Wills, R. G. A.; Shah, A. A.; Walsh, F. C. *ChemPlusChem* 2015, 80, 323.
- (6) Häupler, B.; Wild, A.; Schubert, U. S. *Adv Energy Mater* 2015, 5, 1402034.
- (7) Gong, Y.; Li, M.; Wang, Y. *ChemSusChem* 2015, 8, 931.
- (8) Irimia-Vladu, M.; Sariciftci, N. S.; Bauer, S. *Journal of Materials Chemistry* 2011, 21, 1350.
- (9) Dai, L. *Accounts of Chemical Research* 2013, 46, 31.
- (10) Wang, H.; Dai, H. *Chemical Society Reviews* 2013, 42, 3088.
- (11) Choi, W.; Abrahamson, J. T.; Strano, J. M.; Strano, M. S. *Materials Today* 2010, 13, 22.
- (12) Walther, D. C.; Ahn, J. *Progress in Energy and Combustion Science* 2011, 37, 583.
- (13) Sailor, M. J.; Link, J. R. *Chem Commun* 2005, 1375.
- (14) Langendoen, K.; Voigt, T. *Wireless Sensor Networks. Lecture Notes in Computer Science*; Springer, 2007.
- (15) Abrahamson, J. T.; Song, C.; Hu, J. H.; Forman, J. M.; Mahajan, S. G.; Nair, N.; Choi, W.; Lee, E.-J.; Strano, M. S. *Chemistry of Materials* 2011, 23, 4557.

- (16) Lee, K. Y.; Hwang, H.; Choi, W. *ACS Applied Materials & Interfaces* 2014, 6, 15575.
- (17) Walia, S.; Weber, R.; Balendhran, S.; Yao, D.; Abrahamson, J. T.; Zhuiykov, S.; Bhaskaran, M.; Sriram, S.; Strano, M. S.; Kalantar-zadeh, K. *Chem Commun* 2012, 48, 7462.
- (18) Walia, S.; Weber, R.; Sriram, S.; Bhaskaran, M.; Latham, K.; Zhuiykov, S.; Kalantar-zadeh, K. *Energy & Environmental Science* 2011, 4, 3558.
- (19) Walia, S.; Weber, R.; Latham, K.; Petersen, P.; Abrahamson, J. T.; Strano, M. S.; Kalantar-zadeh, K. *Advanced Functional Materials* 2011, 21, 2072.
- (20) Hong, S.; Kim, W.; Jeon, S.-J.; Lim, S. C.; Lee, H.-J.; Hyun, S.; Lee, Y. H.; Baik, S. *The Journal of Physical Chemistry C* 2013, 117, 913.
- (21) Walia, S.; Balendhran, S.; Yi, P.; Yao, D.; Zhuiykov, S.; Pannirselvam, M.; Weber, R.; Strano, M. S.; Bhaskaran, M.; Sriram, S.; Kalantar-zadeh, K. *The Journal of Physical Chemistry C* 2013, 117, 9137.
- (22) Yeo, T.; Hwang, H.; Jeong, D.-C.; Lee, K. Y.; Hong, J.; Song, C.; Choi, W. *Nanotechnology* 2014, 25, 445403.
- (23) Hong, S.; Hong, S.; Lee, T.-R.; Kim, Y.-J.; Ryu, C.; Baik, S. *Energy & Environmental Science* 2011, 4, 2045.
- (24) Lenert, A.; Bierman, D. M.; Nam, Y.; Chan, W. R.; Celanović, I.; Soljačić, M.; Wang, E. N. *Nature Nanotechnology* 2014, 9, 126.
- (25) Abrahamson, J. T.; Sempere, B.; Walsh, M. P.; Forman, J. M.; Şen, F.; Şen, S.; Mahajan, S. G.; Paulus, G. L. C.; Wang, Q. H.; Choi, W.; Strano, M. S. *ACS Nano* 2013, 7, 6533.
- (26) Johnson, D. H. *Proceedings of the IEEE* 2003, 91, 817.
- (27) Abrahamson, J. T.; Strano, M. S. *The Journal of Physical Chemistry Letters* 2010, 1, 3514.
- (28) Kim, C.; Thomas III, S. W.; Whitesides, G. M. *Angewandte Chemie International Edition* 2010, 49, 4571.
- (29)
- (30) Farhat, H.; Son, H.; Samsonidze, G. G.; Reich, S.; Dresselhaus, M. S.; Kong, J. *Physical Review Letters* 2007, 99, 145506.
- (31) Datas, A.; Algora, C. *Progress in Photovoltaics: Research and Applications* 2013, 21, 1025.
- (32) Rephaeli, E.; Fan, S. *Optics express* 2009, 17, 15145.
- (33) Hwang, H.; Yeo, T.; Um, J.-E.; Lee, K. Y.; Kim, H.-S.; Han, J.-H.; Kim, W.-J.; Choi, W. *Nanoscale Res Lett* 2014, 9, 536.
- (34) Lee, K. Y.; Hwang, H.; Shin, D.; Choi, W. *Journal of Materials Chemistry A* 2015, 3, 5457.

(35) Choi, W.; Hong, S.; Abrahamson, J. T.; Han, J.-H.; Song, C.; Nair, N.; Baik, S.; Strano, M. S. *Nature Materials* 2010, 9, 423.

(36) Abrahamson, J. T.; Choi, W.; Schonенbach, N. S.; Park, J.; Han, J.-H.; Walsh, M. P.; Kalantar-zadeh, K.; Strano, M. S. *ACS Nano* 2011, 5, 367.

(37)

Chapter 3

Electrical Energy Generation via Reversible Chemical Doping on Carbon Nanotube Fibers

Article that contributes to this chapter:

Liu, A. T.*; Kunai, Y.*; Liu, P.; Kaplan, A.; Cottrill, A. L.; Smith-Dell, J. S.; Strano, M. S. *Advanced Materials* (2016), 28, 9752

As cylindrical forms of graphene sheets, carbon nanotubes are unique in their high surface area for molecular adsorption and exceptional electrical conductivity. The theory describing these so-called thermopower waves, self-propagating reaction waves that generate electrical current from a thermally-driven wavefront, explains the resulting power as arising from two additive components: the thermoelectric effect and the chemical potential gradient across the reaction front or excess thermopower. In this work, we build onto this theory by presenting a voltage induction process free from thermoelectricity, and develop, for the first time, an ambient temperature power source driven only by the differences in chemical potential. Electrical current ($11.9 \mu\text{A}/\text{mg}$) is reversibly produced across a carbon nanotube fiber by localized chemical doping with acetonitrile. We show that the voltage is driven by a spatial gradient in the Fermi energy across the carbon conduit and can reach an unprecedented 525 mV in magnitude. Chemical modification of the nanotube surface, specifically, oxidation of the conduit, is shown to enhance the effect by allowing dopant molecules to rapidly intercalate within bundles of CNTs. Closed circuit experiments further reveal an inverse length-scaling of the maximum power as $L^{-1.03}$. The resulting average specific powers, as large as 26.7 kW/kg for oxidized nanotubes, highlight the potential for microscale energy generation.

These results constitute a strong validation of the Excess Thermopower theory and may enable unique power sources capable of continual operation based on repeated solvent exposure.

3.1 Background on Excess Thermopower

Carbon nanotubes (CNTs) are 1-D molecular manifolds with high mechanical strength and excellent electronic properties. Singled-walled carbon nanotubes (SWNTs), specifically, shows chirality dependent metallic, semi-metallic or semiconducting characteristics.¹ Recent advances taking advantage of these physical properties have led to applications of individual or ensembles of CNTs as scanning probes,^{2,3} actuators,⁴ chemical sensors,⁵ nanoelectronic devices,⁶ and even miniature power sources.⁷ Since the discovery of the CNT, a central theme of study has been its electrical or thermal responses to external stimuli (e.g. changes in light emission, mechanical strain, etc.) with existing voltage or temperature biases. This type of study enables CNT-based photonics and sensor research, where electrical resistance, thermoelectric power (Seebeck coefficient), or local density of states are measured and correlated with the respective magnitudes of the stimuli. Of all these stimuli, chemical signals are among the most studied, due to the excellent molecular adsorption properties of CNTs.⁸ Owing to their size, large surface area, and hollow geometry, CNTs are considered as prime materials for gas adsorption,⁹ Li storage,¹⁰ and selective molecular filtering.¹¹ Indeed, many important discoveries have been made towards using chemical interactions with CNT to alter its electrical conductivity.^{5,12} However, virtually no attention has been given to methods to generate electrical potential purely through CNT-chemical interactions, as in the cases of piezoelectric, thermoelectric and the photovoltaic effect. In this work, we demonstrate the first CNT based electrical potential generation via localized chemical doping that can be tuned to reliably reach 500

mV or higher. This reversible, non-invasive, ambient temperature voltage generation forms the basis of a novel CNT-enabled energy source.

There has been significant interests on using CNTs for energy conversion, either in its pure form, or as a nanocomposite.¹³ Over the past decade, researchers have developed polymer-free CNT solar cells,^{14,15} and combined CNTs with semiconducting polymers for photovoltaic applications.^{15,16} Studies have also shown piezoelectric behaviors where an open circuit voltage on the order of several hundred microvolts can be obtained across a CNT film upon elastic straining.¹⁷⁻²⁰ More exotic studies such as using single SWNTs as hydroelectric power converters might also find applications in nanoscale energy conversion.²¹ With a modest Seebeck coefficient,²² CNTs are not typically considered as a prime candidate for thermoelectric energy harvesting, but recent developments that incorporate CNTs as part of a composite have shown enhancements in its thermoelectric figures of merit.²³

Our previous work on the phenomenon of thermopower waves (TPWs) illustrated how a chemical potential gradient can produce an open circuit voltage across ensembles of CNTs through electron coupling to phonon transport.⁷ TPWs convert chemical energy, in the form of an adsorbed fuel (**Figure 1a**), directly to electrical current by means of self-propagating reaction waves guided along nanostructured conduits. Such TPW devices have been shown to exhibit high energy and power density - comparable to that of Li-ion batteries (20 MJ/cm³ and 80 mW/mm³ versus about 80 MJ/cm³ and 10 mW/mm³ demonstrated for Li microbattery).²⁴

In this work, deconvolution of the Seebeck contribution from the overall voltage generated yields the first quantitative experimental evidence of Excess Thermopower. We further show that it is possible to completely isolate the chemical potential input from that of the temperature gradient by mimicking the time scale of a traveling reaction wave with a liquid dopant infiltrating into a CNT network – yielding a reversible process to induce unbiased voltages up to 525 mV across a CNT network via local chemical doping. With excellent control over the peak voltage and duration, this exotic form of electricity enables fundamentally different approaches to CNT-facilitated chemical detection and energy generation.

3.2 From Thermopower Wave to Asymmetric Chemical Doping

Electrical power generation with the propagation of the concomitant reaction wave is described by the theory of Excess Thermopower,²⁵ which attributes the induced voltage as the sum of two distinct sources, namely thermoelectricity and the voltage resulted by the transient chemical potential gradient (or “Excess Thermopower”). The former is driven by the temperature difference existing across the thermal conduit, while the latter arises because of the chemical potential difference existing across the conduit.²⁵

$$\Delta V_{TPW} = S(T_{back} - T_{front}) - \frac{1}{e}(\mu_{back} - \mu_{front}) \quad (31)$$

Here, ΔV_{TPW} is the open circuit voltage generated, S is the Seebeck coefficient of the device; T is the temperature; μ is the chemical potential of the dominant charge carriers in the system, holes or electrons, and the subscripts *front* and *back* denote the spatial front and back of the CNT conduit, respectively.

Introduced previously as viable chemicals for thermopower wave propagation,²⁴ nitrocellulose and sodium azide (NaN_3) are determined to be p- and n-dopants for CNTs, respectively, in a series of Seebeck coefficient measurements. We measure a Seebeck of $31.5 \mu\text{V/K}$ of our bare CNT yarn sample (p-doped by O_2),¹² and $62.7 \mu\text{V/K}$ for the nitrocellulose-doped CNT doped, which further lowers its Fermi energy, and $24.9 \mu\text{V/K}$ for NaN_3 -doped CNT yarns. These values agree with the general trend reported previously.^{26,27} With a precise chemical control over the Fermi level of the CNT conduit (by changing the ratios of nitrocellulose and NaN_3 fuel coating material), we proceed to isolate the effect of chemical potential gradient from thermoelectricity. The device fabrication is based on a wet impregnation of nitrocellulose in acetonitrile solution or NaN_3 in H_2O into pre-synthesized CNT fibers. Transmission electron microscopy (**Figure 3-1a**) indicates annular coatings of solid crystals between 6 and 9 nm in thickness wrapping a multi-walled carbon nanotube (MWNT) of approximately 22 nm in diameter. Upon launching the thermopower wave, we time-sync the overall voltage output with the corresponding temperature profile (**Figure 3-1b**). The chemical potential gradient induced voltages are then calculated by subtracting the thermoelectric voltages from the maximum overall voltage outputs, and they are plotted against different fuel ratios of nitrocellulose and NaN_3 (**Figure 3-1c**). It is clear that a p-doping chemical, such as nitrocellulose, necessarily sets up a negative chemical potential contribution, and this undesired voltage cancelation can be mitigated by utilizing a synergistic, n-doping chemical such as NaN_3 . It should also be noted that the Fermi level corresponding to zero chemical potential gradient is measured to be 0.01 eV (relative to the pristine, undoped SWNT with 0 eV Fermi energy). This indicates that a 0.6 nitrocellulose/ NaN_3 weight ratio returns approximately

the same Fermi level as a pristine SWNT. The fact that this mixture of p- and n-dopants offers zero “Excess Thermopower voltage” strongly supports that those voltages are created by the chemical potential gradient across the wavefront, as rooted in the Excess Thermopower theory.²⁵ We also note that this 0.6 weight ratio of nitrocellulose and NaN_3 yields approximately a 1:1 ratio of the nitro and azide groups. This may explain, on a molecular level, why this particular mixture of the p- and n-dopant affords the electronic structure of a pristine, undoped SWNT yarn.

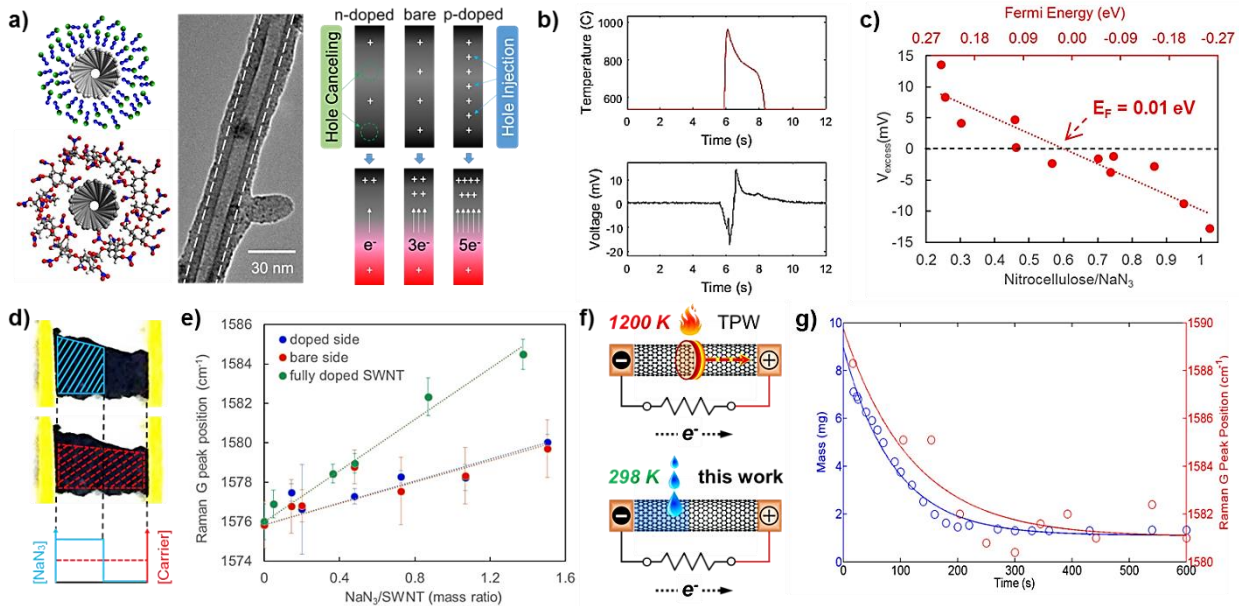


Figure 3-1. (a) Schematic of sodium azide (top left) and nitrocellulose (bottom left) coated CNT. The solid chemicals physically contacts the CNT sidewall. Transmission electron micrograph (middle) of a chemically coated MWNT synthesized by wet impregnation. The dashed line indicates the boundary between the MWNT and chemical coating. Schematic (right) illustrating the effect of doping on the electronic structure of the CNTs as well as the Seebeck coefficients. (b) Typical temperature and output voltage profiles of the thermopower wave launched on a CNT yarn pre-doped with nitrocellulose and sodium azide. (c) A plot of excess thermopower

contribution to the overall output voltage as a function of the mass ratio of nitrocellulose (p-dopant) and sodium azide (NaN_3 , n-dopant) pre-adsorbed onto the CNT network. **(d)** Schematic of a flat CNT fiber half-doped with NaN_3 (blue). Red line indicates the resulted carrier profile after carrier diffusion. **(e)** Raman G peak shift of CNT plotted against the NaN_3/CNT mass ratio. Green represents CNT fiber entirely covered with NaN_3 . For half-doped samples, red reflects the Raman shifts in the undoped (pristine) region, whereas the blue shows the NaN_3 -doped region. **(f)** Contrasting voltage generation mechanisms for conventional thermopower waves (TPW, top) and the reversible chemical doping in this work (bottom). In the new method, liquid chemicals (e.g. acetonitrile, MeCN) are injected onto a suspended CNT fiber and voltages are collected by an oscilloscope connected to the CNT fiber via copper electrodes. **(g)** Time evolution of Raman G peak shift of CNT fibers with MeCN injected at $t = 0$ s. MeCN evaporation is simultaneously monitored by measuring fiber mass as a function of time.

This synergistic effect between the NaN_3 -CNT coupling and thermoelectricity originates from the chemical potential difference between a pristine CNT and a NaN_3 -doped CNT. We further reason that a solid dopant, such as NaN_3 , is not ideal for isolating voltages induced by the chemical potential gradient because the characteristic time scale for NaN_3 to dope the CNT is much larger than the time scale for carrier dissipation by the metallic portion of CNTs in the doped region. This carrier relaxation mechanism, depicted in **Figure 3-1d**, is thought to be responsible for the absence of electrical potential across the doped and undoped region of the CNT fiber coated with a solid dopant. We validate this mechanism by measuring the Raman G band shifts (and hence the Fermi level)^{28,29} of two classes of SWNT fibers, one coated with NaN_3 over the whole surface and the other only over half of the SWNT surface. We see that the electronic structures between the doped

and undoped half are indistinguishable, with the undoped half responding to the dopant concentration (manifested by the NaN_3/SWNT ratio) half as quickly as the samples doped evenly with NaN_3 (**Figure 3-1e**). This clearly indicates that over time the change of carrier density is averaged out over the whole SWNT surface.

The combustion-aided, rapid undoping process resulting from the propagation of a reaction wave in the TPW phenomenon is key to the observed Excess Thermopower (**Figure 3-1f**, top). We develop a method that isolates this chemical potential gradient from thermoelectricity, which also represents the first CNT-based voltage generation process led by chemical doping, free from combustion and parasitic heat loss thereof. This is realized by selectively applying a liquid dopant (e.g. p-doping acetonitrile, MeCN) towards one end of the CNT fiber at room temperature (**Figure 3-1f**, bottom). Raman measurements show that the SWNT G peak shift (red) occurs on a similar time scale to that of the mass reduction (blue) due to evaporation, indicating the rapid chemical-electronic coupling between MeCN and the SWNT fiber (**Figure 3-1g**). The MeCN infiltrated into one end of the SWNT network draws electrical current towards the opposite electrode, immediately inducing a voltage across the SWNT network that slowly decays over time (**Figure 3-2a**). The polarity of this chemically induced voltage also switches as MeCN is applied to either end of the CNT fiber. **Figure 3-2b** summarizes one proposed mechanism for this chemically induced electrical potential. Upon contact, a Schottky barrier (Φ_{SB}) establishes across the Cu-SWNT interface. The subsequent MeCN doping onto the left side of the SWNT network attracts electrons from SWNTs' valence band (VB), causing it to become more p-doped. With the Cu-SWNT Schottky barrier preventing hole movements onto the Cu electrode, these extra holes travel towards the right end of the SWNT network, creating

a corresponding electrical potential difference. For samples where Ag electrodes are used, the metal-SWNT contact becomes Ohmic, and upon MeCN doping, no open circuit voltage is present (**Figure 3-2c**). These observations further substantiate the importance of a Schottky barrier in the metal-SWNT interface for this phenomenon.

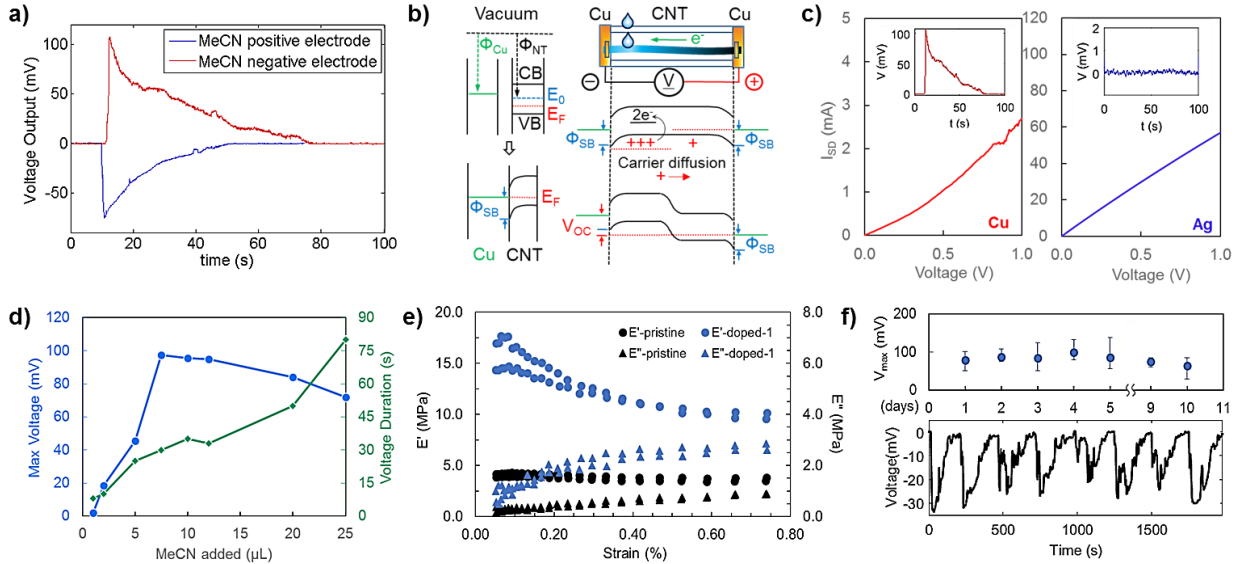


Figure 3-2. (a) Typical open circuit voltage profiles of MeCN (20 μL) injected onto the CNT fiber (0.2 mg, 3 mm \times 15 mm \times 0.1 mm). When MeCN is injected onto the CNT connected to the positive electrode, a negative open circuit voltage (blue) is observed, and vice versa (red). (b) Formation mechanism of a Schottky barrier (Φ_{SB}) in a Cu-CNT metal-semiconductor junction (left), and chemically-induced open circuit voltage across a CNT network. Here, Φ_{M} and Φ_{NT} denote the work functions of the metal (Cu) and CNT, respectively; VB and CB denote the valence and conduction bands for the CNT, respectively; E_0 represents the middle of the CNT band gap, and E_{F} is the Fermi energy of the CNT (naturally p-doped by O_2); V_{OC} denotes the open circuit voltage. (c) Source drain current (I_{SD}) for CNT devices fabricated with Cu (red) and Ag (blue) electrodes plotted against the source drain voltage. The insets are the voltage profiles generated

with each sample. **(d)** Maximum open circuit voltage (blue) and duration of voltage (green) plotted as a function of the amount of MeCN applied. **(e)** Storage modulus (E') and loss modulus (E'') at strains 0.1 – 0.8 % for pristine (black) and 1-time-MeCN-doped (blue) SWNT fiber samples. Measurement frequency is 1 Hz and the temperature is 30 °C. **(f)** Long term (10 days) stability test of voltage generation using the same CNT samples (top). Voltage profile obtained from continuous MeCN addition ($8 \times 20 \mu\text{L}$) within 2000 s (bottom).

The perturbation to the SWNT Fermi energy due to MeCN doping drives a short circuit current with a peak magnitude of 5.03 μA . The resulted open circuit voltage profile is studied as a function of the amount of MeCN applied (**Figure 3-2d**). While the voltage duration seems to increase linearly with the MeCN volume, there is a clear optimum for the voltage magnitude. This is expected because the magnitude of electrical potential difference stems from the MeCN concentration gradient across the CNT network, and the longitudinal transport (between two electrodes) of MeCN via capillary interaction, although undesired, is still present. Furthermore, the evaporation (hence the spontaneous desorption) of the dopant molecule allows for a non-invasive, reversible voltage generation process. We performed electrical conductivity, BET surface area, and mechanical storage modulus (**Figure 3-2e**) analyses on pristine as well as MeCN doped SWNT fibers, and observed no evidence of structural damage caused by MeCN doping. As a result, fibers not only generate voltages without noticeable reduction over 10 days (**Figure 3-2f**, top), they are also capable of continual usage with virtually no intermission time in between cycles over 2000 s (**Figure 3-2f**, bottom). It should also be noted that this voltage generation is not limited to liquid dopants; MeCN in its gaseous state is also capable of adsorbing onto the CNT surface and creating a potential drop. These results pave the way for a different

mode of chemical detection, in which virtually no voltage bias and no electrical power are necessary, and its chemical specificity stems from the various functionalizations that can be installed onto the CNT surface.

To demonstrate that this doping induced electrical potential can be further tuned through chemical modifications of the CNT, we adjust the amount of oxygen bounded to the SWNT surface through either acid treatment (oxidization)³⁰ or pyrolysis (reduction).³¹ Previous work suggests that the oxidized CNT surface enhances its absorption of polar organic solvents,³² and we show that this increased absorption leads to a more thorough MeCN-CNT doping, thus further augmenting the voltage output. **Figure 3-3a** illustrates the macroscopic surface height profiles ($500\ \mu\text{m} \times 500\ \mu\text{m}$) of the SWNT networks with different surface oxygen coverages (determined using XPS), and the Δz measures the maximum altitude change of the surface landscape. It is clear that the increased surface oxygen occupancy corresponds to a more extended and flattened fiber network, which we attribute to the nanotube diameter growth due to its external oxygen functionalization. The corresponding electron micrographs (**Figure 3-3a**, $250\ \text{nm} \times 250\ \text{nm}$) of samples at each oxidation level further reveal the thinning of SWNT bundles and the increased fiber porosity at higher oxygen coverages. This increase in effective surface area is verified using cyclic voltammetry, where the SWNT surface area (available to polar organic solvent molecules) is estimated from the electric-double layer capacitance in an aqueous solution. Specifically, we measure an 11.7 fold-increase in surface area upon acid treatment (from $5.18\ \text{m}^2/\text{g}$ for bare to $60.4\ \text{m}^2/\text{g}$ for acid treated SWNT fibers). It is worth noting that BET surface area analysis with N_2 shows no such increase in fiber porosity upon acid treatment. This suggests that the hydrophobic-to-hydrophilic-switch led by CNT oxidation opens up

more intercalation sites within the CNT bundle for polar organic molecules such as MeCN. The enhanced molecular intercalation is thought to augment the adsorption rate for MeCN. The depth profile of the oxygen atom percentage in the SWNT fiber is also obtained (**Figure 3-3b**). Monatomic depth profiling uses Ar-ion beam to etch layers of the fiber surface, revealing subsurface information. There is a clear reduction of oxygen content deeper into the fiber (longer sputtering time), and this reduction in polar functional groups could also hinder MeCN infiltration, limiting the maximum voltage that can be reached through chemical doping. We further correlate the binding energy of the carbon 1s orbital (C^{1s}) with the SWNT surface oxygen content and find a significant decrease of the binding energy (which translates to an increase in C^{1s} photoelectron kinetic energy) as we increase the oxidation level (**Figure 3-3c**). This upshift of photoelectron kinetic energy of an otherwise unchanged carbon atom suggests the SWNT surface is p-doped by the added oxygen moieties.³³

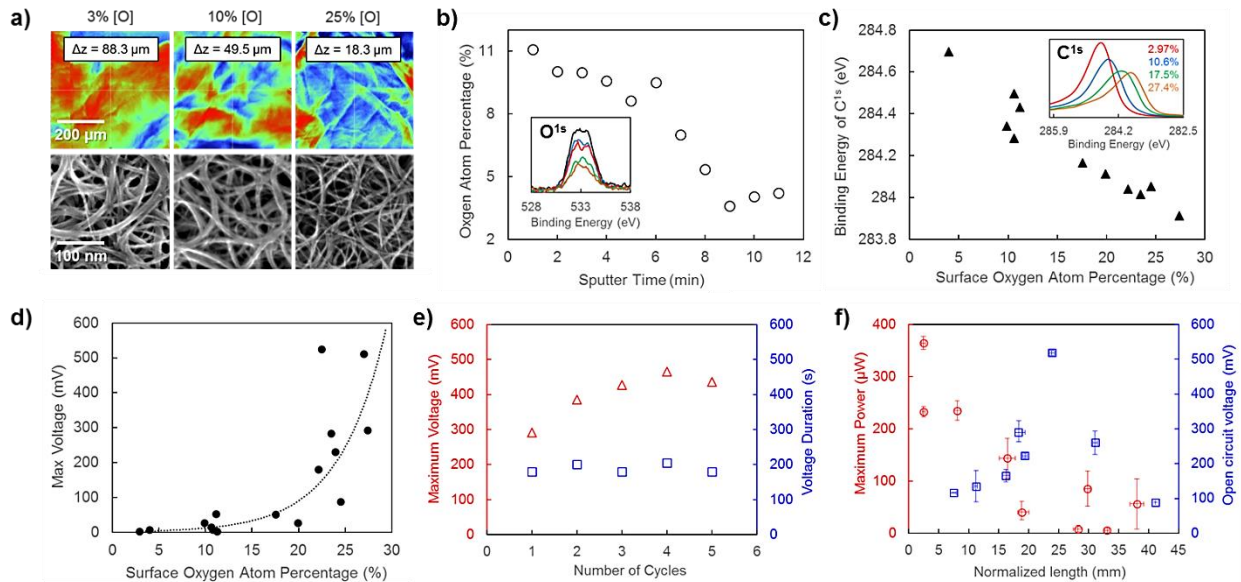


Figure 3-3. (a) Surface depth profiles (top) of CNT fiber samples with various amounts of oxygen containing functional groups, measured using a profilometer (red indicates elevated areas). Each Δz value indicates the maximum height difference observed thereof. The corresponding electron micrograph of each sample is shown at bottom. (b) XPS measured surface oxygen atom percentage plotted as a function of the Ar-ion gun sputtering time, corresponding to the CNT sample depth. The inset shows the XPS peak of the oxygen 1s orbital, with its intensity reducing as the sputtering time increases. (c) Binding energy of the carbon 1s orbital plotted against the fiber surface oxygen atom percentages. The inset shows the right shift (in the increased binding energy direction) of C^{1s} orbital as the oxygen level increases. (d) Maximum MeCN doping voltage plotted against CNT surface oxygen atom percentage determined via XPS. (e) Long term (5 cycles) stability test of voltage generation using oxidized CNT fiber. (f) Closed circuit maximum power (red) and open circuit voltage (blue) generated using acid treated CNT fibers plotted against normalized fiber length. All samples prepared are standardized to 3 mm of width.

To explore the effect of CNT oxidation on its voltage output, we prepare 15 SWNT fiber samples using either pyrolysis or acid treatment at different acid strengths, spanning a variety of surface oxygen concentrations (**Figure 3-3d**). An exponentially increasing output voltage as a function of surface oxygen percentage is observed. The super-linear dependence of the maximum voltage on the oxygen content allows us to achieve over 525 mV at around 25.0% oxidation level. The enhanced voltage generation process with oxidized fibers also appears to be highly reversible. Devices fabricated following this method provide sustainable performances for many cycles (**Figure 3-3e**). Additionally, closed circuit power measurements are performed using the oxidized SWNT samples. Each sample is impedance-matched to maximize the power output, and its maximum power is

plotted against the fiber length (**Figure 3-3f**). Specifically, with a device of length 469 μm , we generate 352 μW of maximum power, resulting in a peak power density of 30.0 kW/kg of oxidized SWNT (with an average value of 26.7 kW/kg). The length scaling of the average gravimetric power output is also presented. It is also noted that the open circuit voltage does not possess the similar inverse scaling; rather, it peaks around a fiber length of 25 mm and starts decaying as the sample becomes smaller. This interesting inverse length-scaling of the maximum power ($P_{\text{max}} \sim L^{-1.03}$) highlights that this CNT-based power generation is enhanced at the microscale, and provides opportunities for further developments towards more efficient micro- or even nanoscale energy harvesting from chemical interactions.

To conclude, we demonstrate in this work a reversible process to induce an unbiased voltage across a CNT network via local chemical doping that leads to more than 0.5 V potential difference across a device. This work also establishes the first experimental validation of Excess Thermopower theory, which predicts that switching from a p-doping to n-doping fuel creates an additive voltage from the transient chemical potential gradient that greatly increases the output from thermopower wave propagation. The theory was published previously but is only validated, to great effect, in this report. Furthermore, we isolate this unique mode of voltage generation, uncoupling the chemical potential gradient from thermoelectricity, by mimicking the time scale of a traveling reaction wave with a liquid dopant (MeCN) infiltrating into a CNT network. This voltage, driven by a spatial disparity in the Fermi energy across the carbon lattice, is shown to be highly tunable through chemical modification of the CNT surface, allowing rapid intercalation of dopant molecules into the CNT bundles, and can reach an unprecedented 525 mV using purely a

chemical-CNT interaction. MeCN is physically adsorbed onto the CNTs under room temperature without compromising the structural integrity of the fiber upon evaporation, thus leading to continual energy conversion with excellent long-term stability. Further improvements towards higher voltage outputs can be realized by additional chemical and physical (e.g., nanotube alignment, porosity, etc.) modifications of the CNT fiber, as well as tuning the dopant molecular structure. This unique electricity occurrence through direct chemical coupling onto a CNT network, together with an excellent control over the peak voltage and duration, enables fundamentally different approaches to CNT-facilitated chemical detection and energy generation.

3.3 Experimental Details

Characterizations of the pristine CNT fibers: Fibers fabricated with MWNT (aspect ratio (L/D) 350-550; 6-8 walls; 70-80% carbon content by TGA; average diameter 10 nm; average length 4 μm ; bulk density 0.06-0.08 g/cm^3) and fibers fabricated with SWNT (diameter 1-1.3 nm; length 1-5 μm ; >85% SWNT purity; 5-15% residual catalyst; bulk density 0.037 g/cm^3) are used in this study. (i) In-situ G peak shift of the CNT bundle is characterized by a confocal Raman spectrometer (Horiba Jobin-Yvon LabRAM Raman Microscope). Time evolution of the G peak position is recorded before and after MeCN addition. Automatic re-focusing is performed in between each measurement to prevent peak shift from the intensity variation. (ii) I-V measurements are performed using a Semiconductor Parameter Analyzer within a probe station. An external source drain voltage (scanning from 0.0 V to 1.0 V) is applied across the CNT sample while the source drain current is measured. (iii) BET measurements with N_2 is done using an Accelerated Surface Area and Porosimetry System from Micromeritics (ASAP 2020). Samples are

degassed at 150 °C, then surface area normalized by weight is measured at -196°C. (iv) A dynamic mechanical analyzer (DMA Q800, TA Instruments) characterizes the mechanical properties of the SWNT fibers before and after doping in a nondestructive way, specifically, we measured the storage modulus and loss modulus of the fibers at multi-strain mode with strain ranging from 0.10 to 0.80%.

Thermopower wave launch, voltage and temperature data collection: Thermopower wave devices with the pre-doped CNT yarns are prepared using copper electrodes and open circuit voltages are measured with an oscilloscope. A Tungsten Joule-heater is used in the ignition process on one end of the CNT. The temporal temperature profile of the CNT is recorded during wave propagation with a pyrometer.

Chemical modification of CNT (acid treatment and pyrolysis): Acid treatments are performed by soaking the CNT into a mixture of H₂SO₄/HNO₃. The degree of modification is controlled by the concentration as well as the ratios of the acids. Concentrated acid solution (3:1 (v/v) of H₂SO₄/HNO₃) and diluted acid solution (3:1:40 (v/v) of H₂SO₄/HNO₃/H₂O) are used. Pyrolysis was performed under N₂ in a quartz tube furnace. Samples are kept at 200 °C for 30 mins, then at 600 °C for 30 mins, and finally at 1000 °C for 30 mins.

Characterizations of the modified CNT fibers: (i) The macroscopic surface landscape of CNT networks is measured using a profilometer (BRUKER DektakXT™). The scan area is 500 μm × 500 μm and the resolution is 0.5 μm/point in the y-axis and 2 μm /point in the lateral direction. (ii) Oxygen atomic concentration on the CNT is characterized using XPS (ULVAC-PHI, INC. PHI VersaProbe II) with a monochromated Al Kα source. The oxygen

content value is calculated as an atomic percentage from the integration of O1s peak and that of C1s peak in the high-resolution scans. (iii) Cyclic Voltammetry is used to estimate the surface area from the electric-double layer capacitance of each CNT fiber in aqueous solution. The electrochemical measurements are performed in a three-electrode configuration cell with a Gamry potentiostat (interface 1000). The voltammograms are obtained in 10 mL of 0.1 M KCl electrolyte prepared in Millipore water (18 M Ω cm) with a glassy carbon electrode (A=0.07cm²), Ag/AgCl in saturated KCl reference electrode and a Pt wire counter electrode (CH Instruments, Inc.).

3.4 References

- (1) M. S. Dresselhouse, G. D., P. C. Eklund *Science of Fullerenes and Carbon Nanotubes*; Academic Press: San Diego, 1996.
- (2) Dai, H.; Hafner, J. H.; Rinzler, A. G.; Colbert, D. T.; Smalley, R. E. *Nature* 1996, 384, 147.
- (3) Wong, S. S.; Joselevich, E.; Woolley, A. T.; Cheung, C. L.; Lieber, C. M. *Nature* 1998, 394, 52.
- (4) Baughman, R. H.; Cui, C.; Zakhidov, A. A.; Iqbal, Z.; Barisci, J. N.; Spinks, G. M.; Wallace, G. G.; Mazzoldi, A.; De Rossi, D.; Rinzler, A. G.; Jaschinski, O.; Roth, S.; Kertesz, M. *Science* 1999, 284, 1340.
- (5) Kong, J.; Franklin, N. R.; Zhou, C.; Chapline, M. G.; Peng, S.; Cho, K.; Dai, H. *Science* 2000, 287, 622.
- (6) Tans, S. J.; Verschueren, A. R. M.; Dekker, C. *Nature* 1998, 393, 49.
- (7) Choi, W.; Hong, S.; Abrahamson, J.; Han, J.; Song, C.; Nair, N.; Baik, S.; Strano, M. *Nat Mater* 2010, 9, 423
- (8) H. Zabel, S. A. S., Eds. *Graphite Intercalation Compounds II: Transport and Electronic Properties*; Springer-Verlag: New York, 1992; Vol. 18.
- (9) Dillon, A. C.; Jones, K. M.; Bekkedahl, T. A.; Kiang, C. H.; Bethune, D. S.; Heben, M. J. *Nature* 1997, 386, 377.
- (10) Nalimova, V. A.; Sklovsky, D. E.; Bondarenko, G. N.; Alvergnat-Gaucher, H.; Bonnamy, S.; Béguin, F. *Synthetic Metals* 1997, 88, 89.
- (11) Tsang, S. C.; Chen, Y. K.; Harris, P. J. F.; Green, M. L. H. *Nature* 1994, 372, 159.
- (12) Collins, P. G.; Bradley, K.; Ishigami, M.; Zettl, A. *Science* 2000, 287, 1801.

- (13) Tan, C. W.; Tan, K. H.; Ong, Y. T.; Mohamed, A. R.; Zein, S. H. S.; Tan, S. H. *Environmental Chemistry Letters* 2012, 10, 265.
- (14) Pfohl, M.; Glaser, K.; Ludwig, J.; Tune, D. D.; Dehm, S.; Kayser, C.; Colsmann, A.; Krupke, R.; Flavel, B. S. *Advanced Energy Materials* 2016, 6, n/a.
- (15) Jain, R. M.; Howden, R.; Tvrdy, K.; Shimizu, S.; Hilmer, A. J.; McNicholas, T. P.; Gleason, K. K.; Strano, M. S. *Adv. Mater.* 2012, 24, 4436.
- (16) Lee, J. M.; Park, J. S.; Lee, S. H.; Kim, H.; Yoo, S.; Kim, S. O. *Adv. Mater.* 2011, 23, 629.
- (17) Walters, D. A.; Ericson, L. M.; Casavant, M. J.; Liu, J.; Colbert, D. T.; Smith, K. A.; Smalley, R. E. *Appl. Phys. Lett.* 1999, 74, 3803.
- (18) Li, Z.; Dharap, P.; Nagarajaiah, S.; Barrera, E. V.; Kim, J. D. *Adv. Mater.* 2004, 16, 640.
- (19) Dharap, P.; Li, Z. L.; Nagarajaiah, S.; Barrera, E. V. *Nanotechnology* 2004, 15, 379.
- (20) Liu, Z.; Hu, L.; Liu, J.; Qiu, C.; Zhou, H.; Hashim, D. P.; Shi, G.; Peng, C.; Najmaei, S.; Sun, L.; Lou, J.; Ajayan, P. M. *Nano Lett.* 2011, 11, 5117.
- (21) Zhao, Y. C.; Song, L.; Deng, K.; Liu, Z.; Zhang, Z. X.; Yang, Y. L.; Wang, C.; Yang, H. F.; Jin, A. Z.; Luo, Q.; Gu, C. Z.; Xie, S. S.; Sun, L. F. *Adv. Mater.* 2008, 20, 1772.
- (22) Romero, H. E.; Sumanasekera, G. U.; Mahan, G. D.; Eklund, P. C. *Physical Review B* 2002, 65, 205410.
- (23) Piao, M.; Joo, M. K.; Choi, J. H.; Shin, J. M.; Moon, Y. S.; Kim, G. T.; Dettlaff-Weglikowska, U. *RSC Adv.* 2015, 5, 78099.
- (24) Mahajan, S. G.; Liu, A. T.; Cottrill, A. L.; Kunai, Y.; Bender, D.; Castillo, J.; Gibbs, S. L.; Strano, M. S. *Energy & Environmental Science* 2016.
- (25) Abrahamson, J. T.; Sempere, B.; Walsh, M. P.; Forman, J. M.; Şen, F.; Şen, S.; Mahajan, S. G.; Paulus, G. L. C.; Wang, Q. H.; Choi, W.; Strano, M. S. *ACS Nano* 2013, 7, 6533.
- (26) Yanagi, K.; Kanda, S.; Oshima, Y.; Kitamura, Y.; Kawai, H.; Yamamoto, T.; Takenobu, T.; Nakai, Y.; Maniwa, Y. *Nano Lett.* 2014, 14, 6437.
- (27) Nonoguchi, Y.; Ohashi, K.; Kanazawa, R.; Ashiba, K.; Hata, K.; Nakagawa, T.; Adachi, C.; Tanase, T.; Kawai, T. *Scientific Reports* 2013, 3.
- (28) Farhat, H.; Son, H.; Samsonidze, G. G.; Reich, S.; Dresselhaus, M. S.; Kong, J. *Physical Review Letters* 2007, 99, 145506.
- (29) Park, J. S.; Sasaki, K.; Saito, R.; Izumida, W.; Kalbac, M.; Farhat, H.; Dresselhaus, G.; Dresselhaus, M. S. *Physical Review B* 2009, 80, 081402.
- (30) Worsley, K. A.; Kalinina, I.; Bekyarova, E.; Haddon, R. C. *Journal of the American Chemical Society* 2009, 131, 18153.

- (31) Li, Y.; Fernandez-Recio, L.; Gerstel, P.; Srot, V.; Aken, P. A. v.; Kaiser, G.; Burghard, M.; Bill, J. *Chemistry of Materials* 2008, 20, 5593.
- (32) Pan, B.; Xing, B. *Environmental Science & Technology* 2008, 42, 9005.
- (33) Graupner, R.; Abraham, J.; Vencelova, A.; Seyller, T.; Hennrich, F.; Kappes, M. M.; Hirsch, A.; Ley, L. *Phys. Chem. Chem. Phys.* 2003, 5, 5472.

Chapter 4

Observation of the Marcus Inverted Region of Electron Transfer from Asymmetric Chemical Doping of Pristine (*n, m*) Single-Walled Carbon Nanotubes

Article that contributes to this chapter:

Kunai, Y.*; Liu, A. T.*; Cottrill, A. L.; Koman, V. B.; Liu, P.; Kozawa, D.; Gong, X.; Strano, M. S. *Journal of the American Chemical Society* (2017), 139, 15328

Recent measurements have shown that when single-walled carbon nanotube (SWNT) papers are asymmetrically exposed to chemical dopants, electrical power is generated. We explore 27 small, organic, electron-acceptor molecules that are shown to tune the output open circuit voltage (V_{OC}) of the asymmetric chemical doping (ACD) across three types of pristine SWNT papers with varying (*n, m*) chirality distributions. A considerable enhancement in the observed V_{OC} , from 80 to 440 mV, is observed for SWNT/molecule acceptor pairs that have molecular volume below 0.12 nm³ and lowest unoccupied molecular orbital (LUMO) energies centered around -0.8 eV. The electron transfer (ET) rate constants driving the V_{OC} generation are shown to vary with the chirality-associated Marcus theory, suggesting that the energy gaps between SWNT and the LUMO of acceptor molecules dictate the ET process. When the ET rate constants and the maximum V_{OC} are plotted versus the LUMO energy of the acceptor organic molecule, volcano-shaped dependencies, characteristic of the Marcus inverted region, are apparent for three different sources of SWNT papers with modes in diameter distributions of 0.95 nm, 0.83 nm, and 0.75 nm.

This observation, where the ET driving force exceeds reorganization energies, allows for an estimation of the outer-sphere reorganization energies with values as low as 100 meV for the (8,7) SWNT, consistent with a proposed image-charge modified Born energy model. These results expand the fundamental understanding of ET transfer processes in SWNT and allow for an accurate calculation of energy generation through asymmetric doping for device applications.

4.1 Background on Asymmetric Chemical Doping

Single-walled carbon nanotubes (SWNTs) are 1-D electronic nanostructures with physical properties that depend upon a chirality or roll-up vector along the graphene plane.¹ Recent advances based on these properties have led to applications of individual or ensembles of SWNTs as scanning probes,^{2,3} actuators,⁴ chemical sensors,⁵ nanoelectronic devices,⁶ and miniature power sources.⁷ Since their discovery, investigations of SWNT have focused on their electrical or thermal responses to external stimuli, including changes in light emission,⁸ and mechanical strain⁹ with existing voltage or temperature biases. Applications have included SWNT-based photonics¹⁰ and sensors¹¹ where electrical resistance,¹² thermoelectric power (Seebeck coefficient),¹³ or local density of states¹² are measured and correlated with the respective magnitudes of the stimuli. Of these stimuli, chemical signals are apparently among the most studied.^{5,11,12,14} Owing to their size,¹ large surface area,¹⁵⁻¹⁸ and hollow geometry,¹ SWNTs are considered as prime materials for gas adsorption,¹⁹ Li storage,²⁰ and selective molecular filtering.²¹ Several studies have investigated chemical interactions with SWNT to alter electrical conductivity.^{5,12} In contrast, minimal attention has been given to methods to generate electrical potential directly through pristine SWNT-chemical interactions. Recently, we have observed the induction of an open circuit voltage (V_{OC}) across a manually exfoliated SWNT fiber via asymmetric chemical doping (ACD)

with a common organic solvent acetonitrile (CH_3CN).²² We proposed that CH_3CN molecules extract electrons from the SWNTs' valence band (VB) upon spatially asymmetric exposure, subsequently creating a chemical potential gradient, and a V_{oc} across the SWNT network. However, a detailed study on the mechanism of this electrical potential generation and its dependence on the chemical structure of the absorbent, as well as the electronic band structure of the SWNTs, is needed for further optimization of the voltage magnitude. In this work, we introduce a paper form of pristine solid SWNTs that offers systematic access to various chirality compositions to investigate this voltage generation mechanism. We study the dependence of the electrical power generation on chemical composition, molecular volume, and carbon nanotube electronic structure, showing that the rate and extent of potential generation can be described by a chirality associated Marcus electron transfer theory.

The ACD mechanism examined in this work is related to and derives from our previous observation of thermopower waves (TPW), which also convert chemical energy, in the form of an adsorbed reactive fuel, directly to electrical current by means of self-propagating reaction waves guided along nanostructured thermal conduits.⁷ Subsequent investigation revealed a mechanism dividing the TPW electrical energy generation into two distinct, additive components, namely a thermoelectric contribution, characterized by the Seebeck coefficient, and the transient chemical potential gradient, which we termed the “excess thermopower”.²²⁻²⁴ In subsequent work, we were able to isolate this “excess thermopower” to create a reversible electrical potential across the SWNTs at room temperature without high temperature reaction event.²² In this previous study, the electrical

coupling between adsorbed CH₃CN molecules and SWNT produced a persistent voltage via an unexplored mechanism.

Herein we investigate the chemical structure of potential acceptor molecules with the distinct lowest unoccupied molecular orbital (LUMO) levels and relate the rate and extent of voltage generation using an electron transfer (ET) description based on the classical Marcus theory.^{25,26} We show for the first time the observation of multiple Marcus inverted regions for ground state ETs between intermolecular solid-liquid interfaces, and reorganization energies as low as 100 meV are obtained for large diameter SWNTs. These efforts also establish the theoretical framework and a reliable procedure to predictively enhance the V_{OC} magnitude through the ACD phenomenon. In one set of experiments, we demonstrate this ability by amplifying the 80 mV CH₃CN doping voltage to 290 mV through injection of chloroacetonitrile (*Cl*-CH₂CN) on a (8,4) enriched HiPCo SWNT paper. To further strengthen support for this ET mechanism, several other types of SWNTs with varying chirality distributions are tested and compared against our theoretical predictions, offering up to 500 % (440 mV) V_{OC} enhancement in the absence of surface modifications. The remarkable agreement between experimental data and the theory described herein pave the way towards a general approach to evaluate SWNT/acceptor ET rates, with far-reaching scientific implications.

4.2 Asymmetric Chemical Doping Mechanism – an Electron Transfer Theory

Previously we observed that a persistent voltage can be generated via what we call asymmetric p-doping of a SWNT network using CH₃CN.²² When a SWNT paper is connected to two electrodes and partially exposed to CH₃CN, creating a doping gradient,

an open circuit voltage (V_{oc}) is generated as large as 100 mV. We postulated that the voltage generation mechanism involves an infiltrated p-dopant CH_3CN that withdraws electrons from the SWNT donor, and this results in an excess of holes on one side of the SWNT network, as shown in **Figure 4-1a**. Subsequent carrier diffusion across the SWNT network in the attempt to equalize the perturbed Fermi level forms a depletion layer, thereby leading to V_{oc} generation. In the current study, we expand the library of electron acceptors from the previous CH_3CN to 27 small molecule candidates, spanning nitrile, alcohol, and ketone functional groups, many of which are known p-dopants to SWNT, and investigate their ability to electrically couple with SWNTs for V_{oc} generation at room temperature. To minimize variations that stem from sample preparation, a new fabrication method for the SWNT fiber is developed, allowing us to precisely control the physical properties and chemical compositions of pristine SWNTs.

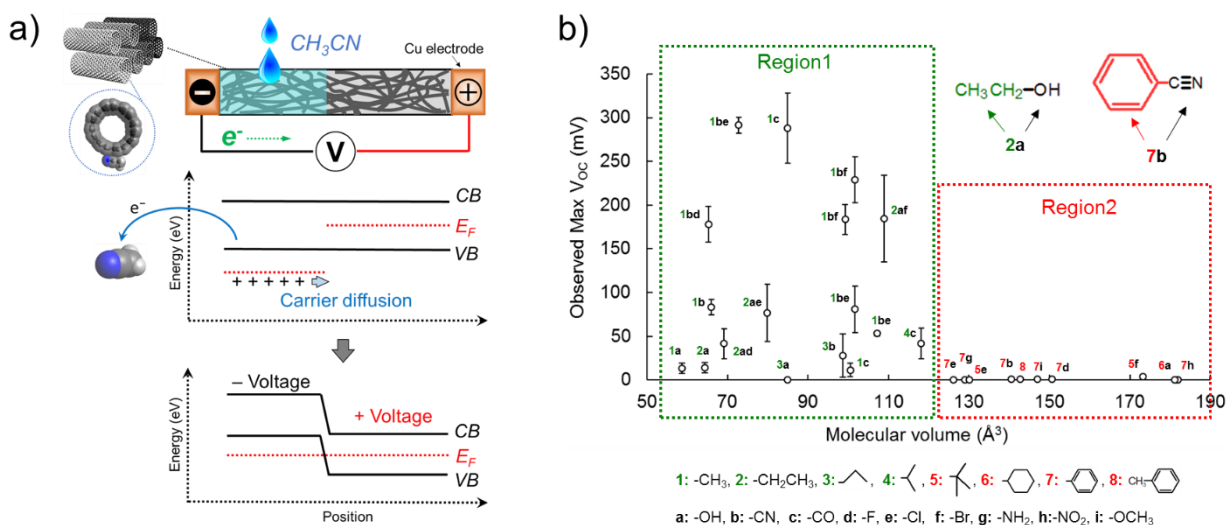


Figure 4-1. (a) Illustration for the generation of an open circuit voltage with asymmetrical acetonitrile (CH_3CN) doping with their Fermi levels (E_F), conduction band (CB), and valence band (VB). Copper electrodes are stacked on the both sides of the SWNT network, and the open circuit

voltage is measured by an oscilloscope through those electrodes. **(b)** Top graph shows maximum open circuit voltages on HiPCo SWNT of many acceptors versus their molecular volume. The error bars represent 95% confidence intervals. The bottom indicates the body structures (number) and functional groups (alphabet) of acceptor molecules.

Figure 4-1b summarizes the correlation between the maximum open circuit voltage (V_{OC}^{\max}) and the molecular volume of acceptor molecules adsorbed onto the (8, 4) enriched HiPCo SWNTs used with non-oxidative purification.²⁷ Clearly, the 27 dopants tested can be divided into two groups based on molecular size, with only smaller molecules in “region 1” yielding a measureable V_{OC} . We calculate the volume of these molecules based on structures optimized using DFT at the B3LYP/6-31G**(d, p) level, and the critical size for effective V_{OC} generation appears to center around 120 \AA^3 . This excludes all the benzene derivatives tested, including the strongly p-doping nitrobenzene.²⁸ It should be noted that a successful voltage generation typically involves a 3-step process, in which acceptor molecules must diffuse, adsorb (k_{ads}) and withdraw electrons (k_{ET}) from the SWNTs:



Where, θ_V refers to an empty site on the nanotube; A refers to a free acceptor molecule; θ_A refers to an adsorbed molecule; and θ_{ET} refers to an acceptor molecule that has undergone electron transfer (ET) with the SWNT. Molecular diffusivity is inversely proportional to the one-third power of its molecular volume,²⁹ but such a dependence is not observed in our study (**Figure 4-1b**), indicating this voltage generation is not diffusion controlled. We note, however, the limited space (0.36 nm of intertube spacing)³⁰ within a SWNT bundle prohibits effective intercalation and anchoring of large molecules, thereby setting an upper

volumetric bound for molecular adsorption and the subsequent ET. Indeed, the observed volumetric constraint of 120 \AA^3 corresponds to a molecular radius of 0.3 nm, a length scale on the same order with the reported intertube spacing. The fact that oversized molecules fail to register any V_{OC} suggests the existence of a limiting time window for ET to occur, beyond which the voltage generation process appears to slow down significantly. This proposed limiting time window is examined and validated below. For now, it suffices to realize its presence, and note that we observe no molecular-size dependency for dopants smaller than 120 \AA^3 (**Figure 4-1b**). Herein, we show that, in the lower size limit, the dominant factor for V_{OC}^{\max} is the rate of ET between the SWNT/acceptor pair.

We measure the V_{OC}^{\max} (blue circles) and initial ET rate (k_{ET} , black triangles) for 17 molecular electron acceptors in the lower size limit with varying LUMO energy levels (**Figure 4-2a**). These results reveal where CH_3CN -doped V_{OC}^{\max} (-0.48 eV, 80 mV) sits in the spectrum of maximum attainable voltages. Several other acceptor molecules more suitable for V_{OC} generation can be identified, given the apparent volcano shape dependence. Specifically, using the (8, 4) chirality enriched HiPCo SWNTs as an electron donor, chloroacetonitrile ($\text{Cl-CH}_2\text{CN}$) significantly outperforms CH_3CN , reaching a V_{OC}^{\max} of 290 mV. More interestingly, the k_{ET} 's, when plotted against the acceptor LUMO levels, exhibit a similar volcano shape (**Figure 4-2a**). It is worth discussing how the k_{ET} 's are measured in these experiments. First, we calculate the number density of electrons for (n, m)-SWNT, $N_e^{(n,m)}$, needed to lower the SWNT's Fermi level by 1 meV upon removal:

$$N_e^{(n,m)} = N_h^{(n,m)} - N_i^{(n,m)} = N_i^{(n,m)} \exp\left(\frac{\Delta E}{k_B T}\right) - N_i^{(n,m)} \quad (33)$$

Here k_B is the Boltzmann constant and T is system temperature, which remains constant at 298 K. ΔE represents the energy difference between the original and the reduced Fermi levels of the SWNT due to ET, which is set to 1 meV by definition. $N_i^{(n,m)}$ and $N_h^{(n,m)}$ represent the corresponding density of holes before and after the Fermi level reduction in the (n, m) -SWNT valance band (VB), respectively. $N_i^{(n,m)}$ is known to be a strong function of the density of state (DOS) of (n, m) -SWNT, and is estimated following a procedure by Marulanda *et. al.*³¹ We then obtain the initial rate of V_{OC} generation (k_{OC}), in units of $\text{mV}\cdot\text{s}^{-1}$, defined as the initial slope of the measured V_{OC} profile (**Figure 4-2b**). This, multiplied by the total number density of electrons needed to be withdrawn from the SWNT to create 1 mV, gives the overall initial ET rate constant, k_{ET} ,

$$k_{ET} = \sum_{(n,m)} k_{ET}^{(n,m)} = k_{OC} \sum_{(n,m)} P^{(n,m)} N_e^{(n,m)} \quad (34)$$

Here, $P^{(n,m)}$ represents the population density for each (n, m) -SWNT chiral components. This is obtained by deconvoluting the UV-Vis spectrum taken for the dissolved SWNT sample (**Figure 4-2c**).^{32,33}

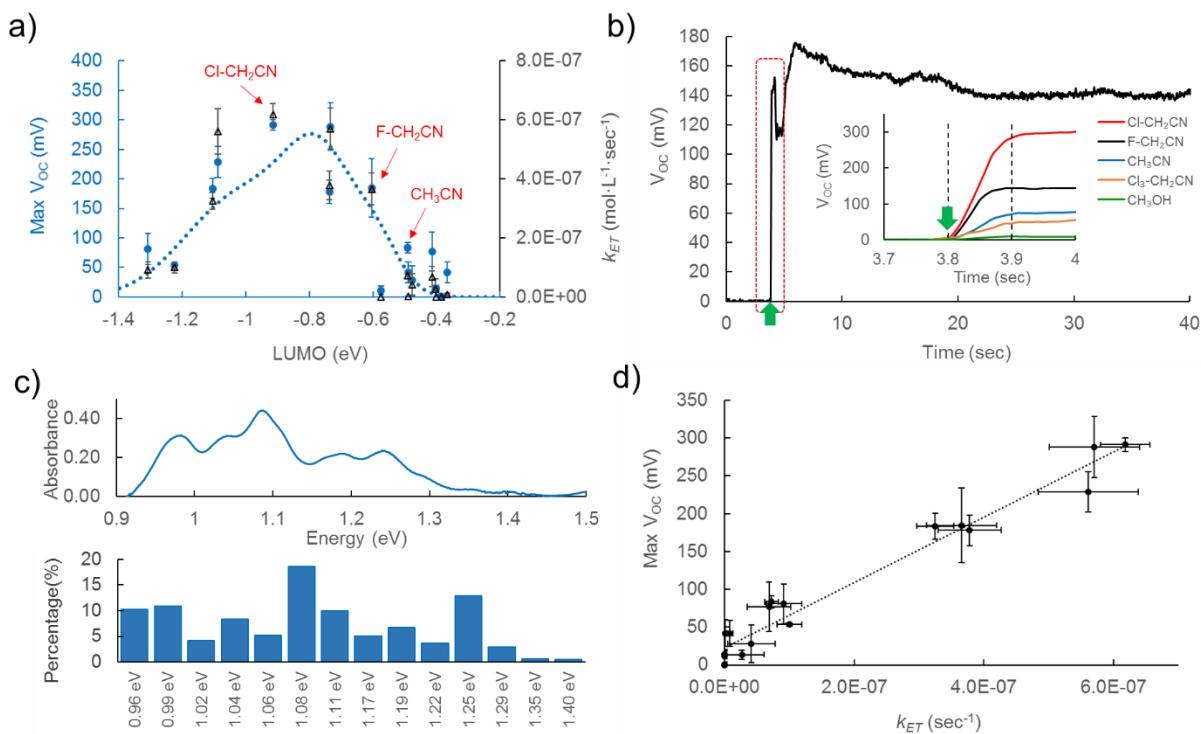


Figure 4-2. (a) Plots of the maximum open circuit voltage (blue) and the rate constant for electron transfer (black) on HiPCo SWNT as a function of the LUMO of molecular acceptors. The error bars represent 95% confidence intervals. LUMO levels were obtained by DFT calculation on B3LYP/6-31G**(d, p) level. The blue dotted line indicates a fitting line based on a Marcus equation for initial rate. (b) Typical open circuit voltage profile of HiPCo SWNT. A green arrow indicates the time when the liquid acceptor was added onto the SWNT network. Inset shows the magnified graph of open circuit voltages on several different acceptors. All of them shows very similar time-scale for their voltage creation. (c) UV-vis spectrum of HiPCo SWNT dispersed in water with 2 wt% SDS (top), and the chirality histogram obtained from the peak deconvolution of the UV-vis spectrum (bottom). The numbers on the bottom are the deconvoluted peak centers of the band gap energy. (d) Correlation between the maximum open circuit voltage and the rate constant for electron transfer on HiPCo SWNT. The error bars represent 95% confidence intervals.

We emphasize that the k_{ET} values measured this way, when plotted against acceptor LUMO's, yield a characteristic volcano shape similar to that of the V_{OC}^{\max} values (**Figure 4-2a**). The conspicuous correlation between a thermodynamic variable V_{OC}^{\max} and its kinetic counterpart k_{ET} is further corroborated by the proportionality shown in **Figure 4-2d**. This linearity between V_{OC}^{\max} and k_{ET} validates the aforementioned limited time window hypothesis to great effect; it further allows us to utilize classic Marcus ET theory,^{25,26} and develop a framework for first-principle calculations of the V_{OC}^{\max} 's as a function of the dopant LUMO levels and the SWNT chirality distributions. First, we formulate the overall ET rate constant k_{ET} using the chirality associated Marcus equation:³⁴

$$k_{ET} = \sum_{(n,m)} P^{(n,m)} k_{ET}^{(n,m)} = \sum_{(n,m)} P^{(n,m)} \gamma_n \pi d^{(n,m)} \exp \left[-\frac{(\lambda^{(n,m)} - \Delta G^{(n,m)})^2}{4\lambda^{(n,m)} k_B T} \right] \quad (35)$$

$$\Delta G^{(n,m)} = \left(E_F^{SWNT} - \frac{E_g^{(n,m)}}{2} \right) - E_F^A \quad (36)$$

where $d^{(n,m)}$, $\lambda^{(n,m)}$, and $\Delta G^{(n,m)}$ represent diameter, ET reorganization energy between a SWNT/acceptor pair, and thermodynamic driving force, for chiral specific (n, m) -SWNTs, with $\pi d^{(n,m)}$ accounting for the surface area differences between different nanotubes. E_F^{SWNT} is the SWNT Fermi level, $E_g^{(n,m)}$ is the (n, m) -SWNT band gap, and E_F^A is the LUMO level of the acceptor molecule A . Here γ_n is referred to as the collision pre-factor, which is left as a fitting parameter, and k_B is the Boltzmann constant. We note the k_{ET} 's calculated from the chirality associated Marcus theory, shown as the dotted blue line in **Figure 4-2a**, agrees extremely well with the k_{ET} 's obtained experimentally. We further note that the experimental rate data, as well as the Marcus theory predictions, both exhibit the

characteristic “Marcus inverted region”, where there exists an optimal thermodynamic driving force for effective ET, and further increase of the driving force actually reduces the ET rate.^{25,26} This is the hallmark of the original Marcus ET theory, which we have observed for the first time in a non-photo-excited ground state SWNT/acceptor system. Prior to this report, such an inverted region has only been seen once in a photo-induced ET system between SWNT and C₆₀,³⁵ or in small molecule pairs without SWNT as a coupling partner.³⁶⁻³⁸ Parenthetically, the existence of the Marcus inverted region in both k_{ET} and V_{OC}^{\max} also supports the voltage creation mechanism proposed in **Figure 4-1a**, which ascertains that the dominant step of the process is the ET from SWNTs to the adsorbed acceptor molecules.

With the overall ET rate determined, we recall the one-to-one linear correspondence between k_{ET} and V_{OC}^{\max} established previously (**Figure 4-2d**), and formulate the maximum open circuit voltage, V_{OC}^{\max} , as

$$V_{OC}^{\max} = Bk_{ET}^{tot} = B \sum_{(n,m)} P^{(n,m)} k_{ET}^{(n,m)} \quad (37)$$

where B is the proportionality constant measured experimentally. In order to validate this model and test its compatibility with other SWNT systems, two additional types of SWNT samples (CG200 and SG65i), with different chirality distributions, are investigated by the same method as the (8, 4) enriched HiPCo SWNT. The results are summarized in **Figure 4-3a** and **b**, with HiPCo samples included in the middle for comparison, and the theoretical predictions are overlaid on top of the V_{OC}^{\max} data as dotted lines. We underscore the level of agreement between experiment and theory for both the magnitude of V_{OC} and its volcano

shape dependence on acceptor LUMO levels. Even though SG65i SWNT devices appear to underperform in terms of the absolute V_{OC} magnitude, its inverted region is still present (**Figure 4-3a**, green inset). The model's predicative potential of optimal electron acceptors for assorted chiral SWNTs is also highlighted. With a similar chirality distribution, both CG200 (red) and HiPCo (blue) SWNTs suggest a -0.75 eV acceptor LUMO level (e.g. fluoroacetone) for optimal V_{OC} generation. SG65i, on the other hand, has $(6, 5)$ -SWNT as a major component; and this increase in its dominant band gap (from 1.08 eV to 1.25 eV, **Figure 4-3b**), corresponding to a reduction of the overall SWNT valence band (VB) energy, is compensated by the observed 0.15 eV downshift in its optimal acceptor LUMO level (from -0.75 eV to -0.90 eV, **Figure 4-3a**).

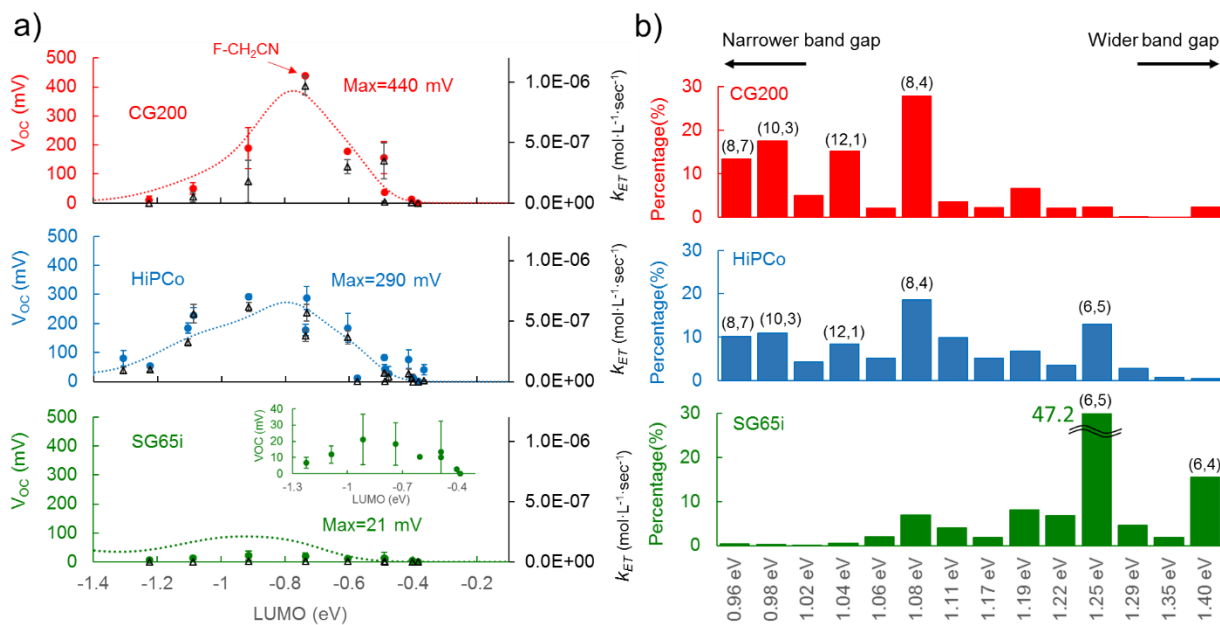


Figure 4-3. (a) The maximum open circuit voltages obtained versus LUMO levels of acceptors with CG200 (red), HiPCo (blue), and SG65i (green) SWNT samples. Black triangles on each graph represent the rate constant of electron transfer. The error bars represent 95% confidence intervals.

Dashed lines indicate fitting lines for maximum voltage by Marcus theory. Inset on the bottom graph is the magnified graph of SG65i. **(b)** Chirality distributions for each SWNT sample obtained from a deconvolution of the UV-vis spectra.

A closer comparison between different samples in **Figure 4-3** reveals that the V_{OC}^{max} depends significantly on SWNT chirality distributions. Within the three samples tested, CG200 includes mostly smaller band gap (1.06 eV; larger diameter) nanotubes; SG65i includes mostly larger band gap (1.24 eV; smaller diameter) nanotubes; and HiPCo has a relatively flat distribution (1.13 eV). Overall, smaller band gap SWNTs tend to generate higher V_{OC} values. This can be understood by (i) the chirality associated band gap differences, and (ii) diameter dependent SWNT reorganization energy variations. In regards to the first reason, there is a larger driving force (ΔG^0) between the donor VB and the acceptor LUMO for SWNTs with narrower band gaps, as shown schematically in **Figure 4-4a**. The larger driving force leads to faster ET, which ultimately creates a higher voltage. Indeed, **Figure 4-4b** illustrates this trend well by correlating the V_{OC}^{max} values measured for the electron acceptor fluoroacetonitrile ($F-CH_2CN$) and the ΔG^0 's (calculated from the concentration weighted average of SWNT band gaps) for different nanotube samples. This argument using a weighted average ΔG^0 simplifies the previous equations, but it effectively explains the V_{OC} magnitudes and their increasing trend favoring narrower band gap SWNTs.

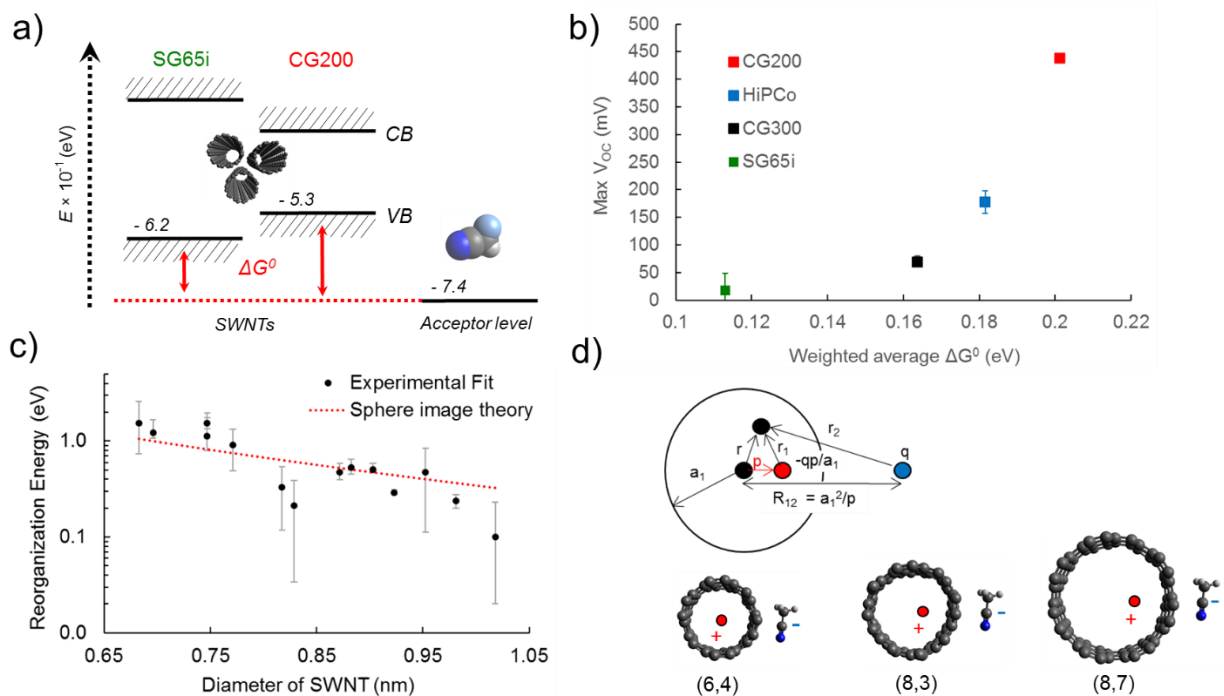


Figure 4-4. (a) Schematic band diagram of SWNTs and an acceptor. *CB* and *VB* refer to the conduction band and the valence band of the SWNT, respectively. ΔG^0 is driving force for electron transfer. SWNTs with narrower band gaps create larger ΔG^0 . (b) Correlation between the maximum open circuit voltage generated by fluoroacetonitrile and the weighted average ΔG^0 . The weighted average ΔG^0 was calculated from the weighted average band gap of each SWNT obtained from the chirality distributions in **Figure 4-3b**. The error bars represent 95% confidence intervals. (c) Black circle indicates reorganization energies against diameter of SWNT obtained from experimental fit, and the error bars represent standard errors. Red circle indicates reorganization energies obtained from modified Marcus equation of reorganization energy using sphere image theory. (d) (Top) Schematic of the sphere image. The blue dot is charged acceptor, having charge q , lying at a distance of R_{12} from the center of SWNT. a_1 and the red dot indicates a radius of SWNT and an image charge of that with $-qp/a_1$ locating inside the SWNT at a distance p from the center, respectively. (Bottom) The images of charge on different diameters of SWNT. Since p

increases with the diameter, in the case of larger diameter SWNT, the position of the image charge is away from center.

The chirality-dependent reorganization energies ($\lambda^{(n,m)}$) are directly related to the observed voltage output. The λ values are obtained by fitting the observed ET rates to Marcus theory. It is difficult to determine λ values with high confidence using HiPCo-SWNTs only, due to its weaker presence in the wider and narrower bandgap regions. CG200- and SG65i-SWNTs, with modes of diameter distributions of 0.95 nm and 0.75 nm, respectively, compensate for wider and narrower band gaps, improving the confidence intervals on λ values. These values are reported in **Figure 4-4c** as a function of SWNT diameter. A strong dependence is observed and the larger diameter SWNTs with smaller band gaps afford smaller λ values. According to Marcus, smaller λ allows for more facile ET (hence a larger voltage), owing to its reduced thermodynamic driving force requirement.^{25,26} Furthermore, this trend agrees well with Marcus's original formulation of the λ value,^{40,41} upon a sphere-image-charge correction.³⁹ In the Marcus scheme, λ can be divided into an inner-sphere (λ_i) and an outer-sphere (λ_o) component. Here, many reports have indicated that highly-conjugated π systems, such as CNTs, exhibit negligibly small λ_i due to their rigid backbones and delocalized electronic structures, rendering the λ_o a more dominant factor.^{35,40} On the other hand, λ_o is expected to vary for SWNTs of different chiralities even though the same acceptor (*i.e.* CH₃CN) is used, owing to the change in SWNT/acceptor molecular distances. The original Marcus equation, we note, is based on small molecule pairs, rightfully ignoring the dielectric image contribution arising from a dielectric surface.^{41,42} SWNT, on the other hand, constitute a continuous large cylindrical molecule, so the effect of the dielectric image is not negligible. With this insight, we modify the

Marcus equation as illustrated in **Figure 4-4d**, where the molecule charge q at the distance R_{12} induces a mirror charge of qR_{12} / a_1 at the distance p . The reorganization energy can therefore be calculated as the sum of free energies of two particles subtracted from the interparticle Coulomb interaction, as shown as follows,

$$\lambda_o = (\Delta e)^2 \left(\frac{R_{12}^2}{2a_1^3} + \frac{1}{2a_2} - \frac{R_{12}^2}{a_1(R_{12}^2 - a_1^2)} \right) \left(\frac{1}{\epsilon_{op}} - \frac{1}{\epsilon_s} \right) \quad (38)$$

where, a_1 , a_2 , r , D_{op} , and D_s indicate radii of SWNT, radii of acceptor, center-to-center separation distance, optical dielectric constant, and static dielectric constant, respectively. The red triangles in the **Figure 4-4c** show the calculated reorganization energies using the above equation, which explains the experimental trend well. Collectively, these two factors, one due to the inherently smaller band gaps and the other owing to the reduced reorganization energies, explain why smaller band gap SWNTs tend to create larger voltages. This consistency between reorganization energies derived from first principles (and zero fitting parameters) and those extrapolated from ET rate measurements highlights the success of the Marcus formalism and further strengthens our confidence over these observed inverted regions among SWNT/acceptor pairs.

A remaining question concerns the linearity between k_{ET} and V_{OC}^{\max} . To address this relationship, we hypothesize the existence of a limiting time window during which the diffusion, adsorption, and ET to the dopant molecules must occur. **Figure 4-2b** shows a typical V_{OC} profile generated from this asymmetric chemical doping technique, characterized by the rapid initial growth lasting approximately 0.1 seconds, beyond which the voltage creation significantly slows down. This sudden reduction of generation rate

seems to always happen at around 0.1 seconds, regardless of dopant identity (**Figure 4-2b** inset). In order to identify the factors preventing further voltage increase beyond the initial limiting time window, we analyze the dopant propagation along the SWNT network surface using high speed photography (**Figure 4-5**). To accurately track the solvent trajectories without edge effects, extended SWNT networks (15 mm in length) are used, as opposed to 5 mm used for the V_{OC} and k_{ET} measurements above. We monitor the wetting dynamics of several types of dopant molecules with distinct LUMO levels, and their initial propagation rate (for $L < 5$ mm) appears to be very similar (**Figure 4-5b**). It can be seen from both the time elapsed images (**Figure 4-5a**; top view) and the corresponding measurements (**Figure 4-5b**), at 0.1 seconds, the dopant molecules have transversed over 5 mm along the SWNT surface, which is the length of a typical device tested previously. This indicates that the entirety of SWNT surface is wetted with liquid dopants by 0.1 seconds, coherent with the observed voltage saturation time window (**Figure 4-2b**). However, it must be noted, that the voltage generation does not cease beyond the limiting time window; rather, the voltage simply recedes from its maximum and sustains for a long period (~ 100 s) before the eventual drop off, presumably led by dopant evaporation. This suggests that the acceptor molecules do not uniformly cover the entire SWNT cross-section, which would have resulted no electrical potential gradient across the device ends, and the recorded liquid spreading remains a surface phenomenon. In other words, the surface dopant concentration is much higher than that in the SWNT interior, due to slow vertical penetration. This through-plane dopant concentration gradient is supported by the time evolution of the fiber height profile (**Figure 4-5a**; side view), which illustrates an upward bending upon dopant addition. This bending event⁴³ can be explained by the

expansion of the SWNT network as the dopant molecules infiltrate the system, and the upward bending stems from a surplus of dopant concentration at the top. We further compare the initial dopant propagation (wetting) rate and the initial voltage generation rate (k_{OC} , **Figure 4-5c**), which clearly indicates that the wetting rate is constant across all dopants, not at all a function of k_{OC} . These evidences further strengthen the uniform “limiting time-window” hypothesis, which assumes equal initial voltage creation time (~ 0.1 s) for all liquid electron acceptors tested. This eventually gives rise to the observed, linear correlation between k_{ET} and V_{OC}^{\max} , shown in **Figure 4-2c**.

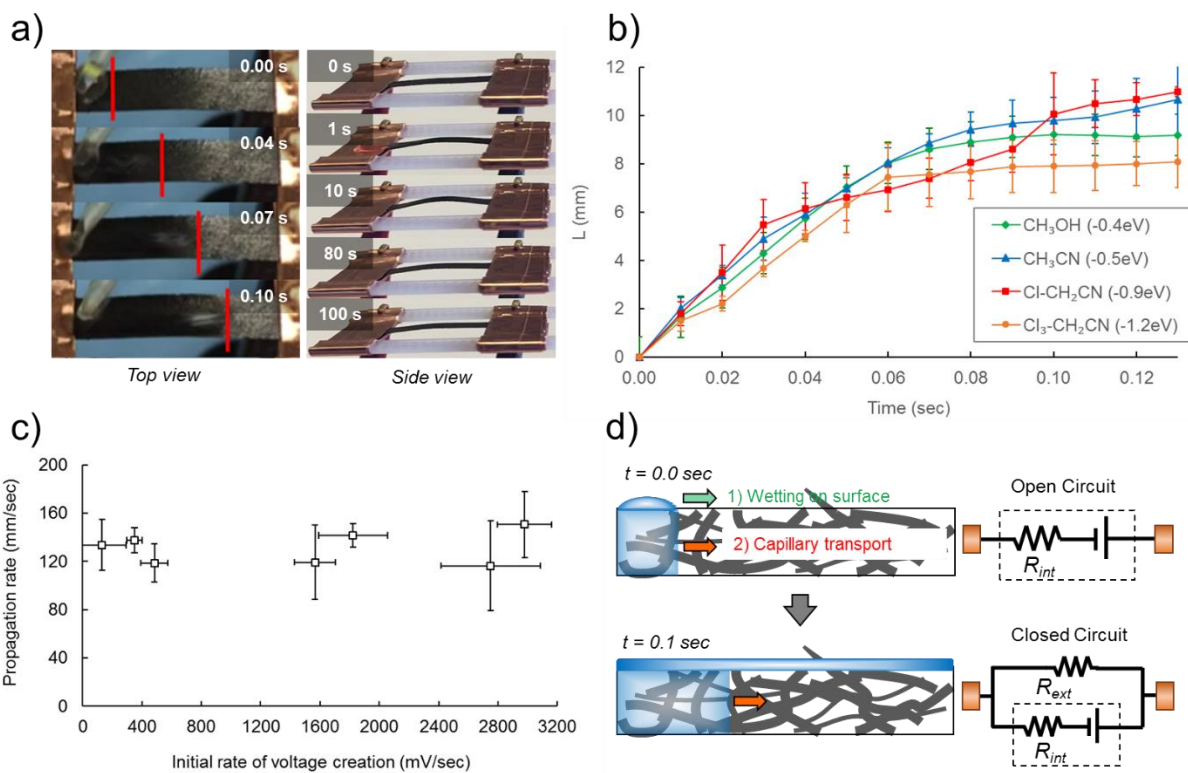


Figure 4-5. (a) (Top view); High speed photography (240 fps) of the CH₃CN propagation on the SWNT surface. Red lines indicate the spreading front of the CH₃CN at various points in time. (Side view); Pictures of the SWNT network from a side view after a liquid acceptor is added. The

SWNT network bends upward as the liquid acceptor is added. **(b)** Time propagation of several types of liquid acceptors, which have different LUMO levels, on a SWNT network, as obtained from slow motion videos. They show similar propagation speeds. The error bars represent 95% confidence intervals. **(c)** Correlation between the initial propagation speeds of liquid acceptors on SWNT and initial rate of voltage creations. It shows that the initial propagation rates are almost constant for all of the initial rates of voltage creation. The error bars represent 95% confidence intervals. **(d)** Schematic illustrations of the double structure model for the propagation of liquid acceptors. **(Top)** $t = 0.0$ sec; initial state before propagation of surface liquid acceptors. There are two types of propagation mechanisms: wetting propagation on the SWNT surface and capillary transport inside the SWNT network. **(Bottom)** $t = 0.1$ sec; the state after propagation of the surface liquid acceptors. Wetting propagation spreads to the entire SWNT surface more rapidly than the capillary propagation. The difference in rates is estimated to be a factor of 300, refer to the SI for the associated calculations. The right-side schematics indicate electrical circuit diagrams of the SWNT system of each state, respectively. Dotted black line indicates the original battery system of asymmetrically doped SWNT network, and R_{int} and R_{ext} indicate an internal resistance and an external resistance, respectively.

The above observations are described using a simple parallel transport model (**Figure 4-5d**), where mass transport of liquid dopants along the SWNT network can be partitioned into two parallel processes: (i) a wetting propagation along the top surface, and (ii) a capillary diffusion through the interior. Initially, the dopant molecules are injected into the SWNT network and the excess dopant forms a small droplet on the surface, which is what we track in slow motion (**Figure 4-5a**). These two liquid fractions traverse the SWNT fiber at considerably different rates, with the surface droplet governed by the classical equations

for wetting dynamics,⁴⁴ and the inner-sphere fraction described by Washburn's law.⁴⁵ These analyses reveal that the surface wetting rate (0.20 sec for 8mm) is approximately 300 times faster than that of the capillary transport (60 sec for 8mm), agreeing well with the difference in time scales measured for droplet spreading (**Figure 4-5a**; top view) and fiber bending (**Figure 4-5a**; side view).

We employ an equivalent circuit model to describe this limiting time window and why the time for voltage saturation seems to coincide with the characteristic time for dopant droplet spreading. During chemical doping, a V_{OC} across the SWNT device is measured through the copper electrodes, and the SWNTs are a voltage source with internal resistance R_{int} (**Figure 4-5d**; top). Once the spreading surface dopants reach the other side of the SWNT fiber, they create a parallel conductive channel (with resistance R_{ext}) bridging the two electrodes (**Figure 4-5d**; bottom). At this point, the original open-circuit voltage (V_{OC}) measurement becomes a closed-circuit one (V_{CC}):

$$V_{CC} = \frac{V_{OC}}{\left(1 + \frac{R_{int}}{R_{ext}}\right)} \quad (39)$$

Once the system becomes a closed-circuit, the measured voltage exhibits an abrupt reduction, the degree to which depends on the magnitude of R_{ext} . Indeed, this drop is repeatedly observed after the initial rapid voltage creation period illustrated in **Figure 4-2b**. This characteristic local minimum in the voltage profile validates the equivalent circuit model, and describes the physical origin of the limiting time window as the time it takes the dopant droplet to spread across the two electrodes, forming the aforementioned

“conductive channel”. We note that this parallel transport model, along with the equivalent circuit model, can be further extended to explain the full voltage profile.

Based on the concept of a chemical-doping SWNT electrical potential generator, various types of electron acceptor molecules are evaluated for their voltage generation capability. Open circuit voltages (V_{OC} 's) up to 440 mV (over 500% increase to the previously demonstrated 80 mV) are attained by optimizing acceptor LUMO levels and chirality distributions of pristine SWNTs. We reveal that the magnitude of the V_{OC} depends largely on the acceptor LUMO level and SWNT valance band (VB) level, and tuning the energy gap between these levels yields an optimal combination for V_{OC} generation. For each SWNT chirality distribution investigated, this optimal point is located at the peak of the volcano plot of the generated V_{OC} as a function of the acceptor LUMO levels. We further establish a linear correlation between the maximum V_{OC} generated and the SWNT/acceptor electron transfer rate (k_{ET}), which allows us to model this phenomenon using a chirality associated Marcus theory with high fidelity. A sphere-image-charge modified Born Energy model is used to understand the reorganization energies (λ 's) obtained, and the λ values as low as 100 meV suggest promising loss minimizations in future energy related ET schemes. This in turn constitutes the first experimental observation of a “Marcus inverted region” between ground state SWNT/acceptor pairs, which we have demonstrated in all three chiral SWNT systems tested. Together, these results provide a theoretical model help to accurately predict output V_{OC} magnitudes from different coupling partners, and also form the basis of a simple yet versatile strategy to characterize a broad library of SWNT/acceptor electron transfer systems otherwise hard to access.

4.3 Experimental Details

Materials: SWNTs powder samples were purchased; HiPCo from Nanointegris Technologies, Inc., CG200 and CG300 from SouthWest Nano Technologies Inc., SG65i from Chasm Advanced Materials Inc. Further purifications were done; firstly, extraction was done with hexane/water system and then purification was done using non-oxidative 37% hydrochloric acid (Aldrich) for 15 min under bath sonication condition, and an additional stirring was done at 45°C for 2 hrs. Purified powder samples were examined by BET, XPS, UV-vis as characterization. SWNTs network was made by hot-press method (5 tons at 50 °C for 10 min) with very small amount of water (50µL of water/30mg of SWNTs powder) to make the network rigid, dried for more than overnight, then cut into specific sizes. The cut SWNTs network was placed on across two copper electrodes then were fixed with another copper to make a device. Polymer (polyvinylalcohol) coating on the copper electrodes were added in order to protect the connection between SWNTs and electrodes from liquid acceptors, if necessary. Liquid Acceptor molecules were all purchased from sigma-aldrich and used without further purification.

Measurements: (i) Open circuit voltages of devices were measured by oscilloscope (Yokogawa Corporation of America, DL1735E). (ii) UV-vis spectra of SWNTs suspended solution were collected using UV-vis spectrometer (SHIMADZU, UV-3101PC). (iii) BET measurements with N₂ is done using an Accelerated Surface Area and Porosimetry System from Micromeritics (ASAP 2020). 30 mg of powder samples after purification were degassed at 150 °C, then surface area normalized by weight was measured at -196 °C. (iv) Oxygen atomic concentration and catalyst residue on the CNT were evaluated using XPS (ULVAC-PHI, INC. PHI VersaProbe II) with a monochromated Al K α source. The oxygen

content value was calculated as an atomic percentage from the integration of O_{1s} peak and that of C_{1s} peak in the high-resolution scans.

DFT calculation: (i) LUMO levels of acceptor molecules were calculated by DFT with B3LYP/6-31G**(d, p) level. Results obtained were corrected using linear relationship to match the experimental values. (ii) Molecular volume was also calculated by DFT with B3LYP/6-31G**(d, p) level, and calculations were done by 3 times and took their average.

4.4 References

- (1) M. S. Dresselhouse, G. D., P. C. Eklund. *Science of Fullerenes and Carbon Nanotubes*. (Academic Press, 1996).
- (2) Dai, H.; Hafner, J. H.; Rinzler, A. G.; Colbert, D. T.; Smalley, R. E. *Nature* 1996, 384, 147.
- (3) Wong, S. S.; Joselevich, E.; Woolley, A. T.; Cheung, C. L.; Lieber, C. M. *Nature* 1998, 394, 52.
- (4) Baughman, R. H.; Cui, C.; Zakhidov, A. A.; Iqbal, Z.; Barisci, J. N.; Spinks, G. M.; Wallace, G. G.; Mazzoldi, A.; De Rossi, D.; Rinzler, A. G.; Jaszinski, O.; Roth, S.; Kertesz, M. *Science* 1999, 284, 1340.
- (5) Kong, J.; Franklin, N. R.; Zhou, C.; Chapline, M. G.; Peng, S.; Cho, K.; Dai, H. *Science* 2000, 287, 622.
- (6) Tans, S. J.; Verschueren, A. R. M.; Dekker, C. *Nature* 1998, 393, 49.
- (7) Choi, W.; Hong, S.; Abrahamson, J.; Han, J.; Song, C.; Nair, N.; Baik, S.; Strano, M. *Nat Mater* 2010, 9, 423
- (8) Barone, P. W.; Baik, S.; Heller, D. A.; Strano, M. S. *Nat Mater* 2005, 4, 86.
- (9) *Journal of Sensors* 2012, 2012, 15.
- (10) Avouris, P.; Freitag, M.; Perebeinos, V. *Nat Photon* 2008, 2, 341.
- (11) Wang, Y.; Yeow, J. T. W. *Journal of Sensors* 2009, 2009, 24.
- (12) Collins, P. G.; Bradley, K.; Ishigami, M.; Zettl, A. *Science* 2000, 287, 1801.
- (13) Nonoguchi, Y.; Ohashi, K.; Kanazawa, R.; Ashiba, K.; Hata, K.; Nakagawa, T.; Adachi, C.; Tanase, T.; Kawai, T. *Scientific Reports* 2013, 3, 3344.
- (14) Yanyan, W.; Zhihua, Z.; Zhi, Y.; Xiaohang, C.; Dong, X.; Yafei, Z. *Nanotechnology* 2009, 20, 345502.

- (15) H. Zabel, S. A. S., Eds. Graphite Intercalation Compounds II: Transport and Electronic Properties. Vol. 18 (Springer-Verlag, 1992).
- (16) Peigney, A.; Laurent, C.; Flahaut, E.; Bacsa, R. R.; Rousset, A. *Carbon* 2001, 39, 507.
- (17) Cassell, A. M.; Franklin, N. R.; Tombler, T. W.; Chan, E. M.; Han, J.; Dai, H. *Journal of the American Chemical Society* 1999, 121, 7975.
- (18) Liu, C.; Fan, Y. Y.; Liu, M.; Cong, H. T.; Cheng, H. M.; Dresselhaus, M. S. *Science* 1999, 286, 1127.
- (19) Dillon, A. C.; Jones, K. M.; Bekkedahl, T. A.; Kiang, C. H.; Bethune, D. S.; Heben, M. J. *Nature* 1997, 386, 377.
- (20) Nalimova, V. A.; Sklovsky, D. E.; Bondarenko, G. N.; Alvergnat-Gaucher, H.; Bonnamy, S.; Béguin, F. *Synthetic Metals* 1997, 88, 89.
- (21) Tsang, S. C.; Chen, Y. K.; Harris, P. J. F.; Green, M. L. H. *Nature* 1994, 372, 159.
- (22) Liu, A. T.; Kunai, Y.; Liu, P.; Kaplan, A.; Cottrill, A. L.; Smith-Dell, J. S.; Strano, M. S. *Advanced Materials* 2016, n/a.
- (23) Mahajan, S. G.; Liu, A. T.; Cottrill, A. L.; Kunai, Y.; Bender, D.; Castillo, J.; Gibbs, S. L.; Strano, M. S. *Energy & Environmental Science* 2016.
- (24) Abrahamson, J. T.; Sempere, B.; Walsh, M. P.; Forman, J. M.; Şen, F.; Şen, S.; Mahajan, S. G.; Paulus, G. L. C.; Wang, Q. H.; Choi, W.; Strano, M. S. *Acs Nano* 2013, 7, 6533.
- (25) Marcus, R. A. *The Journal of Chemical Physics* 1956, 24, 966.
- (26) Marcus, R. A. *Reviews of Modern Physics* 1993, 65, 599.
- (27) Cinke, M.; Li, J.; Chen, B.; Cassell, A.; Delzeit, L.; Han, J.; Meyyappan, M. *Chemical Physics Letters* 2002, 365, 69.
- (28) Oh, J.; Roh, S.; Yi, W.; Lee, H.; Yoo, J. *Journal of Vacuum Science & Technology B* 2004, 22, 1416.
- (29) Zhang, S.; Shao, T.; Kose, H. S.; Karanfil, T. *Environmental Toxicology and Chemistry* 2012, 31, 79.
- (30) Abe, M.; Kataura, H.; Kira, H.; Kodama, T.; Suzuki, S.; Achiba, Y.; Kato, K.-i.; Takata, M.; Fujiwara, A.; Matsuda, K.; Maniwa, Y. *Physical Review B* 2003, 68, 041405.
- (31) Marulanda, J. M.; Srivastava, A. *physica status solidi (b)* 2008, 245, 2558.
- (32) Liu, H.; Nishide, D.; Tanaka, T.; Kataura, H. *Nature Communications* 2011, 2, 309.
- (33) Tvrđy, K.; Jain, R. M.; Han, R.; Hilmer, A. J.; McNicholas, T. P.; Strano, M. S. *ACS Nano* 2013, 7, 1779.
- (34) Nair, N.; Kim, W.-J.; Usrey, M. L.; Strano, M. S. *Journal of the American Chemical Society* 2007, 129, 3946.
- (35) Ihly, R.; Mistry, K. S.; Ferguson, A. J.; Clikeman, T. T.; Larson, B. W.; Reid, O.; Boltalina, O. V.; Strauss, S. H.; Rumbles, G.; Blackburn, J. L. *Nat Chem* 2016, 8, 603.

- (36) Imahori, H.; Guldi, D. M.; Tamaki, K.; Yoshida, Y.; Luo, C.; Sakata, Y.; Fukuzumi, S. *Journal of the American Chemical Society* 2001, *123*, 6617.
- (37) Sun, P.; Li, F.; Chen, Y.; Zhang, M.; Zhang, Z.; Gao, Z.; Shao, Y. *Journal of the American Chemical Society* 2003, *125*, 9600.
- (38) Kumbhakar, M.; Nath, S.; Mukherjee, T.; Pal, H. *The Journal of Chemical Physics* 2004, *120*, 2824.
- (39) Hernandez, J. A.; Assis, A. K. T. *Journal of Electrostatics* 2005, *63*, 1115.
- (40) Hiroshi, I.; Kiyoshi, H.; Tsuyoshi, A.; Masanori, A.; Seiji, T.; Tadashi, O.; Masahiro, S.; Yoshiteru, S. *Chemical Physics Letters* 1996, *263*, 545.
- (41) Marcus, R. A. *The Journal of Chemical Physics* 1965, *43*, 679.
- (42) Marcus, R. A.; Sutin, N. *Biochimica et Biophysica Acta (BBA) - Reviews on Bioenergetics* 1985, *811*, 265.
- (43) Here, it should be noted that the time-scale for MeCN propagation, which is commensurate with the time-scale for voltage creation, and the time-scale for bending are greatly different. Obviously a spreading behavior is much faster than bending one, and bending is mainly proceeding after spreading of MeCN and creation of maximum voltage, so this clearly indicates that the maximum voltage, at least, does not come from the bending phenomenon such as stress-induced voltage creation. .
- (44) Härth, M.; Schubert, D. W. *Macromolecular Chemistry and Physics* 2012, *213*, 654.
- (45) Washburn, E. W. *Physical Review* 1921, *17*, 273.

Chapter 5

Solvent-Induced Electrocatalysis at an Asymmetric Carbon Interface

Article that contributes to this chapter:

Liu, A. T.*; Kunai, Y.*; Cottrill, A. L.; Kaplan, A.; Zhang, G.; Mollah, R. S.; Eatmon, Y. L.; Strano, M. S. *in preparation*

Chemical doping of semi-conductive materials is often used to control the Fermi level¹ for applications that include chemical sensors,² electronic transistors,³ and photovoltaic cells.⁴ Originally named for the substitution of electron withdrawing- or donating-atoms into III-V semiconducting lattices, doping also occurs when surface adsorbed molecules raise or lower the Fermi level of certain low dimensional materials such as carbon nanotubes or graphene.⁵⁻⁸ A gradient in dopant concentration, and hence the chemical potential, across such a material should then generate usable electrical current.⁹ This opens up the possibility of creating asymmetric catalytic particles capable of generating their own galvanic potential, powered by a surrounding solvent that imposes such a gradient, enabling a form of wireless electrocatalysis. The ability to perform electrochemistry at the surface of solvent-immersed particle combines the advantages of wired electrodes and solvent dispersible, high surface area catalysts for chemical transformation, with advantages for selectivity and scalability. In this work, we report that symmetry broken, carbon particles comprised of high surface area single-walled carbon nanotube networks can effectively convert exothermic solvent adsorption into usable electrical potential, turning over electrochemical redox processes *in situ* with no external power supply.

5.1 Asymmetric Chemical Doping to Drive Electrochemical Transformations

Recent advances in understanding molecular interactions with nanostructured materials have led to a myriad of energy harvesting schemes, coupling inputs of various kind to the direct generation of electricity, mediated by the solvent molecules adsorbed onto the nanostructures.¹⁰⁻¹⁵ There have also been examples of electric energy conversion solely from the spontaneous adsorption and desorption of various solvents.¹⁶⁻²¹ The asymmetric adsorption of water molecules across nanostructure protein thin films, for example, have been shown to produce continuous electrical power at 0.5 V and $17 \mu\text{A}\cdot\text{cm}^{-2}$.²⁰ Voltage outputs and power densities exceeding 1.3 V and $1.0 \text{mW}\cdot\text{cm}^{-2}$ have also been reported for water adsorption onto a graphene oxide device with a preformed axial oxygen gradient.¹⁷ Follow-up studies extended such adsorption-based electricity generation into other solvent systems, like methanol (c.a. 30 mV) and acetone (c.a. 20 mV), providing opportunities for electricity generation in non-aqueous environments.¹⁹ Along with these developments, we have introduced *asymmetric chemical doping* (ACD), which involves a chemical potential gradient of electrical carriers in nanostructured carbon materials, established using an asymmetric adsorption of acetonitrile (CH_3CN) molecular dopants, as a mechanism for adsorption-induced electricity generation.^{9,22} In this process, the broken spatial symmetry in the Fermi levels (E_{F}) of electrical carriers inside a single-walled carbon nanotube (SWNT) network translates directly into a voltage potential. This reversible electric output (with specific power as large as $26.7 \text{mW}\cdot\text{mg}^{-1}$) stems from the electron transfer process between the SWNT donors and the p-doping CH_3CN acceptors, and can be generalized into a large family of small molecule organic solvents.^{9,23} With a tunable voltage output (up to 920 mV open circuit potential), and a wide range of compatible solvents including

the CH₃CN, we seek to take advantage of this phenomenon in the design of a particulate platform that generates “packets” of electricity for electrochemical transformations (**Figure 5-1a**). Preparative-scale electrochemical synthesis has a long tradition, with famous examples including the chlor-alkali process, which converts sodium chloride into chlorine and sodium hydroxide, and the Hall-Héroult process for aluminum smelting.²⁴ Recent developments in organic electrosynthesis such as the allylic C–H oxidation²⁵ and the decarboxylative etherification²⁶ provide new opportunities for fine-chemicals industry to use electron current in place of stoichiometric chemical oxidants or reductants. In the present work, we fabricate symmetry broken, carbon particles comprised of high surface area single-walled carbon nanotube networks and demonstrate their ability to convert exothermic solvent adsorption into usable electrical potential, turning over electrochemical redox processes *in situ* with no external power supply. We further demonstrate that the particulate form-factor of such asymmetric carbon generators allows easy integration into existing high-throughput analytical methods (e.g., NMR and UV-Vis plate-reader) for parallel screening. Combining solvent adsorption induced electricity generation with concomitant, colocalized electrochemical transformations paves new directions for electrical energy utilization and reaction condition optimization.

The design of such a particulate voltage generator (**Figure 5-1a**) takes inspiration from previous reports on *asymmetric chemical doping* (ACD),^{9,21} in which a spatial asymmetry in the exposure of SWNT to CH₃CN is achieved by biasing the CH₃CN solvent access towards a particular side of an otherwise symmetric SWNT particle (**Figure 5-1b**). Here, the solvent p-dopes or withdraws electrons from the exposed carbon interface, creating an Fermi level gradient along the SWNTs between the two electrochemically active surfaces,

which ultimately drives the observed electricity.²³ To create particles capable of solvent-induced galvanic potential, we created mm and sub-mm thin, hot-pressed SWNT papers, with one side coated with barrier polymer material such as Nafion, polyvinylalcohol (PVA), or polytetrafluoroethylene (PTFE), which prevents solvent from directly accessing one face of the SWNT paper. Dicing these papers into small mm and sub-mm cubes creates carbon Janus particles (**Figure 5-1c, d, e**), leaving only the exposed (unprotected) surface with direct access to the surrounding solvent. Profilometry shows flat cubic particles with RMS roughness of 23.3 μm , and Raman spectroscopy maps a spatially uniform SWNT Fermi level of -0.19 eV (consistent in an ambient O₂ environment) with G band Raman shifts around $1589 \pm 1 \text{ cm}^{-1}$ (**Figure 5-1f**). Upon insertion of the Janus SWNT/polymer particle into a reservoir of CH₃CN solvent, this polymer layer serves as a transport barrier between the SWNTs from the bulk CH₃CN, providing the spatial asymmetric CH₃CN doping gradient in the axial direction of the underline SWNTs necessary for the induced electric potential (**Figure 5-1h**). The resulted CH₃CN induced Fermi level gradient in SWNTs is seen spectroscopically as a corresponding SWNT Raman G band shift of 15 cm^{-1} between the CH₃CN exposed and polymer protected side (**Figure 5-1f**).

We immersed the pristine (or non-oxidized) SWNT/PVA asymmetric devices into a series of p-doping (electron withdrawing) solvents (rank ordered by the energetics of their lowest unoccupied molecular orbital, or LUMO levels) at ambient conditions, and measured the devices' open circuit voltage output with copper electrodes physically inserted into the two ends of the asymmetric carbon device. Control studies were performed to rule out the electrochemical presence of the copper electrode in the electrical characterizations, and all subsequent electrochemical reaction experiments throughout this study were conducted in

the absence of copper. We observed a strong dependence of the resulted open circuit electrical potential as a function of the dopant LUMO level, in agreement with previous findings.²³ In these devices consist of pristine-SWNTs, chloro-acetonitrile (CH_2ClCN) appears to be the optimal solvent of choice for voltage generation (c.a. 281 mV), whereas CH_3CN doping affords approximately 93 mV. Subsequent oxidations of the pristine SWNTs, following a reported procedure,⁹ enhanced the CH_3CN mediated voltage output monotonically, up to 920 mV (highest for devices fabricated using SWNTs with 25 % surface oxygen atom coverage), owing primarily to the increased effective SWNT surface area.⁹ The correlation between the SWNT oxidation level and voltage output (of the device) highlights the ability to tune to a desired voltage by dialing in a single material parameter.

Based on these results, we selected oxidized-SWNT ($[\text{O}] = 25\%$, abbreviated as o-SWNT here forth) as the active component in the Janus o-SWNT/polymer particulate used throughout this study. We characterized these devices in closed circuit to quantify output power (**Figure 5-1g, top**). An instantaneous electricity generation was observed upon particle immersion into a CH_3CN reservoir, and the discharge curves measured across a 5000 $\text{k}\Omega$ external load suggest a strong volume dependence of the charge capacity (**Figure 5-1g, bottom**), with an estimated total charge of 0.039, 0.065, 0.094 $\mu\text{A}\cdot\text{h}$ for particles of sizes 0.031, 0.063, and 0.093 mm^3 , respectively. This amounts to 1.45 nmol of electrons mobilized by the smallest particle tested, in principle capable of driving a 1.45 mM redox couple in a 1 μL CH_3CN solution. It is also worth noting that these discharges occur approximately at the same voltage (c.a. 730 mV), regardless of particle volume, and remain stable for most of the discharging period. We further characterize device power outputs as

a function of their aspect ratios (defined as the ratio between particle cross-sectional area and its axial length, perpendicular to the Janus faces, **Figure 5-1h, top**). Various external loads are tested to map out the power curves of each device (**Figure 5-1h, bottom**), indicating a linear enhancement in power output with increased particle cross-sectional area (**Figure 5-1h**).

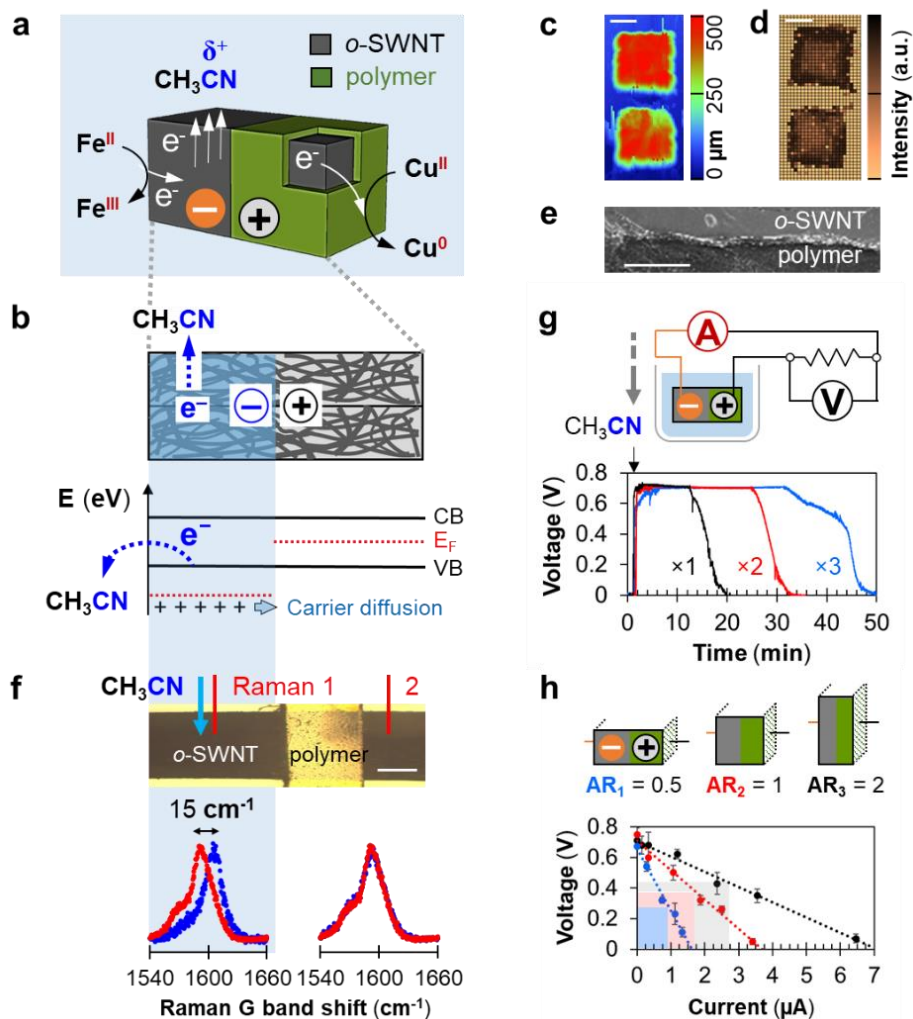


Figure 5-1. A particle capable of inducing electric potentials from within a solvent. (a) Schematic illustration of Janus microparticles generating electricity to power electrochemical redox reactions (e.g., $\text{Fe}^{2+} \rightarrow \text{Fe}^{3+}$ or $\text{Cu}^{2+} \rightarrow \text{Cu}^0$) *in situ*, in lieu of a potentiostat as a voltage

source. **(b)** Schematic illustration of the electricity generation mechanism of the Janus microparticle. Asymmetric chemical doping is realized via spatially asymmetric polymer coating. The partial electron transfer induced by CH_3CN molecules adsorbed on the o-SWNT surface withdraws electron density from the adsorption site, thereby lowering the corresponding Fermi energy (E_F), drawing electron flow following the prescribed E_F gradient.²³ **(c)** Surface profile of two $500\ \mu\text{m} \times 250\ \mu\text{m} \times 250\ \mu\text{m}$ o-SWNT/PTFE Janus particles (color bar range, 0 – 500 μm ; scale bar, 100 μm). **(d)** Raman spectroscopic map showing the intensity of the G band of the o-SWNT side of two $500\ \mu\text{m} \times 250\ \mu\text{m} \times 250\ \mu\text{m}$ o-SWNT/PTFE Janus particles (scale bar, 100 μm). **(e)** Scanning electron micrograph showing the vertical interface of o-SWNT/PTFE interface of the Janus particle (scale bar, 1 μm). **(f) Top:** Raman spectroscopic measurement of o-SWNT G band shift for CH_3CN exposed o-SWNT (Raman 1) and polymer protected o-SWNT (Raman 2). Note a spectroscopic window on the polymer protected side was opened up to avoid polymer interference in Raman measurement. Scale bar, 100 μm . **Bottom:** Raman G band shift of o-SWNT before (red) and after (blue) CH_3CN addition for the exposed (left, Raman 1) and polymer protected (right, Raman 2) side. **(g) Top:** schematic illustration of closed circuit measurements to quantify the electrical output of such Janus particles, in which the particles are lowered into a reservoir of CH_3CN , and the current and voltage profiles across a known external load are recorded. **Bottom:** Measured voltage profiles across a 5000 k Ω external resistor for particle generators of various sizes but identical aspect ratios (black or volume $\times 1$, $500\ \mu\text{m} \times 250\ \mu\text{m} \times 250\ \mu\text{m}$; red or volume $\times 2$, $636\ \mu\text{m} \times 315\ \mu\text{m} \times 315\ \mu\text{m}$, blue or volume $\times 3$, $720\ \mu\text{m} \times 360\ \mu\text{m} \times 360\ \mu\text{m}$). **(h) Top:** schematic illustration of Janus particles of the same volume ($2\ \text{mm}^3$), but different aspect ratios (AR) of 0.5 (blue), 1 (red) and 2 (black). **Bottom:** Current-voltage characteristics of the three particles represented above. Error bars represent standard deviations of

different measurements using different replica of devices ($n = 3$). Colored squares represent the maximum output power of devices at each AR if the external resistance is impedance-matched to the device internal resistance.

Quantitative conversion of ferrocene to ferrocenium ion can be achieved by dropping a $1 \text{ mm} \times 2 \text{ mm} \times 2 \text{ mm}$ o-SWNT/PTFE Janus particle ($\text{AR} = 4$, volume = 4 mm^3) into a well-stirred ferrocene/ CH_3CN solution (0.6 mM, 0.6 mL), using tetrabutylammonium perchlorate (TBAP, 50 mM) as an electrolyte, over a course of 30 minutes under ambient conditions (**Figure 5-2a**). Similar reactivity is observed using 560 smaller particles ($360 \mu\text{m} \times 200 \mu\text{m} \times 100 \mu\text{m}$) with an equivalent effective total volume. Control studies using particles that have either no active generating ingredient (i.e., replacing o-SWNT to pristine-SWNT, with voltage output less than the reductive potential of ferrocene), or an unbroken symmetry (e.g., no Janus PTFE coating), yielded negligible conversions (**Figure 5-2b**), which rules out any non-electricity-assisted chemical pathways. Also, because the ACD electricity can be reversibly generated,⁹ the Janus particles can be “recharged” by drying off CH_3CN from the SWNT surface and re-oxidized in $\text{HNO}_3/\text{H}_2\text{SO}_4$ mixture (2:1 volumetric ratio), allowing multiple cycles of ferrocene oxidation without significant yield degradations (**Figure 5-2c, d**). Furthermore, we note that the oxidation kinetics is influenced by the mass transfer of the electrolyte and the redox pair (for example, $-\text{COOH}$ vs. $-\text{COO}^-$ and H_2) across the polymer membrane on the reducing (PTFE protected) o-SWNT surface (i.e., the cathodic carbon surface, **Figure 5-2b, inset**), which gives rise to the observed monotonic dependence of ferrocene oxidation yield on polymer permeability to CH_3CN , a parameter re-casted in **Figure 5-2e** as the measured electrical conductance. Detailed kinetic analyses reveal that the initial rate of the electrochemical process is limited

by ferrocene adsorption on the anodic (exposed) *o*-SWNT surface. As a cautionary note, only a small fraction of charges mobilized from the ACD manage to successfully couple to the iron (II) oxidation reaction. We attribute this low electro-chemical coupling efficiency (c.a. 0.2 %) to a combination of capacitive and resistive losses between the particle electrodes and electrolyte. Nevertheless, this proof-of-concept experiment demonstrates the potential of exploiting the ACD electric current for chemical transformation, turning the adsorption enthalpy of organic solvent (i.e., CH₃CN) on nanostructured carbon (i.e., *o*-SWNT) into an useful source of electric power, without the use of any complex, external circuitry.

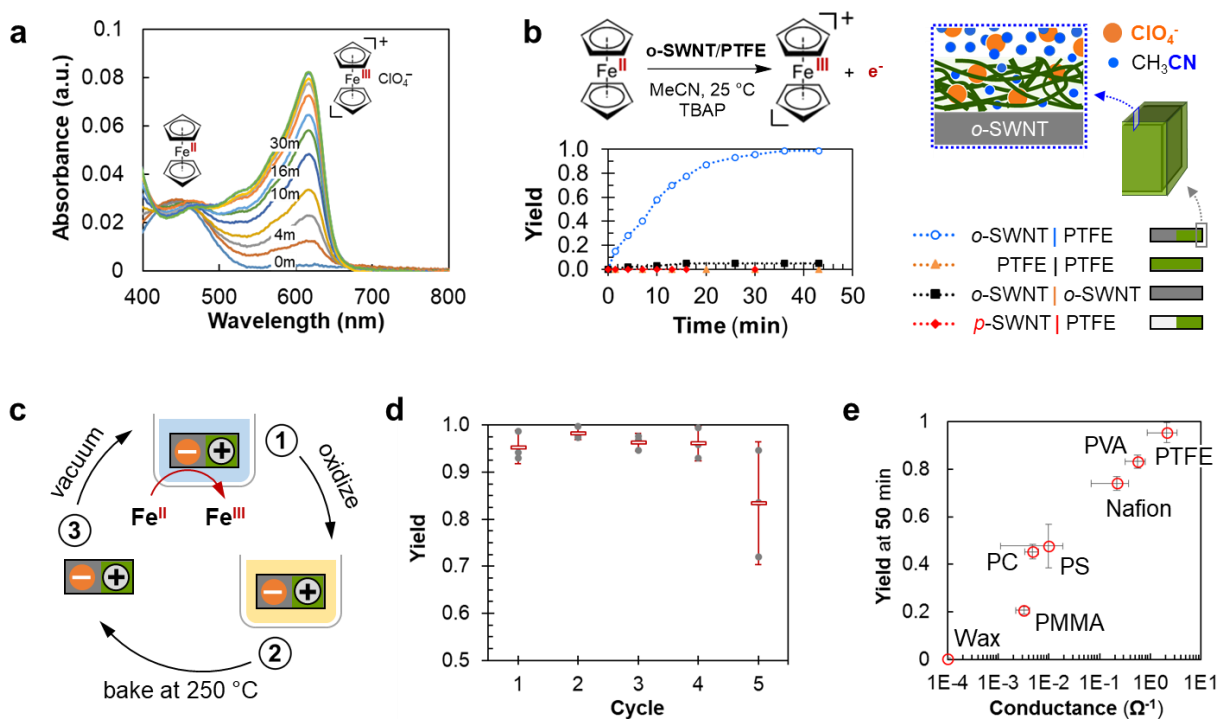


Figure 5-2. Ferrocene oxidation using *in situ* generated electricity. (a) Real time UV-Vis absorption spectra of a well-stirred ferrocene (0.6 mM, in CH₃CN) and tetrabutylammonium perchlorate (TABP, 50 mM, in CH₃CN) solution, upon insertion of one *o*-SWNT/PTFE particle

(1 mm × 2 mm × 2 mm, AR = 4, volume = 4 mm³). The reactant (ferrocene) peak centers around 430 nm, whereas the product (ferrocenium perchlorate) peak centers around 615 nm. **(b) Top-left:** reaction scheme of ferrocene oxidation driven by o-SWNT/PTFE particle generators. **Bottom-left:** control studies of the ferrocene oxidation kinetics using various particle constructs. Blue: standard condition, Janus particle made with o-SWNT half coated with PTFE thin film (100 nm); orange: o-SWNT particle fully coated with PTFE; black: bare o-SWNT particle with no coating; red: Janus particle made with pristine non-oxidized SWNTs (p-SWNT) half coated with PTFE. All reactions are performed at 0.6 mM ferrocene concentration with 50 mM TBAP as electrolyte, with particle dimensions 1 mm × 2 mm × 2 mm. **Right:** schematic illustration of the cross-section of the 100 nm polymer coating. It also allows restricted solvent (blue dot)/electrolyte (orange dot) diffusion, as characterized by the solvent permeability through the polymer membrane. **(c)** The three-step Janus particle “recharging” cycle, consist of (i) re-oxidizing (using 2:1 volumetric mixture of concentrated HNO₃/H₂SO₄) the reduced o-SWNT (during ferrocene electro-oxidation reaction at the exposed, anodic surface) on the cathodic (PTFE protected) o-SWNT surface, (ii) rinsing off adsorbed chemicals on the particle and baking at 250 °C to get rid of rinsing solution and residual acids, and (iii) vacuuming away any residual liquid for the next reaction cycle. **(d)** Calibrated ferrocene yield with recycled Janus particles. Error bars represent the standard deviations of oxidation yields using different particles ($n = 3$). **(e)** Calibrated ferrocene oxidation yield at 30 minutes of reaction time using o-SWNT Janus particles (1 mm × 2 mm × 2 mm) half-coated with different polymers (c.a. 100 nm). Device conductivities are measured between the two terminals of the Janus particles using infiltrated silver (Ag) nanoparticles (initially dissolved in CH₃CN) as electrode contacts, which is a proxy for polymer permeabilities to CH₃CN. Error bars represent

the standard deviations of both reaction yield and conductivity measured within different samples ($n = 3$).

To further explore the physical origin of the ferrocene-to-o-SWNT electron transfer, and how it couples with the driving ACD process, we investigate on which side of the o-SWNT/PVA Janus particle does the ferrocene oxidation occur. This was probed by grafting a thin layer of poly-ferrocenylmethyl-methacrylate (PFMMA)²⁷ over the entire particle surface and subjecting the PFMMA-grafted o-SWNT/PVA into a CH₃CN/electrolyte solution. Since the only ferrocene molecules available for electrochemical oxidation are covalently linked to the PFMMA backbone, they are spatially fixed to the particle surface. Post-reaction analysis reveals that only the ferrocene molecules bound to the bare o-SWNT side were oxidized into ferrocenium, leaving those on the PVA protected side mostly in their original reduced state. This reaffirms the molecular picture that ferrocene exclusively oxidizes on the electron deficient, unprotected o-SWNT surface (i.e., the anode, **Figure 5-1a**), driven by the ACD process that lowered the E_F on that side (**Figure 5-1b**). An interesting corollary of this mechanism states that the electrochemical redox reaction consumes the ACD generated electron flow, and necessarily reduces the solvent-powered closed circuit current, which was also observed experimentally (**Figure 5-3a**).

A particle that generates electricity with controlled charge capacity (i.e., through particle volume), voltage magnitude (i.e., through SWNT oxidation level), and power density (i.e., through aspect ratio) – all of which is triggered by solvent interactions, provides an ideal platform for solution based electrochemistry. Furthermore, the ability to couple the “electricity generated from within” reliably with a chemical process, especially one that

results an appreciable shift in the absorption color spectrum (e.g., from Fe^{2+} to Fe^{3+}), motivates a multiplexed reaction-detection scheme for high through-put reaction monitoring, using standard UV-visible light plate readers. Here we subject 10 ferrocene derivatives prepared with the same exact standard solution (except for modifications on the cyclopentadiene ring, **Figure 5-3b**) to 10 identical o-SWNT/PTFE generators tethered individually to 10 wells (with replica of 2) in a well plate (**Figure 5-3b, left**). Subsequent parallel oxidation reactions occur within a plate reader that follows the product absorption peak for each derivative in real time. The calibrated yields (of the oxidized product, after 30 minutes reaction time, **Figure 5-3b**, black circles) strongly correlated with the reduction potential (RP) of each derivative. With each particle generating approximately the same voltage, the ferrocene derivatives with lower reduction potential (hence higher over potential, η) reacted faster, resulting in higher oxidation yields at 30 minutes. Moreover, we found these results can be described by the Butler-Volmer equation (**Figure 5-3b**, dotted lines), which couples the first order oxidation kinetics (verified previously) to the particle anode current density:

$$[\text{Fe}^{3+}] = [\text{Fe}^{2+}]_0 - [\text{Fe}^{2+}]_0 \exp\left(-t \cdot j_0 \exp\left\{\frac{(1-\alpha)zF\eta}{RT}\right\}\right) \quad (40)$$

Here $[\text{Fe}^{2+}]_0$ denotes the initial ferrocene concentration; t and T represent reaction time and system temperature; j_0 and α are material parameters called exchange current density and charge transfer coefficient; z measures the number of electrons involved in the electrode reaction; F and R are Faraday and ideal gas constant, respectively. The model estimates that the o-SWNT/PTFE would generate 746 mV of equilibrium potential (**Figure 5-3b**, black dotted line), as compared to the closed circuit device voltage output of c.a. 730 mV

across a 5000 k Ω external resistor (**Figure 5-1g**). Additional set of Janus particles was prepared using less oxidized SWNTs ([O] = 15%, known to generate c.a. 550 mV of electric potential). This new set of particles were subjected to identical oxidation reactions using the same 10 ferrocene derivatives, but the reactivity was found to be much lower (**Figure 5-3b**, red circles), a result expected from the above equation, with a reduced particle equilibrium potential. The tunable kinetics, subject to variations of the particle equilibrium potential, (which is ultimately controlled by the oxidation levels of the SWNTs), demonstrated the excellent chemo-selectivity of the electrochemical approach. One can easily reduce the oxidative yield of ferrocenyl-succinimide (RP \approx 490 mV), for example, from 87% to 8%, by simply switching to the less oxidized o-SWNT/PTFE system (from [O] = 25% to 15%, **Figure 5-3b**).

The ACD-powered electrochemistry is not restricted to the Fe²⁺/Fe³⁺ redox pair, rather, it should, in principle, encompass an array of transformations that falls into the electrochemical window (defined by the o-SWNT/PTFE particle), such as, the reduction of copper (II) chloride (Cu²⁺ \rightarrow Cu⁰, RP \approx 337 mV, **Figure 5-3c**). Yield calculations for metal ion reductions, we note, appear to be less straight forward, primarily due to the lack of a spectroscopic signature from the reduction product, as well as product (metal) depositions onto the particle cathode (the PTFE protected side, **Figure 5-3d**). This undesired deposition, however, offers an excellent tool, in this case, to locate where on the particle the reduction has occurred. Both X-ray photoelectron spectroscopy (XPS, **Figure 5-3d**) and energy dispersive spectroscopy (SEM-EDS) elemental analyses revealed substantial Cu⁰ deposition localized only on the PTFE protected cathode, once again validating the proposed ACD-driven reaction mechanism (**Figure 5-1a**). Using

quantitative elemental mapping, it is also possible to estimate a lower bound of the copper (II) reduction yield (c.a. 39.7%), similarly to other metal ions within the electrochemical window, such as cobalt and silver (**Figure 5-3e**).

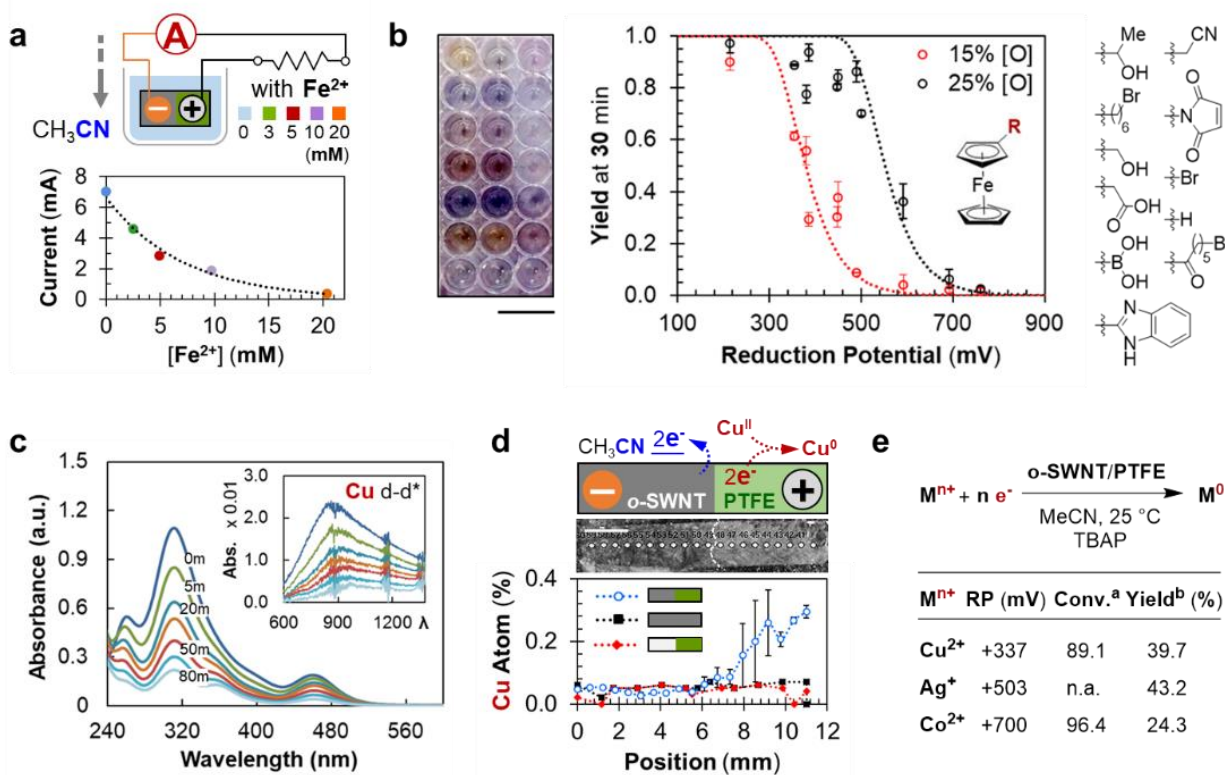


Figure 5-3. Electrochemical characterization using various red-ox pairs. (a) **Top:** schematic illustration of closed circuit current measurements upon inserting a particle generator (1 mm × 2 mm × 2 mm, AR = 4, volume = 4 mm³) into various concentrations of ferrocene CH_3CN solutions. (b) **Left:** Optical image of 10 (in replica of two, so 20 total) parallel oxidation reactions using different ferrocene derivatives followed by a standard UV-Vis plate reader (scale bar, 1 cm). **Right:** Calibrated yields of different ferrocene derivatives measured at 30 minutes of reaction time using o-SWNT/PTFE particles at two SWNT oxidation levels (black: [O] = 25%, standard condition; red: [O] = 15%, as measured by XPS). These plate-reader-determined yields are ranked

with the reduction potentials of these ferrocene derivatives, measured separately using cyclic voltammetry. Error bars represent standard deviations of the calibrated yields ($n = 4$). (c) Real time UV-Vis absorption spectra of a well-stirred copper chloride (CuCl_2 , 0.6 mM, in CH_3CN) and TBAP (50 mM, in CH_3CN) solution, upon insertion of one o-SWNT/PTFE particle (1 mm \times 2 mm \times 2 mm, AR = 4). **Inset:** The absorption peak of the d–d transition of the copper (II) complex (Cu^{2+}). (d) **Top:** schematic illustration of the copper (II) reduction on the o-SWNT/PTFE particle, showing the reduction is expected to take place on the PTFE coating side. **Middle:** Optical image of the 12 mm \times 2 mm \times 160 μm (AR = 0.27, volume = 4 mm³) o-SWNT/PTFE device used, as viewed from the XPS vacuum chamber. Each spot represents a sampling point for X-ray excitation, with the Janus interface indicated by the dotted line (scale bar, 2 mm). **Bottom:** Calibrated metallic copper (Cu^0) atomic percentage along the axial direction of the o-SWNT/PTFE Janus particle (blue) after Cu^{2+} reduction reaction. Control particles of o-SWNT with no PTFE coating (black) and Janus particles made with pristine SWNTs (red) are also tested. Error bars represent standard deviation of XPS atomic ratio measurements using different samples prepared in separate reduction runs ($n = 3$). (e) Reaction scheme, electrochemical reduction potentials,²⁸ conversions and yields estimated for various metal ions. ^a The conversions are determined using UV-Vis absorption spectroscopy. ^b The yields represent lower bounds as estimated from XPS elemental mappings.

One of the key advantages of using CH_3CN as a dopant to power the ACD driven electrochemistry is its prevalence and versatility as an organic solvent. To further demonstrate the synthetic utility of these solvent-derived “packets” of electricity, we turned our attention to an organic system with industrial relevance – the partial oxidation of alcohols to aldehydes or ketones. Selective oxidation of primary and secondary alcohols

to the corresponding carbonyl compounds is a fundamental and important transformation in organic chemistry,²⁹ which is traditionally resolved by an electrochemical oxidation using a nitroxyl radical (2, 2, 6, 6-tetramethylpiperidin-1-yl)oxyl, or TEMPO, as a catalytic mediator (**Figure 5-4a**).³⁰ Here we hope to apply our ACD generated electric potential to drive the desired partial oxidation in a stoichiometric fashion. To lower the detection burden on the analytical methods (i.e., nuclear magnetic resonance, or NMR, spectroscopy), we increased the reactant concentration to 20 mM. This in turn meant that we had to adjust the number of the o-SWNT/PTFE particles accordingly. We observed essentially no desired product in the absence of either the Janus particles, the TEMPO co-oxidant, or the CH₃CN, consistent with an ACD facilitated mechanism (**Figure 5-4a**). A brief optimization on the number of participating Janus particles suggests that 7 generators can fully account for the increase in carriers needed to drive the model amyl alcohol oxidation to completion (**Figure 5-4b**). The linear scaling of the oxidative yield as a function of particle number highlights, once more, the modular nature of such embedded electric energy. This method also proved to be compatible with a range of reactants. An array of primary (entry 1-8) and secondary (entry 9-12) alcohols can effectively couple to the oxidative cycle with good yield (**Figure 5-4c**).

With the reaction condition established, we continued to explore this *in situ* powered electro-oxidation as a high-throughput optimization tool. The mechanistic dichotomy that sets the ACD generated electricity apart from other traditional voltage generators enables inherent scalability and facile multiplexing strategies. To illustrate, we tethered these Janus particles to each of the wells in a standard 96-well plate and transformed them into temporary electrochemical cells. This allows us to evaluate multiple reaction parameters

in parallel. We tested this system on the selective oxidation of propan-1,2-diol (**Figure 5-4d**, top). In order to optimize the selectivity towards the secondary (2°) alcohol over the primary (1°) one, two parameters – that is, the concentration of the TEMPO mediator, and the solvent acidity – were modulated in combination to identify several selectivity hotspots (**Figure 5-4d**, bottom). Both slightly acidic and basic conditions seemed to, surprisingly, favor the oxidation at the 2° -location. This observation, in retrospect, sheds light on a Lewis acid – base protection scheme that kinetically traps the 1° -alcohol at the second step of the TEMPO catalytic cycle (**Figure 5-4a**). The optimized condition (10 mM TEMPO, 5 mM acetic acid additive) selectively furnished the 2° -product (hydroxyacetone) with respectable yield (91%) and selectivity (97%).

As a consequence of the relatively small footprint of these Janus particle generators (e.g., 4 mm^3), one can easily incorporate them into a nuclear magnetic resonance (NMR) tube for *in situ* electrochemical kinetic measurements (**Figure 5-4e**, top). By sinking these particles below the active spectroscopic window, electro-chemical transformations can be followed, in real time, without magnetic interferences. We monitored, for example, the hydroxyacetone electro-oxidation following the reaction conditions optimized above, in deuterated acetonitrile (CD_3CN) as solvent (**Figure 5-4e**, bottom).

The idea of dividing electricity into modular, customizable, LEGO-like units can potentially encourage the development of exotic reactor configurations for larger-scale operations. As such, a packed bed electrochemical reactor (PBER) was built, by vertically stacking 50 of these 4 mm^3 o-SWNT/PTFE generators, in between insulating filter stages, to prevent electric shorts (**Figure 5-4f** and **Figure 5-4g**, left). A syringe pump was used to supply a steady influx ($0.8\text{ mL}\cdot\text{h}^{-1}$) of the reactant (1, 2-propadiol), as well as the prior

optimized reagent composition, all dissolved in CD₃CN, into the PBER for 9 hours of continuous hydroxyacetone production (**Figure 5-4g**, right). These results, we hope, could pave the way towards new perspectives of using electricity in a synthetic setting, or perhaps even galvanize fundamental insights and methodologies developed therefrom, towards joining forces from classically a chemical phenomenon with an explicitly driven flow of electrons, generated *in situ*.

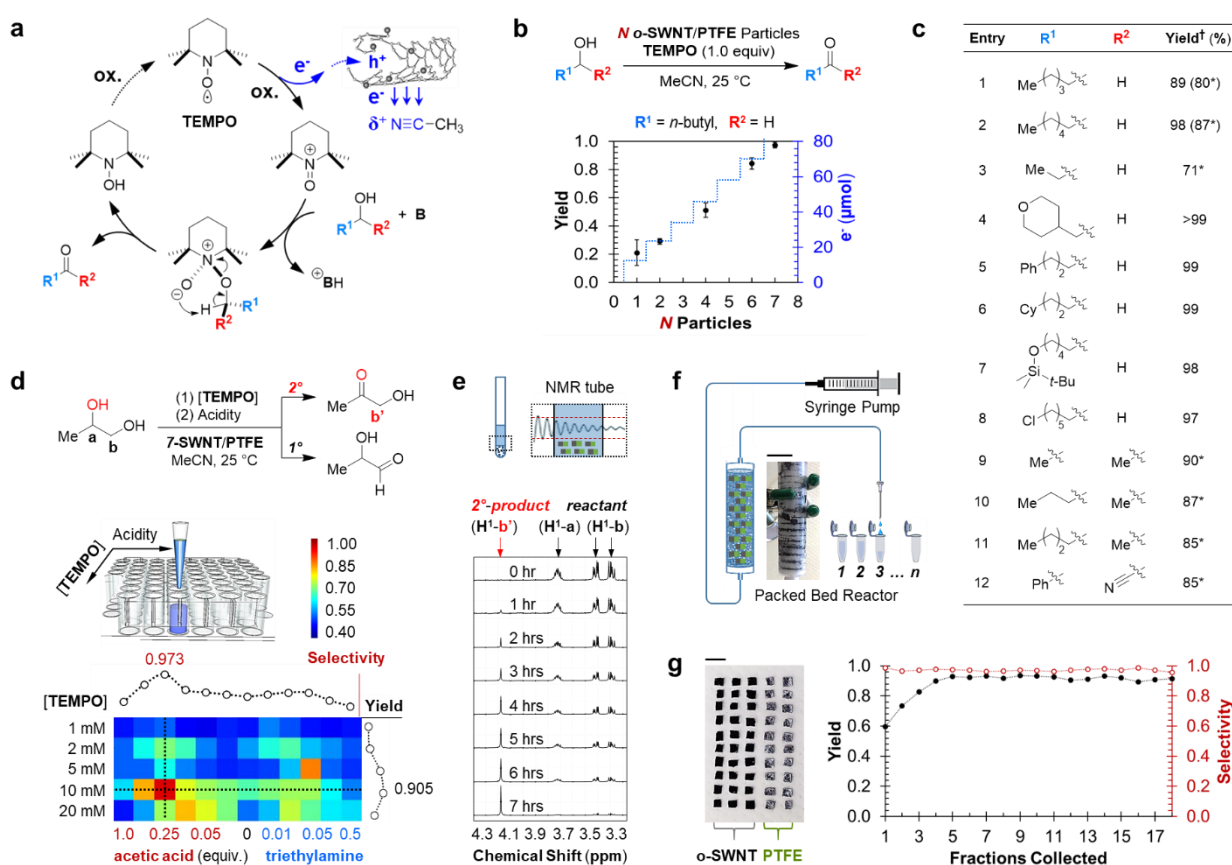


Figure 5-4. *In situ* driven selective alcohol electro-oxidations. (a) Proposed mechanism for o-SWNT/PTFE particle-enabled electrochemical partial oxidation of alcohols to ketones or aldehydes (e.g., R² = H) in CH₃CN, using TEMPO as a co-oxidant. (b) Calibrated yield for the partial oxidation of amyl alcohol to amyl aldehyde electrochemically using various numbers of o-

SWNT/PTFE particles (1 mm × 2 mm × 2 mm). Reactions are conducted under ambient condition for 8 hours at 20 mM reactant concentration. The blue dotted lines represent the total charge capacity of each scenario where N number of generator particles are used. Error bars represent standard deviations of reaction yields collected for each number of particles used ($n = 3$). (c) Variations in the functional group scope tested for this *o*-SWNT/PTFE-enabled electrochemical partial oxidation of both primary (entry 1-8) and secondary (entry 9-12) alcohols. In all cases, the standard condition shown in **5-3b**, with $N = 7$, is applied. †Yields are calibrated with gas chromatography (GC). *For the cases where GC analysis proves to be difficult (e.g., due to molecular weight), proton nuclear magnetic resonance spectroscopy (¹H-NMR) is used instead. (d) Selective oxidation of secondary (2°) over primary (1°) alcohol in 1, 2-propadiol. **Top:** Reaction scheme of (1) TEMPO loading and (2) solvent acidity screen for the *o*-SWNT/PTFE-assisted electrochemical oxidation of 1, 2-propadiol, with both potential oxidation products listed. Protons (¹H-a, ¹H-b) of the reactant, as well as the proton (¹H-b') of the 2°-oxidation product (1-hydroxyl-2-propanone), are labeled accordingly. **Middle:** schematic illustration of using *o*-SWNT/PTFE particles as constant voltage sources for high-throughput combinatorial reaction condition optimization in a 96 well plate. In this case, 60 parallel reactions are screened together, spanning a variety of TEMPO loadings and solvent acidities. **Bottom:** selectivity towards the 2°-oxidation product, displayed both as a function of the TEMPO loading (vertical axis) and solvent Lewis acidity (horizontal axis, tuned via the addition of various equivalents of acetic acid – more acidic – or triethylamine – more basic). (e) **Top:** Schematic illustration of the *in situ* NMR kinetic measurement of 1, 2-propadiol oxidation using the conditions optimized in **5-3d**. D₃-acetonitrile (CD₃CN) is used as the solvent. **Bottom:** Assigned ¹H-NMR spectra for the reaction mixture. (f) Schematic illustration of the packed bed electrochemical reactor (PBER), in which a plug flow

reactor column is packed with 50 standard o-SWNT/PTFE particle electricity generators (1 mm × 2 mm × 2 mm), for multi-stage continuous electrochemical production of 1-hydroxyl-2-propanone. Fractions are collected with an automated system at 30 minutes per cut. A total of 18 fractions are collected for a 9-hour run. **Inset:** the prototype PBER used in this study (scale bar: 1 cm). **(g) Left:** Optical image of the 50 o-SWNT/PTFE particle generators used to construct the PBER, with either the o-SWNT side or the PTFE-coated side facing up (scale bar: 5 mm). **Right:** calibrated yield and selectivity for 1-hydroxyl-2-propanone in each fraction collected from the PBER.

In this study, we have introduced *asymmetric chemical doping* (ACD) as a strategy for solvent-driven electricity generation. We fabricated Janus particles using compressed single-walled carbon nanotubes with symmetry-broken polymer coating that take advantage of this ACD mechanism to induce electric currents from within a solvent (e.g., acetonitrile). These Janus particles generate electrical energy with controlled charge capacity (i.e., through particle volume), voltage magnitude (i.e., through SWNT oxidation level), and power density (i.e., through aspect ratio) – all of which is triggered by solvent interactions. We further exploited this electric current induced *in situ* to a series of classical chemical transformations, turning the organic solvent into an abundant source of “packets” of electric power, without the use of any complex, external circuitry. We demonstrated the potential to couple these particle generators with real-time reaction monitoring, high-throughput parameter optimization, and continuous chemical production schemes. We believe the idea of harvesting and dividing electricity into modular and customizable units and incorporating them as synthetic building blocks, may create new opportunities in using preparative-scale electrolysis for molecular assembly.

5.2 References

- (1) Unvala, B. A. *Nature* 1962, 194, 966.
- (2) Bergveld, P.; DeRooij, N. F.; Zemel, J. N. *Nature* 1978, 273, 438.
- (3) Haynes, J. R.; Shockley, W. *Physical Review* 1949, 75, 691.
- (4) Piwkowski, T. R. *Nature* 1959, 184, 355.
- (5) Kong, J.; Franklin, N. R.; Zhou, C.; Chapline, M. G.; Peng, S.; Cho, K.; Dai, H. *Science* 2000, 287, 622.
- (6) Collins, P. G.; Bradley, K.; Ishigami, M.; Zettl, A. *Science* 2000, 287, 1801.
- (7) Schedin, F.; Geim, A. K.; Morozov, S. V.; Hill, E. W.; Blake, P.; Katsnelson, M. I.; Novoselov, K. S. *Nature Materials* 2007, 6, 652.
- (8) Wehling, T. O.; Novoselov, K. S.; Morozov, S. V.; Vdovin, E. E.; Katsnelson, M. I.; Geim, A. K.; Lichtenstein, A. I. *Nano Lett.* 2008, 8, 173.
- (9) Liu, A. T.; Kunai, Y.; Liu, P.; Kaplan, A.; Cottrill, A. L.; Smith-Dell, J. S.; Strano, M. S. *Advanced Materials* 2016, 28, 9752.
- (10) Ghosh, S.; Sood, A. K.; Kumar, N. *Science* 2003, 299, 1042.
- (11) Dhiman, P.; Yavari, F.; Mi, X.; Gullapalli, H.; Shi, Y.; Ajayan, P. M.; Koratkar, N. *Nano Lett.* 2011, 11, 3123.
- (12) Yin, J.; Li, X.; Yu, J.; Zhang, Z.; Zhou, J.; Guo, W. *Nat Nano* 2014, 9, 378.
- (13) Zhong, H.; Xia, J.; Wang, F.; Chen, H.; Wu, H.; Lin, S. *Advanced Functional Materials* 2017, 27, 1604226.
- (14) Xue, G.; Xu, Y.; Ding, T.; Li, J.; Yin, J.; Fei, W.; Cao, Y.; Yu, J.; Yuan, L.; Gong, L.; Chen, J.; Deng, S.; Zhou, J.; Guo, W. *Nature Nanotechnology* 2017, 12, 317.
- (15) Kim, S. H.; Haines, C. S.; Li, N.; Kim, K. J.; Mun, T. J.; Choi, C.; Di, J.; Oh, Y. J.; Oviedo, J. P.; Bykova, J.; Fang, S.; Jiang, N.; Liu, Z.; Wang, R.; Kumar, P.; Qiao, R.; Priya, S.; Cho, K.; Kim, M.; Lucas, M. S.; Drummy, L. F.; Maruyama, B.; Lee, D. Y.; Lepró, X.; Gao, E.; Albarq, D.; Ovalle-Robles, R.; Kim, S. J.; Baughman, R. H. *Science* 2017, 357, 773.
- (16) Zhao, F.; Cheng, H.; Zhang, Z.; Jiang, L.; Qu, L. *Adv. Mater.* 2015, 27, 4351.
- (17) Zhao, F.; Liang, Y.; Cheng, H.; Jiang, L.; Qu, L. *Energy & Environmental Science* 2016, 9, 912.
- (18) Zhao, F.; Wang, L.; Zhao, Y.; Qu, L.; Dai, L. *Adv. Mater.* 2017, 29, 1604972.
- (19) Xue, J.; Zhao, F.; Hu, C.; Zhao, Y.; Luo, H.; Dai, L.; Qu, L. *Advanced Functional Materials* 2016, 26, 8784.
- (20) Liu, X.; Gao, H.; Ward, J. E.; Liu, X.; Yin, B.; Fu, T.; Chen, J.; Lovley, D. R.; Yao, J. *Nature* 2020, 578, 550.

- (21) Liu, A. T.; Zhang, G.; Cottrill, A. L.; Kunai, Y.; Kaplan, A.; Liu, P.; Koman, V. B.; Strano, M. S. *Adv Energy Mater* 2018, 8, 1802212.
- (22) Mahajan, S. G.; Liu, A. T.; Cottrill, A. L.; Kunai, Y.; Bender, D.; Castillo, J.; Gibbs, S. L.; Strano, M. S. *Energy & Environmental Science* 2016.
- (23) Kunai, Y.; Liu, A. T.; Cottrill, A. L.; Koman, V. B.; Liu, P.; Kozawa, D.; Gong, X.; Strano, M. S. *J. Am. Chem. Soc.* 2017, 139, 15328.
- (24) Horn, E. J.; Rosen, B. R.; Baran, P. S. *ACS Central Science* 2016, 2, 302.
- (25) Horn, E. J.; Rosen, B. R.; Chen, Y.; Tang, J.; Chen, K.; Eastgate, M. D.; Baran, P. S. *Nature* 2016, 533, 77.
- (26) Xiang, J.; Shang, M.; Kawamata, Y.; Lundberg, H.; Reisberg, S. H.; Chen, M.; Mykhailiuk, P.; Beutner, G.; Collins, M. R.; Davies, A.; Del Bel, M.; Gallego, G. M.; Spangler, J. E.; Starr, J.; Yang, S.; Blackmond, D. G.; Baran, P. S. *Nature* 2019, 573, 398.
- (27) Pittman, C. U.; Lai, J. C.; Vanderpool, D. P.; Good, M.; Prado, R. *Macromolecules* 1970, 3, 746.
- (28) Kratochvil, B.; Lorah, E.; Garber, C. *Analytical Chemistry* 1969, 41, 1793.
- (29) Lucio Anelli, P.; Biffi, C.; Montanari, F.; Quici, S. *The Journal of Organic Chemistry* 1987, 52, 2559.
- (30) Semmelhack, M. F.; Chou, C. S.; Cortes, D. A. *J. Am. Chem. Soc.* 1983, 105, 4492.

Chapter 6

Autoperforation of Two-Dimensional Materials as Method to Prepare Electronic Colloids

Articles that contribute to this chapter:

Liu, P.*; Liu, A. T.*; Kozawa, D.; Dong, J.; Yang, J. F.; Koman, V. B.; Saccone, M.; Wang, S.; Son, Y.; Wong, M. H.; Strano, M. S. *Nature Materials* (2018), 17, 1005

Liu, A. T.*; Yang, J. F.*; LeMar, L. N.; Zhang, G.; Pervan, A.; Murphey, T. D.; Strano, M. S. *Faraday Discussions* (2020), *accepted manuscript*

A central ambition of the robotics field has been to increasingly miniaturize such systems, with perhaps the ultimate achievement being the synthetic microbe or cell sized machine. To this end, we have introduced and demonstrated prototypes of what we call Colloidal State Machines (CSMs) as particulate devices capable of integrating sensing, memory, energy harvesting as well as other functions onto a single particle. One technique that we have introduced for creating CSMs based on 2D materials such as graphene or monolayer MoS₂ is “autoperforation”, where the nanometer scale film is fractured around a designed strain field to produce structured particles upon liftoff. While CSMs have been demonstrated with functions such as memory, sensing, and energy harvesting, the property of locomotion has not yet been demonstrated. We also introduce an inversion molding technique compatible with autoperforation that allows for the patterning of an external catalytic surface that enables locomotion in an accompanying fuel bath. Optimal processing conditions for electroplating a catalytic Pt layer to one side of an autoperforated CSM

are elucidated. The self-driven propulsion of the resulting Janus CSM in H_2O_2 is studied, including the average velocity, as a function of fluid surface tension and H_2O_2 concentration in the bath. Since machines have to encode for a specific task, this chapter summarizes efforts to create a microfluidic testbed that allows for CSM designs to be evaluated for the ultimate purpose of navigation through complex fluidic networks, such as the human circulatory system. We introduce two CSM designs that mimics aspects of human immunity to solve search and recruitment tasks in such environments. These results advance CSM design concepts closer to promising applications in medicine and other areas.

5.1 Autoperforation of Two-Dimensional Materials for Generating Two Terminal Memristive Janus Particles

Graphene and other 2D materials possess desirable mechanical, electrical and chemical properties for incorporation into or onto colloidal particles, potentially granting them unique electronic functions. However, this application has not yet been realized as conventional top-down lithography scales poorly for producing colloidal solutions. Herein, we developed an “*autoperforation*” technique that provides a means of spontaneous assembly for surfaces comprised of 2D molecular scaffolds. Chemical vapor deposited 2D sheets can autoperforate into circular envelopes when sandwiching a microprinted polymer composite disk of nanoparticle ink, allowing lift-off into solution and the simultaneous assembly. The resulting colloidal microparticles have two independently addressable, external Janus faces that we show can function as an intraparticle array of vertically-aligned, two-terminal electronic devices. Such particles demonstrate remarkable chemical and mechanical stability and form the basis of particulate

electronic devices capable of collecting and storing information of their surroundings, extending nanoelectronics into previously inaccessible environments.

Griffith showed that during brittle fracture, the energy needed to overcome the chemical bonding within a material is supplied by the surface energy (γ) released upon cracking¹. The former scales quadratically with strain while the latter is linear – such that there is a characteristic length, a_c , below which a pre-existing micro-crack is infinitely stable. Spontaneous cracking proceeds when the applied local stress reduces this Griffith length¹ to the size of an existing defect or micro-crack. The fact that the number and orientation of pre-existing micro-cracks in a material are stochastic, as is the trajectory of a propagating crack, prevents brittle fracture from being used as a controlled nanofabrication technique.²⁻

⁴ Although graphene and other 2D materials have unique mechanical properties, the classic Griffith criterion still applies to their brittle fracture.^{5,6} Large-area graphene or other 2D materials prepared by the chemical vapor deposition (CVD) method,⁷⁻⁹ albeit mechanically robust,¹⁰ usually carry intrinsic nanometer-sized defects originating from the growth and subsequent transfer processes, and this seed crack formation is necessarily stochastic in nature. A recent amendment to the Griffith theory suggested that the imposition of a rigid substrate with Gaussian curvature could predictably control the macroscopic crack growth of a flat elastic sheet upon stretching.¹¹ Such curvature is observed to induce a local stress/strain field that can modify the Griffith length a_c ,

$$a_c \approx \frac{2\gamma}{\pi E \varepsilon^2} \quad (41)$$

Here, γ and E denote the surface energy density and elastic modulus of any given material; whereas ε measures the induced material strain. The value of a_c sets a lower bound on the maximum tolerated seed crack length – spontaneous material rupture would occur if and only if a_c falls below the size of inherent material defects. In this work, we ask if a similar imposition of a strain field at a scale 1000 times smaller could likewise guide spontaneous crack formation in molecularly thin 2D materials,¹² leading to a scalable nanofabrication method to produce new types of electronic colloids capable of complex device operations.

The theoretical approach outlined above¹¹ can be adapted to numerically simulate the graphene fracture process with randomized initial seed cracks. Using the characteristic non-linear stress-strain relation of graphene, for example, our simulation shows that a circular-shaped heterogeneous strain field imposed on a 2D lattice both attracts crack growth, and guides the crack trajectory along the path of maximum hoop strain (**Figure 6-1a**). Empirically, such an annular-shaped stress distribution within the 2D lattice may be introduced via two sequential processes – namely the mold-based folding followed by the solvent-enabled shear straining (**Figure 6-1b**). To elaborate, the initial hoop strain is established by folding/conforming the 2D material embedded elastic sheet (Thin film A of **Figure 6-1b**) over a relatively rigid substrate with Gaussian curvature¹¹ – defined in this study by ink-jet printed disk-shaped polymer protrusions (**Figure 6-1b, c**). Meanwhile, by placing the film A-covered polymer island atop a second layer of compliant film (Thin film B of **Figure 6-1b**), we laminate this protrusion with both films, effectively forming a sandwich structure that reinforces the 2D materials above and below. Additional straining for the thin films occurs when we subject the sandwich structure into an agitated solvent^{13,14} (**Figure 6-1b**). Much of the turbulence-induced shear stress is diverted towards the

laminate-free annular film regions, contributing further lattice straining to the 2D material located around the edges of the printed disk (**Figure 6-1c**). Such shearing effect, combined with the initial folding step, can afford lattice strains up to 1% at a disk aspect ratio of 100:1 (radius versus height) (**Figure 6-1a, c**). This is large enough to reduce the 2D material's local Griffith length (a_c) down to several nanometers, exceeding the maximum tolerated threshold, thereby drives run-away lattice ruptures in a spontaneous, yet still highly controlled, fashion. This strain induced crack propagation, enabled by the Griffith criterion, opens the possibility to use nanometer scale fracture growth as a fabrication method. In this case, it ultimately facilitates the precise cleavage of 2D molecular layers and the subsequent generation of rationally designed circular particulates (**Figure 6-1a**).

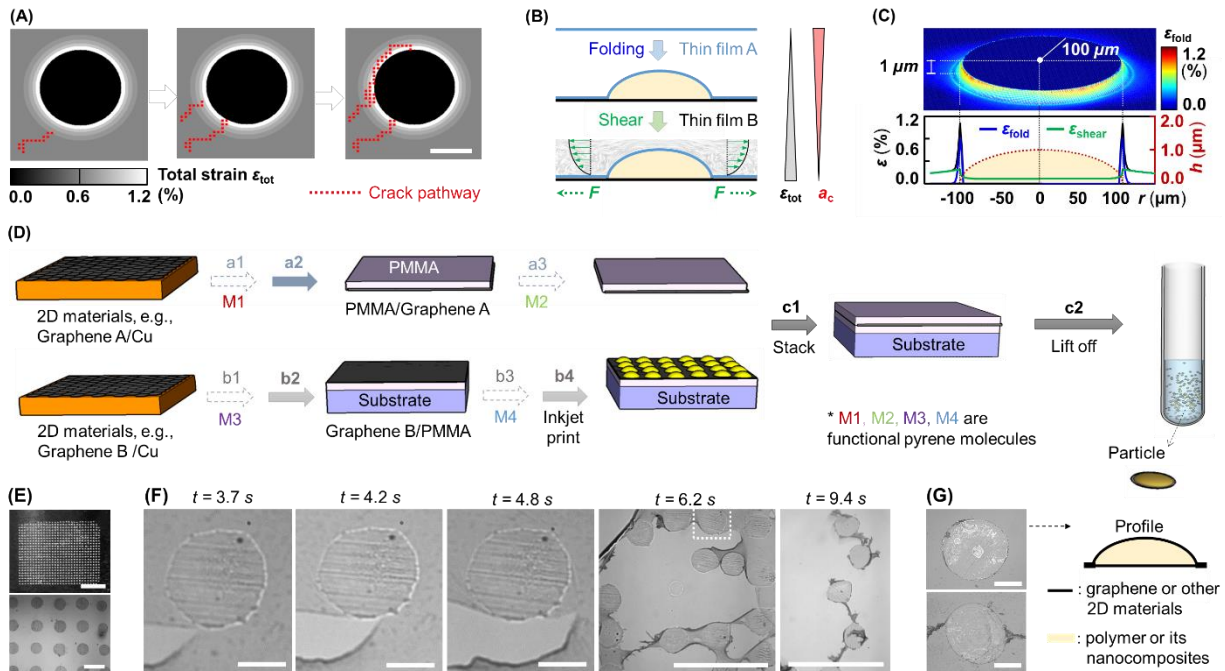


Figure 6-1. Autoperforation of 2D materials to generate colloidal microparticles with 2D

surfaces. (a) Numerical simulation of the fracture propagation within the graphene sheets encapsulating a curved polymer (e.g. polystyrene) disk ($h = 1 \mu\text{m}$), scale bar, 100 μm . (b)

Schematic illustration of the two-step process generating the strain field used in (a). The first step involves folding the graphene-containing thin film A on top of the curved polymer disk printed onto film B, with the same composition as A. The second shearing step is facilitated by flowing an agitated liquid over the film-encapsulated disk, creating a tensile stress within both films synergistic to the folding strain, modeled here as an outward-facing force F pulling uniformly away from the film center. (c) The local strain field after stacking/folding a thin polymer film (200 nm) onto a micro-disk (radius : height = 100 : 1) based on finite element analysis. (d) Microparticle encapsulation within graphene: a1, functionalizing Graphene A with M1; a2, spin-coating poly(methyl methacrylate) (PMMA) and etching out the copper; a3, functionalizing with M2; b1, functionalizing Graphene B with M3; b2, spin-coating PMMA, etching out the copper, and transferring PMMA/GB onto SiO₂/Si or PDMS; b3, functionalizing with M4; b4, inkjet printing nanoparticle ink; c1, stacking; c2, annealing and liftoff via dissolution of the PMMA layers. (e) Optical micrographs of the micro-disk array before liftoff, scale bars, 5.0 mm (top) and 0.5 mm (bottom). (f) Optical micrographs showing fracture and crack propagation of the graphene layers around a single polymer disk ($t = 3.7$ to 4.8 s, the three scale bars are all 100 μm) and multiple spots ($t = 6.2$ - 9.4 s, the two scale bar are both 1 mm) during the liftoff process. (g) Typical microparticles sampled out from the liftoff solution and its schematic profile, the two scale bars are both 100 μm .

Guided by theoretical predictions, we systematically investigated controlled crack propagation in CVD-grown 2D films of various compositions, producing microparticles comprising of a pair of enveloping 2D molecular layers (**Figure 6-1d-g**). As an example, two copper-supported graphene sheets, labeled graphene A and B, first undergo a series of processing steps including optional chemical functionalization, spin-coating of a

poly(methyl methacrylate) (PMMA) layer, copper etching, and inkjet printing of templating disks; These two thin films are then stacked, encapsulating the printed micro-disk array, to form a sandwiched structure on a PDMS or SiO₂/Si support (**Figure 6-1d**). For the inkjet printing step, we used an ink composed of polystyrene (PS) latex nanoparticle solution (1.2 wt%, mean particles size = 50 or 100 nm) or its composites with other nanoparticles like 30 wt% ZnO (8-16 nm size), 1.9 wt% iron oxide (II, III) (30 nm), 0.9 wt% black phosphorous (BP) (liquid-exfoliated, 1-3 layers, ~ 280 nm size), 0.07-1 wt% graphene oxides (GOx), or 0.07 wt% MoS₂, depending on the desired functionality. Subsequent drying at ambient temperature necessarily induces adhesion forces that folds/conforms of the PMMA/graphene sheets onto the micro-disk array (**Figure 6-1e**). Further annealing at 120 °C softens PMMA layers and enhances the non-covalent binding between the two graphene sheets and their interactions (from top and bottom) with the corresponding micro-disks. Lifting off the sandwiched structure by selectively dissolution of the PMMA layer in EtOH/H₂O (4:1 in volume) at 80 °C¹⁵ “hatches” the graphene-sandwiched micro-disks from the substrate into the solution with a nearly perfect yield. The micro-disk array guides the crack path of the conformed graphene sheets along the disk edges during this liftoff (**Figure 6-1f**), and we term this whole process as “*autoperforation*”. Magnetic agitation can induce further lattice stretching and promote autoperforation, generating disk-shape microparticles with diameters around 260 μm (**Figure 6-1g**, recaptured and dried on a microscope slide). These are essentially graphene-laminated colloidal particles that can freely rotate and translocate in solution. They can also be propelled magnetically if one incorporates iron oxide nanoparticles into the PS ink.

The microparticles retain intact graphene mono- or bi-layers on both surfaces, which significantly improve their colloidal stability during the liftoff and storage (**Figure 6-2a**). Raman mapping of the 2D peak signal at 2680 cm^{-1} of a graphene-PS-graphene (G-PS-G) microparticle confirms the complete coverage of graphene on its surface (**Figure 6-2a**). Little change occurs in the graphene G and 2D peak intensities as well as their ratios before and after liftoff. Autoperforation works equally well with just a single sheet of graphene, resulting in micro-disks with graphene coverage restricted to a single surface. To access the microparticles' overall stability upon liftoff, characterized as yields or survival rates over time in a ethanol/water (4:1) storage mixture, we sampled individual particles (up to 173 in one set) at various time points and counted the fraction of which with retained mechanical integrity. For example, G-PS-G exhibited a yield of 80% right after liftoff as compared to the 55% for control particles without graphene encapsulation. This yield linearly decays to 54% after four months of suspension in the liquid phase. Compositing PS with BP nanoflakes increases the yield, reaching 85% after the initial liftoff and 76% after nine weeks of suspension. Interestingly, the modes for mechanical failure of graphene microparticles also differ significantly from that of the controls, with the former more likely to tear and remain intact as individual parts, as opposed to the complete particle dissolution often seen in the controls.

The disk thickness, radius, and vertical profile can be controlled by adjusting the concentration, composition, and the amount of the polymer ink used to form the interior pillar. Lateral force profiles of micro-particles printed with 1 nL of PS nanoparticle ink (**Figure 6-2b-d**) approximate a toroid (**Figure 6-2b**) with average peak height (h_{peak}) of $1.1\text{ }\mu\text{m}$ and valley height (h_{valley}) of $0.4\text{ }\mu\text{m}$ (**Figure 6-2d**). Decreasing the ink concentration

to 0.2 wt% reduces h_{peak} and h_{valley} to 0.6 μm and 0.1 μm respectively at a diameter of 160 μm (**Figure 6-2d**). While the autoperforation of 2D-engrafted colloids with shapes other than circular disks have yet to be systematically explored, the general theory outlined earlier does predict that a strain field imposed by any arbitrarily shaped polymer protrusions will in principle guide 2D material fracturing along that arbitrary path, as already seen in this study for irregularly shaped mis-printed disks. In addition, compositing PS with BP or ZnO nanoparticles alters the overall colloidal shape to a convex ellipsoid (**Figure 6-2c**) with a diameter of 260 μm and tunable h_{peaks} between 0.8 and 1.2 μm (**Figure 6-2d**). One can also manipulate the minimum feature size of the printed micropillars by tuning the ink volume. For example, using volumes of 1 and 10 pL, we were able to print much smaller polymer disks with $d = 18.6$ and 34.2 μm , and $h_{\text{peak}} = 31$ and 290 nm, respectively (**Figure 6-2e**). The smallest autoperforated microparticles with fully-covered graphene surfaces are the 34.2- μm disks. Moreover, the autoperforation protocol can be translated for 2D-engraftment of larger sized colloids. Contact printing with a capillary glass tube produces macroscopic G-PS-G particles, each with mm-size diameter, consistent with our mechanical model.

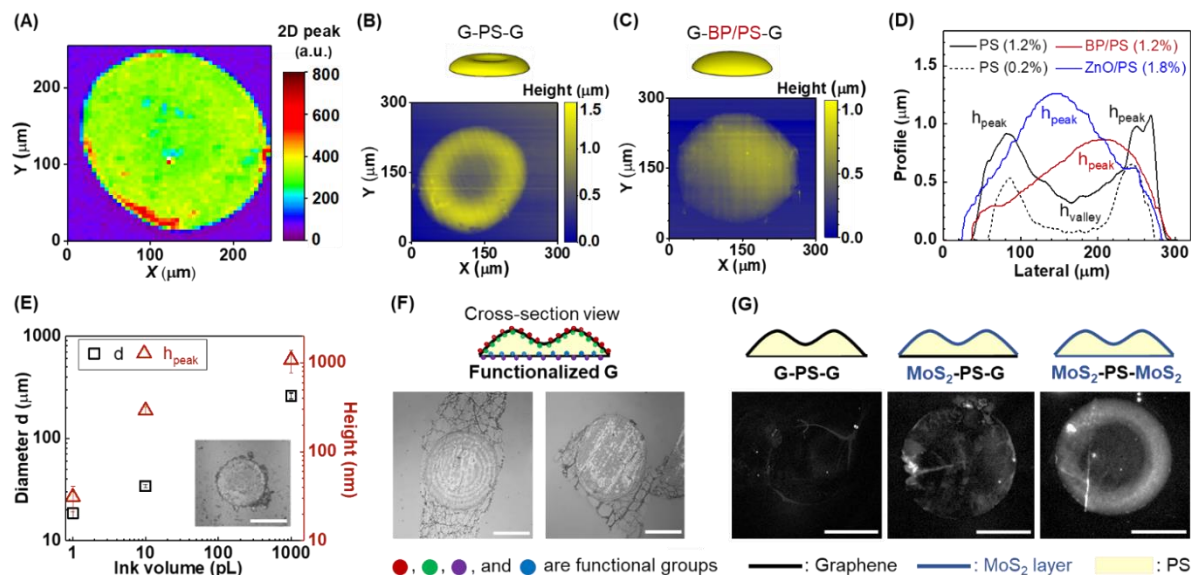


Figure 6-2. Characterization of the microparticles after liftoff. (a) Spatial mapping of the 2D peak (2680 cm^{-1}) intensity of graphene-PS-graphene (G-PS-G) microparticle via Raman spectroscopy. (b) and (c) are the contour profiles of G-PS-G (1 nL, 1.2 wt% ink) and G-BP (0.9 wt%)/PS-G (1 nL, 1.2 wt% ink) microparticle. (d) Lateral profile curves of various microparticles printed with 1-nL ink of different concentrations and compositions. (e) Plot of the diameter (d) and height dependences of G-PS-G microparticles against the ink volume. The inset shows the optical image of a graphene encapsulated particle with $d \sim 34\text{ }\mu\text{m}$, scale bar, $20\text{ }\mu\text{m}$. (f) 2D Janus particles with broken vertical chemical symmetry, scale bars, $100\text{ }\mu\text{m}$. (g) Fluorescence images of microparticles with G/G, G/MoS₂, and MoS₂/MoS₂ surface; G - bilayer graphene and MoS₂ - monolayer molybdenum disulfide; scale bars, $100\text{ }\mu\text{m}$.

We assert that *autoperforation*, as a fabrication method, is particularly enabling in that it allows for selective chemical functionalizations of the two individual 2D surfaces encapsulating the micro-disks with independent control, giving rise to 2D Janus particles with broken materials symmetry (**Figure 6-2f**).¹⁶ This is done without the use of more

complex clean room processing, laser cutting, or particle-by-particle fabrication methods that scale poorly for large-scale 2D material incorporation and functionalization.^{17,18} Pyrene or naphthalene molecules tethered to different functional groups (*e.g.*, $-\text{COOH}$, $-\text{NH}_2$) can be used to modify the chemical composition, as well as to tune physical properties, on the two sides of each graphene sheet noncovalently, as characterized by X-ray photoelectron spectroscopy (XPS), water-contact angle, and Raman spectroscopy measurements. Such non-covalent functionalization breaks the intra-particle axial symmetry, allowing the formation of Janus colloids with four independently addressable faces (two outward-facing, two inward-facing, **Figure 6-2f**), all the while impacting minimally on the overall graphene coverage as well as the particle radial height profile. Interestingly, this type of functionalization, enabled by π - π interactions, appears to further strengthen the graphene surface, giving rise to visible “wings” around the particle exterior upon liftoff, and overall a better encapsulation of the interior composite “cargo” (**Figure 6-2f**). This is evident from the marked improvement in survival rate (70%) even after 8 months of storage in solution. We further confirmed that the non-covalent carboxyl-functionalization of two graphene inner surfaces (that directly contact PS) alone could result in such “wings”. We think that such functionalization can enhance the bonding between the graphene layers and the interior filler, *via* electrostatic interactions. We note that this significantly expands the scope of material options for printing and encapsulation compatible with the autoperforation protocol.

Autoperforation allows for the fabrication of unique combinations of 2D material microparticles. We have successfully prepared microparticles with vertical architectures such as G-PS-MoS₂, MoS₂-PS-MoS₂, and hBN-PS-hBN. Interestingly, fluorescence

imaging of G-PS-G, G-PS-MoS₂, and MoS₂-PS-MoS₂ microparticles with excitation at $\lambda_{\text{exc}} = 550 \text{ nm}$ ¹⁹ demonstrates a stepwise increase of the photoluminescence (PL) intensity (**Figure 6-2g**), indicating an effective coverage of MoS₂ surface layers on the microparticles. Both G-PS-MoS₂, and MoS₂-PS-MoS₂ exhibit PL with the latter approximately twice the former (**Figure 6-2g**), demonstrating the isolation of the 2D exciton to one face of the particle (MoS₂) that would otherwise be quenched by the graphene surface.

Of significant utility is that the resulting disk-shaped microparticles exhibit high surface conductivity such that they can function as two-terminal electronic devices in the vertical direction when captured in the prolate orientation from solution (**Figure 6-3**). The in-plane conductance of the G-PS-G microparticle is about 10^{-5} S , ten orders of magnitude higher than that of the PS control (10^{-15} S) (**Figure 6-3a**). The calculated sheet resistance of the PS supported graphene is $890 \text{ } \Omega/\text{sq}$ as compared to the $4.3 \times 10^{13} \text{ } \Omega/\text{sq}$ for PS, consistent with reported values²⁰ and this necessarily isolates the two opposing 2D material faces. The two vertical graphene terminals are electrically isolated, allowing the design and implementation of through-plane electronic devices in the interior of the microparticle, as we demonstrate below.

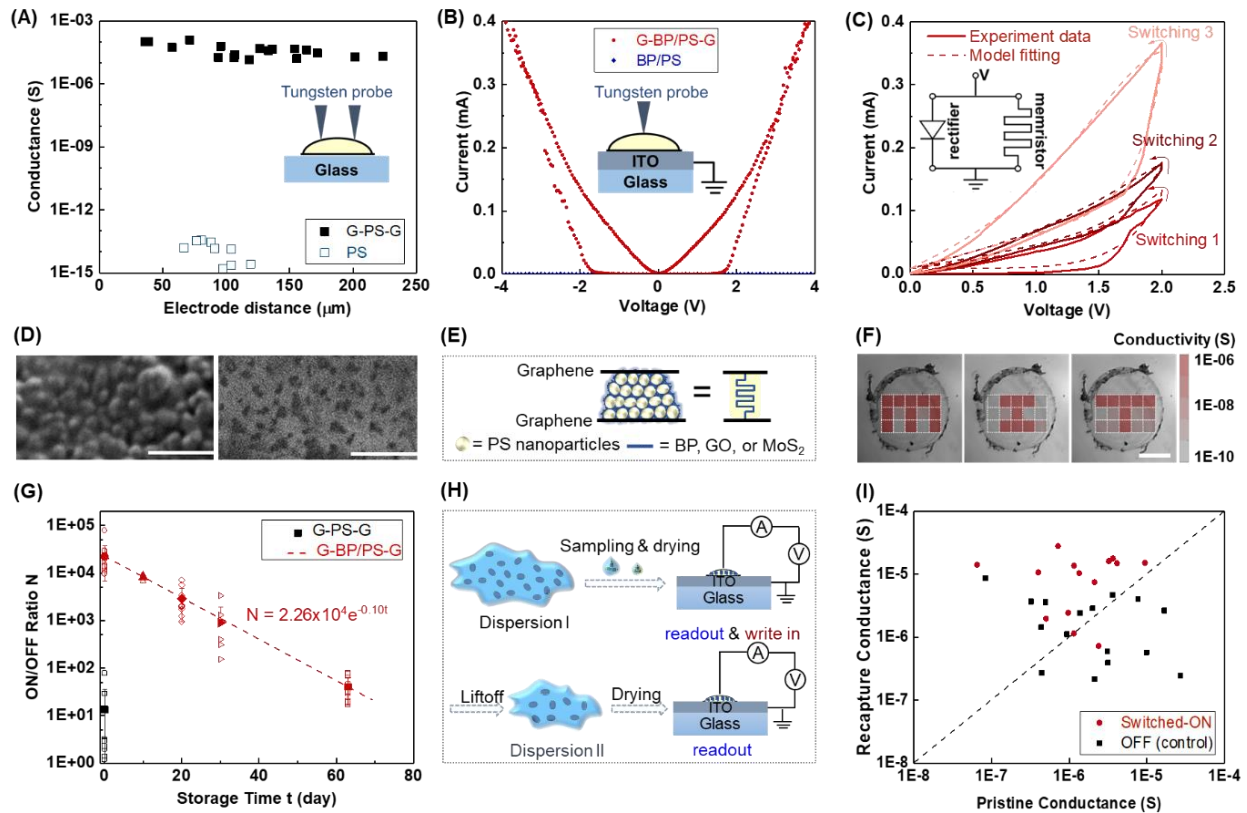


Figure 6-3. Electrical properties and memristive characteristics of the graphene (bilayer) microparticles. (a) Plot of in-plane conductance vs. electrode distance for G-PS-G and PS control, with inset showing the testing configuration. (b) Cross-plane I-V curves of microparticles G-BP (0.9 wt%)/PS-G, G-PS-G, and BP/PS. (c) I-V curves of three successive sweeps of $0 \rightarrow 2 \rightarrow 0$ V (switching 1, 2, 3 and the fitting curves based on the equivalent circuit model shown in the inset). (d) Scanning electron micrographs (SEM) of BP/PS composite cross-section, and the corresponding energy selective back scattering (right panel) showing PS (dark) and BP (light) domains, scale bars = $1 \mu\text{m}$. (e) Schematic illustration of the percolated composite structure as a single memristor element of the microparticle. (f) Digital information storage of letters “M”, “I”, “T” on a 5×3 grid defined laterally within a single G-BP/PS-G microparticle via spatially selective writing/turning ON ($0 \rightarrow 4$ V) or erasing/switching OFF ($0 \rightarrow -4$ V) of individual vertical memory

domains on the grid with a 5 μm probe, scale bar, 100 μm . (g) Plot of the ON/OFF ratio N measured at 0.2 V readout voltage for multiple memristive G-BP/PS-G particles against their storage time (for over two months) in ethanol/water (1:1). Each hollow symbol represents a data point measured from a random position of an individual microparticle. Standard deviation represents an average over ~ 10 microparticles. (h) A schematic illustration of the entire digital information distribution process including particle sampling, information readout & write in, particle liftoff, recapture, and information readout. (i) Scattered plot of the vertical conductance of G-MoS₂/PS-G particles in their pristine states before liftoff against the corresponding post-recapture conductance for domains that were turned on (red) and those that were not (control, black). Data are collected from 4 different G-MoS₂ (0.07%)/PS-G microparticles, each represents the conductance of a specific memristive domain on the microparticle defined by a 2×6 grid. Control domains are distributed around the diagonal line, indicating no significant conductance variations before and after liftoff.

By adding 0.9 wt% BP nanoflakes to the PS during ink-jet printing, we build electrically bistable resistive switches in a parallel configuration throughout the device interior, forming memristive domains (G-PS/BP-G). Together with the two graphene terminals over on top and at the bottom, each domain becomes an electronically isolated, individually addressable non-volatile memory element (**Figure 6-3b**). With this vertical G-PS/BP-G architecture, the microparticle as a whole functions as an array of reversible random access memory (RRAM) elements, demonstrating the characteristic two-terminal resistive switching behavior (**Figure 6-3b, c**). To illustrate, the as-produced vertical stack starts in a high resistance state (HRS or OFF) and a subsequent voltage sweep from 0 to 4 V switches the device to its low resistance state (LRS or ON), corresponding to a “write-in”

event to the digital memory. A reverse sweep from 0 to -4 V or lower switches the device back to OFF as an “erasing” event, and this OFF state persists until a subsequent 0-4 V sweep in the next cycle. Remarkably, the ON/OFF ratio (N) reaches up to 10^4 at a readout voltage of 0.2 V, even though the microparticle contains just 0.9 wt% of BP. Graphene appears to be indispensable in this memory formation process, as the PS/BP particle alone is essentially insulating (**Figure 6-3b**). We confirm that the electrical memory is non-volatile using three consecutive low voltage scans which exhibit a signature sequential step-wise conductivity increase (“switch 1” and “switch 2”). Comparison with the diode-memristor model²¹ suggests quantitative agreement, indicating predictable behavior (**Figure 6-3c**) for future device optimizations.

The memristor function emerges from the reversible chemistry of BP nanoflakes and the percolated structure of the BP/PS composite in the interior. Oxidation of BP nanoflakes during liquid exfoliation introduces phosphate and phosphonate groups on the flake surface or edges,^{22,23} as confirmed by XPS. These oxygen-containing moieties act as insulating charge traps at low bias and conductive channels above a threshold voltage through electromigration of the mobile oxygen vacancies, a common switching mechanism observed in a wide range of memristors.²⁴ Printing BP flakes in the presence of PS nanoparticles forms a percolated network with BP interpolating the vicinal PS,²⁵ and we can characterize this structure using both the cross-section morphology as well as the elemental distribution of the BP/PS composite from scanning electron microscopy (SEM) data (**Figure 6-3d**). This network architecture, using closely-packed PS for structural support without sacrificing BP connectivity, enables the device to function as an active resistive switch with good mechanical integrity at a BP content as low as 0.9 wt%.

Replacing BP with other memristive nanoflakes like MoS₂²⁶ also imparts in the colloidal system similar memristor capabilities, at only a 0.07 wt% MoS₂ loading, further supporting the percolated network hypothesis above.

Figure 6-3e presents a schematic of the percolated composite structure comprising a memristor element with graphene layers as terminal electrodes. The percolated BP (or GOx, MoS₂) network functions as a charge trapping (or memory storage) material, with PS serving as its structural support. These submicron memristive channels are then vertically aligned in a monolithic fashion, affording parallel memory storage domains across the surface of both graphene terminals (**Figure 6-3e**). Applying a local electrical potential across any two opposing points, each on a graphene terminal, can turn these memristive elements ON or OFF over a domain defined by the current spreading radius within the device. As a demonstration, we used a probe with a 5 μm tip diameter to selectively turn ON or OFF 15 domains defined by a 5 × 3 grid on a G-BP/PS-G microparticle. We were able to repeatedly store, read, and erase 15-bit worth of information digitally into a single colloidal microparticle, seen here as spatial patterns of “M”, “I” and “T” on the grid (**Figure 6-3f**), with an average ON/OFF ratio $N \approx 10^4$. At a 100 nm probe diameter, a 100 μm device would yield 10⁶ parallel bits. An alternative way to define different domains (or bits) is to introduce highly conductive metal contact pads on the microparticle. We implemented this idea via an additional printing step of a finer micro-array of silver nanoparticles on top of each printed PS composite disk, prior to the top graphene laminate and final device autoperforation, and the switching behavior of each memristive domain defined by the Ag contact is retained.

Microparticles bounded by graphene surfaces show good chemical and physical stability for memory storage. For example, G-PS-G appears to retain ellipsoidal shapes and mechanical integrity even after an aggressive treatment in an acidic glycine solution (0.4 M, pH = 1.5, adjusted using concentrated HCl) that mimics the harshest of conditions through the human gastrointestinal tract for over 24 hours. Individual G-BP/PS-G devices exhibit robust underwater memory stability (e.g., ON/OFF ratio > 10³), able to tolerate at least seven rounds of repeated water immersion-air drying cycle, with a 10 min immersion time for each test period. This highlights yet another important role graphene plays in this colloidal electronic device – in addition to being a mechanical barrier that prolongs particle in-solution lifetime, an electronic terminal that enables memristive switching (**Figure 6-3a**), it also provides an effective chemical shield against erosive environments detrimental to classic electronic systems. After all, BP is notoriously sensitive to trace oxygen and moisture, rendering it unstable even under ambient conditions²⁶⁻²⁸. Furthermore, we followed the change in *N* values for these memristive colloids during liquid-phase storage in an ethanol/water solution (50 vol%) over 63 days, and observed a half-life of 7 days for the decay of *N* and an average *N* of 41 for microparticles at day 63 (**Figure 6-3g**). The scaling suggests that dissolved oxygen and/or water may gradually permeate into the BP/PS interior through intrinsic defects or nanopores within the CVD graphene membranes.²⁹ Water and oxygen can react with and etch out superficial BP irreversibly,^{26,27} as characterized by XPS measurements comparing multiple 0 and 90-day microparticles. Using 2D materials with fewer of these porous defects may increase the persistence of *N*, thereby prolonging information retention.

As a consequence to the multitude of capabilities brought by the engrafted 2D materials, we can electrically encode digital information into these microparticles, lift them off as mobile dispersing colloids into aqueous or organic solvents, and then recapture them after a certain period of time at a distant location to electrically read out the written data (**Figure 6-3h**). To demonstrate this digital information relay, we deployed a batch of G-MoS₂ (0.07 wt%)/PS-G colloidal devices (with turn-on voltages as low as 2.0 V) in solution, each carrying a sequence of digital information individually written as ON and OFF states within the memristor array. Upon device retrieval, we compared the through-plane conductance of each memory element (normalized against the conductance of each domain's respective pre-written OFF state), and found over an order of magnitude increase in vertical conductance measured for domains set to the ON state (p -value = 0.0004, $n = 14$), while the control domains remained to be OFF ($n = 25$, **Figure 6-3i**). These experiments encourage the use of these microparticles as autonomous colloidal electronic platforms,^{30,31} when coupled to on-board or externally-harvested power,³²⁻³⁵ to actively capture information, storing it for a duration in the memristor array for read-out at a later time.

The particulate nature of these two-terminal devices bestows in them the properties of fluid dispersions, and therefore convective mobility, which allows one to bring electronics into otherwise inaccessible locations. Applications include “aerosolizable electronics” as soft probes for remote sensing and recording of environmental information from unconventional spaces. To test the ability to aerosolize particles with a standard G-PS-G architecture, we used an airbrush pressured to 1.7 atm (**Figure 6-4**), nebulized a 10-mL dispersion of such microparticles, and sprayed them as aerosols over of distance of 30 cm onto a target collector (**Figure 6-4a**). The collected microparticles were studied under an

optical microscope for changes in morphology and deposition location relative to the ejection centerline. **Figure 6-4b** presents the positions of all 460 collected G-PS-G microparticles, 80% of which are located isotropically within a distance of 8 cm from the centerline. Microparticles appear to be mechanically flexible with some samples folded into various 3D structures during the nebulization process without any fracture, and the survival yield is approximately 10% lower than that by evaporative drying. Notably, the graphene surfaces remain intact upon capture, preserving the electronic integrity of the device for further digital information storage. We also found that the use of adhesive tapes, such as a flexible paper tape or conductive copper tape, allows facile transfer of the dried electronic particles out from its initial-captured location. If a copper tape is used, one can also read out and write in digital information just like on top of any other conductive substrates.

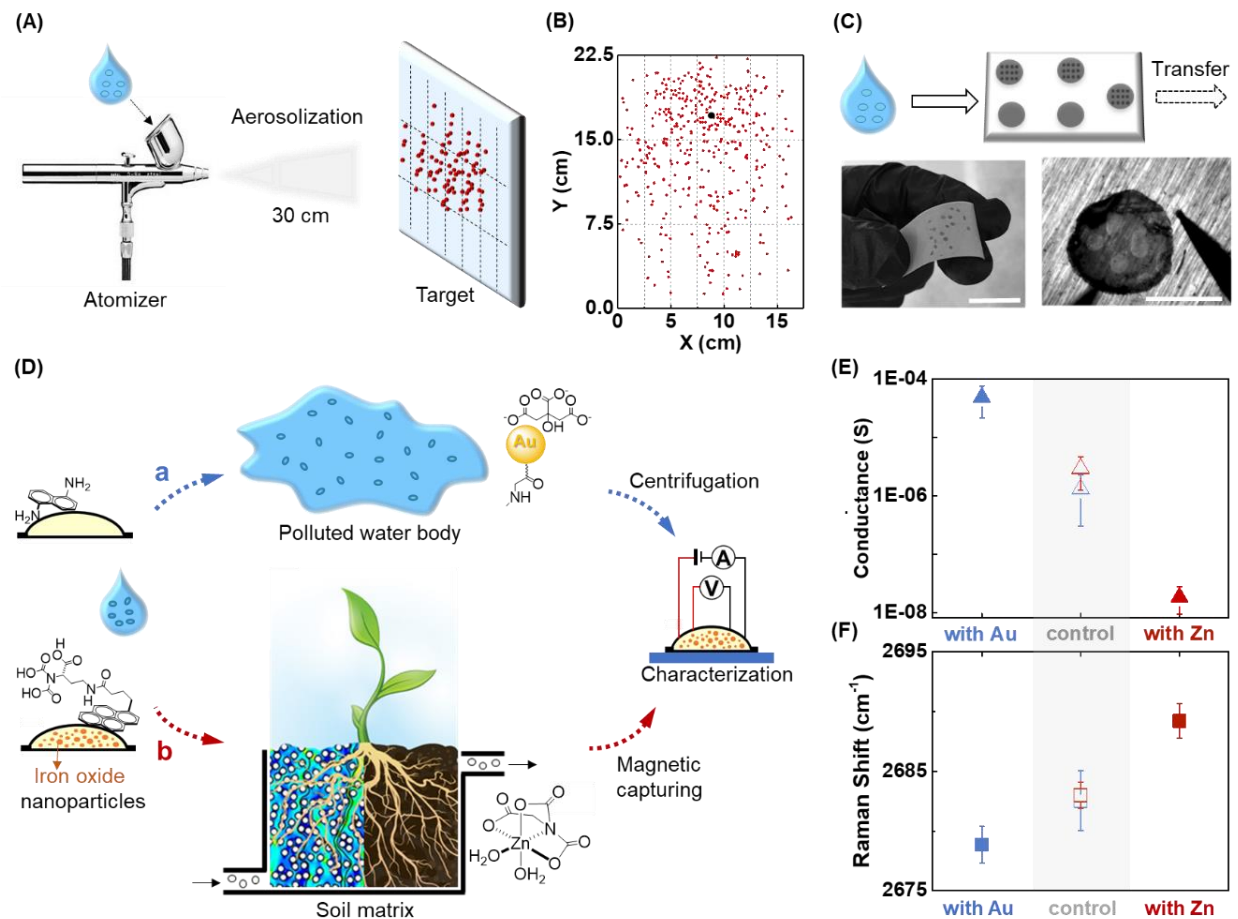


Figure 6-4. G-PS-G microparticles as a platform to sense and record environmental information. (a) Aerosolization of G-PS-G colloids via an airbrush and collection via a Pyrex glass surface approximately 30 cm away. (b) Scatterplot of the isotropic collection pattern for 460 nebulized microparticles suggesting neutral buoyancy and absence of sedimentation. Each red point represents a G-PS-G particle located using optical microscopy. (c) Schematic illustration showing the transfer process of the aerosolized G-PS-G colloids onto a conductive adhesive tape for electrical measurements. Scale bars are 20 mm (bottom left panel) and 1 mm (bottom right panel). (d) Schematic illustration of the deployment of surface-functionalized G-PS-G microparticles as chemical probes to detect and record the presence of various species such as metal nanoparticles and ions in (a) ground water and (b) soil matrix. These colloidal devices can

be retrieved via centrifugation or magnetic capture for electronic and optical read out. (e) The surface in-plane electrical conductance and (f) the graphene Raman 2D peak position of the microparticles retrieved in (d).

Finally, we emphasize that the unique capability for us to engineer both a colloidal particle's surface chemical environment and its interior filler composition, brought about by the autoperforation technique, opens these two-terminal electronic devices up for additional opportunities. For example, non-covalent functionalization of the particle exterior surface with capture sites to ligate with specific metallic residues and ionic species in water bodies and soil matrices, respectively, equips these electronic colloids with a chemical sensory unit that integrate readily into the existing functional modalities (**Figure 6-4d**). Specifically, graphene-based microparticles with tethered surface amine groups can interact with citrate-coated gold nanoparticles in water ($\sim 6.0 \times 10^{12}$ particles/mL, 10 nm) (**Figure 6-4d**), and those with surface nitrilotriacetic acid (NTA) ligands can capture Zn^{2+} ions (an essential nutrient for plant growth²⁹, 10 mM), while traversing the soil bed (**Figure 6-4d**). Such interactions change the state of the in-plane electrical conductivity for the two-terminal devices, i.e., the amine modified devices show more than one order of magnitude increase in the surface conductance upon detection of gold nanoparticles (**Figure 6-4e**, blue triangles), while a two orders of magnitude reduction was observed for the NTA-functionalized particles upon Zn^{2+} exposure (**Figure 6-4e**, red triangles). Raman spectroscopy confirms the two binding events with an observed redshift of the graphene 2D peak for about 3.7 cm^{-1} in amine-Au samples (**Figure 6-4f**, blue squares) and a corresponding blueshift of the same peak for about 6.2 cm^{-1} in NTA- Zn^{2+} samples (**Figure 6-4f**, red squares). As mentioned before, incorporating iron oxide nanoparticles (1.9 wt%)

into the interior filler of the electronic colloids renders them ferromagnetic. This enabled us to retrieve and separate these particles using external magnetic fields from the ground water passing through the soil bed (**Figure 6-4d**). These results demonstrate the potential for these microparticles with functionalized 2D surface layers to be deployed as ubiquitous micrometer scale electronic sensor nodes for the ultimate detection of more sophisticated chemicals with multivariate outputs and high selectivity.

In summary, we introduce *autoperforation* as a nanofabrication method that exploits guided defect self-assembly within atomically thin molecular layers to prepare 2D material encapsulated colloidal Janus microparticles. This represents a mechanistically orthogonal approach to the previously reported folding/scrolling methods to make partially encapsulated²⁹ or self-wrapped object (i.e. a fiber³⁰) with inherently open topological structures. In autoperforation, the controlled cleavage of the 2D sheets along a prescribed trajectory results in sophisticated designs in both the lateral and vertical dimension. Chemical vapor deposited mono- and bi-layer graphene, molybdenum disulfide, and hexagonal boron nitride (hBN) are shown to autoperforate into ellipsoidal, colloidal microparticles with two independently addressable, external Janus faces. We show that such colloidal microparticles can function as intraparticle arrays of parallel, two-terminal electronic devices, equipped with vertical non-volatile memory domains with good chemical and physical stability. We show that they can also function as aerosolizable, dispersible and recoverable particulate electronics within complex environments. *Autoperforation* of 2D materials, in this way, has the potential to become a platform technology, assisting the development of intelligent nano/micro-particles that perform

functions not yet available to colloidal particles, hence further extending nanoelectronics into previously inaccessible environments.

In this following section, we provide one potential application for such multi-bit memristive arrays fabricated above. As we will show, it forms the basis of a completely different timing scheme (as compared to the conventional “tic-toc” scheme in which an oscillator coupled to a counter is used) that in principle can be extended down (both in terms of fabrication feasibility and energy efficiency) towards the colloidal scale.

The miniaturization of robotic systems is currently an accelerating research trend, motivating the exploration towards the trade-off limit between size and function. Accessing temporal information, often enabled by a digital clock circuit, represents one such desirable functions that tend to overload the energy budget, precluding device miniaturization. A transmission cable circuit, equipped with trans-membrane memristive channels, is proposed as an alternative approach to record the passage of time as discrete non-volatile memory bits. We further explore the design and implementation of this timer circuit onto a graphene encapsulated, colloidal electronic device, small enough to access excluded environments. The proposed timing mechanism, based on vertical memristor arrays, provides the theoretical basis for translating temporal evolutions electronically onto the spatial domain, opening avenues for time-dependent chemical sensing, as well as other pace-sensitive functionalities in microscale robotic systems.

Creating a colloidal particle cognizant of the temporal evolution has been a standing goal in the materials community. There are many examples of microscopic probes as chemical sensors or signal transducers. Arming these deployable nodes with access to its information

history as a function of time opens additional opportunities for higher-level autonomous functions. For instance, a multi-channel pH sensor would not be of much use when travelled through a human digestive system without real-time external monitoring; but the same particle capable of sequentially recording pH information at discrete time points can output an acidity map through our entire gastrointestinal tract with no more additional inputs than its residence time. As such, time-awareness, even in its simplest form, allows us to address challenges such as (1) mapping atmospheric compositions over an exceeding large volume; (2) detection of pipeline leaks that traverses long distances; (3) pinpointing locations of inflammation or biomarkers within the mammalian vasculature. In addition, we note that a particle that can record both the local time, as well as its excursion time can precisely access its global longitude. Comparing a local timestamp with the particle's excursion history yields an awareness of its longitudinal position – in the same way as John Harrison's H4 sea clock, for which he won the famous Longitudinal Prize in 1773.

Nearly all contemporary electronic devices exhibit some form of time-awareness. The most common of which relies on a digital clock circuit. Its precise time resolution comes at a price of a complex design and a heavy energy load that prohibit miniaturization, impractical to be implemented as the timing module for colloidal electronic systems that perform tasks in traditionally inaccessible locations. We seek therefore an energetically efficient alternative to the tick-tock that is a classic digital timer, with the understanding that one might trade its infinitesimal temporal resolution for a practical design for microscopic autonomous applications.

On a fundamental level, all methods that keep track of the passage of time and manage the storage thereof involve a transformation of time-varying signals into ones that vary in

space, whether it is in the case of the growth ring of a tree or inside Edison's early magnetic tape recorder. Modern examples of a time recorder on autonomous devices include, on the biological side, a "bacterial nanorecorder" in which genetically engineered *E. coli* records single exposure to chemical stimulus by arresting cell division and activating cell elongation, or a synthetic "time capsule" that takes advantage of specific chemical diffusion and reactions for transforming, and thereby recording, temporal dynamics into spatially varying patterns.

In order to interface these natural "clocking" processes, such as diffusion, with our contemporary electronic infrastructure, it is necessary to couple these structural transformations to non-volatile switchings of electronic states. One way to achieve this is to use a memristor. Discovered just over a decade ago, the two-terminal memristor has been hailed as the fourth fundamental circuit element, alongside the resistor, inductor, and capacitor. A memristor, by definition, is a resistor that possesses memory of its electrical history. Operationally, it has been identified that the resistive switching between low- and high-resistance states within a memristive material stems from migrating charged species, atomic or molecular, driven by an applied electric potential. It is therefore possible to tune the material parameters that govern this electromigration process and obtain the desired time-dependent resistive switching behaviour.

Herein we introduce a timing circuit comprised of tunable chemiresistive and memristive elements. We formulate its functioning mechanism and present a strategy for resistive tuning to accomplish discretely-resolved temporal recording in the spatial domain, compatible with digital read-out schemes.

A portmanteau of ‘memory-resistor’, the memristor represents one of the four fundamental passive two-terminal electrical component, together with resistor, capacitor and inductor. Unlike its time-independent relative – a resistor, the memristor's electrical resistance is highly non-linear, and is function of the current history that had flowed through the device. In other words, its present resistance depends on how much electric charge has flowed through it in times past. As such, the hallmark of a memristor is that the device “remembers” its history – when the electric power supply is turned off, the memristor retains its most recent resistance until it is turned on again. In fact, as we will show, this dynamical behavior of electrical resistance can be leveraged as a means for time keeping.

One phenomenological model that gives rise to the dynamic resistance hysteresis partitions a memristor into two interconvertible material phases, separated by a dynamic phase boundary in between:

$$\frac{d}{dt} w(t) = \frac{\mu_{ion} R_{low}}{L^2} I(t) \quad (42)$$

Here $w(t)$ keeps track of the location of the phase boundary as a function of time, and it can assume any number within the device length L . It divides the two material regions that make up the memristor with resistances R_{high} and R_{low} , respectively. The application of an external bias $V(t)$ across the device with current $I(t)$ will move this boundary between the two material phases by converting one to another, a process analogous to the electromigrative drift of charged species with average ion mobility μ_{ion} . The dynamic electrical switching of the combined memristance $M(t)$, then, naturally falls out as a weighted average between that of the combined phases:

$$V(t) = M(t)I(t) = \left\{ R_{low} \frac{w(t)}{L} + R_{high} \left[1 - \frac{w(t)}{L} \right] \right\} I(t) \quad (43)$$

This constitutive descriptor of the memristance dynamics originates from a microscopic picture of charged dopant drifting within a semi-conductive lattice, and has proven effective in explaining the resistance hysteresis observed in a number of different material systems. These applications notwithstanding, there seems to be an even broader class of natural phenomena whose characteristics resemble that of a memristor. The celebrated Hodgkin-Huxley circuit model of the nerve axon membrane, in particular, has been generalized, and each ion channel is mathematically equivalent to a first-order time-invariant voltage-controlled memristor.

In the Hodgkin-Huxley model, voltage-gated ion channels are governed by a voltage sensitive state variable $n \in (0,1)$ that characterizes the extent of channel opening, much like the memristive phase boundary $w \in (0,L)$ defined above. The only caveat is that w depends on the amount of charges, or the time integral (“history”) of current, that has gone through the memristor; whereas n responds to the instantaneous membrane potential V by approaching its asymptotic limit $n_{\infty}(V)$ – a monotonic function of V – with characteristic time τ :

$$\frac{d}{dt}n(t) = -\frac{1}{\tau} [n(t) - n_{\infty}(V)] \quad (44)$$

The different functional forms between the above governing equations bring about several key features that differentiate the dynamic voltage response of a memristor from that of a Hodgkin-Huxley ion channel. For a sinusoidal potential bias applied across, both state

variables (n for the ion channel and w for the memristor) display a pronounced voltage hysteresis (**Figure 6-5a, b**). As we accelerate the dynamics, however, the ion channel's hysteresis loop dwindles while the memristor's remain unaffected (**Figure 6-5a, b**). Mathematically, if we reduce the time constant for the ion channel dynamics, it will simply relax to its asymptotic value $n_{\infty}(V)$ faster – a process analogous to increasing the restoring force of an elastic spring (in other words, the spring constant. At the limit of infinitely fast dynamics (or equivalently at long times), the spring would become so stiff that we lose its hysteresis behavior entirely, and hence the ion channel's ability to record temporal information. A Memristor, on the other hand, does not have a time-independent asymptotic term in the expression, and will only switch its state in response to the accumulated current history, leading to its rate-independent, non-volatile hysteresis behavior (**Figure 6-5**). The volatile nature of an ion channel's memory is further manifested in its non-zero switching rate $\left(\frac{dn}{dt}\right)$ as V approaches zero (**Figure 6-5a**), in contrast to that of the memristor (**Figure 6-5b**).

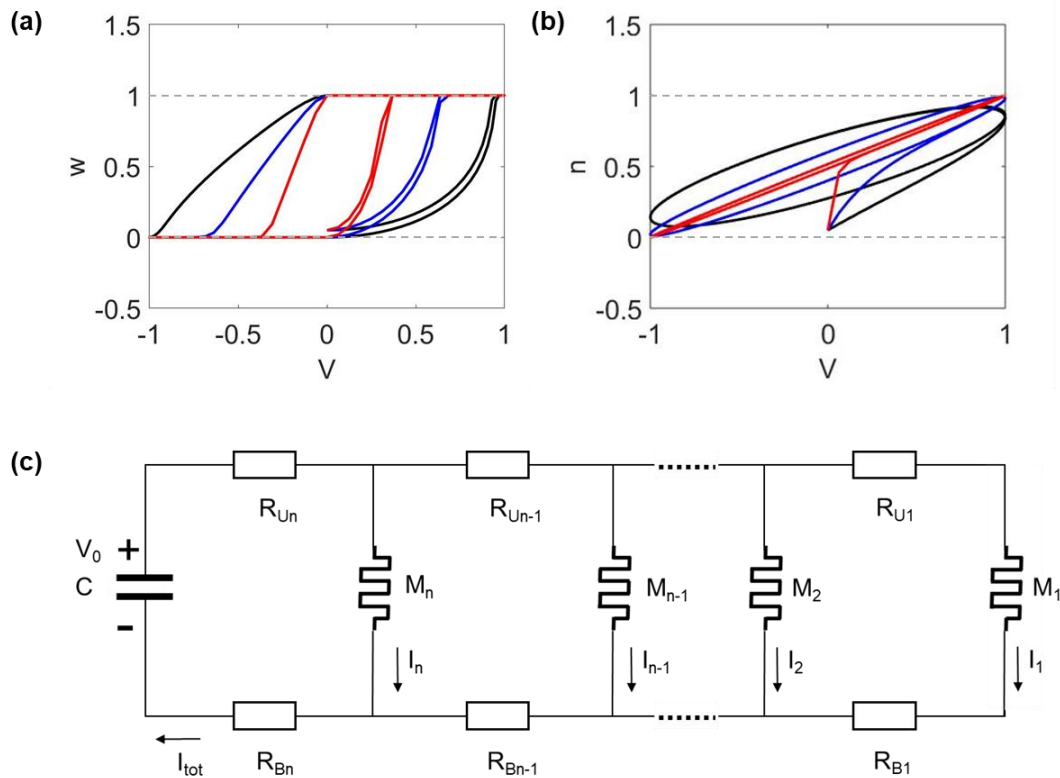


Figure 6-5. State variables for a single memristor channel (a) and a Hodgkin-Huxley’s ion channel (b) plotted as a function of the same oscillatory driving voltage. The voltage applied is a sinusoidal function of time from -1V to 1V. The blue traces are simulated at 3x the dynamic rate for the black, and the red at 20x. (c) The single-lane parallel memristive timing circuit design.

In the Hodgkin-Huxley model, the parameterized dynamic opening and closing of the ion channels can be further coupled into a classical parallel resistor-capacitor transmission cable. The interplay between the state variable n and the corresponding membrane potential then gives rise to the well-characterized neuronal voltage pulses following an exponential rise-and-decay function that transmit down an axon longitudinal axis. The conversion from the temporal state switchings of ion channels to the spatial translation of

the voltage signal via the incorporation of a linear transmission cable model gives inspiration to the memristor array shown in **Figure 6-5c**.

Here the driving voltage V_0 (and current I_{tot}) of this active system is supplied by a large capacitor C pre-charged to a voltage V_{ini} (note one can just as easily replace this voltage source into an on-board battery with a pre-defined voltage input). Along the linear transmission line, instead of placing resistors and capacitors in parallel as one would to account for leakage current, we insert N ideal memristors with memristance M_i ($i = 1, 2, \dots, N$) characterized by Eq. (1) and (2). Along the top and bottom surfaces, the N upper (R_{U_i}) and bottom (R_{B_i}) resistors in series with each corresponding memristors M_i measure the cable's longitudinal resistance to the movement of electric charge. Conceptually, this cross-memristive structure produces a time-variant electric signal traveling down the transmission cable – an effect we exploit to convert temporal evolution into spatial records. By replacing Hodgkin-Huxley's ion channels – which switches on and off based on instantaneous membrane potentials – into ideal memristors that only change conductance states in response to their current history, we obtain at various time points a longitudinally translating vertical conductivity wave – not as membrane potential (or ionic conductance) spikes as appeared in the Hodgkin-Huxley model – but rather, as memristance steps with shifting “wave fronts” (**Figure 6-6**). This time-dependent sequential turn-ON of the memristance staircase, therefore, constitutes the basis for the circuit's “time-awareness”. In other words, by measuring a memristance vector $\vec{M} = (M_N, M_{N-1}, \dots, M_1)$ comprised of N spatially discrete memristors at any given point

in time $t_f > t_0$, where t_0 marks the circuit's time of activation, we can compute the upper and lower bounds on t_f in a deterministic fashion.

One way to describe the system is by modeling the cross-plane (transverse) memristivity ($M(x, t)$) and in-plane (longitudinal) resistance ($R_l(x)$) as continuous variables. In other words, we can treat each memristor node in **Figure 6-5c** as an infinitesimal unit within an otherwise homogenous sheet of memristive material. In the limit of $N \rightarrow \infty$, the spatial gradient of transmitted electrical potential $V(x, t)$ down the longitudinal (\vec{x}) direction is:

$$\frac{\partial}{\partial x} V(x, t) = -R_l(x) \cdot I_l(x, t) \quad (45)$$

where $R_l(x) = R_U(x) + R_B(x)$ measures the total longitudinal resistance per unit length (in $\Omega \cdot \text{m}^{-1}$), and I_l represents the longitudinal current flowing down the potential gradient.

To account for the current that goes through the memristor elements in the transverse direction, a relation between the longitudinal and transverse currents can be established:

$$\frac{\partial}{\partial x} I_l(x, t) = -I_t(x, t) = \frac{V(x, t)}{M(x, t)} = \frac{V(x, t)}{w(x, t) \cdot R_{low} + [1 - w(x, t)] \cdot R_{high}} \quad (46)$$

Here the transverse current per unit length $I_t(x, t)$ has unit ($\text{A} \cdot \text{m}^{-1}$), and the cross-plane memristivity $M(x, t)$ (with unit $\Omega \cdot \text{m}$) is a function of both space and time, as governed by the state variable $w(x, t)$. Like a single memristor, the dynamics of the memristive state is determined by the transverse current that has passed across the distance L :

$$\frac{\partial}{\partial t} w(x, t) = \mu_{ion} \cdot \frac{R_{low}}{L^2} I_t(x, t) \quad (47)$$

Together, these equations give rise to a set of highly coupled, non-linear partial differential equations (PDEs) between $V(x, t)$ and $w(x, t)$ that fully describes the temporal and spatial evolution of the entire memristor array shown in **Figure 6-5c**:

$$\frac{\partial^2}{\partial x^2} V(x, t) = R_l(x) \cdot \frac{V(x, t)}{w(x, t) \cdot R_{low} + [1 - w(x, t)] \cdot R_{high}} \quad (48)$$

$$\frac{\partial}{\partial t} w(x, t) = \mu_{ion} \cdot \frac{R_{low}}{L^2} \frac{V(x, t)}{w(x, t) \cdot R_{low} + [1 - w(x, t)] \cdot R_{high}} \quad (49)$$

This set of PDEs can be non-dimensionalized and solved numerically for a wide parameter space, most notably the driving voltage $V_0(t)$ and the longitudinal resistance $R_l(x)$ that controls array propagation dynamics, μ_{ion} that governs electromigration kinetics of each

memristor node, as well as $\alpha \equiv \frac{R_{low}}{R_{high}}$ defined as the maximum ON/OFF ratio attainable

across various memristor nodes. As an example, we plot here several time-elapsd snapshots of transverse memristivities $M(x)$ as a function of the longitudinal distance x

for a constant voltage input $V_0(t) = V_0$ and a constant longitudinal resistance $R_l(x) = R_l$

(Figure 6-6). The time-dependent advancing of the turned-ON memristive “wave front” effectively translates a temporal evolution into a march in the spatial domain **(Figure 6-6)**.

It can be also seen that in this spatially-invariant longitudinal resistance layout, the memristive writing process slows down as time progresses – presumably due to the build-up of the overall resistance in the memristive array. This erosion in transverse memristor

switching rate can be mitigated through spatial tuning of the longitudinal resistance as a function of x , resulting in uniformly-spaced temporal intervals. We address the spatial resistive tuning using the discretized model of this memristive array in the next section.

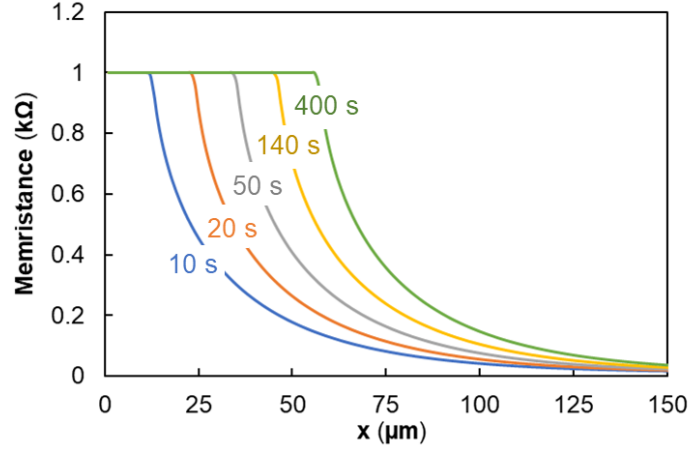


Figure 6-6. Memristance of the 1-dimensional memristor array as a function of distance plotted at various excursion times. Simulation performed using the continuous PDE model presented above.

To simulate the time-dependent sequential switchings of each channel of memristor array requires an analytical model of the depicted circuit arrangement. If we define the lumped resistance of the circuit to the right of the i^{th} memristor (itself included) as R_{L_i} , the ensemble resistance of the memristive channel can be expressed in the following recursive way:

$$\frac{1}{R_{L_2}} = \frac{1}{M_2} + \frac{1}{R_{U_1} + M_1 + R_{B_1}} \quad (50)$$

$$\frac{1}{R_{L_3}} = \frac{1}{M_3} + \frac{1}{R_{U_2} + R_{L_2} + R_{B_2}} \quad (51)$$

$$\frac{1}{R_{L_N}} = \frac{1}{M_N} + \frac{1}{R_{U_{N-1}} + R_{L_{N-1}} + R_{B_{N-1}}} \quad (52)$$

The combined current across the entire channel $I_{tot} = \sum_{i=1}^N I_N$ with total resistance R_{tot} , driven by the discharging potential V_0 from the capacitor, is therefore

$$I_{tot} = \frac{V_0}{R_{tot}} = \frac{V_0}{R_{UN} + R_{LN} + R_{BN}} \quad (53)$$

with the current passing through the N^{th} memristor element as

$$I_N = I_{tot} \cdot \frac{R_{LN} - M_N}{R_{LN}} \quad (54)$$

and each constituent $I_{j \in [1, N-1]}$ that follows obeying Kirchhoff's law

$$I_j = \left(I_{tot} - \sum_{i=N}^j I_i \right) \cdot \frac{R_{Lj} - M_j}{R_{Lj}} \quad (55)$$

The resulted vector $\vec{\mathbf{I}} = (I_N, I_{N-1}, \dots, I_2, I_1)$, combined with the single element memristor dopant electromigration kinetics outlined in Eq. (1) and (2), therefore closes the loop of differential equations that fully describes the temporal evolution of this memristor array:

$$\frac{d}{dt} \vec{\mathbf{w}}(t) = \frac{\mu_{ion} R_{low}}{L} \vec{\mathbf{I}}(t), \text{ with } \vec{\mathbf{M}}(t) = \vec{\mathbf{w}}(t) \cdot R_{low} + (1 - \vec{\mathbf{w}}(t)) \cdot R_{high} \quad (56)$$

$$\frac{d}{dt} V_0(t) = -\frac{I_{tot}(t)}{C}, \text{ where } V_0(t=0) = V_{ini} \quad (57)$$

As previously formulated, $\vec{\mathbf{w}}(t) = (w_N, w_{N-1}, \dots, w_2, w_1)$ here represents the vectorized individual memristor boundaries that separate the two memristive phases of high and low resistances.

The desired sequential state switching can be achieved by first turning all memristors into its low resistance (or “ON”) state at time $t = 0$, and let the capacitor C discharge through the memristor array. The resulted current-driven electromigration will sequentially switch “OFF” the memristors (into the corresponding high resistance state) – starting from the one closest to the capacitor, due to the shorter and lower resistance path. But after the first memristor has been shut off, the current is then funneled towards the second closest, switching the array from ON to OFF one memristor at a time, with the switching dynamics controlled primarily by the memristor dopant electromigration kinetics. Of course, the above idealized events all occur in parallel: what fractions of electrons flow through which memristor element is completely dictated by Kirchhoff’s law, as well as the dynamically evolving memristance ratios. By tuning the surfaces resistances (i.e., R_{vi} ’s) into appropriate values, we show that it is possible to switch off individual memristors down below an arbitrarily prescribed conductive threshold in a step-wise fashion, at uniformly-spaced time intervals (**Figure 6-7**).

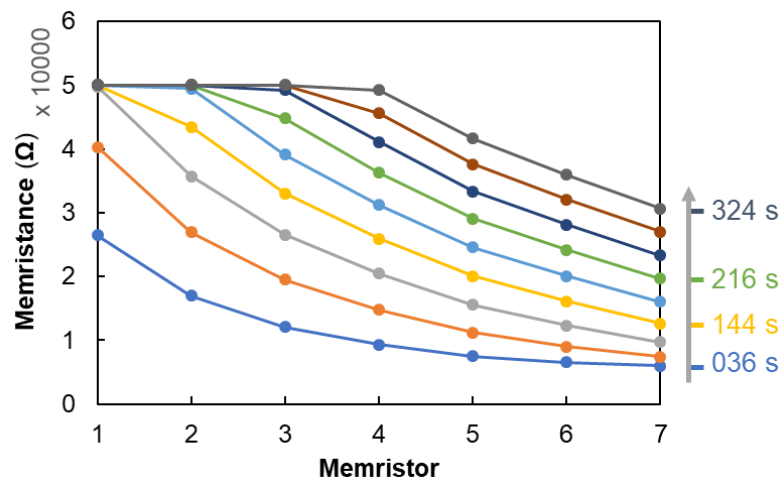


Figure 6-7. Memristance of the 1-dimensional memristor array as a function of distance plotted at various excursion times. Simulation performed using the discrete model presented above. Resistive tuning was performed such that individual memristors are switched off sequentially at uniformly-spaced time intervals.

These results substantiate the feasibility of using the memristive array as an analog timer that records the global excursion time as a vector of binary resistance states. One can design the number of memristors (N) to be fabricated in the array, as well as the dynamic range of the memristor elements, tuning the time interval between the switch of two memristors (τ) within the timescale of interest ($T \leq N\tau$), for a variety of different applications (e.g., seconds in the case of microfluidic chips, minutes in the case of human digestive tract, or hours in the case of an oil pipeline). Once the switching dynamics is prescribed (e.g., 6 seconds for all 6 memristors to be switched OFF), we can estimate the excursion time (t_f , time of resistance measurement) for the host bearing said memristive array for $t_f \in (0, T)$ with $\pm \frac{\tau}{2}$ accuracy. For instance, if we use 0 and 1 to denote the OFF and ON state of any given memristor, respectively, then a memristor array measurement of $\vec{\mathbf{M}}_f^1 = (0, 0, 0, 1, 1, 1)$ gives $t_f^1 = 3 \pm 0.5$ s, and $\vec{\mathbf{M}}_f^2 = (0, 0, 0, 0, 1, 1)$ gives $t_f^2 = 4 \pm 0.5$ s.

With this basic circuit structure, one can extend its capability to recording the time of a chemical event. We can simply swap the bottom resistors (R_{Bi} 's) of the memristor array into chemiresistors tuned to the chemical of interest, such that its adsorption onto the of R_{Bi} 's would increase its resistance by orders of magnitude. This jump in circuit resistance effectively cuts off all conductive paths coming from the capacitor charge source, thereby

freezing memristor states at the moment of local chemical detection. This subsequently motivates a wedged geometric design for a multi-channel, multi-event chemical sensor-timer vertical memristor array, powered by one central capacitor unit. In fact, with m of these “pizza slices”, each patterned with a different chemiresistive backing layer, one can in principle record the onset of $(m-1)$ independent events, together with the global excursion time.

5.2 Autoperforation of Two-Dimensional Materials to Generate Colloidal State Machines Capable of Locomotion

An important theme of the modern robotics and electronics has been miniaturization^{36,37}, towards an artificial version of cell or microbe. Such systems could extend the benefits of electronics, sensing, memory and communications to currently inaccessible applications, such as surveying geological structures, infrastructure monitoring along pipelines, sensing within chemical or nuclear reactors, as well as probing and cargo delivery within the human body for biomedical purposes. This longstanding challenge has inspired both scientist and artist alike. The 1966 science fiction film *Fantastic Voyage* captures the spirit of this endeavor, portraying a lasting image in which a miniaturized submarine “about the size of a microbe” helps to remove a blood clot from a human brain (**Figure 6-8a**).

As a step towards furthering this goal, we have developed a suite of techniques and analysis around what we call *Colloidal State Machines* (CSMs) to differentiate these micrometer-scale entities from what are currently called “microrobots”. The latter term typically refers to centimeter or millimeter-scale ‘minaturized’ robots³⁸, but micrometer-sized, non-sedimenting colloids require different properties. There has been sustained research

interest in responsive micro- and nano-objects such as micro-swimmers and actuators^{39,40} that clearly benefit, can integrate into, and further the goal of the CSM. The ultimate vision is to generate CSMs as (electronically) integrated entities with onboard memory, sensing, energy harvesting, actuation, and communication, able to carry out tasks remotely and autonomously.

It is not immediately obvious that the miniaturization of robotics into the colloidal regime requires completely new fabrication methods, actuation mechanisms, energy sources and device architectures. Roboticists have been successful in reducing the size and weight of macroscopic robots. The record for miniature aerial robots was recently pushed down to 3.5 cm and 259 mg³⁸. Such systems can still obey similar fundamental design principles as their larger counterparts such as the meter-long robotic cheetah⁴¹. Alternatively, CSMs as autonomous machines require components more than a billion times smaller, with the entire device volume under a picoliter and still integrated with the functionalities mentioned above. Therefore, the effort is not the equivalent of making a smaller-sized version of macroscopic counterparts. Physical laws and mechanisms differ at these reduced lengths scales. For example, in the micrometer world, surface forces start to dominate over those that are inertial or volumetric⁴². CSMs have to be designed to consider local hydrodynamics, and can perhaps leverage them by suspension for prolonged periods without sedimentation. Similarly, a macroscopic robotic arm can be driven by electric motors and hydraulics. These actuation mechanism do not efficiently scale to the micron-scale environment. Indeed, microscopic actuators that have been successfully demonstrated are based on different mechanisms such as variance in thermal expansion coefficients⁴³ autonomous origami machines,⁴⁴. At the micron scale, it is well known that mechanical

propellers need to be substituted with time-asymmetric mechanisms like bubbling and phoretic motion by virtue of the Scallop theorem⁴⁵. We can deduce from these examples that the success of a microscale CSM design, therefore, relies much more on intrinsic materials science: thermal, mechanical, and electronic properties, responsiveness to stimuli, compatibility of hetero-integration, as well as electrical energy utilization efficiency, chemical stability and mechanical robustness. In this regard, 2D materials show particular advantages for these tasks.

The expanding family of novel two-dimensional materials (2DMs) has provided an ever-growing arsenal of modules suitable for colloidal robotics. Armed with distinct, and often superior mechanical, chemical, or electrical properties in contrast to their respective bulk counterparts³¹, the wide array of 2DMs have been used to build advanced (bio)sensors, actuators, (opto)electronic devices, logic circuits, memory elements, and power sources⁴⁶⁻⁵⁰. For example, Miskin *et al.*'s graphene-silica bimorph actuators respond to pH variations in fractions of a second, paving the way towards “complex cell-sized machines”⁵¹ towards cell-sized machines. Bessonov and colleagues, on the other hand, developed MoS₂-based memory elements programmable by less than 0.2 V, suitable for the extremely energy-hungry microscale world⁵².

In our own recent work, we have introduced and demonstrated several new CSM prototypes. In Koman *et al.* (2018) we demonstrate the first autonomous CSM: an 2D-electronics-grafted microparticle that can be aerosolized as airborne sensors^{53,54} (**Figure 6-8b**). Powered by a MoS₂/WSe₂ photodiode and connected in series with an analyte-sensing MoS₂ chemiresistor, the inbuilt Au-MoS₂-Ag memristor is switched on only when both light and analyte are present, analogous to an AND logic gate (**Figure 6-8c, d**). A

hexagonal boron nitride (hBN) monolayer meanwhile insulates the sensitive memory element from the environment. Of note, fabricating all the electrical components with 2DM allowed the devices to survive aerosolization and bypass power limitations⁵³. The 2DM enabled electronic particles, or *aerosolizable electronics*, integrate energy harvesting, sensing, and memory into one, presenting a proto-example of CSM (**Figure 6-8e, f**). While the work demonstrates CSMs as autonomous chemical sensors, it also points to promising possibilities of biomedical applications as well. For instance, substituting the chemiresistor with Mannoor *et al.*'s bioselective graphene nanosensors could enable the capture and detection of single bacterial pathogens, as the binding of which triggers a similar resistance change⁵⁵.

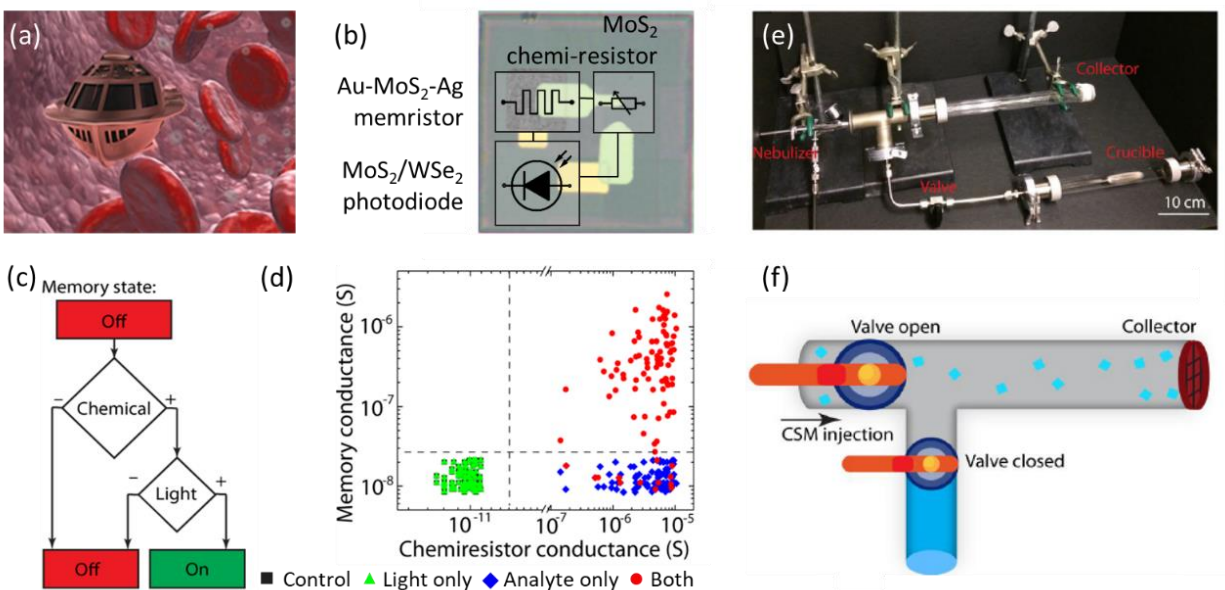


Figure 6-8. Monolithically fabricated Colloidal State Machine enabled by 2DMs. (a) Artistic rendering of a miniaturized submarine in a blood vessel as imagined in 1966's *Fantastic Voyage*. (b) 2DM-enabled aerosolizable sensors with on-board power, memory, and sensing element integrated⁵⁴. Dimension, 100 by 100 μm . (c) Block diagram showing logic of the CSM in (b). The

memristor is switched on if and only if the analyte concentration and the light intensity are both higher than a threshold, as also evidenced by the experimental data in **(d)**. **(e)** Image of the experimental set-up with a crucible filled with chemical analyte. Once the lower valve is open, saturated ammonia vapour (~ 10 kPa) expands into the rest of the system. **(f)** Schematics of the pipe segment system (22 mm inner diameter), which has two separate valves for metering aerosolized CSMs (teal squares) or analyte. To allow for retrieval, a layer of cheesecloth served as a collector at the pipe endpoint.

As an alternative to the top-down approach of Koman *et al.*, we also introduced a bottom-up technique based on “autoperforation”⁵⁶ for producing colloidal microparticles with two independently addressable, external 2D Janus faces via engineered crack propagation **(Figure 6-9a)**. This method, which we employ and build onto in this work, turns crack propagation at the nanometer scale from a nuisance into a useful device fabrication tool in 2DM engineering. The method is distinct from Shim *et al.*, who adopt controlled cracking for high-throughput production of wafer-scale 2DM monolayers⁵⁷. Autoperforation instead uses cracks to scissor or carve out micrometer-sized particles that are templated by a designed strain field **(Figure 6-9b, c)**. We showed that by encapsulating an inkjet-printed array between two layers of 2DM sheets (*e.g.* graphene, MoS₂ and hBN), the engineered strain field guides propagating cracks around the ink pillars, leaving behind individual particles enveloped by 2DMs **(Figure 6-9d)**. Using two monolayer graphene sheets as the top and back electrodes sandwiching memresistive 2DM fillers, we demonstrated unconventional microscopic particles (under 10 picolitre volume) with onboard electrical memory arrays approaching the size of a biological cell **(Figure 6-9e)**. Specifically, the memory states within each particle can be switched by applying a voltage across the

memristive phosphorene, MoS₂, or graphene oxide ink filler, turning each autoperforated CSM into an intraparticle array of parallel, two-terminal electronic memory storage devices (**Figure 6-9f, g**). As a result, chosen regions of a given electronic cell can be selectively switched, recorded, and erased, mapping out the letters “M”, “I”, and “T” in a digital format (**Figure 6-9e**). Furthermore, the unique capability the *autoperforation* technique brings to engineer both the CSM’s surface chemical environment and its interior filler composition opens these two-terminal electronic devices up for additional opportunities. For example, non-covalent functionalization of the particle exterior surface with capture sites to ligate with specific metallic residues and ionic species in water bodies and soil matrices, respectively (**Figure 6-9h**), equips these electronic colloids with chemiresistive (**Figure 6-9i**) and optical (**Figure 6-9j**) sensory units that integrate readily into the existing functional modalities.

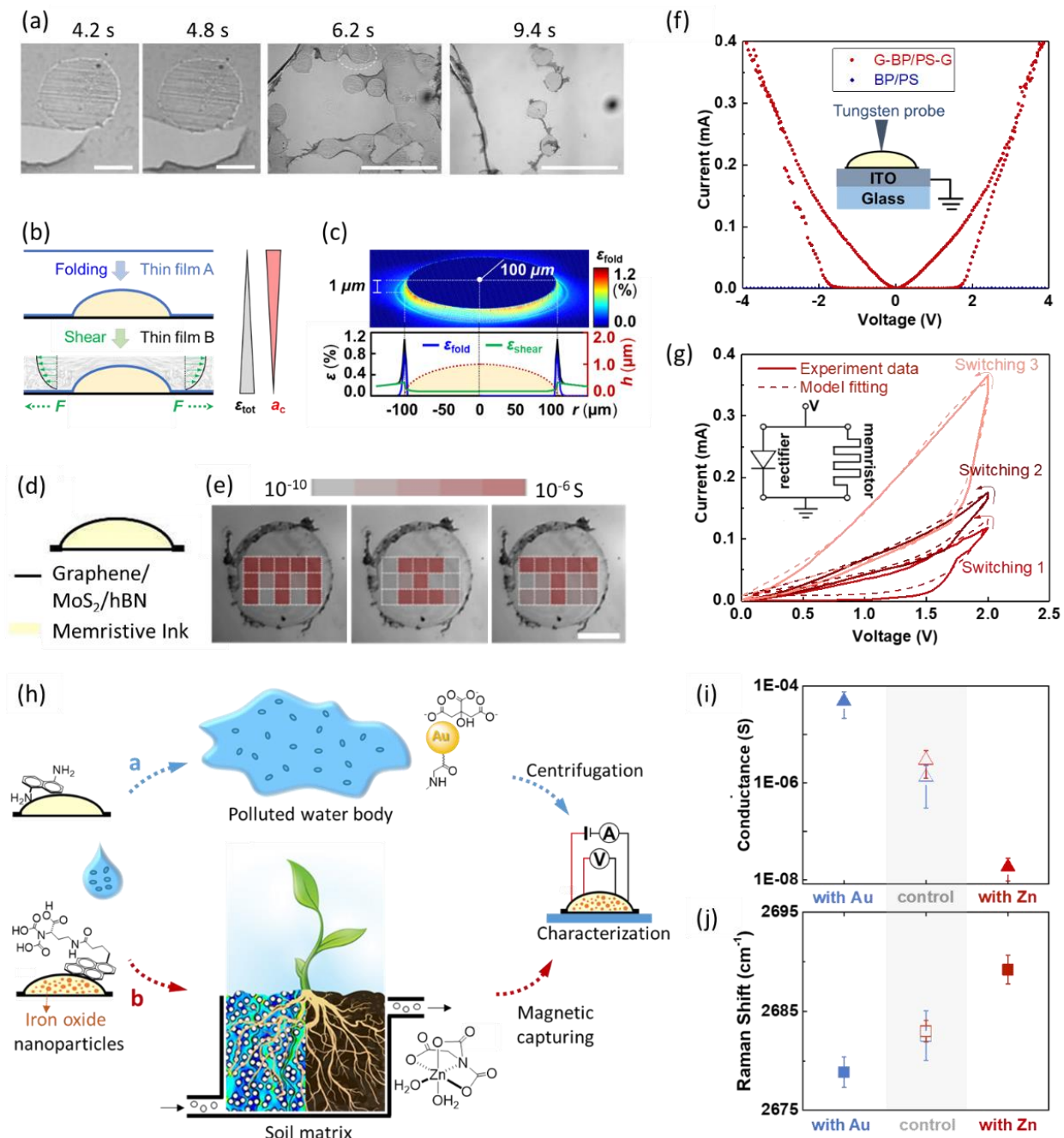


Figure 6-9. Autoperforated Colloidal State Machines enabled by 2DMs. (a) Optical micrographs of the bottom-up autoperforation technique showing the crack propagation in progress⁵⁶. The round shapes correspond to inkjet-printed discs which impose strains. Scale bars represent 100, 100, 1000, and 1000 μm . (b) Schematic illustration of the two-step process

generating the strain field used in **(a)**. The first step involves folding the graphene-containing thin film A on top of the curved polymer disk printed onto film B, which has the same composition as A. The second shearing step is facilitated by flowing an agitated liquid over the film-encapsulated disk, creating a tensile stress within both films synergistic to the folding strain, modelled here as an outward-facing force F pulling uniformly away from the film centre. The total strain (ϵ_{tot}) within the films increases as a result of this two-step process. The Griffith length (a_c), on the other hand, decreases. **(c)** Local strain field after stacking/folding a thin polymer film (200 nm) onto a microdisk (radius:height = 100:1) based on finite-element analysis. **(d)** Schematic of the sandwich CSM carved out by the crack “scissors”, equivalent to an intraparticle vertical memristor array in parallel. The conductivity map in **(e)** shows that each of these memristors can be switched on independently, thus mapping out letters “M”, “I”, and “T”. Scale bar, 100 μm . **(f)** Cross-plane I-V curves of microparticles G-BP (0.9 wt%)/PS-G, G-PS-G, and BP/PS. **(g)** I-V curves of three successive sweeps of $0 \rightarrow 2 \rightarrow 0$ V (switching 1), $0 \rightarrow 4 \rightarrow 0$ V (2), and $0 \rightarrow 6 \rightarrow 0$ V (3) and the fitting curves based on the inset equivalent circuit. **(h)** Schematic illustration of the application of surface-functionalized G-PS/G microparticles or their magnetic counterparts as probes to electronically sense and record chemical species such as metal nanoparticles and ions in **a** water and **b** soil matrix, these microparticles can be collected via centrifugation or magnetic capture for electronic read out. **(i, j)**, Surface in-plane electrical conductance **(i)** and graphene Raman 2D peak position **(j)** of the microparticles retrieved in **(h)**.

It is encouraging to note how the nascent field of CSMs has been steadily expanding⁵⁸ microscopic sensor nodes with 2D materials.^{59,60} Despite this, several technological challenges persist.

One challenge specifically addressed in this work is locomotion. Unlike the features of onboard memory, sensing, and energy harvesting integrated onto colloid-sized machines,

locomotion is an extremely energy intensive function. CSMs published so far travel passively with the surrounding fluids – a feature of the scale of this design. But for many tasks, propulsion will be specifically required. We outline such tasks and potential solutions in the latter parts of this work. As a technological solution to the propulsion problem that builds onto autoperforated CSMs, we leverage advances in the field of micro-propulsion and microswimmers to generate CSMs capable of locomotion. We introduce an inversion molding technique compatible with 2DM autoperforation that allows for the patterning of an external catalytic surface to enable CSM translocation in an accompanying fuel bath. The velocity of the resulting propulsion is evaluated as a function of fuel concentration. We also summarize efforts to define and create a testbed for CSMs designed for complex navigation, such as in the case of the human circulatory system. We introduce conceptual CSM designs capable of solving such complex tasks and further the ultimate goals of this nascent field.

The first goal of this work is to realize self-driven locomotion of autoperforated CSMs in energized environments, such as a surrounding H_2O_2 bath. The approach is to functionalize the CSM with a geometrically defined Platinum (Pt) patch as the catalytic element. In this section, we report the development of a fabrication method compatible with autoperforation⁵⁶ to equip such Pt modules to graphene-CSM surfaces. This clean-room-free method involves a patterned Pt electrodeposition step on chemical vapour deposited (CVD) graphene, followed by an alignment process for the subsequent Pt-graphene-CSM autoperforation.

6.2.1 Patterned Pt Electrodeposition on Graphene Surfaces Defined by Inkjet Printing

The implementation of this Pt-coated autoperforated CSM variant relies on a scalable and reliable method for Pt-deposition in controlled geometric shapes on the graphene “skin” for CSM encapsulation. We developed an inversion-moulding technique that allows us to create size-defined well-shaped patterns via inkjet printing in a high-throughput manner on top of CVD-graphene for Pt electrodeposition, as shown in **Figure 6-10a**. The overall procedure is briefly described as follows. First, an array of carboxymethyl cellulose (CMC) disks were printed onto a monolayer graphene grown via CVD on a Copper (Cu) substrate (**Figure 6-10b**). Second, a thin layer of polymethyl methacrylate (PMMA) was spin-coated atop the CMC array on the graphene/Cu substrate (**Figure 6-10c, d**). The water-soluble CMC was then etched, thus exposing an array of graphene in the form of cylindrical PMMA wells (**Figure 6-10e, f**). Pt was subsequently deposited onto the conductive graphene through electroplating using a platinum (IV) chloride (PtCl₄) solution (**Figure 6-10g**). This entire process is clean-room-free and perfectly compatible with the standard autoperforation method⁵⁶ for CSM production *en masse*. The conditions for printing, spin-coating, and electroplating were optimized to improve the quality of Pt electrodeposition inside these inversion-moulded micro-wells.

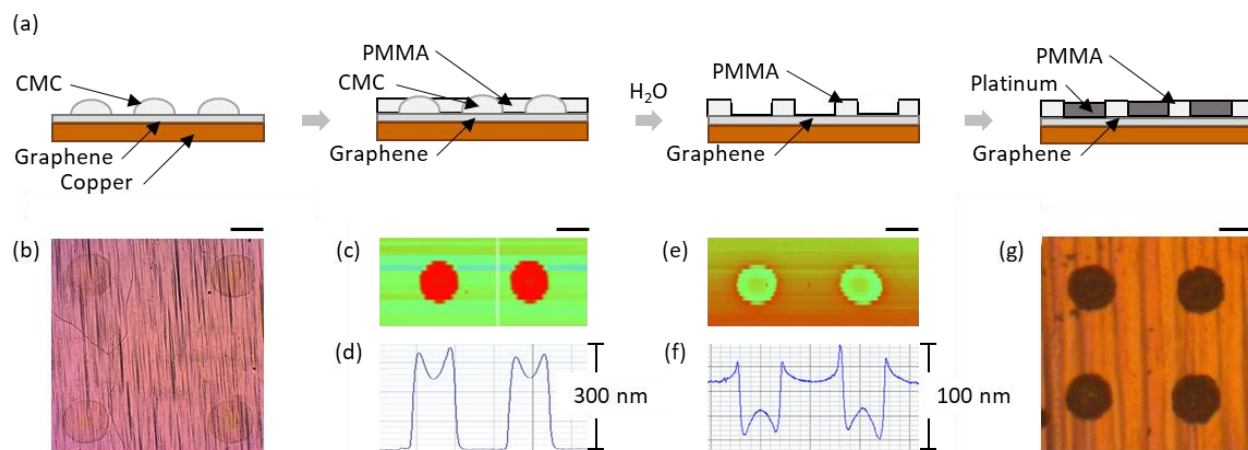


Figure 6-10. (a) Schematic illustration of the inversion-moulding process that patterns Pt arrays on top of monolayer CVD-graphene sheets. (b) Optical micrograph of the inkjet printed CMC/graphene/Cu array. Scale bar, 20 μm . (c) Vertical profile map of the CMC-PMMA/graphene/Cu array. Scale bar, 20 μm . (d) Linear scan of the vertical profile for the CMC-PMMA/graphene/Cu array. (e) Vertical profile map of the PMMA/graphene/Cu well array. Scale bar, 20 μm . (f) Linear scan of the vertical profile for the PMMA/graphene/Cu well array. (g) Optical micrograph of the electroplated Pt/graphene/Cu array. Scale bar, 20 μm .

To better improve the consistency and uniformity of the electrodeposition, extensive parametric studies were conducted. The well depth and electroplating conditions were optimized in order to produce a solid, uniform array of Pt patches. The parameters of interest are the height of printed CMC (controlled by how many layers of CMC printed), height of PMMA (tuned by the PMMA concentration and spin-rate), duration of electroplating, and concentration of the electrolyte solution.

Three sets of samples were prepared using these conditions and were electroplated in 3 mM, 30 mM and 16.5 mM PtCl_4 for 50 min. The 16.5 mM solution was chosen

as the benchmarking condition for the remainder of the study. Five copper-graphene samples were prepared with five arrays on each chip, respectively with 6 layers, 5 layers, 4 layers, 3 layers, and 2 layers of CMC. Each set of copper-graphene chip was then spin-coated for 1 min under one of the five conditions: 2% PMMA at 1000 rpm, 2% PMMA at 2500 rpm, 2% PMMA at 4000 rpm, 4% PMMA at 4000 rpm, and 7% PMMA at 4000 rpm. The sample was then etched in water as described before. Profilometer measurements were taken of each sample. They were subsequently electroplated with a Pt counter electrode for varying times. An optical microscope was used to image each array after every time interval. Five Pt patches were selected from each image and cropped. The integrated intensity was then obtained for each cropped image. The average inverted integrated intensity, or intuitively the “darkness”, was used as a quantitative metric for the electroplating quality.

Figure 6-11 shows the quantified Pt electrodeposition quality for the various conditions tested. Both the spin-rate and concentration of PMMA affect the thickness of the PMMA coating. Figure 3a suggested that when spin-rate is held constant at 4000 rpm, 2% and 4% yield similar results, both of which are significantly darker than that of 7%. We hypothesize that the 7% PMMA coating was too thick that it prevents contact between water and CMC, thus hindering sufficient etching of the CMC. Figure 3b suggested that when concentration is held constant at 2%, 4000 rpm resulted in the densest Pt patches. Higher spin-rates should correspond to a thinner layer of PMMA which would presumably create a shallower well with less volume for deposition.

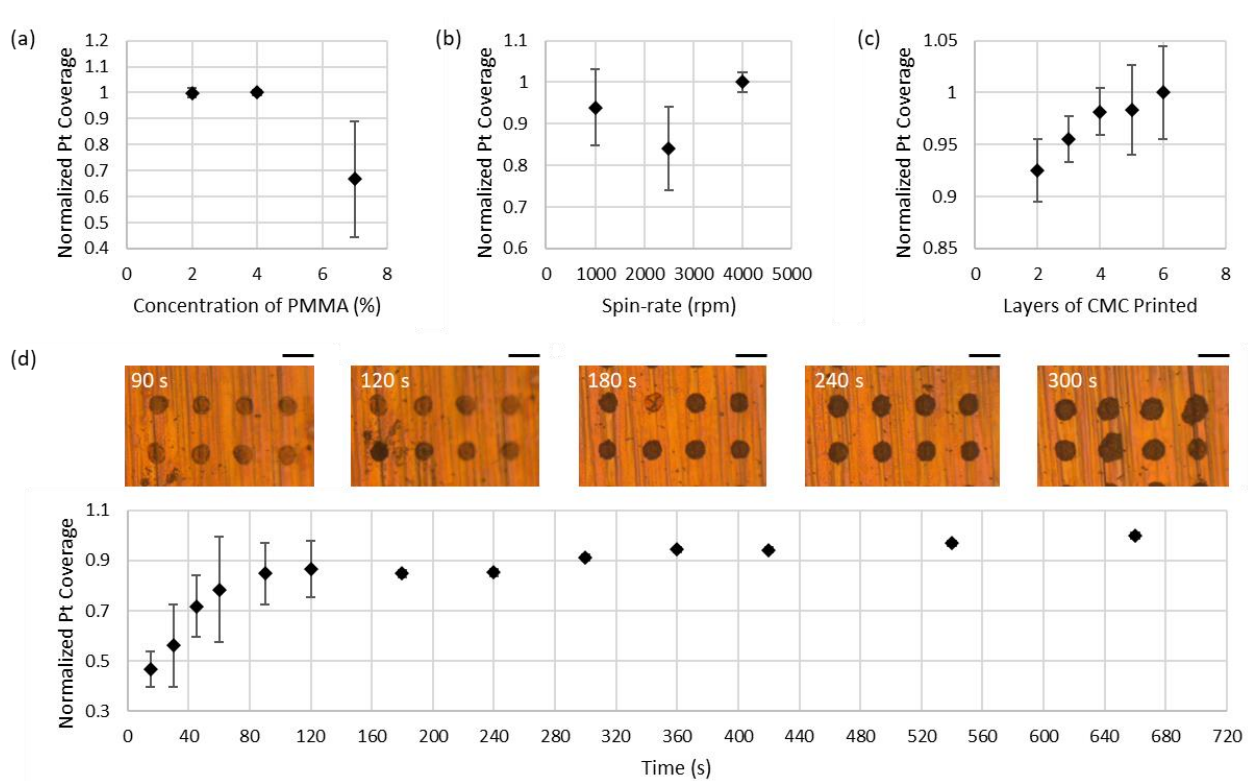


Figure 6-10. Normalized integrated intensity for Pt electroplating for inversion-moulded well samples prepared at various (a) concentrations of PMMA, (b) PMMA spin-coating rates, (c) layers of CMC printed to define the depth of the PMMA well array, and (d) durations of electrodeposition. Inset, time-elased optical micrographs of Pt electrodeposition at various times. Scale bars, 40 μm. Error bars, standard deviations calculated from multiple samples, $n = 15$.

Figure 6-10c showed that the coverage of Pt increases with layers of sacrificial CMC. Increasing the layers of CMC should increase the depth of the well, thus creating more volume for Pt deposition. However, with more layers of CMC, the cross-sectional area of the Pt patch increased, a phenomenon we describe as “spilling-over.” Finding the optimal number of layers requires balancing these two opposing factors. Figure 3d displays a time series of Pt coverage on graphene. The darkness of Pt increases nonlinearly over time and plateaus after around 540 s.

From visual inspection, the Pt appeared to first deposit in a ring around the edge of the well base, deposit within the well until the patch was fully covered, before “spilling-over” occurred.

More insights on factors impacting the inversion-mould patterning were revealed from profilometer measurements of the PMMA wells after CMC etching (**Figure 6-11**). The linear profiles revealed that a bump had formed within each well, creating a barrier and decreasing the volume available for Pt deposition. It seems unlikely that the bump was due to CMC that remained after the etching process given the high solubility of CMC in water and the long duration of etching. We hypothesize that the bump was instead caused by shifting PMMA that migrated into the space evacuated by the CMC. The average well depth and bump height for each condition are shown in **Figure 6-11b–e**. Figure 4b and d revealed that both the well depth and bump height increase as with the concentration of PMMA spun. **Figure 6-11d** shows that the bump height for most layers was higher for 7% PMMA, consistent with the lower Pt coverage for 7% as shown in **Figure 6-10a**. **Figure 6-11c, e** suggested that 1000 rpm has the largest well depth and bump height; however the trend was not monotonically decreasing with spin-rate. The unexpected result for 2500 rpm was observed in both the profilometer measurements and the Pt integrated intensity. This may be the result of an anomaly in the fabrication of the 2500 rpm sample. **Figure 6-11b–e** all suggested that well depth and bump height increase with more layers of CMC. Following the spilling-over observation, the width at the top of each well was extracted from each profilometer measurement. As anticipated, the well width increased with layers of

CMC which is partially due to the nature of vertically stacking layers of an ink and partially due to misalignments across layers. Because of the higher incidence of misalignments with 4-6 layers of CMC, it was determined that 3 layers of CMC was optimal for maximizing Pt deposition and minimizing spilling over.

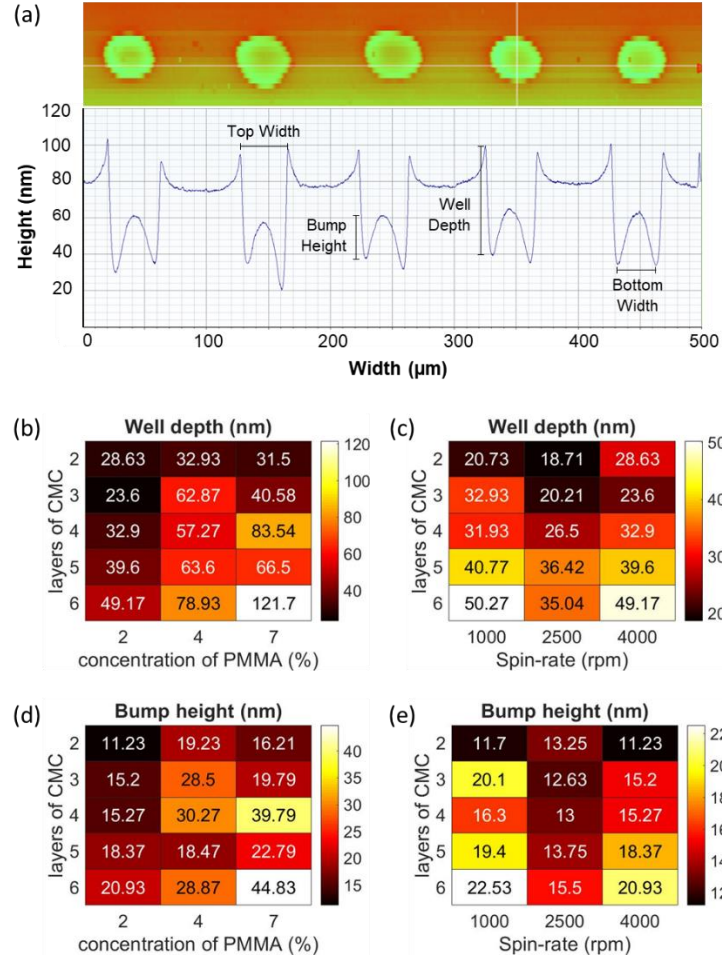


Figure 6-11. (a) Example of profilometer dimensions of interest from a linear scan. The dimensions of interest include the width at the top and bottom of the well, the well depth, and the height of the bump formed at the base of each well. Inset, example of 2D height profile of PMMA wells. (b-e) Summary data for profilometer measurements of the PMMA wells. The heat maps show well depth as a function of (b) layers of CMC and concentration of PMMA, (c) layers of

CMC and spin-rate, as well as bump height as a function of (**d**) layers of CMC and concentration of PMMA, (**d**) layers of CMC and spin-rate.

6.2.2 Pt-Coated Janus Graphene CSMs via Aligned Inkjet Printing and Autoperforation

With the Pt electrodeposition on graphene process optimized, we then developed an alignment method that eventually allowed us to graft this Pt array/graphene stack onto microparticles using a variant of the previous autoperforation method⁵⁶ for large-scale production of Pt/graphene-CSMs. In this process (**Figure 6-12**), a second array of polystyrene/ethylene glycol ink (PS/EG) was aligned, printed onto the Pt array, and capped with a second layer of graphene before lifting-off of the entire stack. Specifically, PMMA was first spun onto the sample, which was then etched for Cu removal (**Figure 6-12c**). The PS/EG ink was then printed onto the PMMA-Pt-graphene vertical stack by a commercial inkjet printer, aligned with the prefabricated array of Pt patches (**Figure 6-12d**). A second layer of PMMA-supported graphene is subsequently transferred atop the sample via the same wet transfer process, resulting in a PMMA-graphene-PS/EG-graphene-Pt-PMMA vertical stack (**Figure 6-12e**). Finally, the entire array of Pt-coated autoperforated cells could be lifted-off simultaneously, allowing for mass production of CSMs (**Figure 6-12f**). It turned out that the Pt-decorated graphene described in the previous section is perfectly compatible with the autoperforation technology. Of note, we anticipate the process to be facilely adaptable for 2DMs beyond graphene as well, as shown in prior literature for MoS₂ and hBN⁵⁶. As patterning of the

PMMA mask works for all 2D substrates, chemical or evaporative deposition methods may substitute electroplating for less conductive materials.

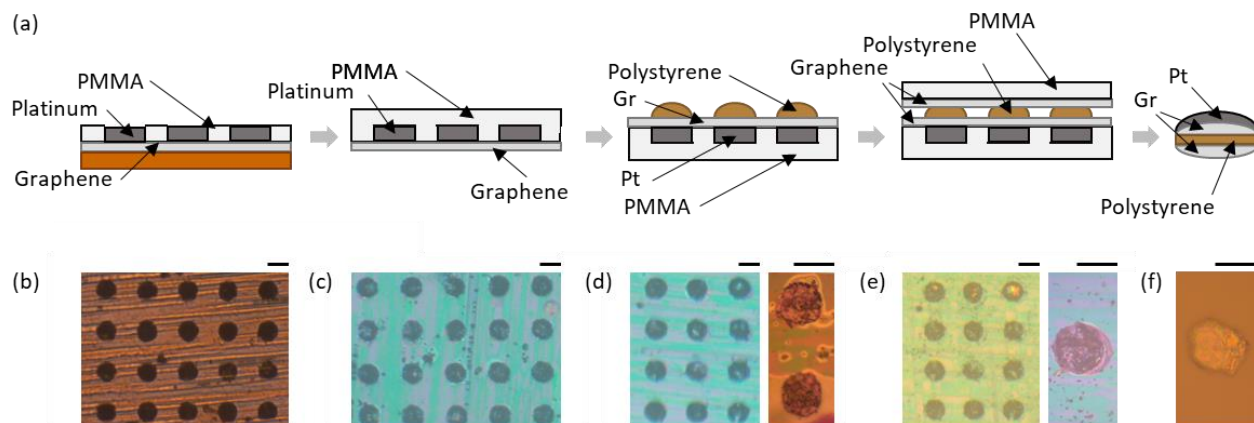


Figure 6-12. (a) Schematic illustration of the alignment, inkjet printing, and autoperforation process that produces Pt-coated graphene-CSMs in solution. (b) Optical micrograph of the electroplated Pt/graphene/Cu array. Scale bar, 20 μm . (c) Optical micrograph of the spin-coated PMMA/Pt/graphene array with Cu etched away. Scale bar, 20 μm . (d) Optical micrographs of the inkjet printed polystyrene aligned over the PMMA/Pt/graphene array. Scale bars, 20 μm . (e) Optical micrographs of the PMMA/graphene encapsulated polystyrene-PMMA/Pt/graphene array. Scale bars, 20 μm . (f) Optical micrographs of the autoperforated Pt-coated graphene-CSM (Pt/graphene/polystyrene/graphene) dried on a glass slide. Scale bar, 20 μm .

6.2.3 Self-Driven Locomotion of Pt-Coated Janus Graphene-CSMs in H_2O_2

These Pt-coated graphene-CSMs (**Figure 6-12f**) translocate inside a H_2O_2 bath via the generation of O_2 bubbles (**Figure 6-13a**). We observed a strong H_2O_2 concentration dependence for the locomotion speed of the Pt/graphene-CSMs. In one set of experiments, we recorded the particle trajectory of two or more particles and plotted their average distances with respect to their centre of mass as a function

of time in an aqueous solution (**Figure 6-13b**, black) and ethanol/water mixture (**Figure 6-13b**, red), and calculated their average speed of translocation, respectively. In both cases, increased H_2O_2 concentration increases their speed of translocation (**Figure 6-13b**). Notably, the CSMs appear to translocate more slowly in ethanol/water diluted H_2O_2 solution, which has a significantly reduced surface tension (as compared to the aqueous H_2O_2 solution), consistently across all H_2O_2 concentrations tested (**Figure 6-13b**). Assuming a constant H_2O_2 decomposition (O_2 generation) rate at similar H_2O_2 concentrations, we attribute the reduced CSM motility to the reduced critical radii for O_2 bubble burst in ethanol/water mixtures as a result of the reduced surface tension.

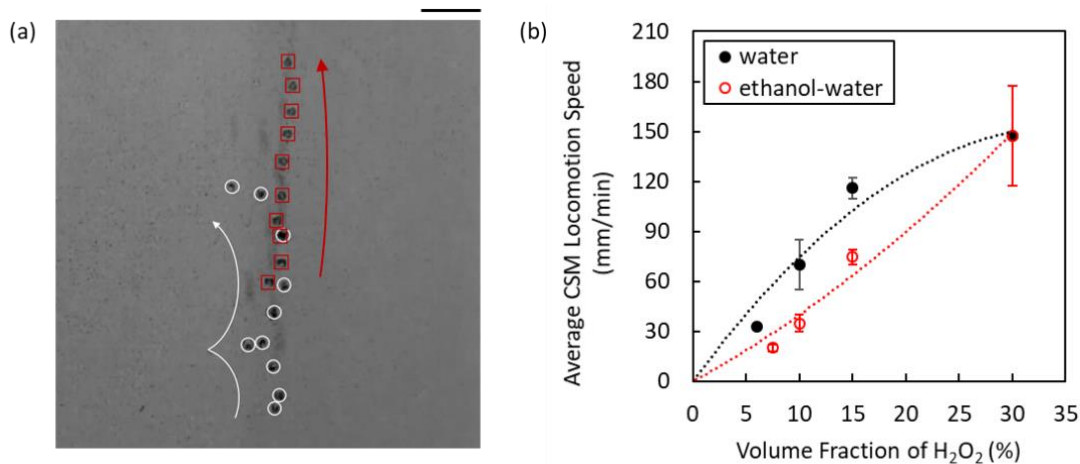


Figure 6-13. (a) Superimposed images of sequential frames show the locomotion of two Pt/graphene-CSMs (white circles and red squares). Arrows indicate the migration direction. Scale bar, 100 μm . (b) Averaged CSM translocation speed for Pt/graphene-CSMs in 30 volume percent H_2O_2 aqueous solution diluted using water (black) or ethanol (red). Data averaged from two experiments and the error bars represent their deviation. The dashed lines are guide for the eye.

For ethanol-diluted solution, the volumetric ratios of ethanol:water solution used are (from left to right): 3:1, 2:1, 1:1, 0.

6.2.3 Towards Navigation in a Complex Fluidic Network

The complex biomedical task of navigation in a fluidic network, perhaps exaggerated in *Fantastic Voyage*, has been critically deconstructed recently by Berrueta *et al.* and Pervan *et al.*^{61,62} Using a classical physiological model of the human circulatory system⁶³, they abstracted the latter as a complex fluidic network (**Figure 6-14a, b**). The central machine task of the CSM is embodied in a simple *test cell* in the form of interconnected double circular paths (**Figure 6-14c**). Particles circulate and initially select paths 0 or 1 randomly. A particle or CSM must be able to discover or otherwise identify a *signal* (marked by ×), permanently select this correct path, and recruit all others to select this path to the exclusion of the other in a form of reinforcement learning, akin to the immune response of leukocytes. This test cell and the task it embodies can be used to gauge the efficacy of algorithms and functions of the candidate CSMs. Aspects such as error correction, response time, and failure rates can be quantitatively assessed with such a test cell. Pervan *et al.* argue that particles capable of accomplishing this double circular closed path task have the basic architecture in the form of computation and actuation to navigate a more complex network with an eye towards the human circulatory system⁶².

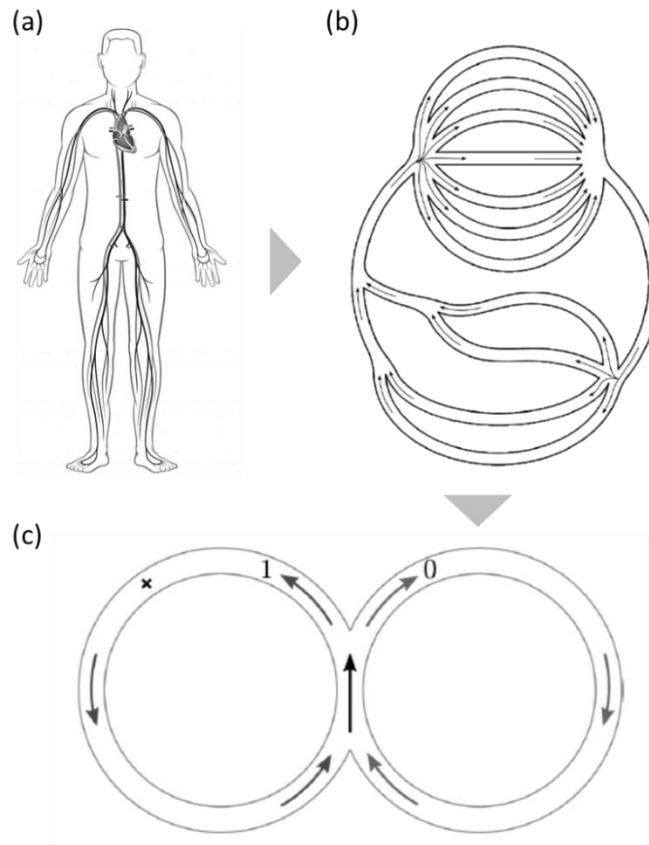


Figure 6-14. CSM conceptual design for a collective immune-like response. (a) The human circulatory system is a complex environment for CSMs to navigate, comprising branches and bifurcations as seen in (b) the corresponding abstracted graph. However, recent theoretical analyses^{61,62} have proven that the success of an immune response in the complex landscape can be extrapolated from the CSM’s performance in (c) a simplified double circular track. The CSM should recruit its peers when a signal (the × mark) is detected.

The locomotion ability compatible with autoperforation that we report in the previous section opens up possibilities for integrated smart CSMs which autonomously and actively explore their immediate environment. Wired with on-board CSM electronics previously reported^{58,59}, the self-driven colloidal robots may soon find uses in probing confined and remote spaces guided by user-defined

rules⁶⁴. This motivates new CSM conceptual designs that integrate locomotion, sensing, memory and communication in responses that mimic elements of human immunity.

6.2.3.1 Demonstrating a Collective Immune Response using CSMs: Design 1

It is possible to design CSMs capable of complex, ensemble behaviours since their fabrication is scalable to large populations. With each CSM equipped with a Pt module, their collective locomotion upon interaction will allow for the investigation of how ensemble-level motility scales with system size, say, as the number of CSMs is increased from 3 to more than 1000. We are specifically interested in emergent properties only observable in large populations^{65,66}. In addition, we can look for emergent swarm behaviours of these smart particles under fundamentally different conditions from those covered by their macroscopic counterparts^{67,68}. As an example, while random behaviours might be a challenge in and of themselves for macroscopic systems, stochastic dynamics is readily available, and essentially “programmed in”, for these microscopic CSMs immersed in a thermal bath. There are aspects of collective behaviour that can only be observed via a system in such a context with a layer of stochastic noise constantly pumping energy and perturbation into the ensemble.

Before diving directly into the CSM design that navigates the aforementioned complex fluidic channels, we first start with a simpler system targeting the peer recruitment sub-task – a feature of the human *immune system*. The fabrication approach of autoperforation allows one to create symmetry broken particles easily,

and this can be leveraged for task-driven collective motion. Particles can be programmed to locate a chemical signal and move towards it, to then signal similar particles in a recruiting effort. The result is that a single trace signal can result in an amplified response and amassing of resources to a specific location. This requires CSMs capable of complex chemotactic behaviour, inter-particle communication, memory and control. Building upon the existing Pt/graphene-CSM system fabricated in the previous section, chemo-responsive hydrogels can be added. As schematically shown in **Figure 6-15**, we may program the Hydrogel 1 (H_1) over the Pt-free side to release a substance I (for “inhibitor”), in the presence of a source signal. Next, the released I in the surrounding environment in turn triggers the contraction of Hydrogel 2 (H_2) over the Pt patches, thereby cutting off their access to the fuel, H_2O_2 .

On a macroscopic level, the increased propensity for the CSMs to halt (measured by the decreased particle diffusivity) as they approach the point source should in principle formulate a strategy for the particles to “locate” the source position. With this specific example, we anticipate a collective behaviour or a large ensemble of chemically communicating, chemotactic CSMs that detect a signal and recruit others like a cascade. This behaviour will be manifestly analogous to the engulfing behaviour of biological immune cells, or the foraging behaviour of a group of ants⁶⁹.

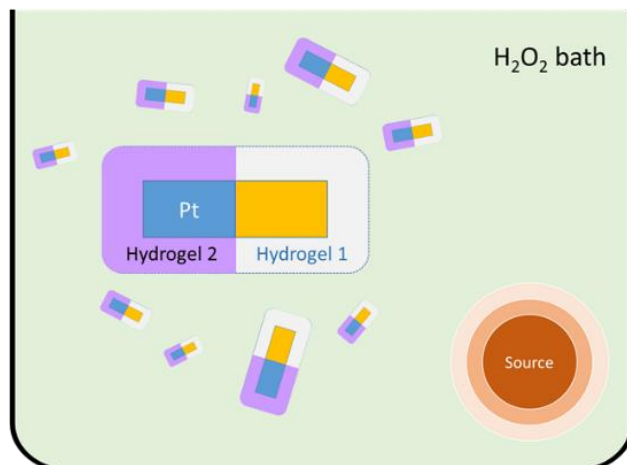


Figure 6-15. Schematic representation of the Pt/hydrogel-CSM Design 1 inside a H_2O_2 bath with a Gaussian source signal.

The chemical reactions that occur in this control system can be described by the following chemical kinetics:



Here SH_1 is the activated state of H_1 and IH_2 is the contracted state of H_2 . Assuming fast equilibration,

$$[\text{SH}_1] = \frac{K_1[\text{S}]}{1 + K_1[\text{S}]} \quad (60)$$

$$[\text{IH}_2] = \frac{K_2[\text{I}]}{1 + K_2[\text{I}]} \quad (61)$$

where $[SH_1]$ and $[IH_2]$ denote the fractions of particles in the corresponding states. The concentration of I, denoted $[I]$, will be dictated by its release rate from SH_1 , say $kA[SH_1]$ for a slow kinetics, where k is a rate constant and A the gel surface area.

In the scenario that we have (i) an infinite reservoir of H_2O_2 , and (ii) a point source S with a finite depletion mechanism in H_2O_2 such that S 's concentration profile $[S]$ is not a function of time, the following governing equations serve to describe the probability distribution of the particle (P_p):

$$\frac{\partial P_p}{\partial t}(\vec{x}, t) = \vec{\nabla} \cdot \left\{ D_p([IH_2]) \vec{\nabla} P_p(\vec{x}, t) \right\} \quad (62)$$

$$\frac{\partial [I]}{\partial t}(\vec{x}, t) = D_I \nabla^2 [I] + kA[SH_1]P_p \quad (63)$$

Here D_I denotes the diffusivity of I and D_p , the particle diffusivity in H_2O_2 . The first equation therefore describes the Fickian diffusion of the particles, while the second is the reaction-diffusion equation for $[I]$. D_p will be a decreasing function of the contracted state fraction $[IH_2]$, for instance $D_p = D_\infty / (1 + \alpha[IH_2]P_p)$ where D_∞ is the $[IH_2]$ -free diffusivity and α a finite constant. We note that typically $D_p \ll D_I$, as D_p describes the mobility of a microparticle, whereas D_I is the diffusivity of a molecule.

The coupled system of partial differential equations then solves the probability of finding the particle as a function of the position vector and time, which motivates a kinetic Monte-Carlo simulation of the particle trajectory.

6.2.3.2 A CSM Solution to the Double Circular Cell: Design 2

Design 1 uses coupled locomotion and analyte sensing to achieve an analogous immune response. This can be used in a CSM design to address the task encoded by the double circular cell (**Figure 6-14c**) as discussed earlier. This cell is meant to mimic the critical tasks involved in navigating the human circulatory system, for instance, as an ultimate biomedical application for CSMs. The actual system contains numerous bifurcations and branches which complicate targeted exploration (**Figure 6-14a, b**). In this section, we show that Design 2 (**Figure 6-16**) enables an immune response in the context of the double circular cell (**Figure 6-14c**) using only rudimentary forms of sensing and locomotion. That is, we envision a CSM to detect this target and inform its peers of the location.

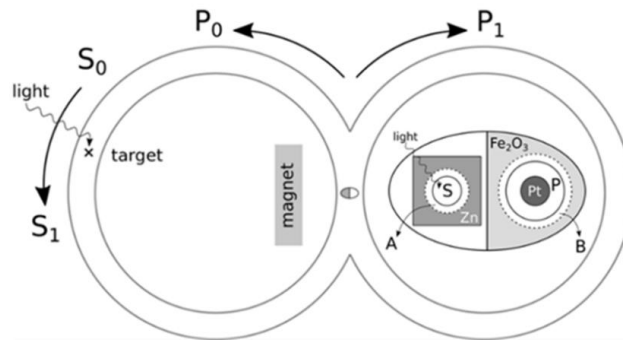


Figure 6-16. A physical system proposed for the double circular test. CSMs will be able to detect the target and then communicate to their counterparts where they have discovered it. The CSMs on the receiving end of this communication will interpret the chemical signals, and alter their behaviour accordingly. Inset: Schematic of the CSM design showing the success bit, S, and the policy bit, P. The emission of chemical A occurs when the signal is detected, indicating that the CSM has found the target (S_1), and no chemical A is released otherwise (S_0). By default, the

magnetic locomotion policy is employed (P_0). When Pt is exposed to H_2O_2 , the CSM drives itself the opposite way (P_1), releasing chemical B at the same time.

To enable this function, our conceptual design of a self-driven CSM system takes full advantage of the binary nature of bifurcations detailed in Pervan *et al.* Shown in **Figure 6-16**, the proposed learning algorithm requires two bits of memory on each CSM, a feature already reported previously^{54,56}: one to store the control policy (either P_0 or P_1 , for left or right) and one to store whether the goal has been detected (either S_0 or S_1 , for non-success or success). The mechanism is simple from the control theory point of view: once an agent encounters the target, S_0 is switched to S_1 . When this P_xS_1 CSM encounters another pristine P_yS_0 agent, the latter's policy bit P_y is switched to P_x only when $P_x \neq P_y$. Table 1 shows that both agents will end up moving towards the signal as directed by the aligned P states.

Table 6-1. All possible scenarios when a pristine CSM (P_yS_0) encounters one that has seen the target signal (P_xS_1). The pristine CSM will align its policy bit with the signal CSM in the end.

Case	Pristine CSM state (P_yS_0)	Signal CSM state (P_xS_1)	Final P states
I	P_0	P_0	Both P_0
II	P_1	P_0	Both P_0
III	P_0	P_1	Both P_1
IV	P_1	P_1	Both P_1

A physical system requires more details. We propose that a CSM will be driven by both the global magnetic attraction and its own bubble propulsion (**Figure 6-16**). While, by default, it enters the left loop in a flowing fluid due to the magnet (policy

P_0), it can also defy the field and take the right path when self-driven locomotion is activated (policy P_1). For example, it can be a Pt-decorated autoperforated cell with a switchable access to H_2O_2 .

When this CSM encounters the target stimulus, say light, a chemical A is released. Experimentally, this can be realized by installing an irreversible light-sensitive pocket, the state of which determines the success bit (S in **Figure 6-16** inset):



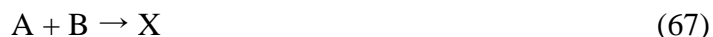
The policy bit (P in **Figure 6-16** inset) will be another hydrogel patch (with chemical B embedded) over the Pt metal. When this patch is in its ‘open’ state, the Pt interacts with the H_2O_2 , and at the same time, chemical B is released. This constitutes our two-bit system: the presence of chemical A indicates that a CSM has found the target (S_1) and the absence of A indicates the opposite (S_0). The presence of chemical B indicates the Pt policy is being used (P_1) and the absence of chemical B, the magnetic policy (P_0).

The next step is to realize the P bit switching when a pristine CSM (P_yS_0) meets one that has seen light (P_xS_1). Note that physically, P_1 switching to P_0 and P_0 to P_1 should be triggered by two distinct mechanisms, which we term X and Y. If X and Y are chemical signals, they should be released when the two P states differ, hence corresponding to Cases II and III in **Table 6-1**:





As chemicals A and B are present for both cases, the differentiation of X (for switching P₁ to P₀) and Y (for P₀ to P₁) relies on determining whether A and B are released from the same CSM or separately. For this reason, we imagine that each cell has access to a constant on-board power source (*i.e.* a Zn-air battery). This enables us to differentiate Cases II and III using a carefully chosen A-B pair such that the following requirement is satisfied:



Note that X and Y must be two distinct products and cannot be inter-converted. The final **Table 6-2** tabulates all possible encounter scenarios. We see that with the proposed physical system, a CSM that has seen that target will be able to recruit its peers by aligning their policy bits with that of itself. A similar system therefore should succeed in induction of immune-like response in a complicated maze as well, as proven earlier theoretically^{61,62}.

Table 6-2. All possible scenarios of the encounter for the proposed physical system (Design 2). The CSMs communicate with one another via chemicals A, B, X, and Y. Eventually the policies are aligned towards the signal location after the encounter, as seen in **Table 6-1**.

Case	Pristine CSM state	Signal CSM state	Chemical signal	Final CSM states
I	P ₀ S ₀	P ₀ S ₁	A	P ₀ S ₀ and P ₀ S ₁

	(no signal)	(A)	(no reaction)	(no change)
II	P_1S_0	P_0S_1	$A + B \rightarrow X$	P_0S_0 and P_0S_1
	(B)	(A)	$P_1 + X \rightarrow P_0$	P_1 switch off
III	P_0S_0	P_1S_1	Y	P_1S_0 and P_1S_1
	(no signal)	$(A + B + e^- \rightarrow Y)$	$P_0 + Y \rightarrow P_1 + B$	P_0 switch on
IV	P_1S_0	P_1S_1	B, Y	P_1S_0 and P_1S_1
	(B)	$(A + B + e^- \rightarrow Y)$	(no reaction)	(no change)

In summary, we expanded upon the previously reported autoperforation techniques to introduce the locomotion functionality to colloidal robotics. The new process, which requires simply a conventional inkjet printer, allows Pt patches to be selectively patterned and electroplated onto 2DMs, followed by the standard autoperforation procedure. The resultant Pt-decorated CSMs thereby demonstrate self-driven locomotion in an energized environment. We have shown via extensive parametric studies that the Pt motor element, designed to be very compatible with the autoperforation platform, can be facilely tailored for a desired coverage and thickness. The impact of the surrounding environment on the locomotion is thoroughly explored as well. Lastly, we demonstrated the implication of the new functionality on enabling complex CSM tasks by outlining two designs for a collective immune-type response. Overall, this work establishes the first step towards self-driven CSM locomotion within the autoperforation framework, and expands the armoury of functionalities available to researchers of colloidal robotics.

6.2.4 Experimental Details

We grew monolayer graphene on Cu substrates with the following protocol. Hydrogen, methane, and argon canisters feed into a quartz mixing tube inside a CVD furnace. CVD growth of graphene is carried out by heating copper foil to 1000° C with a constant 30 sccm flow of hydrogen. The temperature is held constant at 1000° C for 20 min. Methane is injected into the mixing tube at a constant flowrate of 0.5 sccm for 15 min. The sample is then bathed in hydrogen for 5 min before the furnace is turned off and allowed to cool to room temperature. The sample is then bathed in argon and allowed to return to standard pressure.

The as-prepared graphene/Cu substrate is used directly for the subsequent inversion-moulding step. A carboxymethyl cellulose ink was prepared by dissolving 285 mg sodium carboxymethyl cellulose (Sigma-Aldrich, average Mw ~90000) in 100 mL deionized water. A commercial Fujifilm Dimatix Materials Printer DMP-2850 was used to print a 6×20 array of CMC disks of radius 20 μm with 100 μm spacing onto graphene. 2% PMMA (MicroChem) was spun onto the sample at a typical spin-rate of 4000 rpm for 1 min. The sample was then etched in water for approximately 18 h. 1 cm^2 of the sample was electroplated in a 3 mM PtCl_4 solution with a Pt counter electrode and a constant 0.1 A current. Graphene is conductive which allows for the Pt to deposit only on the array of exposed graphene wells.

For the subsequent autoperforation process, a layer of 7% PMMA was spin-coated onto the sample at a spin-rate of 500 rpm for 10 min then 4000 rpm for 2 min. The

sample was floated on APS-100 Cu etchant for approximately 2 h or until the Cu was completely etched away. The sample was then flipped onto a SiO₂ wafer resulting in a PMMA-Pt-graphene vertical stack. The sample was annealed for 10 min at 125° C. A dyed PS-EG ink was prepared by mixing 2 mL polystyrene and 2 mL ethylene glycol (both from Sigma-Aldrich), and dissolving approximately 2 mg Rhodamine B in the mixture. DMP-285 printer was used to print a 6 × 20 array of PS-EG aligned to the prefabricated array of Pt patches. The printed sample was annealed for 10 min at 125° C. A separate sample of graphene was transferred by spin-coating 4% PMMA onto the graphene-copper for 1 min at 4000 rpm. The sample was then placed in APS-100 for approximately 2 h or until the copper was completely etched away. The PMMA-Pt-graphene-PS-EG vertical stack was capped with this second layer of graphene-PMMA and annealed for 10 min at 125° C. The complete vertical stack is PMMA-graphene-PS-EG-graphene-Pt-PMMA. The sample was lifted-off in 10 mL of 80% ethanol heated from room temperature using a hot plate set to 120° C with magnetic stirring. After 10 min, the lifted-off cells were centrifuged and rinsed with 12-13 mL of deionized water three times.

6.3 References

- (1) Griffith, A. A. *Philosophical Transactions of the Royal Society of London. Series A, Containing Papers of a Mathematical or Physical Character* **1921**, 221, 163.
- (2) Nam, K. H.; Park, I. H.; Ko, S. H. *Nature* **2012**, 485, 221.
- (3) Kim, B. C.; Moraes, C.; Huang, J.; Thouless, M. D.; Takayama, S. *Biomaterials Science* **2014**, 2, 288.
- (4) Kim, M.; Kim, D.-J.; Ha, D.; Kim, T. *Nanoscale* **2016**, 8, 9461.
- (5) Zhang, P.; Ma, L.; Fan, F.; Zeng, Z.; Peng, C.; Loya, P. E.; Liu, Z.; Gong, Y.; Zhang, J.; Zhang, X.; Ajayan, P. M.; Zhu, T.; Lou, J. *Nature Communications* **2014**, 5, 3782.

- (6) Yin, H.; Qi, H. J.; Fan, F.; Zhu, T.; Wang, B.; Wei, Y. *Nano Letters* **2015**, 15, 1918.
- (7) Reina, A.; Jia, X.; Ho, J.; Nezhich, D.; Son, H.; Bulovic, V.; Dresselhaus, M. S.; Kong, J. *Nano Letters* **2009**, 9, 30.
- (8) Kim, K. S.; Zhao, Y.; Jang, H.; Lee, S. Y.; Kim, J. M.; Kim, K. S.; Ahn, J.-H.; Kim, P.; Choi, J.-Y.; Hong, B. H. *Nature* **2009**, 457, 706.
- (9) Li, X.; Cai, W.; An, J.; Kim, S.; Nah, J.; Yang, D.; Piner, R.; Velamakanni, A.; Jung, I.; Tutuc, E.; Banerjee, S. K.; Colombo, L.; Ruoff, R. S. *Science* **2009**, 324, 1312.
- (10) Lee, G.-H.; Cooper, R. C.; An, S. J.; Lee, S.; van der Zande, A.; Petrone, N.; Hammerberg, A. G.; Lee, C.; Crawford, B.; Oliver, W.; Kysar, J. W.; Hone, J. *Science* **2013**, 340, 1073.
- (11) Mitchell, N. P.; Koning, V.; Vitelli, V.; Irvine, W. T. M. *Nat Mater* **2017**, 16, 89.
- (12) Zhang, T.; Li, X.; Gao, H. *International Journal of Fracture* **2015**, 196, 1.
- (13) Hsu, P. I.; Huang, M.; Xi, Z.; Wagner, S.; Suo, Z.; Sturm, J. C. *Journal of Applied Physics* **2004**, 95, 705.
- (14) Sun, J.-Y.; Lu, N.; Yoon, J.; Oh, K.-H.; Suo, Z.; Vlassak, J. J. *Journal of Applied Physics* **2012**, 111, 013517.
- (15) Wu, X.; Lee, I.; Dong, Q.; Yang, K.; Kim, D.; Wang, J.; Peng, Y.; Zhang, Y.; Saliganc, M.; Yasuda, M.; Kumeno, K.; Ohno, F.; Miyoshi, S.; Kawaminami, M.; Sylvester, D.; Blaauw, D. In *2018 IEEE Symposium on VLSI Circuits 2018*, p 191.
- (16) Zhang, L.; Yu, J.; Yang, M.; Xie, Q.; Peng, H.; Liu, Z. **2013**, 4, 1443.
- (17) Dendukuri, D.; Pregibon, D. C.; Collins, J.; Hatton, T. A.; Doyle, P. S. *Nat. Mater.* **2006**, 5, 365.
- (18) Walther, A.; Müller, A. H. E. *Chemical Reviews* **2013**, 113, 5194.
- (19) Splendiani, A.; Sun, L.; Zhang, Y.; Li, T.; Kim, J.; Chim, C.-Y.; Galli, G.; Wang, F. *Nano Letters* **2010**, 10, 1271.
- (20) Lee, S.; Lee, K.; Liu, C.-H.; Zhong, Z. *Nanoscale* **2012**, 4, 639.
- (21) Yang, J. J.; Pickett, M. D.; Li, X.; OhlbergDouglas, A. A.; Stewart, D. R.; Williams, R. S. *Nat Nano* **2008**, 3, 429.
- (22) Brent, J. R.; Savjani, N.; Lewis, E. A.; Haigh, S. J.; Lewis, D. J.; O'Brien, P. *Chemical Communications* **2014**, 50, 13338.
- (23) Hanlon, D.; Backes, C.; Doherty, E.; Cucinotta, C. S.; Berner, N. C.; Boland, C.; Lee, K.; Harvey, A.; Lynch, P.; Gholamvand, Z.; Zhang, S.; Wang, K.; Moynihan, G.; Pokle, A.; Ramasse, Q. M.; McEvoy, N.; Blau, W. J.; Wang, J.; Abellan, G.; Hauke, F.; Hirsch, A.; Sanvito, S.; O'Regan, D. D.; Duesberg, G. S.; Nicolosi, V.; Coleman, J. N. *Nature Communications* **2015**, 6, 8563.
- (24) Hao, C.; Wen, F.; Xiang, J.; Yuan, S.; Yang, B.; Li, L.; Wang, W.; Zeng, Z.; Wang, L.; Liu, Z.; Tian, Y. *Advanced Functional Materials* **2016**, 26, 2016.

- (25) Grunlan, J. C.; Mehrabi, A. R.; Bannon, M. V.; Bahr, J. L. *Advanced Materials* **2004**, 16, 150.
- (26) Island, J. O.; Steele, G. A.; van der Zant, H. S. J.; Castellanos-Gomez, A. *2D Mater.* **2015**, 2, 6.
- (27) Huang, Y.; Qiao, J.; He, K.; Bliznakov, S.; Sutter, E.; Chen, X.; Luo, D.; Meng, F.; Su, D.; Decker, J.; Ji, W.; Ruoff, R. S.; Sutter, P. *Chemistry of Materials* **2016**, 28, 8330.
- (28) Youngwoo, S.; Daichi, K.; Albert Tianxiang, L.; Volodymyr, B. K.; Qing Hua, W.; Michael, S. S. *2D Mater.* **2017**, 4, 025091.
- (29) O'Hern, S. C.; Stewart, C. A.; Boutilier, M. S. H.; Idrobo, J.-C.; Bhaviripudi, S.; Das, S. K.; Kong, J.; Laoui, T.; Atieh, M.; Karnik, R. *ACS Nano* **2012**, 6, 10130.
- (30) Koman, V. B.; Liu, P.; Kozawa, D.; Liu, A. T.; Cottrill, A. L.; Son, Y.; Lebron, J. A.; Strano, M. S. *Nature Nanotechnology* **2018**.
- (31) Liu, P.; Cottrill, A. L.; Kozawa, D.; Koman, V. B.; Parviz, D.; Liu, A. T.; Yang, J.; Tran, T. Q.; Wong, M. H.; Wang, S.; Strano, M. S. *Nano Today* **2018**, 21, 18.
- (32) Mahajan, S. G.; Liu, A. T.; Cottrill, A. L.; Kunai, Y.; Bender, D.; Castillo, J.; Gibbs, S. L.; Strano, M. S. *Energy & Environmental Science* **2016**, 9, 1290.
- (33) Liu, A. T.; Kunai, Y.; Liu, P.; Kaplan, A.; Cottrill, A. L.; Smith-Dell, J. S.; Strano, M. S. *Advanced Materials* **2016**, 28, 9752.
- (34) Kunai, Y.; Liu, A. T.; Cottrill, A. L.; Koman, V. B.; Liu, P.; Kozawa, D.; Gong, X.; Strano, M. S. *Journal of the American Chemical Society* **2017**, 139, 15328.
- (35) Cottrill, A. L.; Liu, A. T.; Kunai, Y.; Koman, V. B.; Kaplan, A.; Mahajan, S. G.; Liu, P.; Toland, A. R.; Strano, M. S. *Nat Commun* **2018**, 9, 664.
- (36) Han, K.; Shields, C. W.; Velev, O. D. *Advanced Functional Materials* **2018**, 28, 1705953.
- (37) Sitti, M. *Nature* **2009**, 458, 1121.
- (38) Jafferis, N. T.; Helbling, E. F.; Karpelson, M.; Wood, R. J. *Nature* **2019**, 570, 491.
- (39) Yan, X.; Zhou, Q.; Vincent, M.; Deng, Y.; Yu, J.; Xu, J.; Xu, T.; Tang, T.; Bian, L.; Wang, Y.-X. J.; Kostarelos, K.; Zhang, L. *Science Robotics* **2017**, 2, eaaq1155.
- (40) Yigit, B.; Alapan, Y.; Sitti, M. *Advanced Science* **2019**, 6, 1801837.
- (41) Park, H.-W.; Wensing, P. M.; Kim, S. *The International Journal of Robotics Research* **2017**, 36, 167.
- (42) Sitti, M. **2017**.
- (43) Miskin, M. Z.; Dorsey, K. J.; Bircan, B.; Han, Y.; Muller, D. A.; McEuen, P. L.; Cohen, I. *Proceedings of the National Academy of Sciences* **2018**, 115, 466.
- (44) Zhu, S.-E.; Shabani, R.; Rho, J.; Kim, Y.; Hong, B. H.; Ahn, J.-H.; Cho, H. J. *Nano Letters* **2011**, 11, 977.
- (45) Moran, J. L. In *Robotic Systems and Autonomous Platforms*; Elsevier: 2019, p 129.

- (46) Chhowalla, M.; Shin, H. S.; Eda, G.; Li, L.-J.; Loh, K. P.; Zhang, H. *Nature Chemistry* **2013**, 5, 263.
- (47) Chhowalla, M.; Jena, D.; Zhang, H. *Nature Reviews Materials* **2016**, 1.
- (48) Maily-Giacchetti, B.; Hsu, A.; Wang, H.; Vinciguerra, V.; Pappalardo, F.; Occhipinti, L.; Guidetti, E.; Coffa, S.; Kong, J.; Palacios, T. *Journal of Applied Physics* **2013**, 114, 084505.
- (49) Wang, Q. H.; Kalantar-Zadeh, K.; Kis, A.; Coleman, J. N.; Strano, M. S. *Nature Nanotechnology* **2012**, 7, 699.
- (50) Zhang, H. *ACS Nano* **2015**, 9, 9451.
- (51) Miskin, M.; Dorsey, K.; Bircan, B.; Han, Y.; Muller, D.; McEuen, P.; Cohen, I. *Bulletin of the American Physical Society* **2018**.
- (52) Bessonov, A. A.; Kirikova, M. N.; Petukhov, D. I.; Allen, M.; Ryhänen, T.; Bailey, M. J. A. *Nature Materials* **2014**, 14, 199.
- (53) Georgescu, I. *Nature Reviews Materials* **2018**, 3, 227.
- (54) Koman, V. B.; Liu, P.; Kozawa, D.; Liu, A. T.; Cottrill, A. L.; Son, Y.; Lebron, J. A.; Strano, M. S. *Nature Nanotechnology* **2018**, 13, 819.
- (55) Mannoor, M. S.; Tao, H.; Clayton, J. D.; Sengupta, A.; Kaplan, D. L.; Naik, R. R.; Verma, N.; Omenetto, F. G.; McAlpine, M. C. *Nature Communications* **2012**, 3.
- (56) Liu, P.; Liu, A. T.; Kozawa, D.; Dong, J.; Yang, J. F.; Koman, V. B.; Saccone, M.; Wang, S.; Son, Y.; Wong, M. H.; Strano, M. S. *Nature Materials* **2018**, 17, 1005.
- (57) Shim, J.; Bae, S.-H.; Kong, W.; Lee, D.; Qiao, K.; Nezich, D.; Park, Y. J.; Zhao, R.; Sundaram, S.; Li, X.; Yeon, H.; Choi, C.; Kum, H.; Yue, R.; Zhou, G.; Ou, Y.; Lee, K.; Moodera, J.; Zhao, X.; Ahn, J.-H.; Hinkle, C.; Ougazzaden, A.; Kim, J. *Science* **2018**, 362, 665.
- (58) Hempel, M.; McVay, E.; Kong, J.; Palacios, T. *Bulletin of the American Physical Society* **2018**, 63.
- (59) Lee, S.; Cortese, A. J.; Gandhi, A. P.; Agger, E. R.; McEuen, P. L.; Molnar, A. C. *IEEE Transactions on Biomedical Circuits and Systems* **2018**, 12, 1256.
- (60) Miskin, M. Z.; Cortese, A. J.; Cohen, I.; McEuen, P. L. *Bulletin of the American Physical Society* **2019**, 64.
- (61) Berrueta, T. A.; Pervan, A.; Murphey, T. D. Freiburg, Germany, 2019.
- (62) Pervan, A.; Murphey, T. *arXiv* **2020**, preprint, 2003.03793.
- (63) Hardy, H. H.; Collins, R. E.; Calvert, R. E. *Medical & Biological Engineering & Computing* **1982**, 20, 550.
- (64) Yang, J. F.; Liu, P.; Koman, V. B.; Liu, A. T.; Strano, M. S. In *Robotic Systems and Autonomous Platforms*; Elsevier: 2019, p 361.
- (65) Redner, G. S.; Hagan, M. F.; Baskaran, A. *Physical Review Letters* **2013**, 110.
- (66) Redner, G. S.; Baskaran, A.; Hagan, M. F. *Physical Review E* **2013**, 88.

- (67) Rubenstein, M.; Cornejo, A.; Nagpal, R. *Science* **2014**, 345, 795.
- (68) Savoie, W.; Berrueta, T. A.; Jackson, Z.; Pervan, A.; Warkentin, R.; Li, S.; Murphey, T. D.; Wiesenfeld, K.; Goldman, D. I. *Science Robotics* **2019**, 4, eaax4316.
- (69) Chadab, R.; Rettenmeyer, C. *Science* **1975**, 188, 1124.

Chapter 7

Collective Synchronization in Self-driven Chemo-mechanical Relaxation Oscillators

Article that contributes to this chapter:

Liu, A. T.*; Yang, J. F.*; Brooks, A. M.; LeMar, L. N.; Strano, M. S. *in preparation*

In this chapter, I present a prototype chemo-mechanical relaxation oscillator system that exhibit an emergent self-synchronized rhythmic beating at the microscale. We observed that a group of microscopic particles, when placed together, become a self-synchronized relaxation oscillator (as an ensemble). Their rhythmic beating only emerges as a result of their interactions with one another. This complex system-level oscillation emerging from particles sharing a deceptively simple physical design exhibits highly tunable frequency. This simple chemo-mechanical oscillator provides a widely accessible experimental design to probe how rhythmic beating could come about amongst early multi-cell organisms, and illustrate how primitive entities could self-synchronize and exhibit complex collective behaviors.

7.1 Background on Emergent Behavior and Relaxation Oscillators

Emergence occurs when an entity is observed to have properties its parts do not have on their own. These properties or behaviors emerge only when the parts interact in a wider whole. Emergence plays a central role in theories of integrative levels and of complex systems. For instance, the phenomenon of life as studied in biology is an emergent property of chemistry, and psychological phenomena emerge from the neurobiological phenomena

of living things. An emergent behavior or emergent property can appear when a number of simple entities (agents) operate in an environment, forming more complex behaviors as a collective. The complex behavior or properties are not a property of any single such entity, nor can they easily be predicted or deduced from behavior in the lower-level entities, and might in fact be irreducible to such behavior. The shape and behavior of a flock of birds or school of fish are good examples of emergent properties. One reason emergent behavior is hard to predict is that the number of interactions between a system's components increases exponentially with the number of components, thus allowing for many new and subtle types of behavior to emerge. Systems with emergent properties or emergent structures may appear to defy entropic principles and the second law of thermodynamics, because they form and increase order despite the lack of command and central control. This is possible because open systems can extract information and order out of the environment.

The term relaxation oscillator is also applied to dynamical systems in many diverse areas of science that produce nonlinear oscillations and can be analyzed using the same mathematical model as electronic relaxation oscillators. For example, geothermal geysers, networks of firing nerve cells, thermostat controlled heating systems, coupled chemical reactions, the beating human heart, earthquakes, the squeaking of chalk on a blackboard, the cyclic populations of predator and prey animals, and gene activation systems have been modeled as relaxation oscillators. Relaxation oscillations are characterized by two alternating processes on different time scales: a long relaxation period during which the system approaches an equilibrium point, alternating with a short impulsive period in which the equilibrium point shifts. The period of a relaxation oscillator is mainly determined by the relaxation time constant.

7.2 The Physical Design that Results Synchronized Oscillation

The physical design of the chemo-mechanical oscillator is extremely simple: a clean-room fabricated SU8 disk supporting a concentric Pt disk (smaller in radius) on top (**Figure 7-1**). When placed at the liquid-air interface of a droplet of H_2O_2 solution (Pt facing down), the Pt catalyzed decomposition of H_2O_2 generates a large O_2 bubble trapped underneath the particle (**Figure 7-1**).

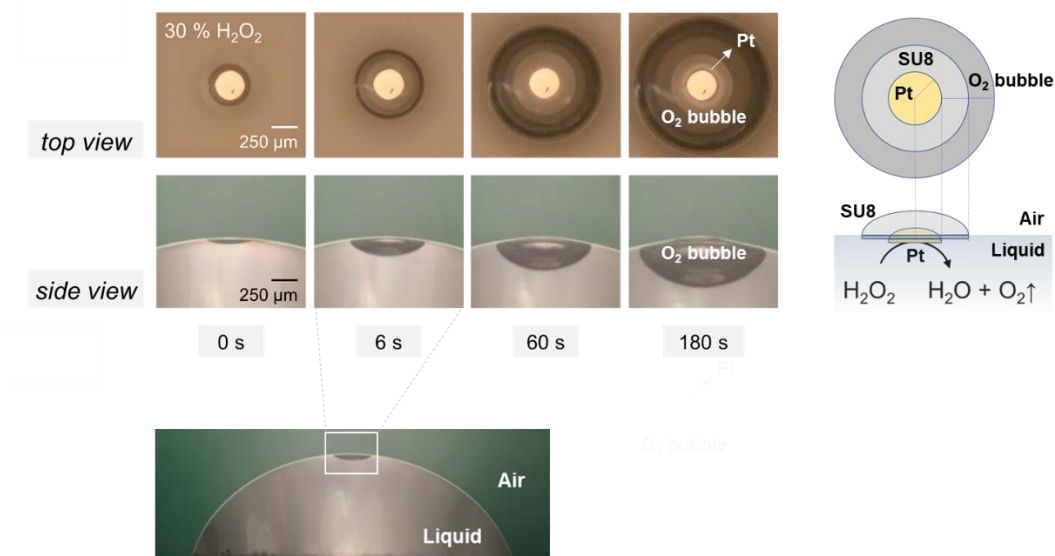


Figure 7-1. (Top-left) Time elapsed optical micrographs of one SU9-Pt particle sitting at the liquid-air interface of a droplet of 30% H_2O_2 water solution. (Top-right) Schematic illustration of the physical design of the SU8-Pt chemo-mechanical oscillator. (Bottom) Zoomed-out optical image of the H_2O_2 droplet used for this study.

When placed in the H_2O_2 solution by itself, the buoyancy of the expanding O_2 bubble continuously raises the SU8-Pt particle on top, presumably increasing the length H_2O_2 needs to diffuse within the liquid thin film separating the O_2 bubble from entering the air

space above the liquid droplet, effectively slowing down the rate of bubble growth (**Figure 7-1**). This can be seen in **Figure 7-2**, where we tracked the bubble volume as a function of time. It should be noted that with a single particle, the O_2 bubble can be stabilized by the presence of the particle on top and the particle remains stationary (in the xy-plane seen from the top) for a prolonged time.

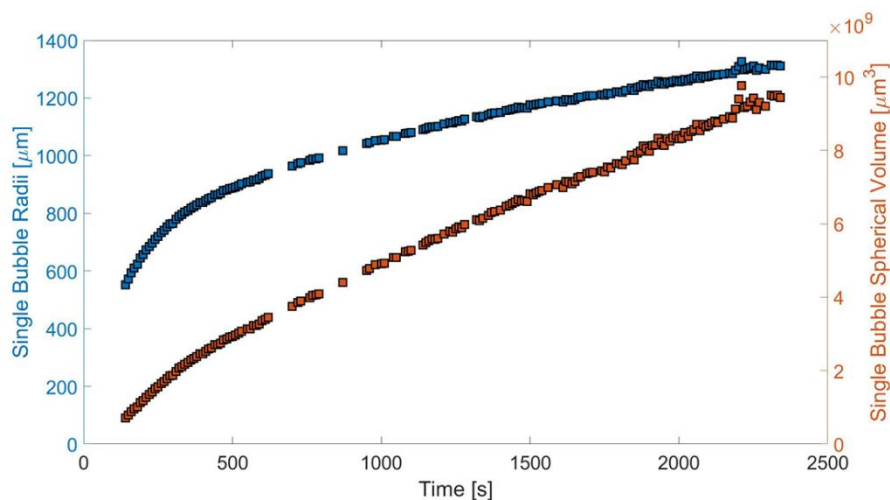


Figure 7-2. Oxygen bubble size tracking as a function of time. The radius of the bubble grows (blue). If we approximate the bubble as spheres, we get a volume trajectory (orange).

When two identical SU8-Pt particles are placed inside the H_2O_2 droplet, however, we observe a sustained rhythmic expansion-contraction at a regular frequency (**Figure 7-3**). We observe the particles attract each other towards the vertex of the H_2O_2 droplet curvature, and the respective O_2 bubbles localized underneath each particle merge upon contact (presumably to reduce overall surface area and thus minimizing surface tension). This merging event frees up both particles' Pt disk surface to further catalyze the decomposition of H_2O_2 , feeding the center O_2 bubble until it ruptures. The mechanical

impulse pushes the particles away from each other and the oscillation cycle repeats (**Figure 7-3**).

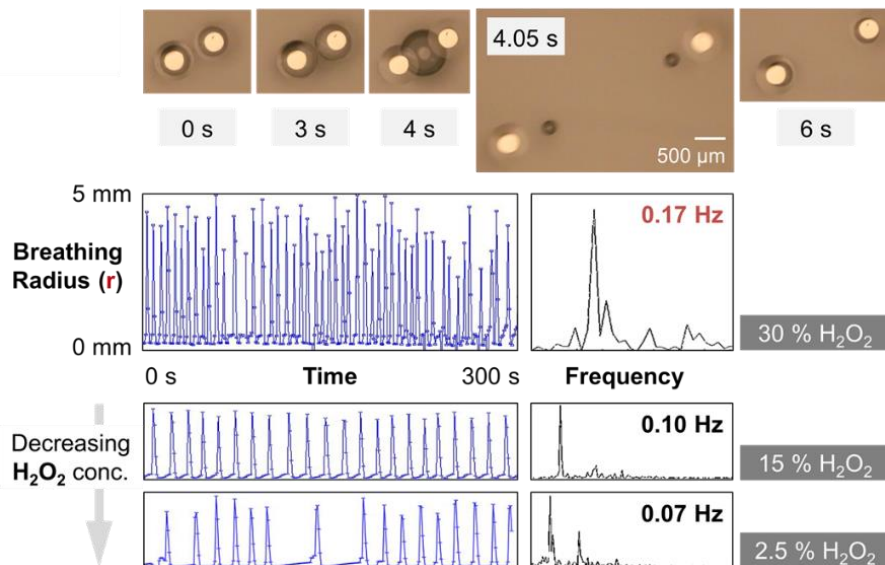


Figure 7-3. (Top) Time elapsed optical micrographs of SU8-Pt particles demonstrating collective expansion-contraction behavior in a time-oscillatory fashion. (Bottom) Breathing radius (averaged particle distances from the system’s centroid) plotted as a function of time (and its Fast Fourier Transform (right panel) for frequency identification) for oscillators in droplets of different H₂O₂ concentrations.

If we define the averaged distances for each particle from the system’s centroid as a parameter called “breathing radius” and plot it as a function of time, we can visualize this oscillation and track its dominant oscillation frequency (**Figure 7-3**). We note that the oscillation frequency of this simple two-particle chemo-mechanical oscillator can be tuned by varying the concentration of H₂O₂ in the droplet (**Figure 7-3**, **Figure 7-4b**). We further note that the breathing radius is not a strong function of the concentration of the H₂O₂ solution used (**Figure 7-4a**).

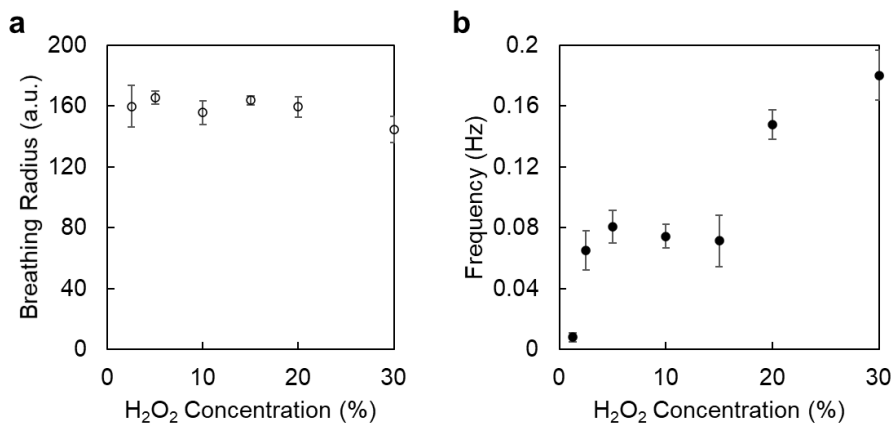


Figure 7-4. (a) Two-particle chemo-mechanical oscillator breathing radius plotted as a function of the H₂O₂ concentration used inside the liquid droplet. (b) Two-particle chemo-mechanical oscillator frequency plotted as a function of the H₂O₂ concentration used inside the liquid droplet.

7.3 An Analytical Model that Captures the Primary Mode of Oscillation

To understand the mechanistic origin of this emergent chemo-mechanical oscillation, we introduce a physical model to describe the three key steps within each cycle of this relaxation oscillator: (1) particle attraction, (2) O₂ bubble expansion, and (3) bubble bursting.

In the first step, each particle experiences three types of forces throughout: (a) a global restoring force (F_{dome}) as determined by the dome shape of the droplet that always attract the particle towards the droplet vertex (center origin in the top view); (b) a lateral capillary attractive force (F_{cheerio}) between pairs of particles (also known as the “Cheerios” force); (c) a drag force (F_{drag}) exerted by the liquid onto the particle (or bubble) to reduce its velocity.

$$F_{dome} = -k_{dome} \cdot \gamma_{LV} \cdot a^4 \left(\exp\left(\sqrt{x_i^2 + y_i^2}\right) - 1 \right) \quad (69)$$

$$F_{cheerio} = -\frac{2(\rho_L - \rho_V)gh^2 \exp(-qd)}{(1 + \exp(-qd))^2}, \text{ where } q = \sqrt{\frac{(\rho_L - \rho_V)g}{\gamma_{LV}}} \quad (70)$$

$$F_{drag} = -6\pi\mu a \sqrt{\dot{x}_i^2 + \dot{y}_i^2} \quad (71)$$

In our notation, x and y denote spatial position of each particle while \dot{x} and \dot{y} denote its speed along each direction; k_{dome} is a scaling coefficient; γ_{LV} is the liquid-vapor surface tension; a is particle radius; h is the particle height; d is the distance between each pair of particles; ρ represents density of substance; g is gravitational constant; and μ denotes dynamic viscosity. The combined forces acting on each particle (bubble) is used to formulate equations of motion that describe the dynamics of the system.

In the second step, the rate of volume (V_{O_2}) expansion of the O_2 bubble formulated as a first order process with rate constant k_{rxn} :

$$\frac{dV_{O_2}}{dt} = \frac{dn_{O_2}}{dt} \left(\frac{RT}{P_{O_2}} \right) = k_{rxn} C_{H_2O_2}^{\infty} \pi \left(\frac{a}{2} \right)^2 \left(\frac{RT}{P_{O_2}} \right) \quad (72)$$

Here n_{O_2} denotes the number (in moles) of O_2 molecules converted; R is the gas constant; T is temperature; P_{O_2} is the O_2 pressure inside the bubble, which is treated as 1 atmospheric pressure; $C_{H_2O_2}^{\infty}$ is the concentration of H_2O_2 in the bulk droplet (ignoring the transport boundary layer and diffusion limitation).

The third step involves the impulse of a bursting bubble on the subjected particle. To estimate this mechanical impulse, we first must get an expression of the critical radius of

the O₂ bubble at the moment of bursting. This is calculated by considering a force balance on the liquid film of a spherical bubble at the liquid-air interface. At the critical radius, the surface buoyancy force (by the O₂ bubble underneath) pushing the liquid film up balances the surface tension integrated along the bubble circumference contour pulling the liquid film down, resulting the following expression:

$$\left(\gamma_{LV} \cdot \frac{2}{R_C} \right) \cdot \pi \cdot R_C^2 = \frac{4}{3} \pi \cdot \rho_L g \cdot R_C^3 \quad (73)$$

The equation above gives an analytical expression for the critical bubble radius (R_C), which is then plugged in the expression of the instantaneous force (F_{burst}) (time rate change of the momentum) felt by the particle at the moment of bubble rupture:

$$\begin{aligned} F_{burst} &= \frac{d}{dt} (m_{O_2} \cdot v_{O_2}) = \frac{d}{dt} \left(\frac{P_{O_2} V_{O_2} M_{O_2}}{RT} \cdot v_{O_2} \right) = \frac{d}{dt} \left(\frac{2\gamma_{LV}}{r} \frac{M_{O_2}}{RT} \frac{4}{3} \pi r^3 \cdot \frac{d}{dt} \left(\frac{4\pi r^3}{3 \cdot 2\pi r^2} \right) \right)_{r=R_C} \\ &= k_{burst} \gamma_{LV} R_C^3 = k_{burst} \gamma_{LV} \left(\sqrt{\frac{3\gamma_{LV}}{4\rho_L g}} \right)^3 \end{aligned} \quad (74)$$

With this model, we simulate a two-particle oscillator system at various H₂O₂ concentration and observed quantitative agreement with the experimental result (**Figure 7-5**).

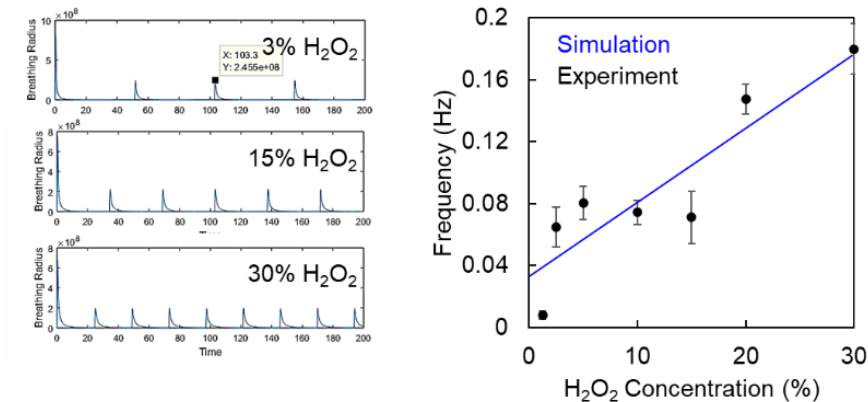


Figure 7-5. (Left) Simulated breathing radius (averaged particle distances from the system's centroid) plotted as a function of time (and its Fast Fourier Transform (right panel) for frequency identification) for oscillators in droplets of different H_2O_2 concentrations. (Right) Overlay of simulated results on top of experimental data for chemo-mechanical oscillator frequency plotted as a function of H_2O_2 concentration.

This quantitative agreement between simulation can be extended to five particle systems (**Figure 7-6**), with experimental result plotted on top and simulation underneath.

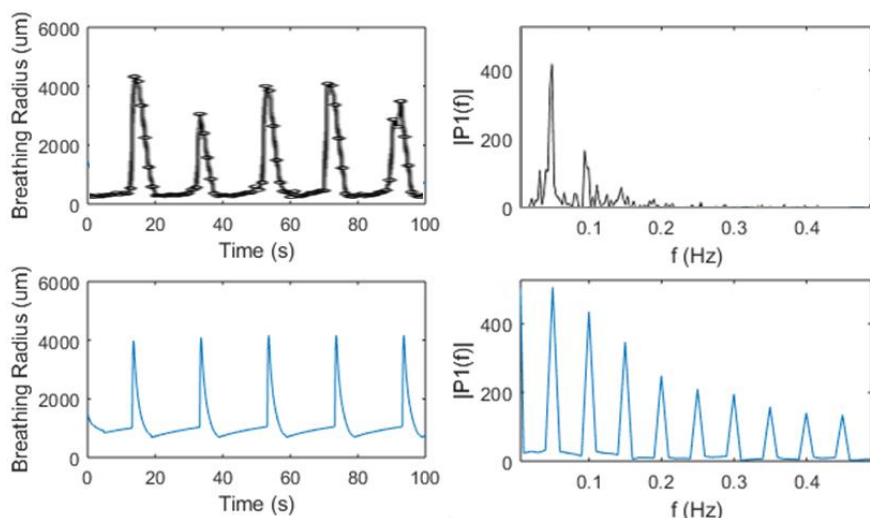


Figure 7-6. (Top) Breathing radius (averaged particle distances from the system's centroid) plotted as a function of time (and its Fast Fourier Transform (right panel) for frequency identification) for a 5-particle chemo-mechanical oscillator in 30% H_2O_2 solution. (Bottom) Simulated breathing radius (averaged particle distances from the system's centroid) plotted as a function of time (and its Fast Fourier Transform (right panel) for frequency identification) for a 5-particle chemo-mechanical oscillator in 30% H_2O_2 solution.

It is worth noting that this type of oscillator has a large parameter space in which the rhythmic beating is present and are not limited to clean-room fabrication. Indeed, we fabricated a magnetic version such Pt catalyzed active particles using a previously reported autoperforation method, and observed the similar chemo-mechanical oscillation inside H_2O_2 (30%) (**Figure 7-7**).

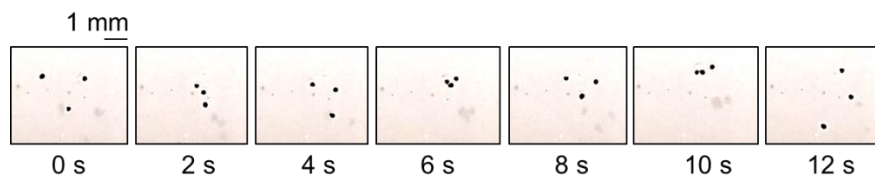


Figure 7-7. Time elapsed optical micrographs of three Pt-Gr-Fe₂O₃/PS-Gr colloidal particles demonstrating collective expansion-contraction behavior in a time-oscillatory fashion.

Chapter 8

Outlook on Colloidal Electronics

The design, fabrication and integration of **colloidal electronics** (sub-picolitre electronic devices embodied within colloidal microparticles) into task-oriented systems – **colloidal electronic matter** – represent an emerging area at the intersection of materials science and chemical engineering. Approaching the form-factor of living biological cells, colloidal electronics offer new modalities of electronics-cell interactions. When different types of specialized, ‘differentiated’ colloidal electronic ‘cells’ congregate into synergistic ‘tissue’-like scaffolds, they bring sensing, communication, and computation to previously inaccessible locations, creating new opportunities in medicine, environmental studies, and human-machine interface.

The four thrusts of my thesis research have sought to tackle the central challenges in the nascent field of colloidal electronic matter: **(1) energy access (Chapter 2–4)**, **(2) decentralized communication (Chapter 5)**, **(3) information gathering and storage (Chapter 6)**, and **(4) systems assembly (Chapter 7)**. The long-term trajectory of my future research will be defined by developing the chemical tools and engineering principles guided by the following questions: **(I)** How do individual devices assemble into higher-order purpose-oriented structures? **(II)** How do simple interactions transmit information hierarchically? **(III)** How can we harness and coordinate these interactions to efficiently create dynamic and complex systems? My future research efforts will leverage expertise in *materials processing*, *chemical catalysis*, and *electronic device fabrication* to help answer these questions that may bear far-reaching scientific and engineering significance. In this outlook chapter, I will outline several promising directions that builds upon my thesis research to address the key challenges associated with **colloidal electronics**.

8.1 Across the Solid-Liquid Interface: Energy Harvesting for Distributed Colloidal Electronic Systems

In *Chapter 1*, I described the mismatch between the electrical energy supply and demand at the microscale. To bridge this energy gap, one could build upon prior work and continue to explore different liquid-based energy harvesting methods that are classified as the ‘*solvo-voltaic*’ effect,¹ a phenomenon whereby various local energy inputs are converted into electricity within a quantum-confined nanostructure (*e.g.*, single-walled carbon nanotube, or SWCNT) by virtue of interactions with the surrounding solvent molecules. This technique stands out as a promising candidate to complement existing energy generation schemes like the photovoltaics, whose utility is diminished where visible light is not present.

Initial efforts could focus on fundamental mechanistic studies aiming to elucidate and generalize the *solvo-voltaic* voltage generation mechanism. One could set up single SWCNT device studies where certain dopant species can be introduced to the surface of a chirality controlled SWCNT device via a microfluidic channel; simultaneously, the electrical and optical (*e.g.*, Raman) responses will be monitored (**Figure 8-1**). The output voltage can be optimized by systematically tuning several input parameters: (1) dopant identity (from which the propensity for electron transfer between itself and the SWCNT device, as characterized by the free energy difference of electron transfer ΔG_{ET} , can be calculated), (2) flow velocity profile $\mathbf{v}(\mathbf{r})$ around the SWCNT device (from which the slip velocity of the liquid dopant can be determined), (3) radiative energy (heat $k_{\text{B}}T$ and light $h\nu$) input into the SWCNT device, (4) lattice deformation under axial stress \mathbf{F} modulated

by a mechanical actuator, and (5) covalent or non-covalent functionalization of the SWCNT lattice (which fine-tunes its electronic structure that in turn affects ΔG_{ET}). These fundamental single device studies will give rise to mechanistic insights that ultimately guide designs for *solvo-voltaic* modules optimized for a variety of solvent (dopant) compositions, flow patterns, temperatures, *etc.* as encountered by colloidal electronics in various application scenarios.

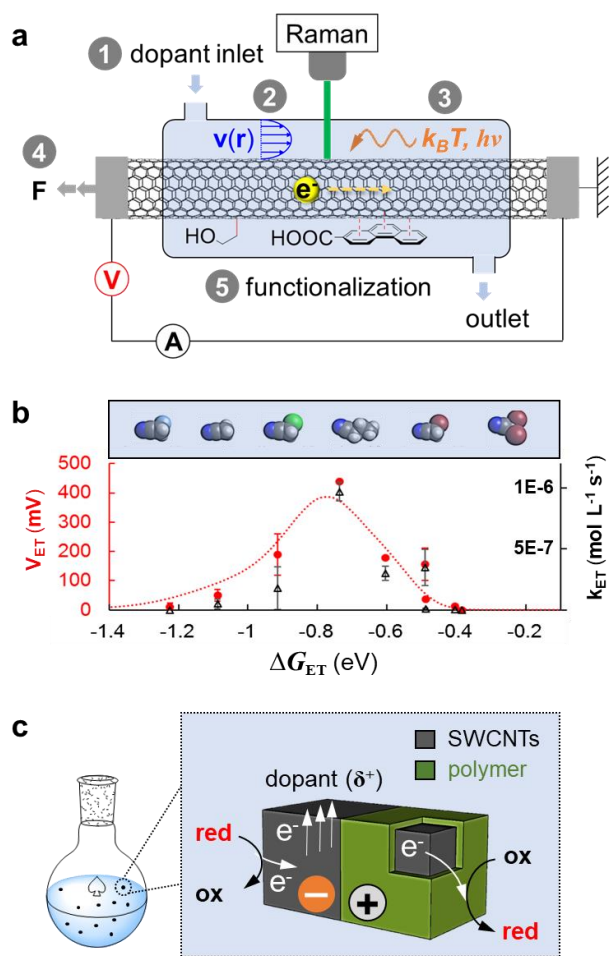


Figure 8-1. (a) Experimental setup for single-SWCNT *solvo-voltaic* electricity harvesting studies. Parameters that can be controlled are: (1) dopant identity, (2) dopant flow rate and velocity profile, (3) heat or light inputs, (4) SWCNT mechanical deformation, and (5) SWCNT functionalization.

(b) Voltage (V_{ET} , red) and rate of electron transfer (k_{ET} , black) measured as a function of the free energy available (ΔG_{ET}) for the SWNT-to-dopant electron transfer. (c) Colloidal *solvo-voltaic* generators for self-powered electrochemistry.

By tuning these five parameters independently, this research direction seeks to construct a generalized *solvo-voltaic* electricity generation scheme that incorporates several orthogonal processes. One such process isolates the effect of electron transfer (ET) between the dopants and the SWCNT. My previous work in **Chapter 4** showed that the rate of electron transfer (k_{ET} , **Figure 8-1b**, black) between SWCNT and the electron deficient (*p*-type) dopants can be calculated from the free energy difference between the SWCNT donor and the dopant acceptor (ΔG_{ET}) using the Marcus ET theory:²

$$k_{ET} = \pi d \exp \left[-\frac{(\lambda - \Delta G_{ET})^2}{4\lambda k_B T} \right] \quad (75)$$

Here d represents the diameter of the SWCNT device and λ denotes the solvent reorganization energy that accounts for the thermally induced reorganization of the solvation shell prior to the SWCNT-dopant electron transfer event. With this model, one can make quantitative predictions to the voltage generated (V_{ET} , **Figure 8-1b**, red) across a SWCNT device in this ET process. Future research could expand upon this theoretical framework to incorporate other processes involving fluidic shear (V_{SH} , parameter 2), heat and light excitation (V_{RAD} , parameter 3), and lattice vibration (V_{LV} , parameter 4) into the combined *solvo-voltaic* voltage output (V):

$$V = V_{ET}(k_{ET}) + V_{SH}(\mathbf{v}) + V_{RAD}(k_B T, h\nu) + V_{LV}(\mathbf{F}) \quad (76)$$

Ultimately, this will enable the fabrication of *solvo-voltaic* devices that integrate many forms of energy input (*e.g.*, mechanical, chemical, thermal). Different types of electronic materials (*e.g.*, graphene, MoS₂) and device configurations (**Figure 8-1c**) will be tested, with the goal of creating a broad-band energy harvesting module compatible with a library of solvent compositions (organic or aqueous) under a variety of flow regimes (turbulent or laminar). Apart from powering conventional micro-electronic devices on-board, one could explore using the electricity generated for self-powered electrochemical conversions *in situ* (**Figure 8-1c**), a process that unlocks the ability for colloidal electronic particles to communicate between one another, as well as with biological cells. I expect the artificial *solvo-voltaic* ‘mitochondria’ will play a key role in powering important processes such as communication (**Section 8.2**) and data storage (**Section 8.3**) for next-generation colloidal electronics.

8.2 Self-powered Electrocatalysis as Means of Interparticle & Particle-to-Cell Communication

Decentralized (unit-to-unit) communication enables neighboring electronic colloids to *transmit* and *receive* information between one another. *On-demand* synthesis and release of messenger molecules remains a less explored strategy for enabling inter-unit communication in synthetic systems, despite its prevalence in nature – from the use of hormones for long-distance control of biological processes to the production of neurotransmitters across synaptic clefts for information relays. This modality of signal transmission is particularly effective between microscopic units in confined spaces (*e.g.*, low diameter pipe flow with a large Péclet number). With the ability to generate electricity

locally, one could explore *in situ* electrocatalytic syntheses of messenger molecules (*e.g.*, small organic molecules, hormones, neurotransmitters) as a means of interparticle communication. This also opens up the possibility for a colloidal electronic device to ‘communicate’ with an adjacent biological cell (*e.g.*, by generating action potentials and receiving synaptic outputs, **Figure 1-2a**) – a prospect that could change the landscape of human-machine interaction, as well as that of precision medicine for local intervention of pathological cellular processes.

Energy issues aside, the electrocatalytic synthesis of complex molecules with high selectivity poses challenge of its own. Recent advances in realizing molecularly precise interfaces have created new opportunities towards selective electrocatalysts based on design principles derived from enzymes. This section aims to present future directions for the **creation of enzyme-inspired electrocatalytic active sites** by **(8.2.1)** controlling the polarizing static electric field *at*, and **(8.2.2)** introducing metal-organic framework (MOF) based catalytic pockets *around* an electroactive metal.

8.2.1 Field-assisted Electro-reduction of CO₂ to C₂₊ Products on Morphologically Controlled Metal Surfaces

Developing active and selective catalysts for electrochemical CO₂ reduction to C₂₊ feedstocks stands not only an important objective for closing the carbon cycle, but also a critical first step for building up molecular complexity at places where synthetic precursors are difficult to come by. *In many natural systems, CO₂ represents an abundant source of carbon that colloidal electronic devices can harness as the building-block for complex messenger molecules.* To guide catalytic

selectivity towards higher order C₂₊ product (*e.g.*, propanol-C₃ or butanol-C₄), enzymes have evolved chemical directing groups that polarize reactive intermediates into configurations favorable for the desired products. This research direction aims to mimic this effect by introducing a carefully tuned static electric field at electrocatalytic sites. Recently it has been suggested that electric fields over 0.1 V/Å can alter the energies of adsorbate molecular orbitals, perturbing the activation barriers for different reaction pathways and hence the associated product selectivity.³ Using electrode surface features with small local radii of curvature (< 1 nm), one could seek to generate local electric fields greater or comparable to 1 V/Å, effectively (de)stabilizing transition states of the (un)desired reactive intermediates (**Figure 8-2**). One could introduce morphologically controlled ‘roughness’ to the metal electrode in the form of geometrically defined shapes (*e.g.*, nanopyramids, nanorods, nanotubes, *etc.*). This can be achieved using a combination of top-down (*e.g.*, photo-, e-beam lithography) and bottom-up (*e.g.*, electrochemical, chemical vapor deposition) methods. The resulted ‘roughened’ surfaces can be characterized via scanning electron microscopy (SEM) and atomic force microscopy (AFM). The measured radii of curvature for the surface features will yield an estimation of the generated static electric field that can be calibrated using scanning tunneling microscopy (STM). One could then use these modified electrodes for the model CO₂ reduction reaction at various conditions and monitor the product formation via mass spectrometry and *in situ* Raman or infra-red (IR) spectroscopy. Ultimately, the product distributions can be correlated to the corresponding electric fields – with the goal of elucidating the role static electric

fields play in electrocatalytic selectivity and using this knowledge to guide future catalytic surface designs.

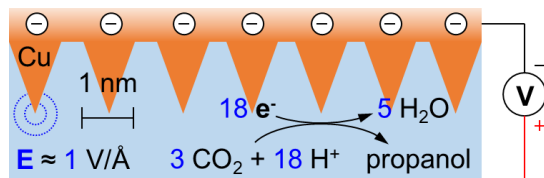


Figure 8-2. Morphologically controlled Cu surface for electrocatalytic CO₂ reduction.

8.2.2 MOF-Metal Hybrid Electrodes with Engineered Catalytic Pockets for Electro-Oxidative C-C Coupling

With access to C₂₊ feedstocks from CO₂ reduction, *C-C coupling chemistry can help further build up the structural complexity of the messenger molecules, enabling colloidal electronic devices to transmit more complex signals* – especially when interfaced with biological cells (*e.g.*, neuron synapses). The electrocatalytic synthesis of elaborate compounds like, for example, the neurotransmitter **dopamine** requires control over not only the catalytically active sites themselves, but also reactant access towards them. Present-day electrocatalysts are much like enzymes stripped down to the bare catalytic site, providing little control over the positioning of chemical species with respect to the active sites and thus severely limiting the possibilities for selectivity modulation. In order to provide a catalytic pocket for controlling the configurations of the chemical species at an electrode, one could develop a hybrid electrocatalyst consisting of a few-layer metal-organic framework (MOF) on the surface of a metal electrode. *Through steric interactions with the reactants and products, the porous MOF will provide a precise handle for*

tuning the selectivity of the underlying electrocatalytic metal. The initial efforts can focus on developing an oxidative C-C coupling reaction known as Kolbe electrolysis (formally a decarboxylative dimerization), via a metal electrode modified by MOFs that possess enzymatic heme-like Fe-oxo centers for promoting oxidative C-H activation (**Figure 8-3**).⁴ The MOF layers therefore not only act as molecular sieves that minimize electrode access from undesired reactive species, eliminating side reactions such as amine oxidation, they also provide a chemically tunable environment around the catalytic site that stabilizes the reactants at a configuration favorable for the desired C-C bond formation.

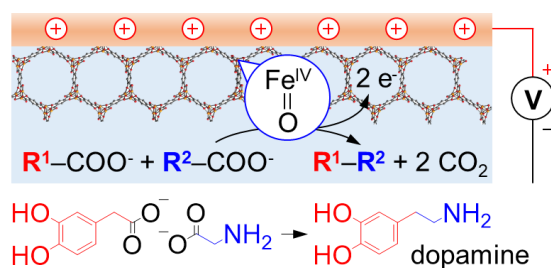


Figure 8-3. MOF-metal hybrid catalytic pockets for Kolbe C-C coupling.

These MOF-metal hybrids combine the molecular-level specificity of homogeneous catalysts with the tunable redox potential of electrochemical catalysts. For distributed colloidal electronics, the improved catalytic selectivity will open possibilities far beyond small molecule electrosynthesis – towards applications such as selective neuronal modulation via the local production of neurotransmitters. Using the Kolbe electrolysis, **dopamine**, for example, is readily available through a one-step synthesis between *glycine* and *3,4-dihydroxyphenylacetate* – metabolites found in high abundance among neurons

(Figure 8-3). The *on-demand* local production of neurotransmitters with micron-level spatial precision shed light on new modalities of intervention to neurological disorder. For instance, Parkinson's Disease (PD), a motor neuron degenerative disorder, is characterized by the progressive loss of the dopamine releasing neuron that promotes motor function. Due to the challenges associated with dopamine delivery across the blood-brain-barrier, the two currently available methods for alleviating PD symptoms are either through (1) the general administration of L-DOPA (*dihydroxyphenylalanine*), a natural precursor of dopamine that can cross the blood-brain-barrier, or (2) the deep-brain electrode silencing of the neurons involved in motor activity inhibition. Between the two unimodal (chemical or electrical) methods, (1) suffers from off-target side-effects due to lack of local control and (2), while highly location specific, is much less effective because it functions by turning OFF an *inhibition* pathway for motor activities, as oppose to directly turning motor functions ON using dopamine. In contrast, the proposed colloidal electronic scheme, whereby dopamine is locally synthesized and released in an electrocatalytic cycle, bypasses the disadvantages from the either unimodal method alone, affording specificity and efficacy simultaneously.

In addition, a general method for controlled local production of neurotransmitters offers new perspectives on human-machine (*i.e.*, neuro-electrode) interfaces – systems that currently rely heavily on direct electrical signal detection from, or stimulation of, the neurons.⁵ The ability to *transmit* (or *receive*) local chemical information *to* (or *from*) the corresponding neurons will greatly increase the dimensionality of the information communicated across the neuro-electrode

interface, and may pave the way to disruptive innovations in this emerging field. To be sure, developing electrocatalysts tuned to specific molecular transformations *without much control over the prescribed local physiological conditions* is a challenging task. This is a task, however, that nature has solved long ago with enzymes, and one that today's chemical engineers are well poised to solve, thanks to the endless list of possible material structures one can create *at or around* the electrocatalytic surface.

8.3 Low-power Nano-electronic Circuits and Their Incorporation into Microparticle Tracers to Enable Time-dependent Sensing and Continuous Information Recording

Nano-electronic materials enable low-power circuit elements that are critical for the power management of colloidal electronics. There are many different nano-electronic modules one can incorporate into the colloidal electronic platform. In this thrust, the initial efforts can be focused on developing one such low-power circuit element – a **memristor** – and using it to build **colloidal electronic sensors** that record **time-dependent** information.

8.3.1 Fabrication of Vertically Aligned Memristor Arrays

Hailed as one the four fundamental circuit elements (together with resistors, capacitors and inductors), **memristors** (or ‘memory-resistors’) are two-terminal electrical resistors that possess two interchangeable memristance states: ON and OFF. The first memristor⁶ was experimentally demonstrated in 2008 using a nanometer-thin TiO₂ junction, and has since generated a lot of interest due to its

potential use in ultra-low-power digital information storage and for applications such as neuromorphic computing. *Chapter 6* describes our initial effort implementing the first memristor design compatible with soft colloidal particles capable of carrying on-board digital information when dispersed in aqueous solutions (**Figure 8-4**).⁷ To achieve this we developed the ‘*autoperforation*’ technique that uses guided 2D material fracture to produce colloidal micro-disks encapsulated within two independently addressable 2D electronic surfaces.⁷

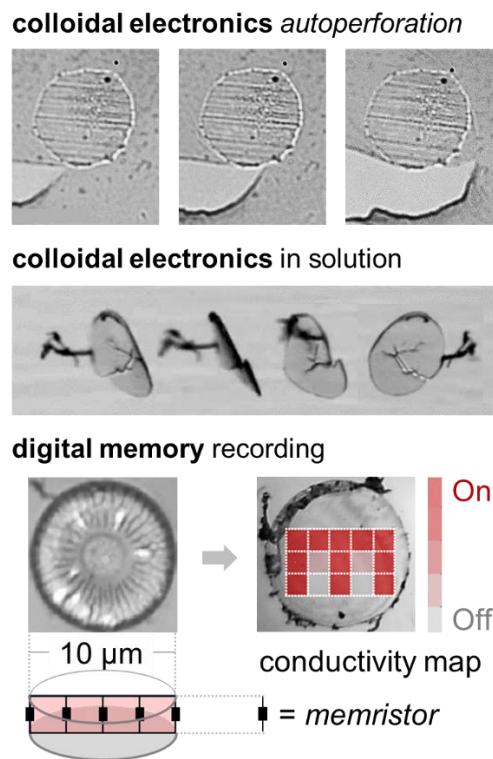


Figure 8-4. Top: guided fracture of graphene around a micro-disk in solution; Middle: a colloidal electronic device (10 μm) traveling in solution; Bottom: vertical **memristive** channels inside a colloidal electronic device with the letter “M” written in digital form.

Future studies could focus on advancing the designs for energy efficient memristive channels – aimed to minimize the amount of energy needed for **memristors** to switch between ON (conductive) and OFF (insulating) states. Different combinations of active memristive materials (*e.g.*, phosphorene, ZnO) can be explored, along with a library of 2D material current collectors (*e.g.*, MoS₂, WSe₂) used for the top and bottom terminals. One could construct a detailed mechanistic model to guide the search for new memristive channels with ultra-low turn-ON/OFF voltages. In addition, one can develop methods to fabricate electronic circuitries consisting of different combinations of the memristor element, via a combination of optical lithography and precision printing techniques. The goal is to produce colloidal devices bearing a parallel array of vertically aligned memristive channels – a device architecture that allows the particle to become time-aware (discussed below).

8.3.2 Design and Optimization of a Local Timing Mechanism

While timing presents little challenge for macroscopic electronic systems (*i.e.*, a digital clock), a downward scalable and energy-efficient timing module does not yet exist for colloidal electronics.⁸ A simple timing circuit can be built, consisting of a memristor array connected in parallel with a single power source (**Figure 8-5**). My initial simulation results suggest that if all memristors in the array were initially turned ON, they will switch OFF sequentially as a function of time, driven by a constant voltage input. The memristor closest to the power source will be switched OFF first, and the furthest one last. As a result, the temporal evolution is transformed into the spatial ON/OFF pattern recorded inside the vertical memristor

array. By measuring a binary (ON/OFF) memristance array at the time of retrieval, the colloidal device's **excursion time** (time elapsed between release and retrieval) can be recorded (**Figure 8-5**, black). Modifications of this original circuit design brings further capabilities. By judiciously incorporating irreversible (or reversible) chemiresistors (resistors that change conductance upon binding to an analyte) in the array, the colloidal sensors bearing these circuits will be able to record the **on-set detection time** of an analyte of interest (or the **duration of a detection event**) (**Figure 8-5**, blue and orange). Ultimately, this study seeks a fundamentally new way for colloidal electronic systems to digitally record time-dependent information via a system of memristors that are highly energy efficient.

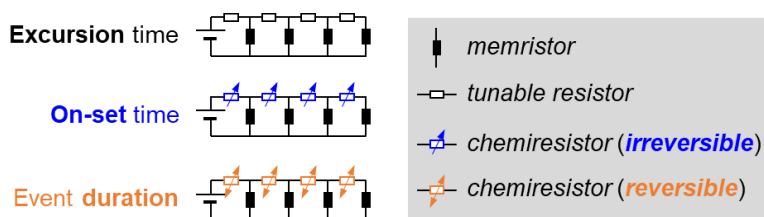


Figure 8-5. A timing circuit designed for low-power **colloidal electronics**, consisting of a *memristor* array connected in parallel with a single power source. Different surface resistor designs give rise to time recordings of different types.

8.3.3 Engineering Time-aware Colloidal Tracers for Time-dependent Continuous Information Recording

The *autoperforated* electronic micro-disks such as those fabricated in **8.3.1** are the ideal vehicles to realize the timing circuit proposed in **8.3.2**. One could explore complex variations of the timing circuit (*e.g.*, two-dimensional ‘bottlebrush’

memristor arrays, **Figure 8-6**, bottom-right) that enable continuous measurements of analyte concentrations as a function of time. The prospect of deploying these electronic microparticles as highly dispersed, nearly massless tracers to *obtain digitized, time-dependent recordings of various environmental attributes* opens exciting possibilities in medicine, environmental monitoring and reaction engineering.

One application that takes full advantage of the microscopic and dispersive nature of these time-aware colloidal tracers is the profiling of the microbiome composition within the GI tract. In humans, this densely packed microbial ecosystem contains 100 trillion endogenous bacteria that help metabolize otherwise indigestible complex carbohydrates into short-chain fatty acids (SCFA), crucial for the modulation of immune response. Dysregulation of the gut flora has already been linked to a host of inflammatory and autoimmune conditions such as *inflammatory bowel disease, asthma, and diabetes mellitus* (both type I and II). There has even been evidence suggesting a causal relation between gut microbiota and *Parkinson's Disease*, through the proinflammatory metabolites that travel across the gut-brain axis.⁹

There is a strong incentive to develop a simple method to track the composition of mammalian gut microbiota and their metabolites. If we model the GI tract as a linear series of plug flow reactors (**Figure 8-6**), the microbial composition down its longitudinal axis varies significantly from stomach to colon – a rich source of spatial information currently inaccessible for disease diagnosis. My group will deploy time-aware pH and SCFA (*e.g.*, acetate, propionate and butyrate) colloidal

sensors into a simulated GI tract, and optimize their designs for accurate concentration read-out. The long-term goal of this study is to establish a general method for mapping the mammalian gut microbiota and the corresponding metabolite compositions with high spatial resolution – aided by advances in time-aware colloidal electronic tracers.

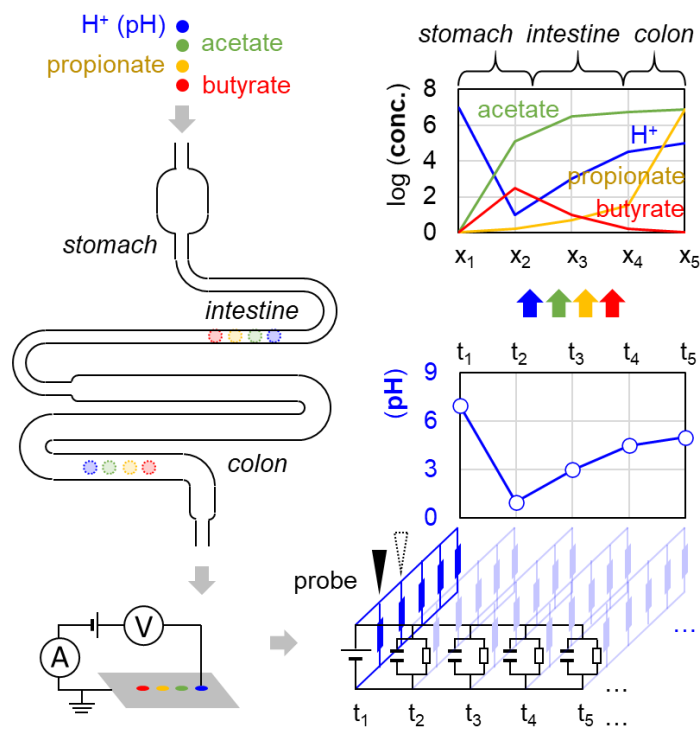


Figure 8-6. Schematic illustration for spatial profiling of gut microbiota metabolite concentrations using **colloidal electronic tracers** with digital readouts. When these tracers are extracted and queried, an electronic probe scans through the surface of each micro-disks, reading a matrix of binary memristance (ON/OFF) values that maps directly onto a concentration profile recorded as a function of time.

8.4 Putting It All Together – Static (Equilibrium) and Dynamic (Non-equilibrium) Assembly of Electronic Colloids into Integrated Electrical Networks

Functional self-assembly is the autonomous organization of components into task-oriented systems. The ability to overcome the entropic barrier to form hierarchical structures is an essential process in biology as well as the overarching objective of **colloidal electronic matter**. The goal here is to develop higher order organizations of **colloidal electronic devices** with spatial heterogeneity, exhibiting ensemble-level functional utilities that push the limit of traditionally inanimate systems at the microscale. Specifically, one direction can be to leverage recent advances in both **top-down** (*e.g.*, additive 3D printing) and **bottom-up** (*e.g.*, guided self-assembly) techniques for colloidal electronic device integration in a distributed manner.

8.4.1 Top-down Integration of Colloidal Electronics into Functional Composites

Most functional materials today are single-level assemblies of monomeric units. In contrast, biological systems have taken a multi-layered approach (*i.e.*, organelles → cells → tissues, *etc.*), allowing multiple control checkpoints to be established at different levels. The initial efforts could focus on incorporating them within existing materials such as *fabrics* and *paint*. Colloidal ink mixtures composed of miniscule electronic devices can be extruded into fibers, and subsequently weaved into *textiles*. When dispersed in solution or a polymer matrix, these electronic colloids can also be directly sprayed onto various surfaces. These approaches will enable smart coatings that can measure temperature, pH or concentrations of

various biomarkers with the stroke of a paintbrush, or enable garments to perform biometric sensing such as sweat analysis for real-time health monitoring.

8.4.2 Bottom-up Assembly of Colloidal Electronics into Artificial Efferent Neurons

Biology is replete with examples of dynamically assembled structures such as flocks of birds or foraging ant colonies. Translating these versatile organizations into inanimate systems requires an understanding of how dissipation of energy can lead to the emergence of ordered structures from disordered components. Because the components in dynamic self-assembling systems interact with one another nonlinearly, their behavior is often complex. As a result, formulating the interaction forces (attractive and repulsive) into design principles that govern the assembly of colloidal electronics is not trivial. One could develop mathematical models to quantify relevant interactions in solution (or at phase boundaries) with the goal of engineering electrical contacts between assembled colloidal devices, and offer practical routes for synthesizing functional device networks *in situ* (e.g., into *parallel* and *serial* electrical circuits¹⁰).

One could prepare different derivatives of colloidal electronic ‘cell lines’ (that specialize in various functions such as *sensing*, *signal amplification*, and *transduction*), use them as constitutive building blocks, and direct their self-ordering into lower-entropy ensembles capable of performing integrated functions (such as an *artificial nerve*, **Figure 8-7**). DNA-mediated docking mechanisms, patchy surface hydrophobicity and a variety of other techniques will be explored to facilitate the assembly of the desired structure. In this design, multiple chemical

inputs can be detected (by ‘*dendritic sensory colloids*, **8.3**), stimulating an amplifying electrical signal (through the energy harvesting *colloidal ‘axons’*, **8.1**), and subsequently be converted into neurotransmitters such as dopamine (via the ‘*synaptic electrocatalytic colloids*, **8.2**). Recently, the fabrication of the first centimeter-scale artificial *afferent* neuron (for ascending sensory signals to the brain) using flexible organic materials was reported.¹¹ Building on the wealth of existing knowledge in colloidal science, these efforts seek to develop an artificial *efferent* neuron (for descending motor signals from the brain) – with a sub-millimeter overall system footprint. This demonstration, if successful, can provide the technological basis for building artificial systems that strengthen, weaken, or make new neuronal connections for treating ailments such as spinal cord injury, Parkinson’s disease, and other neurodegenerative disorders.

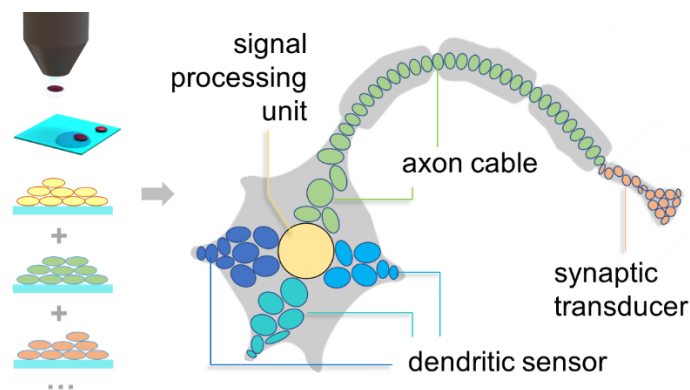


Figure 8-7. Schematic illustration of an **artificial efferent nerve** assembled (via 3D printing or guided self-assembly) from **electronic colloids** designed for different specialized functions.

8.5 References

- (1) Liu, A. T.; Zhang, G.; Cottrill, A. L.; Kunai, Y.; Kaplan, A.; Liu, P.; Koman, V. B.; Strano, M. S. *Adv Energy Mater* **2018**, *8*, 1802212.
- (2) Kunai, Y.; Liu, A. T.; Cottrill, A. L.; Koman, V. B.; Liu, P.; Kozawa, D.; Gong, X.; Strano, M. S. *Journal of the American Chemical Society* **2017**, *139*, 15328.
- (3) Che, F.; Gray, J. T.; Ha, S.; Kruse, N.; Scott, S. L.; McEwen, J.-S. *ACS Catalysis* **2018**, *8*, 5153.
- (4) Xiao, D. J.; Bloch, E. D.; Mason, J. A.; Queen, W. L.; Hudson, M. R.; Planas, N.; Borycz, J.; Dzubak, A. L.; Verma, P.; Lee, K.; Bonino, F.; Crocellà, V.; Yano, J.; Bordiga, S.; Truhlar, D. G.; Gagliardi, L.; Brown, C. M.; Long, J. R. *Nature Chemistry* **2014**, *6*, 590.
- (5) Hong, G.; Fu, T.-M.; Qiao, M.; Viveros, R. D.; Yang, X.; Zhou, T.; Lee, J. M.; Park, H.-G.; Sanes, J. R.; Lieber, C. M. *Science* **2018**, *360*, 1447.
- (6) Strukov, D. B.; Snider, G. S.; Stewart, D. R.; Williams, R. S. *Nature* **2008**, *453*, 80.
- (7) Liu, P.; Liu, A. T.; Kozawa, D.; Dong, J.; Yang, J. F.; Koman, V. B.; Saccone, M.; Wang, S.; Son, Y.; Wong, M. H.; Strano, M. S. *Nature Materials* **2018**, *17*, 1005.
- (8) Liu, A. T.; Strano, M. S. *Nature Reviews Materials* **2019**.
- (9) Sampson, T. R.; Debelius, J. W.; Thron, T.; Janssen, S.; Shastri, G. G.; Ilhan, Z. E.; Challis, C.; Schretter, C. E.; Rocha, S.; Gradinaru, V. *Cell* **2016**, *167*, 1469.
- (10) Gracias, D. H.; Tien, J.; Breen, T. L.; Hsu, C.; Whitesides, G. M. *Science* **2000**, *289*, 1170.
- (11) Kim, Y.; Chortos, A.; Xu, W.; Liu, Y.; Oh, J. Y.; Son, D.; Kang, J.; Foudeh, A. M.; Zhu, C.; Lee, Y.; Niu, S.; Liu, J.; Pfattner, R.; Bao, Z.; Lee, T.-W. *Science* **2018**, *360*, 998.